Spectral evolution of hot hydrogen-rich white dwarfs

Dissertation

der Mathematisch-Naturwissenschaftlichen Fakultät

der Eberhard Karls Universität Tübingen

zur Erlangung des Grades eines

Doktors der Naturwissenschaften

(Dr. rer. nat.)

vorgelegt von

Semih Filiz

aus Konak/Türkei

Tübingen

2026

Gedruckt mit Genehmigung der Mathematisch-Naturwissenschaftlichen Fakultät der Eberhard Karls Universität Tübingen.

Tag der mündlichen Qualifikation:	24.07.2026
Dekan:	Prof. Dr. Thilo Stehle
1. Berichterstatter:	Prof. Dr. Klaus Werner
2. Berichterstatter:	Prof. Dr. Andrea Santangelo

Table of Contents

1 Introduction **10**
- 1.1 Final stages of stellar evolution . . . 11
- 1.2 Atmospheric composition of white dwarfs . . . 12
- 1.3 Spectral evolution of hot H-rich white dwarfs . . . 14
- 1.4 Model atmospheres of hot white dwarfs . . . 15
- 1.5 Photometric variability in hot white dwarfs . . . 16
- 1.6 Motivation and sample selection . . . 17

2 Work in context **19**
- 2.1 Spectral evolution of hot hybrid white dwarfs: I. Spectral analysis . . . 19
- 2.2 Spectral evolution of hot hybrid white dwarfs: II. Photometry . . . 20

3 Results & discussion **21**
- 3.1 Analysis Methods . . . 21
  - 3.1.1 Spectral analysis with the Tübingen Model Atmosphere Package . . . 21
  - 3.1.2 Spectral energy distribution fitting . . . 25
  - 3.1.3 Time-series photometry . . . 27
- 3.2 Results . . . 29
  - 3.2.1 Stellar parameters . . . 29
  - 3.2.2 Infrared excess & photometric variability . . . 31
- 3.3 Discussion . . . 33
  - 3.3.1 Mass-loss, diffusion, and accretion . . . 33
  - 3.3.2 Central stars of planetary nebulae . . . 38
  - 3.3.3 Mass discrepancy . . . 40

4 Outlook **42**

Bibliography **43**

A Original publications **56**

Zusammenfassung

Die Atmosphären Weißer Zwerge (WDs) mögen auf den ersten Blick täuschend einfach erscheinen. Tatsächlich zeigen die meisten WDs in ihren optischen Spektren ausschließlich Wasserstoff (Spektraltyp DA) oder Helium (Spektraltypen DO und DB). Sowohl theoretische Studien als auch Beobachtungen in verschiedenen Wellenlängenbereichen während der letzten Jahrzehnte haben jedoch gezeigt, dass die Atmosphären Weißer Zwerge entlang ihrer Abkühlungssequenz erhebliche Veränderungen in ihrer chemischen Zusammensetzung durchlaufen können – ein Prozess, der als spektrale Entwicklung bezeichnet wird. Diese Transformation kann entweder durch einen einzelnen Elementtransportmechanismus oder durch das Zusammenspiel mehrerer Prozesse beeinflusst werden, darunter gravitative Sedimentation, radiative Auftrieb, Massenverlust, Konvektion und Akkretion.

Während das Auftreten nur eines Elements im Spektrum die häufigste Konfiguration darstellt, zeichnet sich eine kleine Gruppe von WDs dadurch aus, dass sowohl Wasserstoff- als auch Heliumlinien in ihren optischen Spektren vorhanden sind. Diese sogenannten hybriden WDs (Spektraltyp DAO) bilden den Großteil der wasserstoffdominierten Sterne am heißen Ende der Abkühlungssequenz Weißer Zwerge ($T_{\rm eff} \approx 100\,{\rm kK}$). Im theoretischen Rahmen wurde Massenverlust als verantwortlicher Mechanismus für das Vorhandensein von Helium in den Atmosphären der DAO-WDs etabliert, und neuere Studien zeigten, dass die Mehrheit (≈75%) der WDs eine hybride Phase durchläuft. Ein klarer evolutionärer Zusammenhang zwischen DAO- und DA-WDs konnte jedoch bislang nicht eindeutig beobachtend nachgewiesen werden. Das Haupthindernis hierbei liegt in der Modellierung der Sternatmosphären und der Spektralanalyse, insbesondere bei der Verwendung optischer Spektren. Dies liegt hauptsächlich daran, dass die optische Analyse heißer wasserstoffreicher WDs systematischen Effekten unterliegt, die eine präzise Bestimmung der Atmosphärenparameter erschweren. Glücklicherweise können Atmosphärenparameter mithilfe ultravioletter (UV) Spektroskopie hochpräzise bestimmt werden, indem die Ionisationsgleichgewichte mehrerer metallischer Spezies ausgenutzt werden.

Das primäre Ziel dieser Dissertation bestand daher darin, die spektrale Entwicklung heißer ($T_{\rm eff} \geq 60\,{\rm kK}$) wasserstoffreicher (13 DAO- und 19 DA-) WDs mittels Spektralanalyse sowohl im UV als auch im optischen Bereich zu untersuchen. Unter Verwendung modernster Modelle im Rahmen des nichtlokalen thermodynamischen Gleichgewichts (NLTE) wurden $T_{\rm eff}$, $\log\, g$ sowie Elementhäufigkeiten aus beiden Wellenlängenbereichen bestimmt. Dadurch konnten die untersuchten Objekte präzise auf der Abkühlungssequenz Weißer Zwerge eingeordnet sowie die evolutionären Veränderungen ihrer Häufigkeitsmuster analysiert werden. Dies ermöglichte es, den evolutionären Übergang von DAO- zu DA-WDs eindeutig aufzuzeigen, den Übergangsbereich bei $T_{\rm eff} \approx 75-85\,{\rm kK}$ zu bestimmen und die zugrunde liegenden Elementtransportmechanismen zu identifizieren. Das Häufigkeitsmuster der DAO-WDs zeigt, dass bei Temperaturen von $\geq 105\,{\rm kK}$ Massenverlust der dominierende Mechanismus ist. Unterhalb dieser Temperaturen lassen sich die kombinierten Auswirkungen atomarer Diffusion und radiativer Auftrieb aus der Abnahme leichter Metalle und der Zunahme von Elementen der Eisengruppe ableiten. Unterhalb des Übergangsbereichs verlieren radiative Kräfte allmählich ihre Wirksamkeit gegenüber der gravitativen Sedimentation. Dies wird im Kontext der Diffusionstheorie weiter diskutiert.

Darüber hinaus wurden Radien, Leuchtkräfte und Massen durch Anpassung der spektralen Energieverteilungen (SEDs) der untersuchten Objekte bestimmt. Die beobachtete Korrelation zwischen den Heliumhäufigkeiten und den Leuchtkräften hybrider WDs unterstreicht den Einfluss strahlungsgetriebener Winde. Ebenfalls diskutiert wurde die Diskrepanz zwischen verschiedenen Methoden zur Massenbestimmung heißer WDs – ein

seit Langem bekanntes Problem zwischen den aus SED-Anpassungen bestimmten Massen und denjenigen, die aus stellaren Evolutionsmodellen interpoliert werden. Der Einsatz von Atmosphärenmodellen, die den Einfluss von Metallinien berücksichtigen, sowohl in der Spektralanalyse als auch bei der SED-Anpassung wurde zuvor als mögliche Lösung vorgeschlagen. Die Einbeziehung von Metallopazitäten in die Modelle löst jedoch die in dieser Arbeit festgestellte Massendiskrepanz nicht.

Schließlich zeigen sechs der untersuchten Objekte einen Infrarot-(IR) Exzess, während vier Objekte als photometrisch variabel identifiziert wurden. Die Ursache des IR-Exzesses und/oder der photometrischen Variabilität wurde für die Mehrheit dieser Objekte bereits in der Literatur beschrieben. Dennoch konnten in dieser Dissertation für einige von ihnen neue Erkenntnisse gewonnen werden.

Abstract

White dwarf (WD) atmospheres may, at first glance, appear deceptively simple. Indeed, the majority of WDs exhibit only hydrogen (spectral type DA) or helium (spectral types DO and DB) in their optical spectra. However, both theoretical studies and multi-wavelength observations in the last decades has proven that WD atmospheres can undergo a significant change in composition on the cooling sequence, which is referred to as spectral evolution. This transformation may be influenced by an individual element transport mechanism or an interplay of several processes, such as gravitational settling, radiative levitation, mass-loss, convection, and accretion.

While single element spectral appearance is the most common configuration, a small group of WDs are distinguished with both hydrogen and helium lines in their optical spectra. These so-called hybrid WDs (spectral type DAO) comprise the majority of hydrogen dominated stars at the hot end of the WD cooling sequence ($T_{\rm eff} \approx 100\,{\rm kK}$). In theoretical framework, mass-loss was established as the responsible mechanism for presence of helium in the DAO atmospheres and recent studies showed that the majority ($\approx$75%) of WDs run through hybrid phase. However, a clear evolutionary link between DAO and DA WDs is yet to be observationally demonstrated. The main obstacle in this endeavour is the stellar atmosphere modelling and the spectral analysis, namely employing optical spectra. This is mainly because optical analysis of hot hydrogen-rich WDs are subject to systematic effects that hinder accurate measurements of the atmospheric parameters. Fortunately, atmospheric parameters can be determined via ultraviolet (UV) spectroscopy in high precision by exploiting ionization equilibria of multiple metallic species.

Therefore, the primary goal of this dissertation was to inspect the spectral evolution of hot ($T_{\rm eff} \geq 60\,{\rm kK}$) hydrogen-rich (13 DAO and 19 DA) WDs via spectral analysis in both UV and optical. By using state-of-the-art nonlocal thermodynamic equilibrium (NLTE) models, $T_{\rm eff}$, $\log\, g$, and element abundances were determined from both wavelength ranges and the sample objects were accurately located on the WD cooling sequence as well as the evolutionary change in their abundance patterns. This allowed us to clearly reveal the DAO to DA evolutionary channel, to mark the transition region at $T_{\rm eff} \approx 75{-}85\,{\rm kK}$, and to identify underlying element transport mechanisms. The abundance pattern of the DAO WDs reveals that at temperatures above $\geq 105\,{\rm kK}$ mass-loss is the dominant mechanism. Below said temperatures, combined impacts of atomic diffusion and radiative levitation can be deduced from the abundance decrease in light metals and increase in iron group elements. Below the transition region, radiative forces gradually lose effectiveness against gravitational settling. This is further discussed in the context of diffusion theory.

Moreover, radii, luminosities, and masses were derived by fitting the spectral energy distributions (SEDs) of the sample objects. The correlation observed between the helium abundances and luminosities of hybrid WDs supports the influence of the radiation driven winds. The discrepancy in the mass-derivation methods of hot WDs were also discussed, which is a longstanding problem encountered between the ones determined from the SED fitting and interpolated from stellar evolutionary tracks. Employing fully metal line blanketed atmosphere models in both spectral analysis and SED fitting was previously suggested as a possible solution. However, inclusion of metal opacities in the models does not resolve the mass discrepancy detected in this work.

Finally, six sample objects show an infrared (IR) excess, whereas four objects are identified as photometrically variable. The source of the IR excess and/or photometric variability for the majority of these objects has been already reported in the literature. However, new information has been uncovered for a few of them in this dissertation.

Abbreviations

AGB	Asymptotic Giant Branch
ATLAS	Asteroid Terrestrial-impact Laser Alert System
BLP	Balmer Line Problem
CSPN	Central Star of the Planetary Nebula
CSS	Catalina Sky Survey
DFG	Deutsche Forschungsgemeinschaft (German Research Foundation)
ESA	European Space Agency
EUV	Extreme Ultraviolet
FUSE	Far Ultraviolet Spectroscopic Explorer
HRD	Hertzsprung-Russell diagram
HST	Hubble Space Telescope
IR	Infrared
LTE	Local Thermodynamic Equilibrium
LWRS	Low Resolution Spectrograph (on FUSE)
NLTE / non-LTE	Non-Local Thermodynamic Equilibrium
SDSS	Sloan Digital Sky Survey
STIS	Space Telescope Imaging Spectrograph (on HST)
TESS	Transiting Exoplanet Survey Satellite
TMAD	Tübingen NLTE Model-Atom Database
TMAP	Tübingen NLTE Model-Atmosphere Package
TP	Thermal Pulse
UV	Ultraviolet
UVES	Ultraviolet and Visual Echelle Spectrograph
VLT	Very Large Telescope
WD	White Dwarf
ZTF	Zwicky Transient Facility

Original publications

Paper I "Spectral evolution of hot hybrid white dwarfs. I. Spectral analysis."
Filiz, S.; Werner, K.; Rauch T.; Reindl N.; 2024 A&A, 691, A290

Paper II "Spectral evolution of hot hybrid white dwarfs. II. Photometry."
Filiz, S.; Reindl, N.; Jones, D.; Sowicka, P.; Dorsch, M.; Rauch, T.; Werner, K.; 2026 A&A, 706, A152

Declaration

This is to certify that, to the best of my knowledge, this thesis is a product of my independent research. The concepts and discoveries detailed herein are entirely original, with proper credit given to collaborators as documented in the respective publications. No additional sources beyond those referenced in the bibliography and related articles have been used.

Tübingen, 2026

Semih Filiz

1 Introduction

"It is reasonable to hope that in the not too distant future we shall be competent to understand so simple a thing as a star."[1] In retrospect of Sir Arthur Eddington's insights, our understanding of stars has substantially increased over the past century. Although it would be unwise to claim that this understanding is complete, many fundamental questions have been addressed since then, including the energy production mechanisms in stars, the origin of chemical elements, star formation, and stellar lifecycles. Among these subjects, stellar evolution is particularly interesting. Contrary to the ancient perception of stars as unchanging and everlasting heavenly bodies, stars go through distinct evolutionary phases characterised by different physical properties (Fig. 1). For the vast majority of stars, this journey culminates in the white dwarf (WD) stage, representing the final evolutionary phase of low and intermediate mass stars.

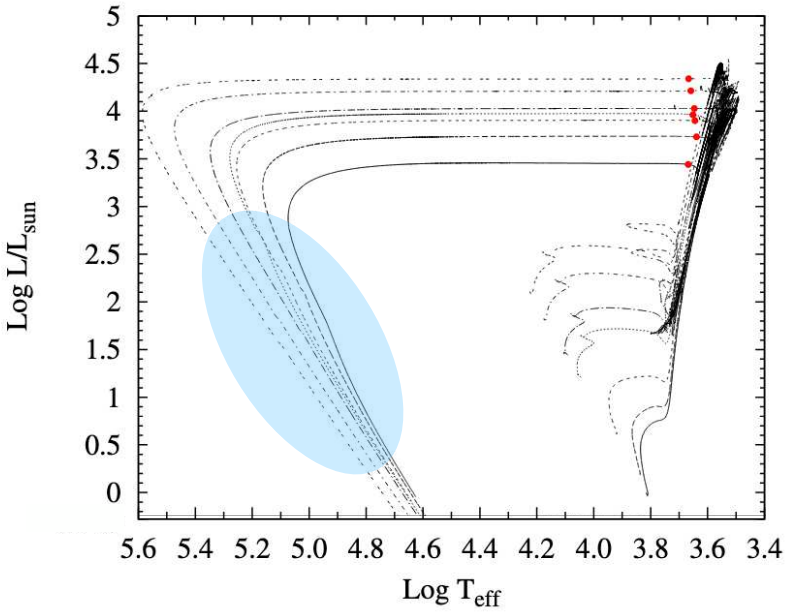


Figure 1: Evolutionary tracks of stars with initial masses $M_i = 0.9{-}3.0\ M_\odot$ in the Hertzsprung-Russell diagram. The approximate location of the white dwarfs subject to this dissertation is highlighted with a blue ellipse. Modified from Fig. 7 of Miller Bertolami (2016).

[1] Sir Arthur S. Eddington, The Internal Constitution of the Stars (1926).

WDs carry a wealth of information and serve as tools for various scientific interests such as determining ages of different Galactic populations (Fontaine et al. 2001; Kalirai 2012; Kilic et al. 2017), investigating internal composition of accreted planetary material (Swan et al. 2023), deriving atomic data of heavy elements (Rauch et al. 2012, 2020), and calibration of astronomical observatories (Rauch 2012; Rauch et al. 2013; Bohlin et al. 2020). Directly or indirectly, all of these studies rely on the information from the WD atmospheres (e.g., surface composition) either in an individual case or of the subgroup that they are associated with. Therefore, accurate modelling of WD atmospheres is essential.

On the other hand, WD atmospheres are governed by several element transport mechanisms, which can lead to substantial changes in the surface composition, the umbrella term of it known as spectral evolution. In this context, this thesis focuses on the spectral evolution of hot hydrogen-rich WDs through spectral analysis and photometry. The remaining of this chapter gives an overview on the WDs in the context of their evolution, atmospheric composition, observational properties, modelling requirements, with an emphasis on the hot H-rich WDs and concludes with the motivation of this study and the sample selection. In Sect. 2, a summary of the research papers subject to this dissertation is provided. The results and their implications are discussed in Sect. 3. Sect. 4 concludes this thesis and gives an outlook on the future work.

1.1 Final stages of stellar evolution

The final stages of low- and intermediate-mass ($0.8 - 8\,M_{\odot}$) stars are governed by a variety of complex and interconnected physical processes, but their structure in the asymptotic giant phase (AGB) is comparatively well-understood. At this stage, the AGB star has already completed core H and He burning and the nuclear reactions transitioned to a shell configuration, where the degenerate carbon−oxygen core is surrounded by a He burning and a H burning shell. In between these two shells lies an intershell region, accumulating more fusion product from above H burning shell that is encompassed by a convective envelope (Fig. 2). At the end of the AGB phase, the He burning shell undergoes a series of energetic instabilities known as thermal pulses (TP).

One of the distinct properties of the AGB stars is mass-loss. Considering low surface gravity and high luminosity, outer layers of the AGB star are gradually expelled. When the mass falls below a critical threshold, the star can no longer stay as a giant and contracts, initiating the post-AGB phase. The post-AGB star evolves at nearly constant luminosity with increasing effective temperature ($T_{\rm eff}$). If the star reaches high enough temperatures ($T_{\rm eff} \approx 30\,{\rm kK}$), it ionizes the expelled material, evolving as a central star of a planetary nebula (CSPN). It is predicted that only objects with initial masses ranging from $1\,M_{\odot}$ to $8\,M_{\odot}$ produces planetary nebulae (Weidmann et al. 2020). Once the fusion processes entirely stop, the star enters the WD cooling sequence. WDs are perceived as "dead" stars due to exhaustion of nuclear reactions. This notion might unintentionally imply termination of all physical processes, but for reasons that will become obvious, this is not the case.

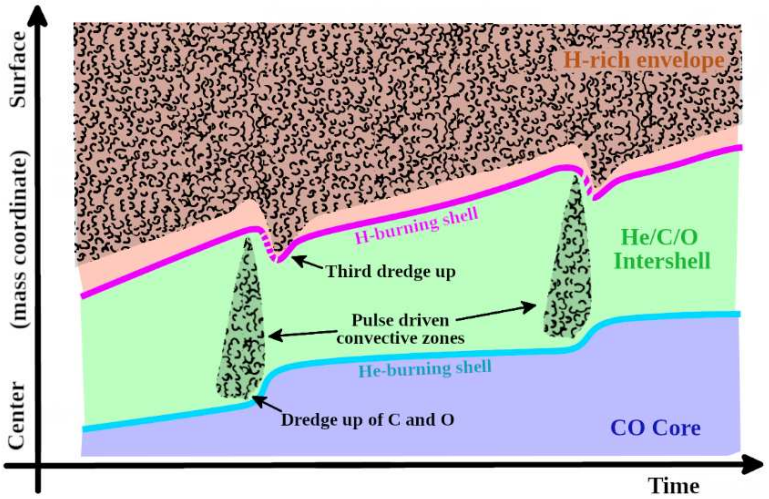


Figure 2: Time evolution of the internal structure of an AGB star displayed in a schematic Kippenhahn diagram. Image taken from Miller Bertolami (2024).

1.2 Atmospheric composition of white dwarfs

After experiencing substantial mass-loss in the AGB phase, the remnant WD is left with a typical mass of $0.6\,M_{\odot}$ that is crammed into an Earth-like size, resulting in an immense surface gravity. A WD retains the majority of the mass in its core, which is composed of carbon and oxygen in most cases. Encasing the core is a helium envelope and an overlying hydrogen layer, a tiny fraction of which comprise the observable atmosphere. Here, the canonical stellar evolution theory paints a picture where WDs with hydrogen-dominated atmospheres (spectral type DA) are the default end products. However, about a quarter of known WDs (Fontaine et al. 2001) instead have helium-dominated atmospheres[2].

On one hand, a large fraction of the WDs fits into this simplistic pure-H or pure-He atmosphere classification, which mainly emerges due to a diffusion process known as gravitational settling. As a consequence of the extreme gravitational field of WDs, heavy elements sink towards the core while the lightest element remains on top, resulting in a layered structure. Gravitational settling occurs on a very short timescale (Dupuis et al. 1992; Koester 2009), which gives the characteristic single element spectral appearance to many of these WDs. On the other hand, spectral classification of WDs might not wholly reflect the atmospheric composition, because WD spectral types are conventionally assigned based on the lines (or lack thereof) detected in their optical spectra[3] (Table 1). In essence, surface compositions of WDs are far more diverse than the H-dominated − He-dominated dichotomy as many objects also contain traces of other elements alongside the main atmospheric marker. If the additional element is detectable in the optical spectra, these objects are classified as hybrid WDs (e.g., spectral types DAO, DBA, and DOZ). Moreover, trace amounts of other elements might be still present in the atmosphere, but

[2]The born again scenario (Iben et al. 1983; Iben 1984) is one of the possible scenarios that creates the H-deficient atmospheres, in which the object experiences a late thermal pulse in the post-AGB phase and the star ascends back to AGB (Werner and Herwig 2006). Another way to create H-deficient atmospheres might be through binary interactions, namely through common envelope evolution or double WD mergers (Reindl et al. 2014a,b; Werner et al. 2017).

[3]H and He transitions are not excited below certain temperatures. Therefore, objects with He-dominated atmospheres ($T_{\rm eff} \lesssim 10\,$kK) have the spectral appearance of cool DQ, DZ, or DC WDs (depending on presence of C or other metals), whereas objects with H-dominated atmospheres ($T_{\rm eff} \lesssim 5\,$kK) have the spectral appearance of DZ or DC WDs (depending on presence/absence of metals).

Table 1: White dwarf spectral types and features.

Spectral type	Spectral features
DA	H lines
DO	He II lines ($T_{\rm eff} \geq 80\,$kK)
	He II and He I lines ($45\,$kK $\leq T_{\rm eff} \leq 80\,$kK)
DB	He I lines
DQ[a]	Molecular and/or atomic C lines
DZ	Metal lines
DC	Featureless spectrum

(a) DQ WDs are found in two subgroups: cool DQs ($T_{\rm eff} \lesssim 10\,$kK) and hot/warm DQs ($10\,$kK $\lesssim T_{\rm eff} \lesssim 25\,$kK; temperature ranges compiled from Bédard 2024). The distinction being rather than a mere temperature difference, these two subtypes of DQ WDs have different atmospheric compositions and go through different evolutionary channels.

go undetected without the availability of ultraviolet (UV) spectra.

From the previous paragraph, the reader might have already inferred that WD atmospheres are not stagnant, but dynamical systems. Indeed, studies conducted in the last four decades has proven that atmospheric composition of WDs undergo a drastic change in the course of their cooling, which is termed as **spectral evolution**. All things considered, the diversity and alteration in the atmospheric composition of WDs cannot be attributed solely to gravitational settling, but rather to processes (e.g., convection, accretion, radiative levitation and mass-loss) that compete against it. Therefore, it is worthwhile to briefly introduce these phenomena.

As the post-AGB star enters the WD cooling sequence, the primary mechanism capable of counteracting diffusion appears to be stellar winds. In hot stars, winds are driven predominantly by the radiative forces acting on metals, which subsequently transfer momentum to the bulk material (H and He, Krtička et al. 2020). As the outward radiative force overcomes gravity, the outer layers of the atmosphere are expelled. Since the resulting mass-loss is chemically homogenous, the development of any compositional stratification due to gravitational settling is effectively inhibited. The presence of mass-loss can be spectroscopically identified through characteristic P Cygni line profiles, which are detected in many CSPNe during their constant luminosity evolution (Herald and Bianchi 2011; Guerrero and De Marco 2013). Just prior to entering the WD cooling track, however, mass-loss begins to gradually weaken, making direct detection unattainable. This is because predicted mass-loss rates ($\approx 10^{-11}\ M_\odot {\rm yr}^{-1}$; Unglaub and Bues 2000) for hot (pre-)WDs fall below the detection threshold from spectroscopy.

Theoretical estimates show that the wind is terminated[4] at the early points of the WD stage (Unglaub and Bues 2000), leading to observable influences of the diffusion in atmospheric composition (Werner et al. 2019). Below this theoretical wind limit, however, metals are still detected in hot WD atmospheres. A key mechanism that can support these elements in the atmosphere is radiative levitation, in which absorption of outgoing radiation provides an upward acceleration to certain ions. In this equilibrium state, metals remain suspended in the atmosphere rather than sinking out of it. Unlike mass-loss, radiative levitation is selective, of which effectiveness is linked to the radiation flux and the opacity (Chayer et al. 1995a, and references therein). This means that heavy ions

[4] Unglaub and Bues (2000) show that mass-loss ceases earlier in the H-rich envelopes than He-rich ones.

with many electron states absorb photon momentum more efficiently with their numerous line transitions than the lighter ones (Rauch et al. 2015; Werner et al. 2019; Löbling et al. 2020). Radiative levitation is most effective in hot white dwarfs and progressively weakens during cooling, impact of which substantially decrease below ≈30 kK (Chayer et al. 1995b), but can still be noticed down to 20 kK depending on the opacity source (Chayer 2014).

One of the most prominent mechanisms for the cool WDs[5] is convection. As the WDs cool, the energy transport in the stellar envelope via radiation becomes ineffective. On the other hand, energy transfer can effectively occur when the hot material from the lower layers is exchanged with cool material from the higher layers of the stellar envelope. This mixing procedure is so effective that it completely erases the imprint of diffusion (Bédard 2024). It is predicted that residual C in H-deficient WDs is efficiently dredged-up due to convection, which provides an explanation for the existence of cool DQ WDs[6] (Bédard et al. 2022, and references therein).

Interestingly, other metals are also detected in the optical spectra (spectral types DAZ, DBZ, and DZ) of many objects below ≈25 kK (Zuckerman et al. 2003; Kilic et al. 2006; Dufour et al. 2007; Koester and Kepler 2015; Hollands et al. 2017). Considering short diffusion time-scales of these cool WDs (Koester 2009) and ineffectiveness of radiative levitation, the presence of the metals is explained by an ongoing or recent accretion episode. Metals in these cool WDs originate from remnant planetary material, which is well established through the detections of many WDs hosting gaseous and dusty debris disks (Jura 2003; Manser et al. 2020; Melis et al. 2020), tidally disrupted planetesimals (Manser et al. 2019), and giant planet candidates (Gänsicke et al. 2019; Vanderburg et al. 2020).

1.3 Spectral evolution of hot H-rich white dwarfs

As mentioned in Sect. 1.2, study of spectral evolution in WDs dates back almost half a century. Early investigations revealed that WDs atmospheres are not as pure as expected from the effectiveness of gravitational settling. As the sample size of the objects showing trace elements increased, it became clear that presence of other competing mechanisms must be invoked (Fontaine and Wesemael 1987, and references therein). A particularly intriguing and, perhaps at the time, quite puzzling case was the presence of helium in the atmospheres of hot H-rich WDs.

Assuming pure-H atmospheres devoid of any He and trace metals, models predicted a high level of soft X-ray/extreme ultraviolet (EUV) flux from hot ($T_{\rm eff} \geq 30$ kK) DA WDs. However, observed X-ray fluxes remained below the predictions for the majority of hot DA WDs, which was presumed to be caused by trace amounts of He in the atmosphere. Early studies, hence, used this prescription to infer the presence of He ($N({\rm He})/N({\rm H}) = 10^{-2.3}$–$10^{-5.3}$) that was otherwise undetectable in the optical spectra (Vennes et al. 1988, and references therein). Initially, radiative levitation was invoked as the supporting mechanism of He in the atmosphere. However, Vennes et al. (1988) demonstrated that the radiative forces could not sustain the amount of He required for the observed short wavelength flux deficiency. Instead, same authors proposed a stratified atmospheric structure in which a thin H-layer ($M_{\rm H}/M_* = 10^{-15}$–10^{-13}) covers the He envelope. This configuration allowed the optical spectrum to still appear DA-like, yet also provided the required He opacity

[5] H-rich WDs start developing a convective envelope at $T_{\rm eff} \approx 16$ kK. In contrast, a small convection zone in the envelope first appears at $T_{\rm eff} \approx 60$ kK for He-rich WDs, which substantially expands below 20 kK (Bédard 2024).

[6] PG1159 - DO - DB - DQ evolutionary channel.

to explain the measured flux deficiency. However, this scenario contradicts canonical stellar evolution theory, which predicts that WDs are born with thick hydrogen envelopes ($M_{\rm H}/M_* = 10^{-4}$, Blöcker et al. 1997). Subsequent studies showed that stratified models did not accurately represent EUV fluxes of many other hot DA WDs, instead EUV flux deficiency was tied to metal opacities (Vennes et al. 1989; Vennes 1992; Vennes and Fontaine 1992).

On the other hand, the prototype of so called hybrid WDs (spectral type DAO) that can be identified from a weak He II λ 4686 Å line in their optical spectra had been long discovered (Eggen and Greenstein 1965). Analysis of known four DAO WDs proved that these objects are more He rich than the DAs inferred from EUV flux deficiency (Wesemael et al. 1985). They measured a typical He abundance of $N({\rm He})/N({\rm H}) = 10^{-2}$ for DAO WDs, which was consistent with the expected amount from stratified atmospheres (Vennes et al. 1988). However, the extensive spectral analysis of Bergeron et al. (1994) revealed that stratified models failed to replicate the observations in almost all cases (except for one object). Instead, chemically homogenous model atmospheres provided a better fit to the optical spectra of hybrid WDs in their sample.

Another significant finding of Bergeron et al. (1994) was that their spectral analysis was heavily affected by the Balmer-line Problem (BLP). This issue is commonly encountered in the optical analysis of hot DA and DAO WDs and designates the inability of achieving simultaneous fits to all Balmer lines with the same atmospheric parameters. Bergeron et al. (1994) concluded that the BLP emerges due to metal opacities present in the atmosphere. Since radiation pressure has been already measured to be insufficient to prevent gravitational settling of He, Bergeron et al. (1994) proposed that presence of He in the DAO atmospheres might be connected to the mass-loss. While direct detection of mass-loss in the hot WD spectra is not possible, indications of it can be still inferred indirectly. Napiwotzki (1999) identified a correlation between the He abundance and luminosity in their DAO type CSPNe sample. As the mass-loss is expected to be radiation driven in these hot WDs, detection of decreasing He abundances with respect to luminosities offered a strong evidence for the case (Napiwotzki 1999).

The impact of radiation driven winds on the atmospheric composition of hot (pre-)WDs was further inspected by Unglaub and Bues (1998, 2000). These authors on a theoretical framework demonstrated that mass-loss rates with $\dot{M} \geq 10^{-12}\ M_\odot {\rm yr}^{-1}$ can prevent the gravitational settling of He in the DAO atmosphere. Once the wind ceases to exist, He can no longer be sustained in the atmosphere. Consequently, a quick transformation from DAO to DA WDs is expected. Considering all the observational evidence and theoretical findings, it was later suggested that DAO and DA WDs share a common evolutionary channel (Gianninas et al. 2010; Bédard et al. 2020).

1.4 Model atmospheres of hot white dwarfs

French philosopher, Auguste Comte's (1798-1857) views on stars are frequently quoted in astronomical textbooks. In his Cours de Philosophie Positive (1835), he wrote:

> We understand the possibility of determining their shapes, their distances, their sizes and their movements; whereas we would never know how to study by any means their chemical composition, or their mineralogical structure...
>
> ... I persist in the opinion that every notion of the true mean temperatures of the stars will necessarily always be concealed from us.

As opposed to Comte's justifiable arguments at that time, stellar spectroscopy today allows us to determine physical parameters of the stars. All this information on the physical parameters is mainly obtained through the star's atmosphere which is the only part that can be directly observed. Compared to overall size of the star, the photosphere can be visualized as a thin layer which is an intermediary between the stellar interior and the space. In that sense, the photosphere is far from being an isolated environment. Therefore, thermodynamic equilibrium (TE) can not be expected.

In reality, stellar atmospheres are open systems with density and temperature gradients. However, if the temperature and density gradients in the gas are small enough and the particle collisional rates are large enough, a small volume element of the gas can reach TE. Thus, the system can be assumed to be in local thermodynamic equilibrium (LTE). Although the LTE assumption is reasonable for high gravity and low temperature stars, such as cool WDs, it fails to represent hot (pre-)WD atmospheres, such as our objects', in which the photon mean free path is large and the collisional rates are low. Therefore, the non-local thermodynamic equilibrium (NLTE) assumption is essential for our purposes. However, constructing NLTE model atmospheres is a challenging task. The radiative transfer equations should be simultaneously solved with the equations of radiative, hydrostatic, and statistical equilibrium, which means that even small changes in the radiation field defines the state of the matter. As a consequence, NLTE modelling requires long computation times and numerical instabilities are frequently encountered.

For most stars, conceptualizing the stellar atmosphere as a static thin layer is reasonable. Consequently, most of the stellar atmosphere studies and grids were generally conducted via computing either LTE (Bergeron et al. 1995; Koester 2010; Bonifacio et al. 2011) or NLTE (Allard 2016; Bédard et al. 2020) model atmospheres in hydrostatic equilibrium assuming plane-parallel geometry (1-D). However, hydrostatic 1-D models are not suitable for each star. Wind models are needed for objects with strong mass-loss, such as Wolf-Rayet stars (Gräfener et al. 2002; Hamann and Gräfener 2003). Since the mass-loss rates of the WDs subject to this dissertation are too low, 1-D NLTE modelling is appropriate.

1.5 Photometric variability in hot white dwarfs

Recurrent brightness changes of the stars can reveal important information about them, including details of their interiors (e.g. pulsations, magnetic fields) or their exteriors (e.g. binarity). Generally, close binarity is the first presumed reason in case a hot WD is subject to photometric variability (Steen et al. 2024; Oliveira da Rosa et al. 2024). Irradiation effect systems are a good example for this, which are composed of a hot primary and a cool secondary. It is expected that the rotational period of the secondary is synchronized to the orbital period of the system (Nebot Gómez-Morán et al. 2011). Hence one hemisphere of the much cooler secondary is constantly irradiated by the primary, which leads to periodic light variations as the projection of the cool companion varies by phase.

In general, intrinsic variability is considered less except for H-deficient GW Vir pulsators (Werner and Herwig 2006). For hot ($T_{\rm eff} \geq 40\,{\rm kK}$) H-rich pre-WDs with different metallicities, g mode pulsations with 40 to 200 s periods are theoretically predicted (Kawaler 1988; Maeda and Shibahashi 2014; Calcaferro et al. 2017). However, no object was found to this date. On the other hand, magnetic fields could also cause photometric variability. Formation of bright spots on the WD surfaces is predicted due to metals gathering near magnetic poles (Hermes et al. 2017b) and rotational modulation caused by surface inhomogeneities has been reported for several hot WDs with $T_{\rm eff} \geq 30\,{\rm kK}$ (Hermes et al. 2017a). Moreover, the occurrence of UHE phenomenon was associated to weak mag-

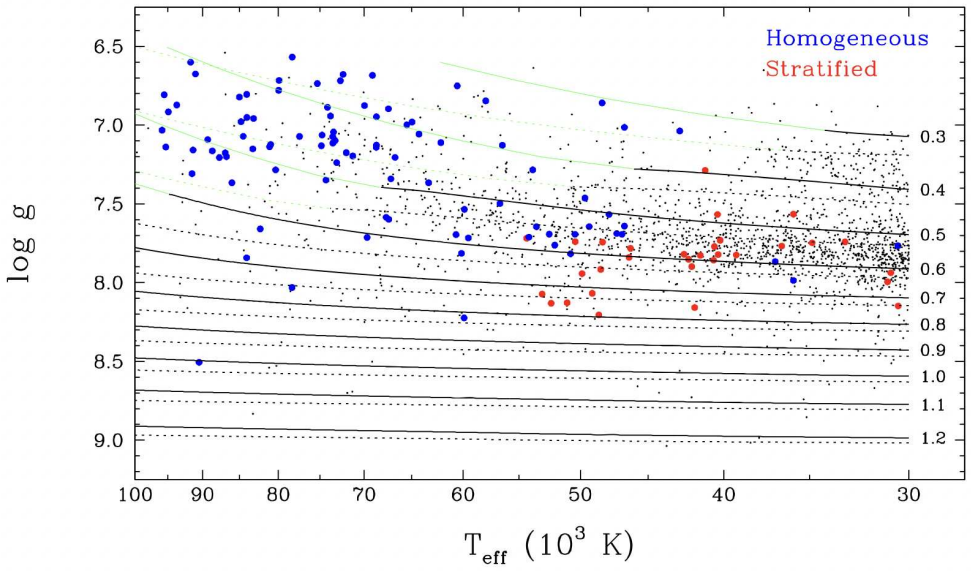


Figure 3: Hybrid WDs shown in the $T_{\rm eff} - \log\, g$ diagram. Image taken from Bédard et al. (2020).

netic fields, in which the photometric variability stems from the rotational modulation of a circumstellar magnetosphere and/or spots (Reindl et al. 2019, 2021).

1.6 Motivation and sample selection

Observational evidence indicates that ≈75% of WDs are born H-rich (Bédard et al. 2020). Although they represent the majority of all WDs, H-rich WDs are rarely found at the beginning of the cooling sequence[7]. Among these H-dominated objects, a particular group stands out with traces of He that they exhibit as a secondary spectral feature. These so called hybrid WDs (DAO) comprise 25−30% of hot H-rich WDs (Bédard 2024, and references therein) and are divided into two subgroups: homogenous and stratified DAOs. Although Bergeron et al. (1994) noted that the DAO WDs in their sample did not belong to a unique sequence, the distinction between homogeneous and stratified hybrids only recently became clear. While homogenous hybrids are found generally above $T_{\rm eff} \approx 60\,$kK, stratified DAOs are exclusively detected below 55 kK (Fig 3). It was demonstrated that stratified DAOs follow the DO − DAO − DA evolutionary channel (Manseau et al. 2016; Bédard et al. 2020), which was explained as the float up of the residual H in the atmosphere.

On the other hand, homogenous DAOs (the subject of this study) are expected to be the progenitors of DA WDs, meaning all H-rich WDs are canonically born as hybrids and with the inevitable termination of mass-loss they transform to DA WDs (Unglaub and Bues 2000; Gianninas et al. 2010; Bédard et al. 2020). Although the DAO to DA channel reflects decades of theoretical and observational inquiry reasonably well, this interpretation is subject to several caveats. First, analyses of hot DAO and DA WDs revealed that the observed wind limit corresponds to a lower $T_{\rm eff}$ than the theoretical prediction (Gianninas et al. 2010; Bédard et al. 2020). In addition, $T_{\rm eff}$ and log g compilation from earlier studies showed that both DA and DAO WDs occupy the same region in the Kiel ($T_{\rm eff} - g$) diagram (Fig. 4). This result was mainly deduced from the analysis of optical

[7]This is mainly because cooling to ≈65 kK takes about a million years, whereas lower $T_{\rm eff}$ is reached in the order of billion years (Renedo et al. 2010).

spectra (Bergeron et al. 1994; Gianninas et al. 2010, 2011) which comprise the bulk of the hot H-rich WD studies. Although, some stars were also analysed via UV spectroscopy (Good et al. 2005; Ziegler 2012; Barstow et al. 2014; Preval et al. 2019), deviations in $T_{\rm eff}$ and log g inferred from two different wavelength regimes are in multiple cases non-negligible (Barstow et al. 2003a; Good et al. 2004). Finally, comparison of observed metal abundances in the hot H-rich WDs and predicted abundances from the diffusion theory revealed inconsistencies (Chayer et al. 1995a,b). This was interpreted as, in addition to the equilibrium of gravitational settling and radiative levitation, a third physical mechanism was needed in the theoretical diffusion calculations, which was generally regarded as mass-loss (Chayer et al. 1995a,b; Gianninas et al. 2010; Rauch et al. 2013). In contrast, due to similarities in the observed species, it was speculated that metals observed in hot DA WD atmospheres originate from accretion of planetary material (Barstow et al. 2014; Preval et al. 2019). Discord in the findings begs to ask these questions:

- If the mass-loss is recognized as the responsible mechanism for the presence of He in the DAO atmospheres, then why DA WDs with the same atmospheric parameters **cannot** drive winds that are strong enough to prevent gravitational settling of He?
- Does a well-defined wind limit exist?
- What parameters other than $T_{\rm eff}$ and log g might influence the termination point of the wind?
- Do metals in all H-rich WDs really originate from the external sources?

Since the optical analyses of hot H-rich WDs are heavily hindered by the BLP and metal abundances can only be measured in the UV, to shed light on these questions, a sample of H-rich (19 DA and 13 DAO) WDs with $T_{\rm eff} \geq 60\,$kK was selected, decisive factor in the selection being the the availability of archival Far Ultraviolet Spectroscopic Explorer (FUSE) or Space Telescope Imaging Spectrograph (STIS) spectra.

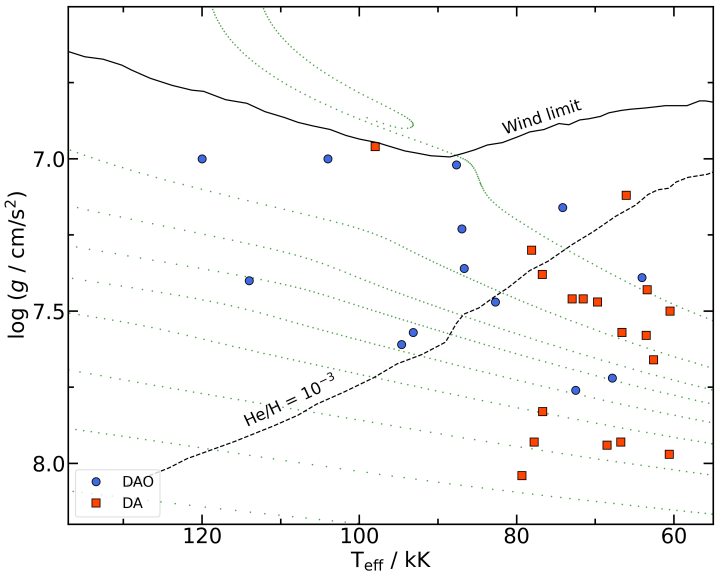


Figure 4: Sample objects with $T_{\rm eff}$ and log g from Gianninas et al. (2010, 2011), Ziegler (2012), and Barstow et al. (2014).

2 Work in context

2.1 Spectral evolution of hot hybrid white dwarfs: I. Spectral analysis

The first paper of the series focuses on a NLTE analysis of 19 DA and 13 DAO WDs with $T_{\rm eff} > 60$ kK, for which we present a combined study of UV and optical spectra. We precisely determined $T_{\rm eff}$, log g, and abundances by exploiting the ionization equilibria of the metal lines in the UV and analysed optical spectra to constrain the atmospheric parameters. This allowed us to accurately locate each object in the $T_{\rm eff} - \log g$ diagram, in which we interpolated masses ($M_{\rm Kiel}$) from the theoretical evolutionary tracks.

As opposed to previous studies, the spectral analysis conducted in this work revealed a clear a distinction between the locations of the DAO and DA WDs, which supports the predicted DAO to DA evolutionary channel. The distinction between observational and theoretical wind limit was further elaborated. The underlying physical mechanisms such as mass-loss, gravitational settling and radiative levitation and their effect on the spectral evolution of hydrogen rich WD are thoroughly discussed. The measured element abundances were also inspected under the theoretical framework of diffusion calculations. Moreover, the plausibility of the accretion scenario was scrutinized with respect to observed abundance patterns. Finally, we discussed the impact of UV analysis on our results and draw a comparison with the earlier studies that relied on optical spectra, only.

Author's contribution
Archival UV and optical data subject to Paper I was collected by the author of this dissertation. The author also computed the model atmospheres and synthetic spectra of the sample WDs and conducted the spectral analysis. The entire manuscript was written by the author.

2.2 Spectral evolution of hot hybrid white dwarfs: II. Photometry

The second paper of the series focuses on the photometric analysis of the sample objects from Paper I. We calculated a generalized Lomb-Scargle periodogram to detect photometric variability in the archival data of the sample objects and measured peak-to-peak amplitudes from the phase-folded light curves. We found that four DA WDs in our sample show photometric variability. The spectral energy distributions of the sample WDs were fitted by utilizing the model spectra calculated in Paper I, to calculate radii, masses ($M_{\rm grav}$), and luminosities. Additionally, we found that six stars in our sample exhibit infrared (IR) excess. All the objects marked as photometrically variable and/or with IR excess were discussed case by case. We further explored the correlation between He abundance and luminosity in the context of spectral evolution of hybrid WDs. Finally, we compared $M_{\rm grav}$ to $M_{\rm Kiel}$ derived in the paper and discussed the implications of the results.

Author's contribution
Archival data of the light curves subject to Paper II was collected and analysed by the author. Only, the light curve analysis of WD 0232+035 required contributions from two co-authors of the paper. The fits to SEDs were also performed by the author of this thesis. 90% of the manuscript was written by the author.

3 Results & discussion

This chapter provides key findings from the spectral and photometric analysis of 19 DA and 13 DAO WDs published in Papers I and II. First, the analysis methods are briefly introduced. Then, an overview of the results are given. The implications of the results are discussed subsequently.

3.1 Analysis Methods

3.1.1 Spectral analysis with the Tübingen Model Atmosphere Package

The NLTE analysis of this work was conducted with the Tübingen Model Atmosphere Package (TMAP[8], Werner and Dreizler 1999; Werner et al. 2003, 2012), which assumes plane parallel geometry (1-D) and computes chemically homogeneous model atmospheres in hydrostatic and radiative equilibrium. Our fully metal line blanketed models include the opacities of H, He, C, N, O, Si, P, S, Fe, and Ni. While atomic data of hydrogen to sulphur were collected from the Tübingen Model Atom Database (TMAD, Rauch and Deetjen 2003), the Tübingen Iron-group opacity interface (TIRO, Rauch and Deetjen 2003; Müller-Ringat 2013) was used for iron and nickel to create model atoms. The need for different tools arises due to the atomic structure of the iron-group elements, namely their large number of atomic energy levels and millions of line transitions which makes a detailed consideration impossible. Therefore, the TIRO tackles this issue with a statistical approach by combining all atomic energy levels of a specific ion to 7 energy bands (or super levels) and each of these bands is treated as a NLTE level. In a similar manner, sampled lines of a specific ion are then combined to super lines.

[8] http://astro.uni-tuebingen.de/~TMAP

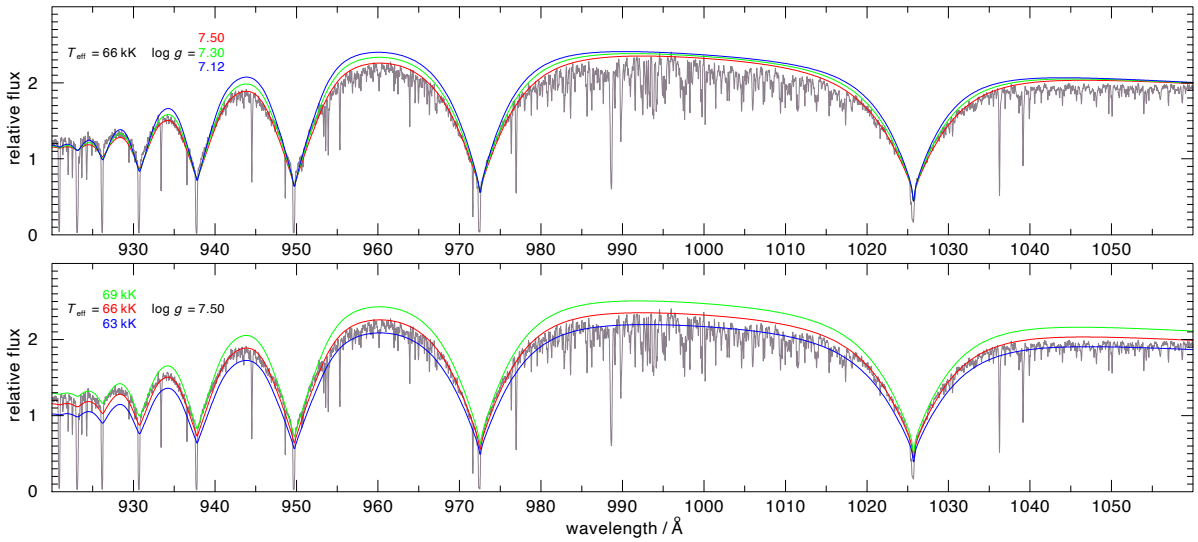


Figure 5: Initial $T_{\rm eff}$ and log g estimations of the DA WD 0621-376 based on FUSE spectra (gray) by using pure-hydrogen TMAP models.

A typical model atmosphere presented in this work is composed of more than 650 NLTE levels (extended model atom). To prevent numerical instabilities and an excessive amount of computation time, however, fully metal line blanketed models were initially built with relatively small model atoms (∼235 NLTE levels). Once they converged, the model atoms were extended without changing the atmospheric structure. Considering millions of narrow Fe and Ni sample lines, model atmospheres calculated in this work employed a fine frequency grid with more than 45 000 frequency points. The strategy for calculating models is outlined below[9].

1. Create a model atom using TMAP with the atomic data acquired from TMAD, in which ionization stages of a particular element are tailored to the desired $T_{\rm eff}$ and log g (for LTE and NLTE models).

2. Create a frequency grid for a given $T_{\rm eff}$, which is needed for the model atmosphere calculations (for LTE and NLTE models).

3. Compute a LTE model for a given $T_{\rm eff}$, log g, and element abundance, which can be used as a start model for the next step.

4. Compute a NLTE model for a given $T_{\rm eff}$, log g, and element abundance.

5. Compute the emergent synthetic spectrum in which the Stark broadening tables of Tremblay and Bergeron (2009) and Schoening and Butler (1989) were used to generate line profiles of H I and He II, respectively.

[9]This process holds for the calculation of pure H/ H+He models as well as metal line blanketed ones.

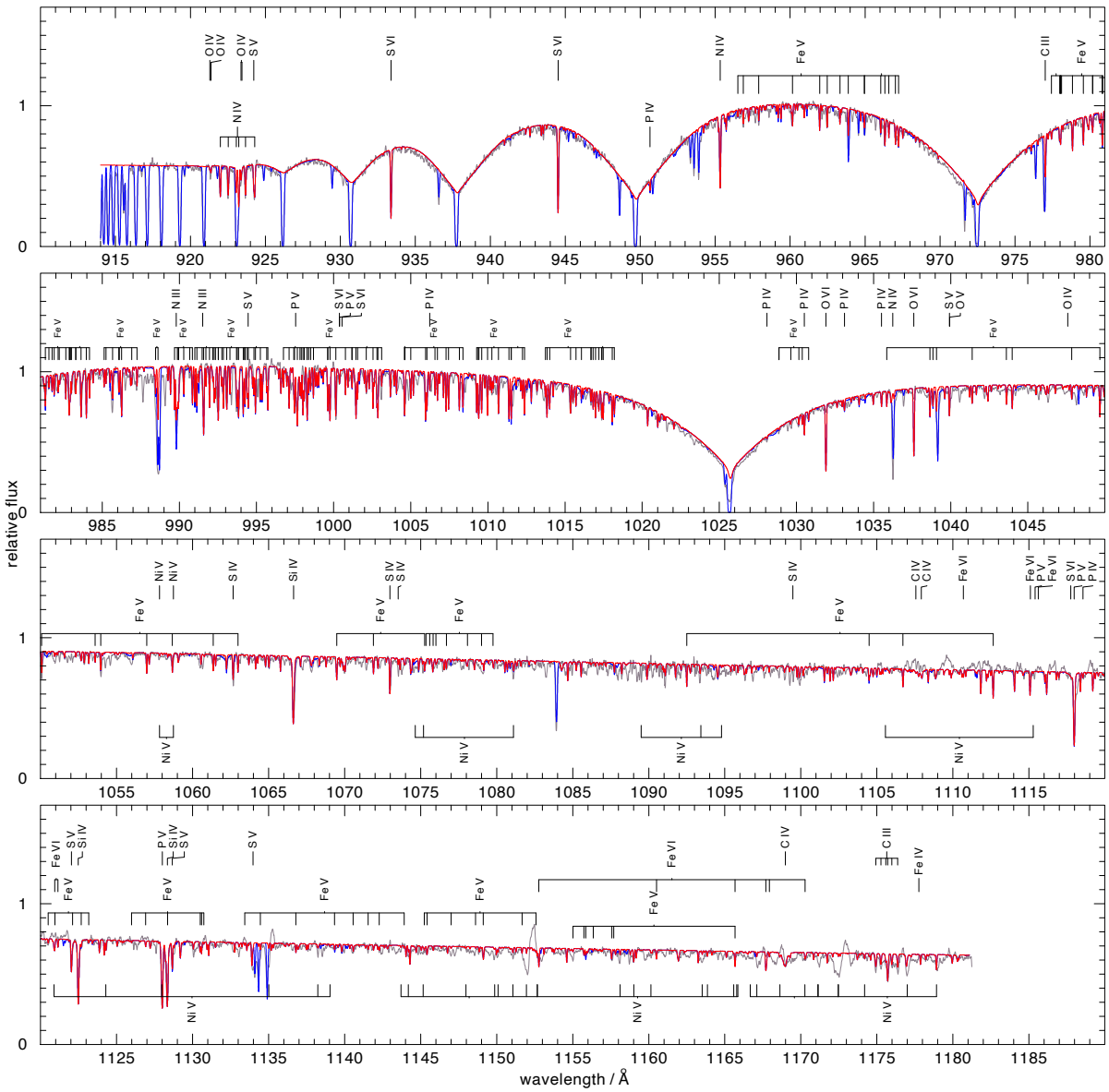


Figure 6: FUSE spectrum (gray) of the DA WD 0621-376. Overplotted is the fully metal-line blanketed TMAP model (red) with $T_{\rm eff} = 65\,{\rm kK}$, $\log\, g = 7.5$ (g/cm^2). The blue graph shows the same model including the ISM lines.

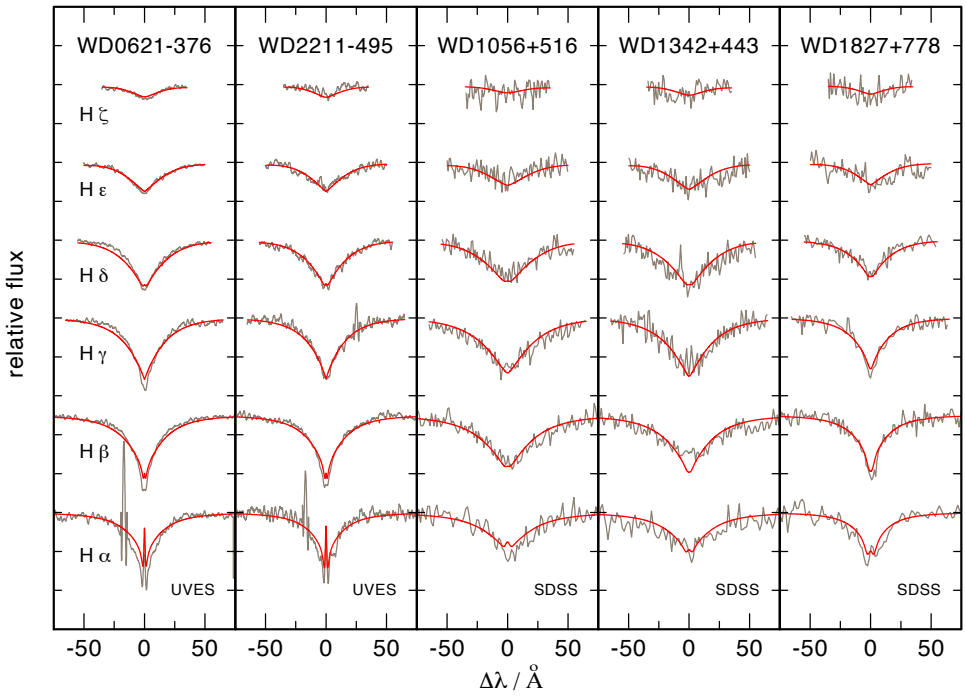


Figure 7: UVES and SDSS spectra of several DA WDs. Overplotted are the TMAP models (red).

As mentioned in Sect. 1.4, constructing NLTE model atmospheres is computationally expensive. Since the target DA and DAO WDs of this work are found in a wide $T_{\rm eff}$, log g, and abundance range, creating an extensive model atmosphere grid was not possible. Instead, it was more feasible to follow an iterative process and to approach each object individually. First step was to calculate a small grid of pure H and H+He models around the literature parameters of DA and DAO WDs, respectively, which enables us to crudely estimate for $T_{\rm eff}$ and log g via the inspection of Lyman lines in the FUSE range (Fig. 5). Second, fully metal line blanketed models were computed with the updated $T_{\rm eff}$ and log g. In this step, multiple ionization equilibria were used to accurately pinpoint the $T_{\rm eff}$ of the stars and metal abundances were determined (Fig. 6). The final step involved the analysis of the optical spectra to further constrain log g (Fig. 7).

3.1.2 Spectral energy distribution fitting

The χ^2 fitting routine explained in Heber et al. (2018) and Irrgang et al. (2021) is utilized to analyze the spectral energy distributions (SEDs) of the sample WDs, which allows us to measure the radius (R), luminosity (L), and gravity mass ($M_{\rm grav}$) of each sample object. In short, the procedure involves conversion of user supplied model spectra (fluxes) to filter-averaged magnitudes, which is then compared to the photometric data[10]. The fitting routine employs the interstellar reddening law of Fitzpatrick et al. (2019) with an extinction coefficient of $R_{55} = 3.02$ and the colour excess $E(44–55)$ which is measured with monochromatic filters at 4400 Å and 5500 Å. The SED fitting was performed with fixed atmospheric parameters ($T_{\rm eff}$, log g, and He abundance) which were already determined via spectral analysis. Only the angular diameter, Θ, and $E(44–55)$ remained free parameters. Fig. 8 illustrates SED fits to a DAO and a DA WD as an example.

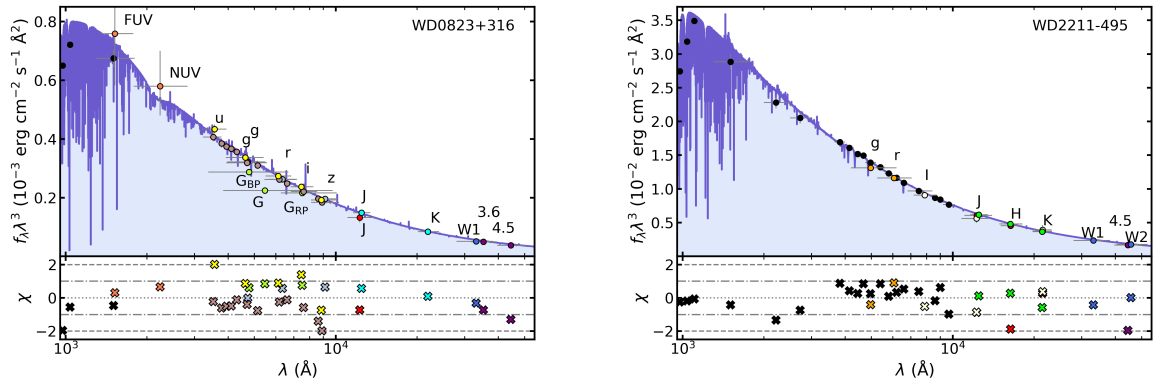


Figure 8: Spectral energy distribution fits to a DAO (left) and a DA (right) WD. Dots represent observations from different bands (surveys), whereas residuals are shown with crosses. Dark purple line represents the best fit TMAP model. For clarity, the y axes of all panels are shown in the form of $f_\lambda\,\lambda^3$.

In case of an infrared (IR) excess detection (Fig. 9), a multi-component fit was performed using the synthetic fluxes obtained via spectral analysis and PHOENIX model grid (Husser et al. 2013) that covers the wavelength range of 500 Å $\leq \lambda \leq$ 55 000 Å and $T_{\rm eff}$ range from 2300 K to 15 000 K. If the SEDs exhibited mid-IR excess in bands such as W3, W4, and Spitzer 24 μm, those were fitted with one or two blackbody components.

[10]Photometric data were automatically acquired from the following surveys and catalogues: *Gaia* (Riello et al. 2021), Skymapper (Onken et al. 2019), Sloan Digital Sky Survey (SDSS; Alam et al. 2015), the Galaxy Evolution Explorer (GALEX; Martin et al. 2005; Bianchi et al. 2017), the Panoramic Survey Telescope and Rapid Response System (Pan-STARRS; Flewelling et al. 2020), the Spitzer Space Telescope (Fazio et al. 2004; Rieke et al. 2004), the UK Infra-Red Telescope (UKIRT) Hemisphere Survey (UHS; Dye et al. 2018), the Visible and Infrared Survey Telescope Survey (VISTA; McMahon et al. 2013), the Wide-field Infrared Survey Explorer (WISE; Wright et al. 2010; Schlafly et al. 2019; Marocco et al. 2021) and Two Micron All Sky Survey (2MASS; Skrutskie et al. 2006).

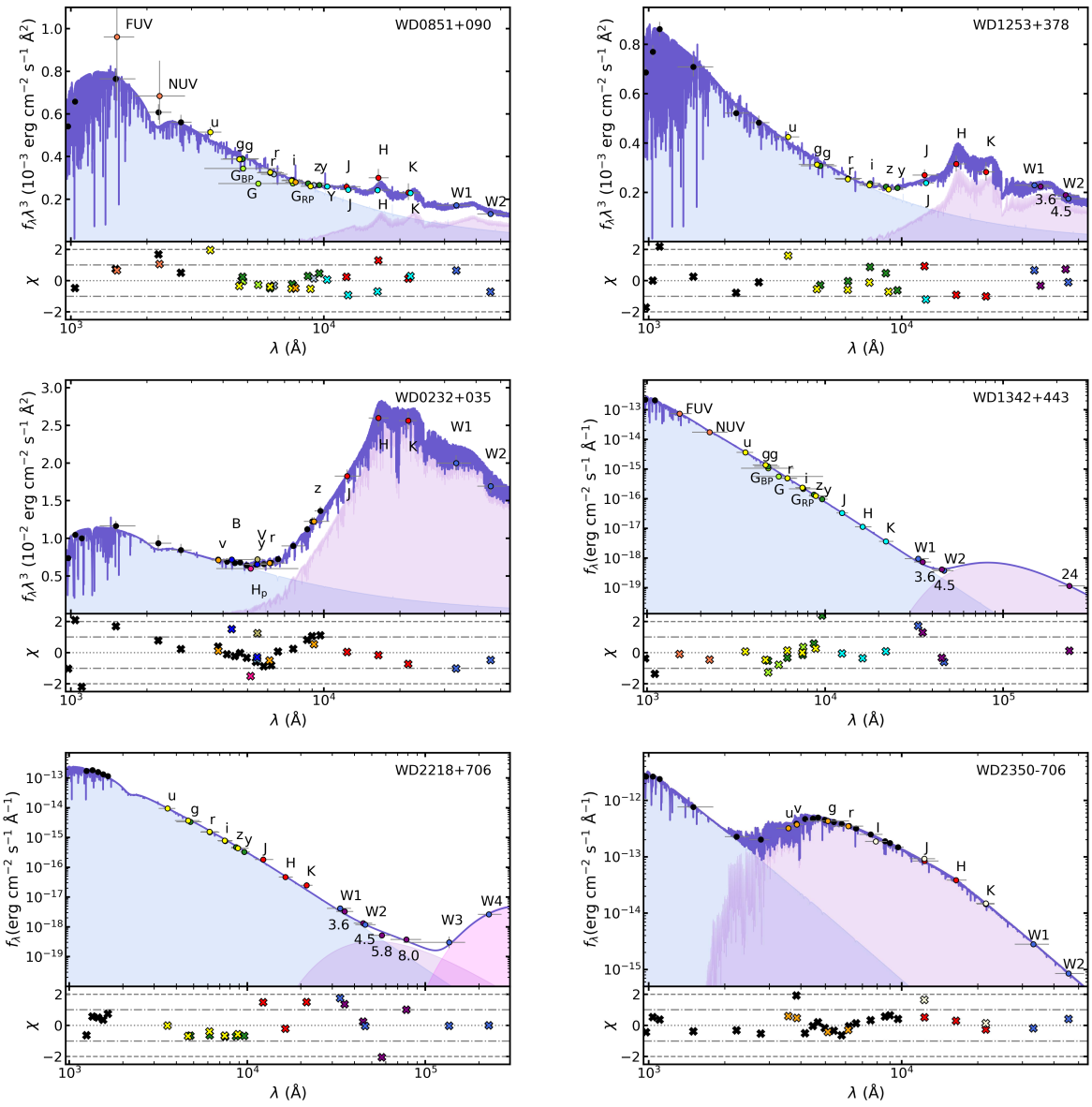


Figure 9: Spectral energy distribution fits to the sample objects with IR excess. All panels (first row: DAO; second and third row: DA) depict objects with a near- and/or far-IR excess, modeled with best fit TMAP models and either a best-fit late-type star model from the PHOENIX grid or one or two blackbody component(s). Dots represent observations from different bands (surveys), whereas residuals are marked with crosses. Each colour represents a single survey or mission. The dark purple line shows the best fit (combined) model; and blue and purple areas respectively show the fluxes from the WD and the cool component. For clarity, the y axes of all panels are shown in the form of $f_\lambda\,\lambda^3$, except for WD 1342+443, WD 2218+706 and WD 2350−706, where f_λ is shown on a logarithmic scale.

Parallax (ϖ) measurements are a requirement to derive the stellar parameters, which are accessible[11] for all sample WDs thanks to the *Gaia* mission. The stellar parameters R, L, and $M_{\rm grav}$ were calculated with following equations:

$$R = \frac{\Theta}{2\varpi} \tag{3.1}$$

$$\frac{L}{L_\odot} = \left(\frac{R}{R_\odot}\right)^2 \left(\frac{T_{\rm eff}}{T_{\rm eff,\odot}}\right)^4 \tag{3.2}$$

$$M_{\rm grav} = \frac{gR^2}{G} \tag{3.3}$$

where Θ was adopted from the SED fitting, ϖ from the *Gaia* mission, $T_{\rm eff}$ and g from the spectral analysis and G is the gravitational constant.

3.1.3 Time-series photometry

At least one archival light curve for all sample WDs was acquired from the following surveys: the Transiting Exoplanet Survey Satellite (TESS, Jenkins et al. 2016), the Zwicky Transient Facility (ZTF, Bellm et al. 2019; Masci et al. 2019), the Catalina Sky Survey (CSS, Drake et al. 2009), the Asteroid Terrestrial-impact Last Alert System (ATLAS, Tonry et al. 2018), and the third data release of *Gaia* mission (Gaia Collaboration et al. 2023). The light curve analysis in this work follows the same procedure described in Reindl et al. (2021, 2023, 2024), in which the program VARTOOLS (Hartman and Bakos 2016) was utilized. Periodic signals were detected by calculating a generalised Lomb-Scargle (LS) periodogram (Press et al. 1992; Zechmeister and Kürster 2009). The periodogram generates a false alarm probability (FAP) for each periodic signal, which in turn can be used to verify variability. Hence, a particular object showing periodic signals with log(FAP)$\leq$ -4 were classified as photometrically variable. However, the LS periodogram generated more than one significant period for several objects. In these cases, the most significant periodic signal was removed from the light curve and the periodogram was recalculated (whitening cycle), which was repeated until the periodogram did not generate any significant period. Then, the light curves of the variable objects were phase-folded to the strongest period and peak-to-peak amplitudes were calculated by fitting a harmonic series. Fig. 10 depicts the Lomb-Scargle Periodograms (top) and phase-folded light curves (bottom) of the variable objects.

A known drawback of the TESS data is contamination by nearby sources due to the satellite's large plate scale (21"/pixel) (Huang et al. 2018; Pedersen and Bell 2023). This necessitates to associate the detected periodic signal with the correct target. For that reason, target pixel files (TPFs) `tpfplotter`[12] (Aller et al. 2020) of all variable candidates were examined. However, finding no visible contamination in the TPFs does not directly prove the link between the signal and the target object (Aller et al. 2024). Therefore, `TESS_localize`[13] (Higgins and Bell 2023) was used to confirm the detected signal in the TESS data.

[11] Zero-point correction was applied to the *Gaia* parallaxes by following Lindegren et al. (2021), whereas parallax uncertainties were corrected with the function suggested by El-Badry et al. (2021).

[12] `https://github.com/jlillo/tpfplotter`

[13] `https://github.com/Higgins00/TESS-Localize`

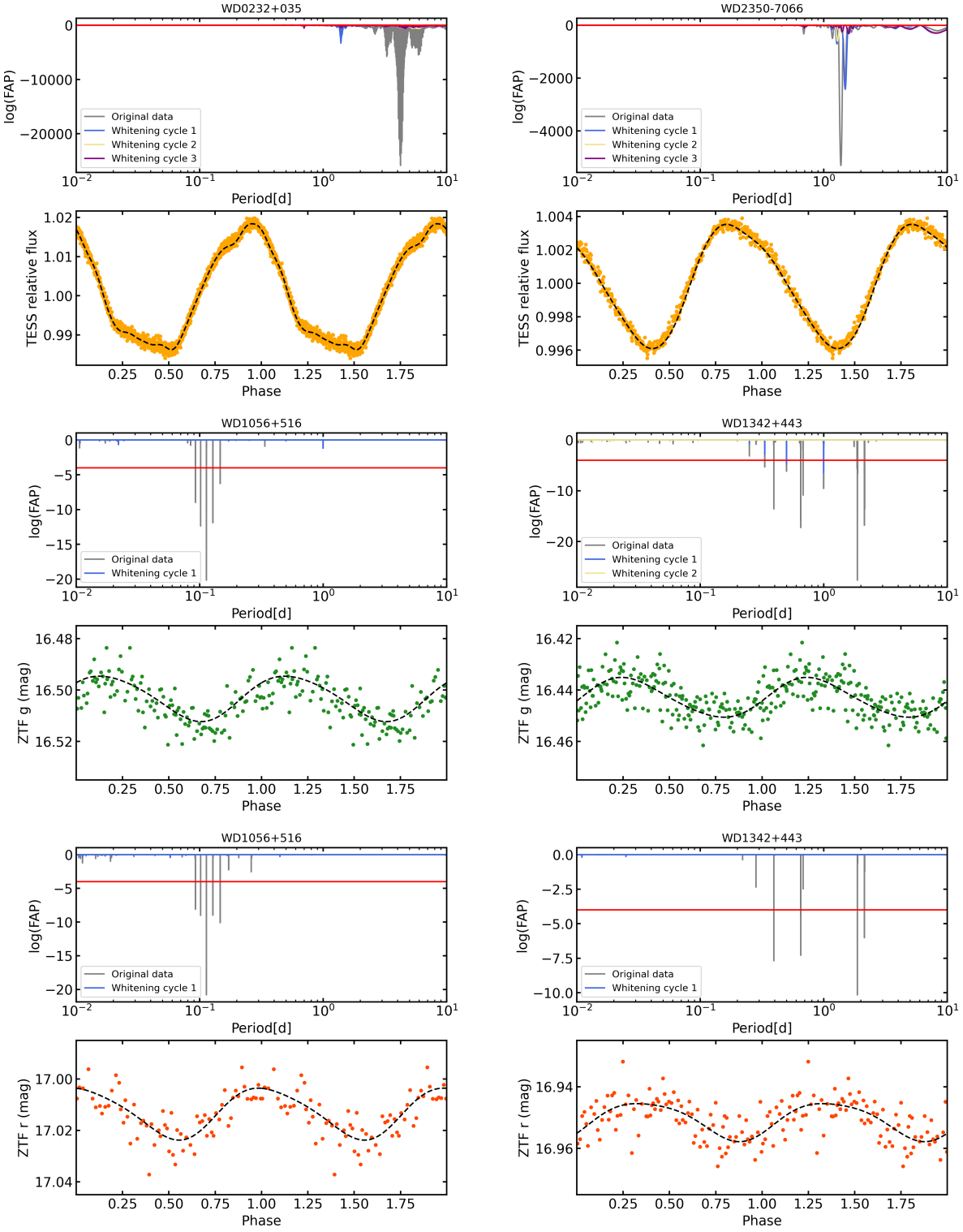


Figure 10: Lomb-Scargle Periodograms (top panels) and phase-folded light curves (bottom panels) of the variable objects. Top panels: The grey lines in the periodograms represent the original data. Data after each respective whitening cycle are shown with a different colour. The red horizontal lines represent the variability threshold $\log(\mathrm{FAP}) = -4$. Bottom panels: Phase-averaged TESS (orange) and phase-averaged ZTF (green and red) light curves were fitted by harmonic series (dashed lines).

3.2 Results

3.2.1 Stellar parameters

$T_{\rm eff}$, log g, and element abundances[14] of the sample objects were derived with fully metal line blanketed NLTE model atmospheres, in which both optical and UV spectra were utilized to reach a unified result for both wavelength ranges. By using a χ^2 minimization routine, fitting the SEDs enabled the measurement of R, L, and $M_{\rm grav}$ of the sample objects. Additionally, the evolutionary tracks of Renedo et al. (2010) were used to interpolate masses in the Kiel diagram ($M_{\rm Kiel}$), in which the uncertainties were determined using a Monte Carlo method. $T_{\rm eff}$, log g, R, L, $M_{\rm grav}$, and $M_{\rm Kiel}$ are listed in Table 2.

The spectral analysis conducted in this work reveals a narrow $T_{\rm eff}$ ($83\,{\rm kK} \geq T_{\rm eff} \geq 59\,{\rm kK}$) and a wide log g range ($8.0 \geq \log g \geq 7.3$) for DA WDs (Fig 12). Conversely DAO WDs are found within a wider $T_{\rm eff}$ ($134\,{\rm kK} \geq T_{\rm eff} \geq 83\,{\rm kK}$), but a narrower log g range ($7.2 \geq \log g \geq 6.9$). Only one DAO and a few DA WDs have comparable effective temperatures and surface gravities to each other, whereas the rest of their respective samples extend to opposite ends of the $T_{\rm eff}$ and log g range.

The results from SED fitting show that the DAO WDs are significantly more luminous ($310\,L_\odot \geq L \geq 29\,L_\odot$) than the DAs ($20\,L_\odot \geq L \geq 1.7\,L_\odot$), whereas DA WDs ($\langle M_{\rm grav\text{-}DA}\rangle = 0.52\ M_\odot$, $\sigma = 0.13\ M_\odot$) are on average more massive than DAOs ($\langle M_{\rm grav\text{-}DAO}\rangle = 0.36\ M_\odot$, $\sigma = 0.12\ M_\odot$). On the other hand, interpolation from evolutionary tracks results in larger masses on average for both DA ($\langle M_{\rm Kiel\text{-}DA}\rangle = 0.59\ M_\odot$, $\sigma = 0.05 M_\odot$) and DAO WDs ($\langle M_{\rm Kiel\text{-}DAO}\rangle = 0.55\ M_\odot$, $\sigma = 0.02\ M_\odot$). A comparison to earlier studies shows that the mean Kiel masses of both DA and DAO WDs determined in this work are consistent with those reported by Gianninas et al. (2010); Bédard et al. (2020); Reindl et al. (2023). In contrast, a substantial difference is found between the mean gravity mass of DAO WDs in this study and those of cool H-rich WDs ($\langle M_{\rm grav}\rangle = 0.61^{+0.14}_{-0.08}\,M_\odot$) reported by (Raddi et al. 2025). This strongly suggest that the Kiel masses obtained here are more reliable than gravity masses.

The inconsistency between mass estimates derived from evolutionary tracks and those based on observed parallaxes is a well-known issue for hot white dwarfs (Löbling et al. 2020; Reindl et al. 2023). This problem also manifests in another form as a disparity between spectroscopic and parallax distances (Napiwotzki 2001; Rauch et al. 2007; Ziegler 2012; Reindl et al. 2024). The discrepancy between $M_{\rm Kiel}$ and $M_{\rm grav}$ requires further investigation and will be discussed in Sect. 3.3.3.

[14] Abundance patterns of both DA and DAO WDs will be discussed in Sect. 3.3.1.

Table 2: Effective temperatures, surface gravities, radii, luminosities, gravity and Kiel masses of DAO and DA WDs.

Name	$T_{\rm eff}$ [K]	$\log g$ [cm/s^2]	R [$R_\odot$]	L [$L_\odot$]	$M_{\rm grav}$ [$M_\odot$]	$M_{\rm Kiel}$ [$M_\odot$]
			DAO			
Longmore1	118000 ± 5000	7.0 ± 0.3	$0.0419^{+0.0015}_{-0.0014}$	$310.0^{+70.0}_{-60.0}$	$0.64^{+0.70}_{-0.40}$	0.56 ± 0.06
WD 0439+466	97000 ± 5000	7.0 ± 0.2	$0.0243^{+0.0002}_{-0.0002}$	$47.0^{+11.0}_{-10.0}$	$0.22^{+0.13}_{-0.08}$	0.54 ± 0.06
WD 0500−156	104000 ± 6000	7.2 ± 0.2	$0.0270^{+0.0007}_{-0.0007}$	$77.0^{+20.0}_{-17.0}$	$0.42^{+0.25}_{-0.16}$	0.57 ± 0.06
WD 0615+556	101000 ± 5000	7.2 ± 0.2	$0.0223^{+0.0007}_{-0.0007}$	$47.0^{+11.0}_{-9.0}$	$0.29^{+0.18}_{-0.11}$	0.57 ± 0.05
WD 0823+316	98000 ± 4000	7.1 ± 0.2	$0.0251^{+0.0009}_{-0.0009}$	$53.0^{+13.0}_{-11.0}$	$0.29^{+0.18}_{-0.11}$	0.55 ± 0.05
WD 0834+500	90000 ± 3000	7.0 ± 0.3	$0.0306^{+0.0010}_{-0.0009}$	$55.0^{+9.0}_{-8.0}$	$0.34^{+0.21}_{-0.13}$	0.53 ± 0.05
WD 0851+090	106000 ± 5000	7.2 ± 0.2	$0.0273^{+0.0010}_{-0.0009}$	$85.0^{+21.0}_{-18.0}$	$0.43^{+0.28}_{-0.18}$	0.57 ± 0.07
WD 1111+552	110000 ± 5000	7.1 ± 0.3	$0.0339^{+0.0015}_{-0.0014}$	$152.0^{+33.0}_{-28.0}$	$0.53^{+0.54}_{-0.27}$	0.56 ± 0.06
WD 1214+267	91000 ± 3000	7.1 ± 0.3	$0.0240^{+0.0009}_{-0.0008}$	$35.0^{+6.0}_{-5.0}$	$0.26^{+0.27}_{-0.14}$	0.54 ± 0.06
WD 1253+378	93000 ± 4000	7.0 ± 0.2	$0.0282^{+0.0012}_{-0.0011}$	$54.0^{+13.0}_{-11.0}$	$0.29^{+0.19}_{-0.12}$	0.53 ± 0.05
WD 1957+225	134000 ± 10000	6.9 ± 0.4	$0.0325^{+0.0006}_{-0.0006}$	$310.0^{+110.0}_{-90.0}$	$0.31^{+0.47}_{-0.19}$	0.56 ± 0.06
WD 2226−210	120000 ± 5000	7.2 ± 0.3	$0.0218^{+0.0002}_{-0.0002}$	$89.0^{+16.0}_{-14.0}$	$0.27^{+0.28}_{-0.14}$	0.59 ± 0.06
WD 2342+806	83000 ± 5000	7.2 ± 0.2	$0.0259^{+0.0003}_{-0.0003}$	$29.0^{+8.0}_{-7.0}$	$0.39^{+0.23}_{-0.15}$	0.53 ± 0.05
			DA			
WD 0027−636	59000 ± 5000	8.0 ± 0.2	$0.0146^{+0.0001}_{-0.0001}$	$2.3^{+0.9}_{-0.7}$	$0.77^{+0.46}_{-0.29}$	0.69 ± 0.07
WD 0229−481	62000 ± 5000	7.8 ± 0.2	$0.0171^{+0.0002}_{-0.0001}$	$3.9^{+1.5}_{-1.2}$	$0.67^{+0.40}_{-0.25}$	0.62 ± 0.07
WD 0232+035	63000 ± 3000	7.5 ± 0.2	$0.0207^{+0.0003}_{-0.0003}$	$6.1^{+1.4}_{-1.2}$	$0.49^{+0.32}_{-0.20}$	0.54 ± 0.07
WD 0311+480	70000 ± 5000	7.3 ± 0.4	$0.0285^{+0.0004}_{-0.0004}$	$18.0^{+13.0}_{-9.0}$	$0.60^{+0.90}_{-0.40}$	0.52 ± 0.11
WD 0343−007	63000 ± 4000	7.7 ± 0.2	$0.0183^{+0.0002}_{-0.0002}$	$4.7^{+1.4}_{-1.1}$	$0.61^{+0.36}_{-0.23}$	0.59 ± 0.07
WD 0455−282	66000 ± 3000	7.5 ± 0.2	$0.0166^{+0.0007}_{-0.0007}$	$4.7^{+1.1}_{-0.9}$	$0.32^{+0.20}_{-0.12}$	0.55 ± 0.05
WD 0615+655	83000 ± 10000	7.6 ± 0.4	$0.0171^{+0.0003}_{-0.0003}$	$13.0^{+8.0}_{-6.0}$	$0.43^{+0.65}_{-0.26}$	0.61 ± 0.10
WD 0621−376	65000 ± 3000	7.5 ± 0.4	$0.0232^{+0.0001}_{-0.0001}$	$8.7^{+1.8}_{-1.5}$	$0.60^{+1.00}_{-0.40}$	0.54 ± 0.10
WD 0939+262	66000 ± 3000	7.7 ± 0.2	$0.0173^{+0.0002}_{-0.0002}$	$5.1^{+1.0}_{-0.9}$	$0.54^{+0.32}_{-0.21}$	0.60 ± 0.06
WD 1056+516	63000 ± 5000	7.9 ± 0.2	$0.0110^{+0.0003}_{-0.0002}$	$1.7^{+0.7}_{-0.5}$	$0.35^{+0.21}_{-0.13}$	0.66 ± 0.07
WD 1342+443	62000 ± 5000	7.7 ± 0.3	$0.0167^{+0.0005}_{-0.0005}$	$3.7^{+1.4}_{-1.1}$	$0.51^{+0.52}_{-0.26}$	0.59 ± 0.08
WD 1738+669	78000 ± 6000	7.6 ± 0.4	$0.0154^{+0.0001}_{-0.0001}$	$7.9^{+2.8}_{-2.2}$	$0.34^{+0.52}_{-0.21}$	0.60 ± 0.10
WD 1827+778	78000 ± 10000	7.4 ± 0.4	$0.0212^{+0.0004}_{-0.0004}$	$15.0^{+10.0}_{-7.0}$	$0.41^{+0.63}_{-0.25}$	0.55 ± 0.09
WD 2046+396	64000 ± 5000	7.8 ± 0.3	$0.0164^{+0.0001}_{-0.0001}$	$4.0^{+1.5}_{-1.2}$	$0.60^{+0.70}_{-0.40}$	0.63 ± 0.09
WD 2146−433	66000 ± 4000	7.5 ± 0.3	$0.0197^{+0.0004}_{-0.0004}$	$6.7^{+1.8}_{-1.5}$	$0.45^{+0.45}_{-0.23}$	0.55 ± 0.08
WD 2211−495	68000 ± 4000	7.4 ± 0.3	$0.0211^{+0.0001}_{-0.0000}$	$8.6^{+2.3}_{-1.9}$	$0.41^{+0.41}_{-0.21}$	0.53 ± 0.08
WD 2218+706	78000 ± 5000	7.4 ± 0.3	$0.0249^{+0.0010}_{-0.0008}$	$20.1^{+7.0}_{-6.0}$	$0.57^{+0.70}_{-0.40}$	0.55 ± 0.07
WD 2350−706	75000 ± 5000	7.9 ± 0.3	$0.0155^{+0.0008}_{-0.0004}$	$6.9^{+2.6}_{-2.1}$	$0.70^{+0.90}_{-0.50}$	0.68 ± 0.09
WD 2353+026	61000 ± 5000	7.5 ± 0.3	$0.0164^{+0.0004}_{-0.0004}$	$3.4^{+1.3}_{-1.0}$	$0.31^{+0.32}_{-0.16}$	0.53 ± 0.08

3.2.2 Infrared excess & photometric variability

The SEDs of six objects in the sample show an infrared (IR) excess, of which $T_{\rm eff}$, R, and surface ratios relative to the WD are listed in Table 3. The radii of the IR sources were determined under the assumption of same distance with the WD. Four of these IR sources were previously classified as companions in close (DA WD 0232+035[15]) and wide binary (DAO WD 0851+090[16], DAO WD 1253+378[17], and DA WD 2350−706[18]) systems, whereas the remaining two sources were identified as cold/warm dust (DA WD 1342+443[19], DA WD 2218+706[20]). The parameters presented in Table 3 agree with previous studies and are consistent with earlier IR source identifications.

Among 32 sample WDs, only four objects show photometric variability (Table 4), which translates to a variability rate of 13^{+8}_{-4}%. This result is consistent with the variability rate of hot H-rich WDs without UHE phenomenon reported by Reindl et al. (2021). Two of these objects (WD 0232+035[21] and WD 2350−706[22]) have been previously reported to be photometrically variable, whereas the other two (WD 1056+516 and WD 1342+44) are, to the best of my knowledge, first-time detections.

WD 0232+035 is a reflection-effect system in which one hemisphere of the much cooler companion is irradiated due to its synchronous orbit and periodic light variations are observed. The detected 4.23 d photometric period agrees with previously determined orbital period of the system (Thorstensen et al. 1978; Vennes et al. 1991; Vennes and Thorstensen 1994). Due to the emission-line complex observed in the optical spectra, photometric variability (1.87 d) detected in WD 1342+443 might be related to an irradiated sub-stellar companion that is hidden in the SED. However, future IR and time-resolved spectroscopic observations is needed for a sound conclusion. On the other hand, WD 2350−706 is a component of a wide non-interacting binary system and the detected periodicity (1.37 d) most likely corresponds to the rotational period of the companion. Among them, only WD 1056+516 does not show infrared excess and likely the photometric variability is not caused by binarity. Instead, the observed variability (0.11 d) of this object might be related to bright spots generated by magnetic fields. Even though no Zeeman-splitting is detected in the spectra, surface inhomogeneities can still be caused by weak magnetic fields (Reindl et al. 2019).

[15] Greenstein and Eggen (1966); Thorstensen et al. (1978); Vennes et al. (1991); Vennes and Thorstensen (1994); Kawka et al. (2008); Guo et al. (2015)
[16] Ciardullo et al. (1999); Frew (2008); De Marco et al. (2013)
[17] Brown et al. (2011)
[18] Barstow et al. (1994); Vennes et al. (1998); Barstow et al. (2001); Holberg et al. (2013)
[19] Chu et al. (2011)
[20] Bilíková et al. (2012)
[21] Brightness changes were previously reported by Benedict et al. (2000), but the 4.23 d photometric periodic is, to the best of my knowledge, a first-time detection in this work.
[22] Colman et al. (2024)

Table 3: Names and spectral types of the sample objects showing IR excess as well as temperatures, radii, and surface ratios of the IR sources.

Name	Spectral Type	$T_{\rm eff\,1}$ [K]	R_1 [$R_\odot$]	Surface Ratio$_1$	$T_{\rm eff\,2}$ [K]	Surface Ratio$_2$
WD 0232+035	DA	3710^{+70}_{-60}	$0.395^{+0.011}_{-0.011}$	-	-	-
WD 0851+090	DAO	2920^{+210}_{-380}	$0.260^{+0.040}_{-0.040}$	-	-	-
WD 1253+378	DAO	3220^{+120}_{-100}	$0.337^{+0.022}_{-0.020}$	-	-	-
WD 1342+443	DA	346^{+17}_{-17}	-	$1.4^{+0.5}_{-0.5} \times 10^5$	-	-
WD 2218+706	DA	560^{+190}_{-210}	-	$1.7^{+11.0}_{-1.1} \times 10^3$	80^{+16}_{-20}	$5^{+49}_{-4} \times 10^8$
WD 2350−706	DA	6280^{+50}_{-40}	$1.210^{+0.070}_{-0.070}$	-	-	-

Table 4: Names, spectral types, observed bands, false alarm probabilities, periods, and peak–to–peak amplitudes of the variable objects.

Name	Spectral Type	Band	log(FAP)	Period [d]	Amplitude [mag]
WD 0232+035	DA	TESS	–25834.57	4.231915	0.032
			–3304.41	1.391210	0.007
		ATLAS-c	-	-	0.029
		ATLAS-o	–12.60	4.229050	0.046
		CSS-V	–9.28	4.368181	0.160
WD 1056+516	DA	ZTF-g	–20.15	0.113279	0.018
		ZTF-r	–20.81	0.113279	0.020
		ZTF-i [a]	-	-	0.020
WD 1342+443	DA	ZTF-g	–27.60	1.873020	0.015
		ZTF-r	–10.15	1.873207	0.012
		ZTF-i [a]	-	-	0.010
WD 2350−706	DA	TESS	-5306.25	1.373420	0.008

(a) LS periodograms of WD 1056+516 and WD 1342+443 did not generate any significant period in the ZTF-i band, which were phased to a significant period found in the respective ZTF-g band.

3.3 Discussion

3.3.1 Mass-loss, diffusion, and accretion

Theoretical calculations of Unglaub and Bues (1998, 2000) showed that chemically homogeneous winds of DAO WDs could impede the gravitational settling of He. Once the mass-loss is suspended, He can no longer be homogeneously afloat in the atmosphere. With the upward diffusion of H, a subsequent transformation from DAO to DA WD is anticipated. These theoretical findings of DAO to DA evolutionary sequence were also observationally supported by Gianninas et al. (2010, 2011), and Bédard et al. (2020), who reported a higher $T_{\rm eff}$ for the DAOs than DAs. However, a partial overlap in their $T_{\rm eff}$ − log g diagram between two species still remained.

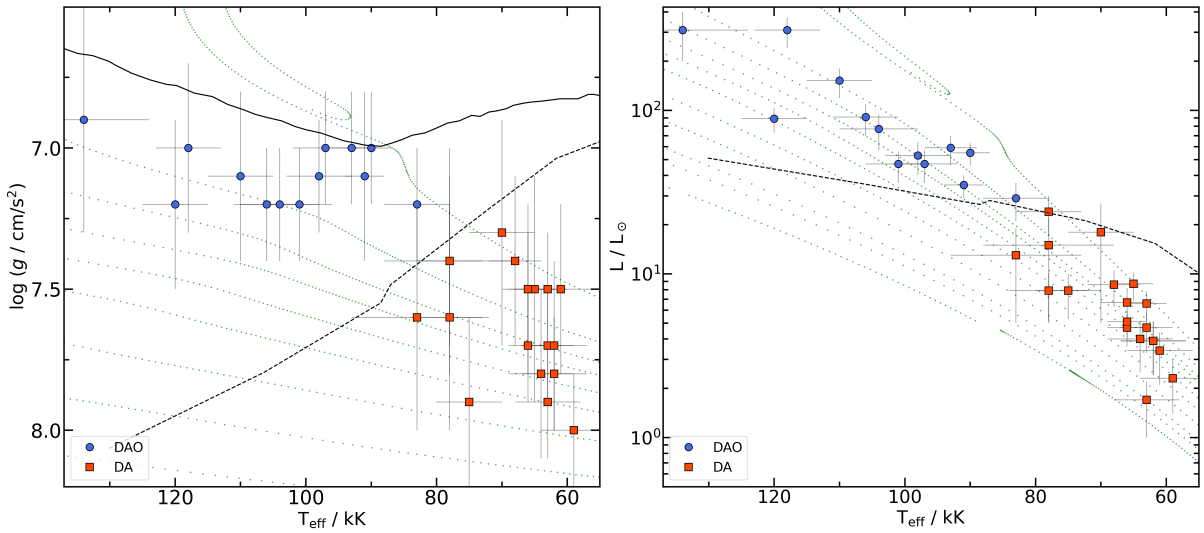


Figure 11: Sample objects shown in the $T_{\rm eff}$ − log g diagram (left) and the HRD (right). The solid black line in the left panel represents the theoretical wind limit by Unglaub and Bues (2000). Dashed black lines in both panels corresponds to predicted He abundance (N(He)/N(H) = 10^{-3}) in the cooling sequence by the same authors. The green dotted lines (left: 0.525, 0.570, 0.593, 0.609, 0.632, 0.659, 0.705, 0.767, and 0.837 $M_{\odot}$, right: 0.525 − 0.935 $M_{\odot}$) are evolutionary tracks of H-rich WDs (Z=0.01) from Renedo et al. (2010).

As opposed to earlier studies, spectral analysis of this work reveals a clear segregation of DA and DAO WDs in the Kiel diagram (Fig. 11, left), which heavily implies that they represent distinct and subsequent evolutionary stages. The same outcome is also evident by the positions of DA and DAO WDs in the HRD (Fig. 11, right). The DAO to DA transformation region is marked at $T_{\rm eff} \approx 83$ kK. These results are further reinforced by the He abundance pattern of the sample objects. At the highest temperatures, DAO WDs have solar He abundance (Fig. 12). With decreasing temperature, He abundances of DAO WDs also diminish. Once the transition region is reached, theoretical calculations of Unglaub and Bues (2000) predict that the He abundance should have dropped to N(He)/N(H) = 10^{-3} which also coincides with the detection limit of He in the optical spectra.

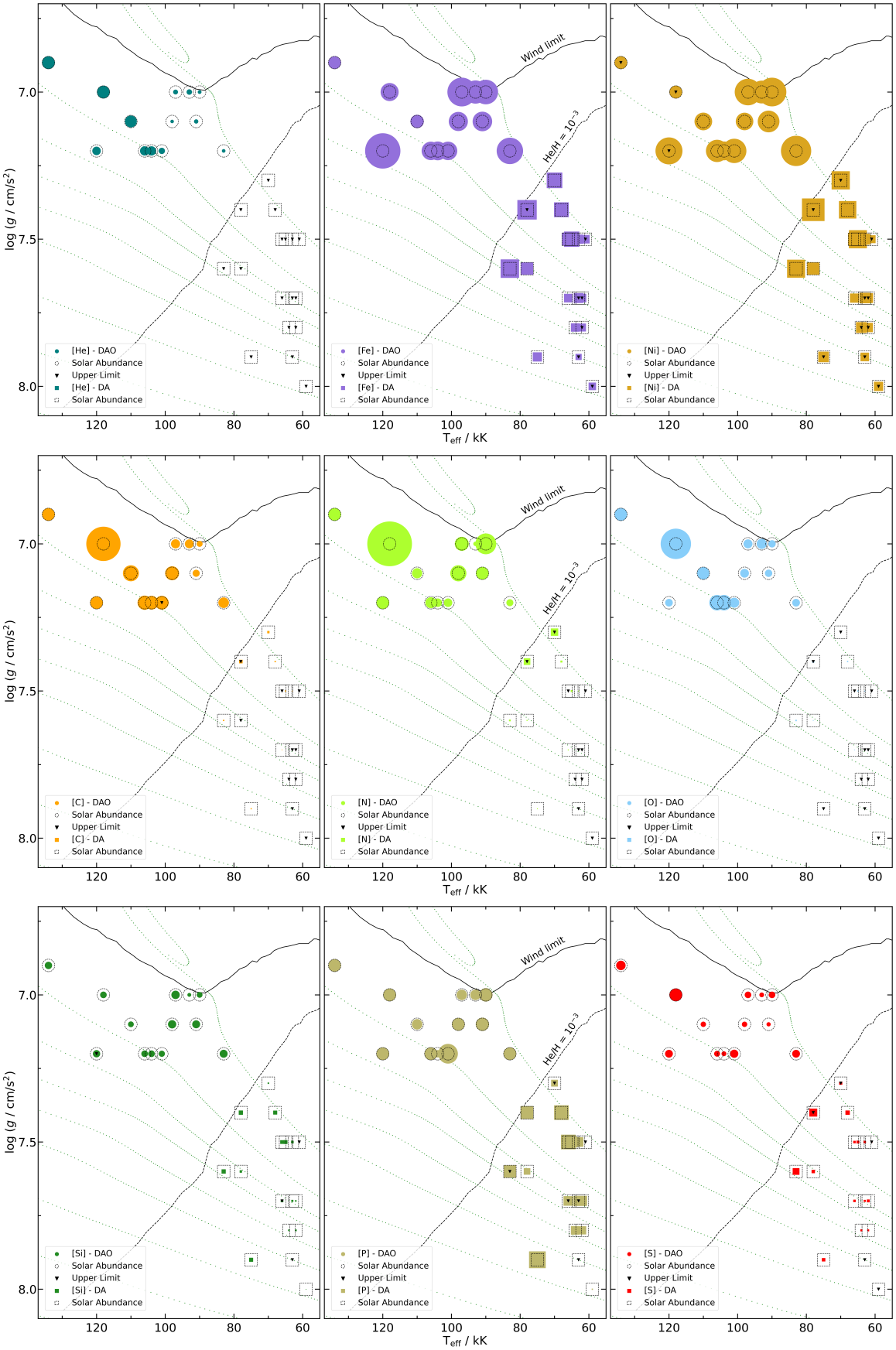


Figure 12: Element abundances of the sample objects in the Kiel diagram (panels from upper left to lower right: He, Fe, Ni, C, N, O, Si, P, and S). The abundances are shown with filled circles and squares for DAO and DA WDs, respectively. The filled symbol size is proportional to the mass fraction of the respective element. The dashed symbols show solar element abundances (Asplund et al. 2009). Upper limits are marked with triangles.

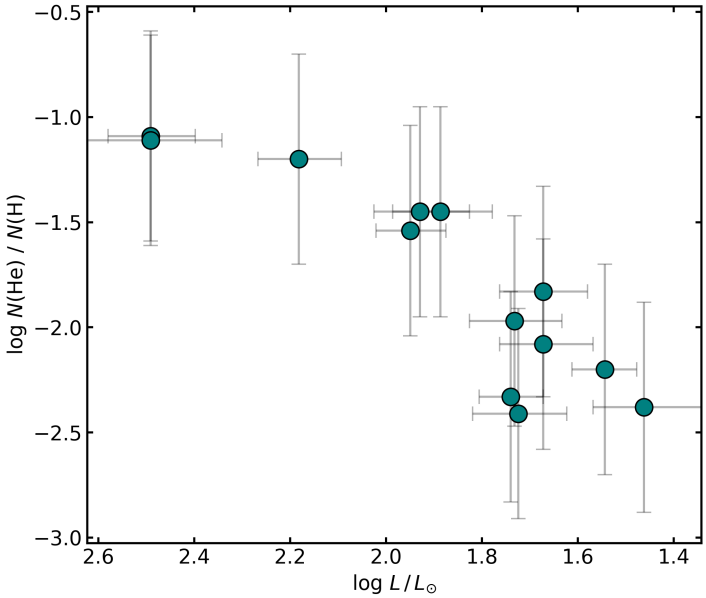


Figure 13: He abundance in DAO WDs as a function of luminosity.

A pattern similar to He can also be observed for C, N, and O abundances (roughly solar at highest $T_{\rm eff}$, Fig. 12), though C, N, and O diminish less quickly as predicted by Unglaub and Bues (2000). However, below the transition region C, N, and O abundances are extremely sub-solar for DA WDs. A somewhat similar but a more irregular pattern is observed for Si, P, and S abundances (Fig. 12). Although Si, P, and S abundances of DAO WDs are roughly solar, the abundance decrease below the transition region is not as severe as the He, C, N, and O. In fact, multiple DA WDs retain their roughly solar Si, P, and S abundances, especially P. On the other hand, abundance patterns of Fe and Ni do not resemble that of other elements (Fig. 12). At high temperatures, DAO WDs have roughly solar Fe and Ni. However, as the temperature decreases Fe and Ni abundances increase until the transition region, which is a stark contrast to He, C, N, and O, whereas below the transition region, DA WDs have roughly (over-)solar Fe and Ni. With decreasing $T_{\rm eff}$ and increasing log g, a decrease in Fe and Ni abundances can be observed.

A closer examination of the abundance patterns of the sample objects reveals ongoing physical processes through the cooling sequence of hot H-rich WDs. At highest temperatures, a weak stellar wind should be the governing mechanism in the atmosphere, which mainly develops because of the radiative forces on metals. In contrast, radiative forces are very low on the bulk of the wind material (H and He). However, metals in turn transfer momentum to H and He via Coulomb collisions and the wind emerges homogeneously (Krtička et al. 2020). A direct evidence for the presence of stellar winds in WD atmospheres can not be expected. Because, Unglaub and Bues (2000) showed that predicted mass-loss rates are too low to utilize P Cygni line profiles for a spectroscopic detection. On the other hand, Napiwotzki (1999) reported a correlation between decreasing He abundance and luminosity among the hybrid CSPNe in their sample, which can be interpreted as an indirect evidence for radiation-driven winds. The same trend is also apparent in the DAO WDs of this work, as shown in Fig. 13. This means that as long as the mass-loss is prominent, it homogenizes the DAO atmosphere and gravitational settling is counteracted (Werner et al. 2018b). This is what we observe for the DAO WDs with $T_{\rm eff}$ $\geq$ 118 kK (Fig. 12), because all of these objects have roughly solar element abundances. WD 2226−210 ($T_{\rm eff}$ =120 kK) is an exception to this case which has sub-solar He, but

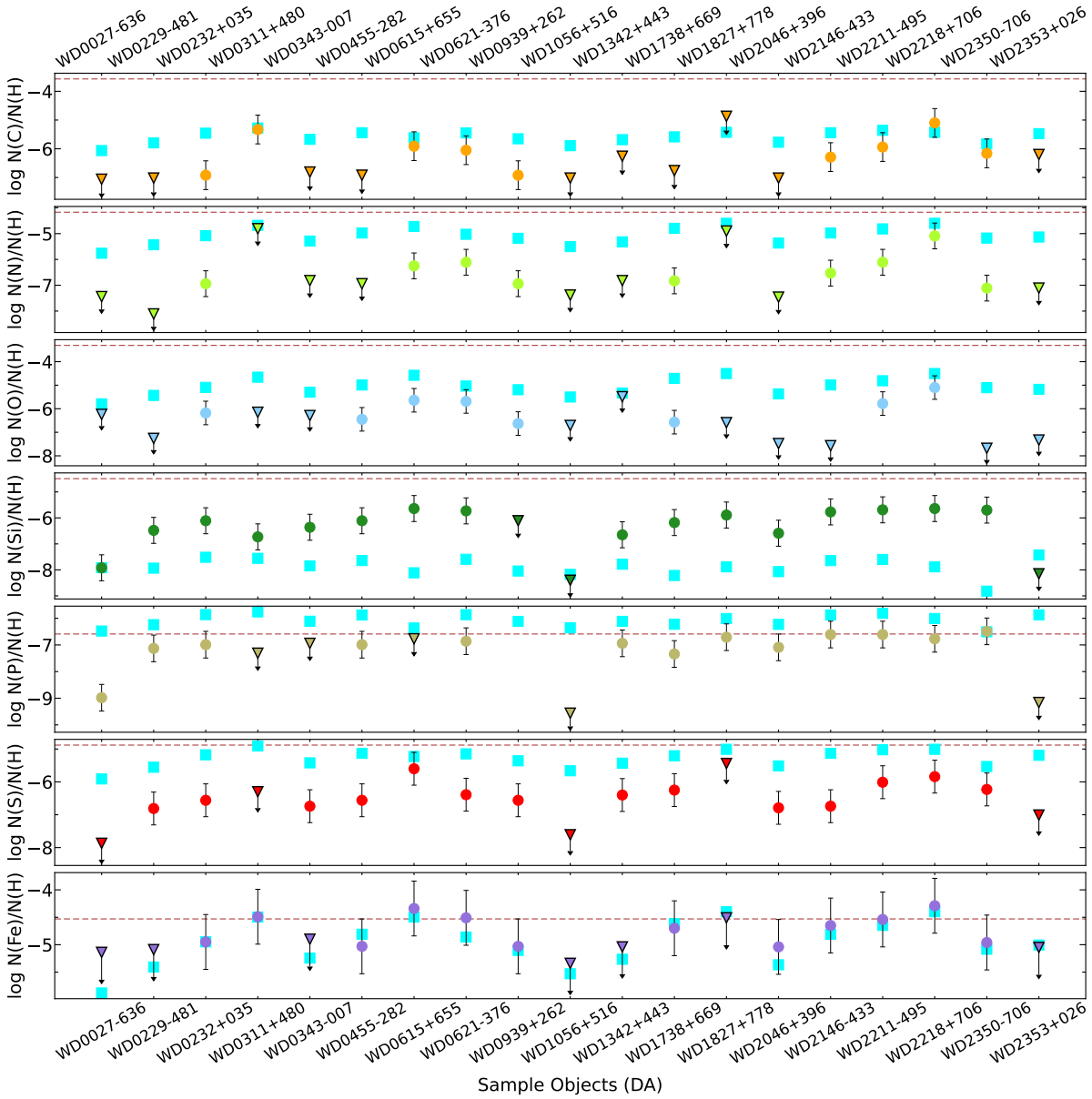


Figure 14: Comparison of DA metal abundances (colored circles; triangles for upper limits) to predictions (turquoise squares) of diffusion theory by Chayer et al. (1995b) and Vennes et al. (1996). The dashed line in each panel represents the solar abundance of the respective element.

conversely over-solar Fe and Ni abundances like the rest of the DAO WDs ($T_{\rm eff} \leq 118\,$kK).

In essence, an increase in the heavy-element abundances points out to the impact of radiative levitation (Rauch et al. 2016). Consequently for these objects, it is safe to speculate that a combination of weak mass-loss and diffusion (Werner et al. 2018a; Löbling et al. 2020) accounts for their observed abundance pattern. Below the transition region, heavily depleted He and CNO in the DA atmospheres signal the termination of mass-loss and increasing effects of the gravitational settling. In contrast, radiative levitation loses efficiency which can be inferred from the diminishing heavy element abundances as the DA WDs cool. This strongly indicates that atmospheres of DA WDs are mainly influenced by an interplay between radiative levitation and gravitational settling (Werner et al. 2019).

As opposed to the implications, however, the theoretical predictions show contrasting results to the observations. Fig. 14 depicts a comparison of DA abundances derived in

this work to the diffusion calculations of Chayer et al. (1995b) and Vennes et al. (1996). Although individual agreements are observed for a particular star, excluding Fe, discrepancies are evident for each element. The general trends show that the theory overpredicts C, N, O, P, and S abundances, but Si abundances are underpredicted. Similar results were also reported in previous studies (Chayer et al. 1995a,b; Barstow et al. 2003b; Dobbie et al. 2005; Werner et al. 2007; Rauch et al. 2013; Barstow et al. 2014; Preval et al. 2019). The mismatch between observations and diffusion theory shows that the abundance pattern of DA WDs cannot be simply explained by the equilibrium of radiative levitation and gravitational settling, but a third mechanism is required. Chayer et al. (1997) theoretically showed that including either accretion or selective mass-loss in the diffusion calculations mitigates the discrepancy in Si abundance between observation and theory.

Rauch et al. (2013) reported that it was not possible to simultaneously fit all oxygen lines from different ions[23] in the spectra of the hot ($T_{\rm eff}$ = 60 kK) DA-type WD G191-B2B, where fits to O VI resonance lines yield much lower O abundance than fits to O V and O IV lines. They achieved better fits with self-consistent diffusion models when the O abundance is decreased only in the outer atmosphere where the observed O VI resonance line originate from. The same authors suggested that a weak mass-loss in the outer atmosphere might be responsible for the observed O VI line profiles. On the other hand, due to the clear excess of Si with respect to theoretical estimates, Barstow et al. (2014) stated that the abundance pattern of hot DA WDs in their sample indicates accretion from short lived gaseous disks. They also argued that hot DA WDs do not innately contain the observed metals, but rather, based on relatively high abundance of P and Si, metals are possibly accreted from planetary material and radiatively levitated. Furthermore, Preval et al. (2019) invoked ongoing accretion from external sources due to an order of magnitude excess in observed Fe and Si abundances in their hot DA WD sample compared to the diffusion theory.

The accretion scenario, however, appears unlikely. First, according to SED fitting performed in this work, only four DA WDs show infrared excess. If observed metal abundances were tied to ongoing accretion of planetary material, we would have observed IR excess for all DA WDs in our sample. Second, comparing abundances of objects with possible companions and single WDs shows that the abundance patterns of close binary and single stars in this sample are similar (Fig. 15). In case of accretion, a clear distinction in abundance patterns of close binary and single stars would have been expected. Finally, the intense radiation pressure of hot WDs ($T_{\rm eff} \geq$ 59 kK) in this sample could possibly counteract infall of material and prevent formation of gaseous disks. Instead of accretion from external sources, weak mass-loss seems more likely. Although, chemically homogeneous winds are not predicted for a WD with (sub-)solar metallicity, $T_{\rm eff}$ = 60 kK and above log g = 7.0 (Unglaub 2007), selective winds that only act on metals are a possibility for WDs (Unglaub 2007).

[23]It was suggested that the imbalance in the O lines were caused by the inhomogeneous oxygen stratification in the atmosphere (Vennes et al. 2000; Vennes and Lanz 2001; Chayer et al. 2006; Rauch et al. 2013).

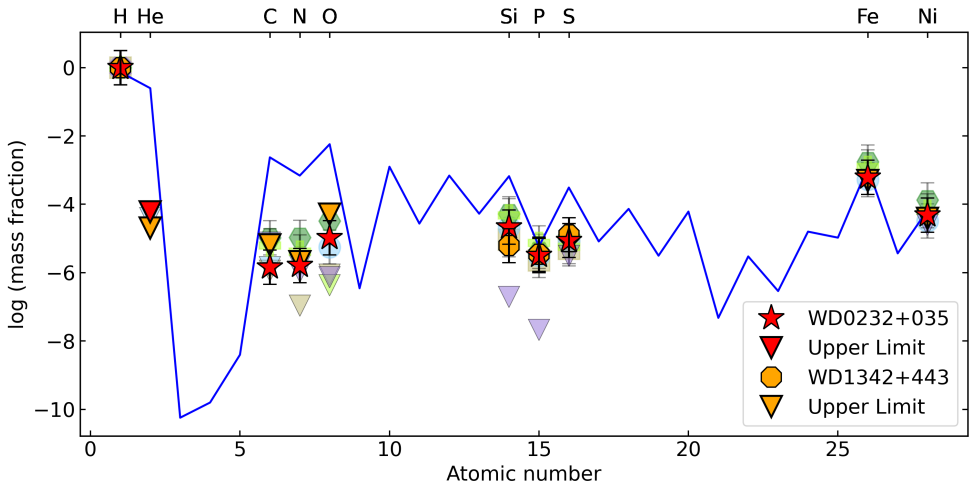


Figure 15: Abundance comparison between WD 0232+035 (red stars), WD 1342+443 (orange octagons), and single WDs (one color and shape for each object) with similar parameters in this sample. All upper-limits are marked with triangles. The blue line represents the solar abundances.

3.3.2 Central stars of planetary nebulae

Central stars of planetary nebulae (CSPNe) offer a valuable insight to the previous evolutionary phases. Since the PN is formed through the ejection of the stellar envelope, the nebular abundances can be used to uncover different nucleosynthesis processes that happened in the AGB phase (García-Rojas et al. 2013) and progenitor masses utilizing stellar evolution models (Pottasch et al. 2011; García-Hernández et al. 2016). On the other hand, a comparison between nebular and photospheric abundances might reveal physical process that take place in the CS's atmosphere. Since the expanding nebular gas is a snapshot of the surface composition, without any post-ejection changes, a close agreement between the photospheric and nebular abundances can be expected. However, onset of diffusion in the atmosphere erases the chemical imprint of the progenitor star, which leads to abundance differences between the PN and its CS. Therefore, comparing the nebular and photospheric abundances might hint at onset of diffusion or effectiveness of the mass-loss.

Fig. 16 shows a comparison between photospheric and PNe abundances available in the literature[24]. As expected, CS and PN abundances are consistent, except for N abundances of WD 0615+556 and Fe abundances of WD 1111+552. A lower nebular Fe abundance is not surprising since this was systematically found for large number of PNe and was explained as Fe depletion into dust grains (Delgado Inglada et al. 2009; Delgado-Inglada and Rodríguez 2014; Stanghellini et al. 2024). The agreement between nebular and photospheric abundances implies that gravitational settling is not working in the CSPNe atmospheres.

The kinematic age of a PN refers to the time elapsed since its ejection and can be used to determine the evolutionary stage of the nebula (Guillén et al. 2013). The kinematic age is also used to estimate central star's parameters (i.e. mass) by using evolutionary tracks (Gesicki et al. 2003; Fragkou et al. 2025), where it serves as a proxy for the star's cooling age. Cooling ages for the sample CSPNe were derived using the evolutionary

[24]PNe abundances are compiled from Barker (1984); Kaler et al. (1990); Henry et al. (1999); Kwitter and Henry (2001); Henry et al. (2004); Stanghellini et al. (2006); Delgado Inglada et al. (2009); Holovatyy and Havrilova (2005).

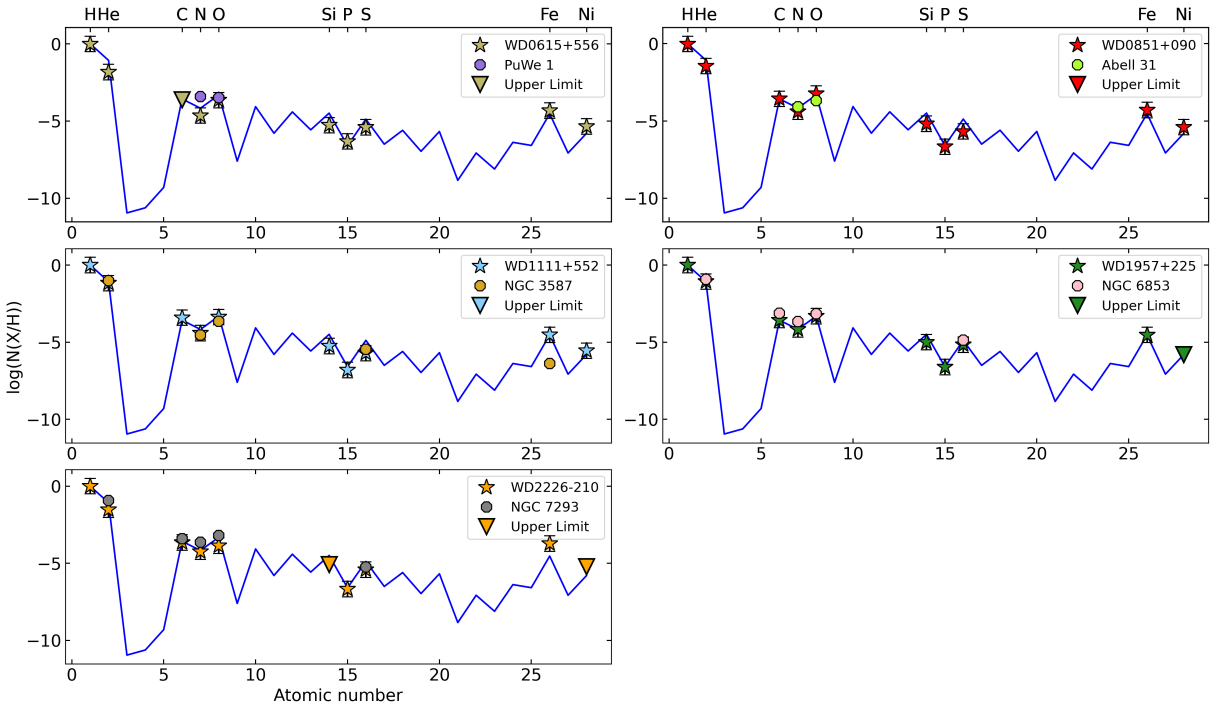


Figure 16: Comparison of photospheric abundances (stars) determined with TMAP and nebular abundances (filled circles) from the literature. Blue lines represents solar abundances.

tracks of Miller Bertolami (2016), which were then compared to kinematic ages of the PNe (if available) reported by González-Santamaría et al. (2021). As seen in Fig. 17, kinematic ages of the PNe are generally lower than cooling ages, where for the older PNe the discrepancy seems to be larger. This shows that kinematic ages of PNe might not be an accurate representation for cooling ages of CSs. Therefore, caution should be taken while using this method to determine CSs' masses.

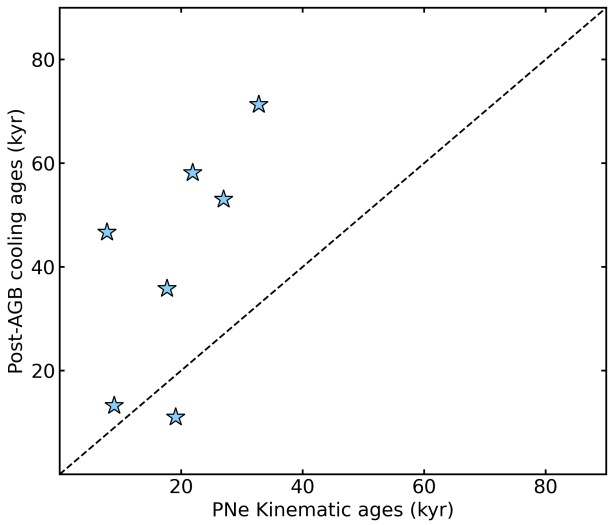


Figure 17: A comparison of PNe kinematic ages to post-AGB cooling times of CSs.

3.3.3 Mass discrepancy

In Sect. 3.2.1, the discrepancy between $M_{\rm Kiel}$ and $M_{\rm grav}$ was reported on average. An individual comparison of each object (Fig. 18) shows that a 1 σ agreement between the two mass derivation methods is 83% (15/18) for DAs[25], whereas this percentage is only 38% (5/13) for DAO WDs. Mass estimations of DAO WDs using different methods are clearly more prone to inconsistencies than DA WDs, which was also reported by Reindl et al. (2023) for their hot WD sample. Since the $T_{\rm eff}$ and log g measurements of hot H-rich WDs are heavily affected by the Balmer line problem (BLP), the same authors argued that an improvement to the mass discrepancy could be achieved if the atmospheric parameters were precisely determined through UV spectral analysis using fully metal-line blanketed NLTE models. Since this work utilizes metals in the model atmospheres, to test this argument, the SED fitting was repeated with fixed atmospheric parameters by using the pure H and H+He model grids of (Reindl et al. 2023) for the DA and DAO WDs, respectively. As opposed to expectations, Fig. 19 shows that metal-line blanketed models slightly deteriorates the problem instead of mitigating it, where the H/H+He models lead to slightly larger $M_{\rm grav}$ than the models with metals. This is because the flux distribution from far-UV to near-IR is slightly lower for the metal free models than the metal blanketed ones. Considering the fixed $T_{\rm eff}$ and log g, lower model flux results in a larger angular diameter for a given observed flux and parallax[26], which consequently translates to larger R and $M_{\rm grav}$ for metal free models.

In all cases showing statistical disagreement, the mass discrepancy in this work emerges in the form of a lower $M_{\rm grav}$ than $M_{\rm Kiel}$ without an exception. Since the gravity mass directly depends on log g, one might argue that the log g values are systematically underestimated. However, when log g of each object is increased by 0.3 dex and both masses are recalculated, $M_{\rm grav}$ of 65% of the objects becomes unrealistically high, reaching up to $\sim$0.8 $M_{\odot}$ differences in comparison to $M_{\rm Kiel}$. Therefore, this test implies that a systematic error in the log g measurements is unlikely. Nonetheless, lower log g uncertainties might help mitigating the problem.

While no apparent correlation is found between the mass discrepancy and photometric variability, presence of IR excess or interstellar reddening, the disagreement in mass estimates appears more frequent among higher $T_{\rm eff}$ objects (50% for $T_{\rm eff} > 70$ kK) than among cooler ones (15% for Teff $\leq$ 70 kK). On the other hand, 40% of the objects with *Gaia* parallaxes $\varpi < 5$ mas have inconsistent $M_{\rm grav}$ and $M_{\rm Kiel}$, whereas this fraction drops to 27% for the objects with *Gaia* parallaxes $\varpi \geq 5$ mas. However, this trend might simply indicate the tendency for closest objects to be cooler. Overall, the exact origin of the mass disagreement remains unclear, but, it likely arises from a combination of systematic uncertainties in both the observations and the atmospheric parameters.

[25] WD 0455−282 was excluded from this comparison due to its unusually high RUWE value of 8.65.

[26] $f(\lambda) = \Theta^2\ F(\lambda)/4$, where $f(\lambda)$ is the observed stellar flux at earth and $F(\lambda)$ is the model flux at the stellar surface.

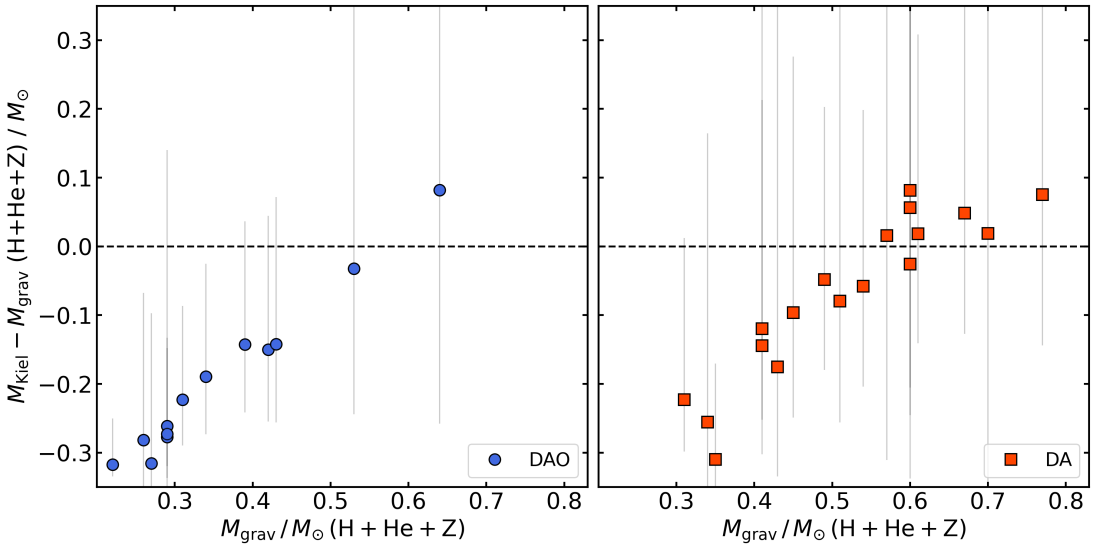


Figure 18: Comparison between gravity and Kiel masses of DAO (blue dots) and DA (red squares) WDs. The dashed line refers to a 1:1 comparison.

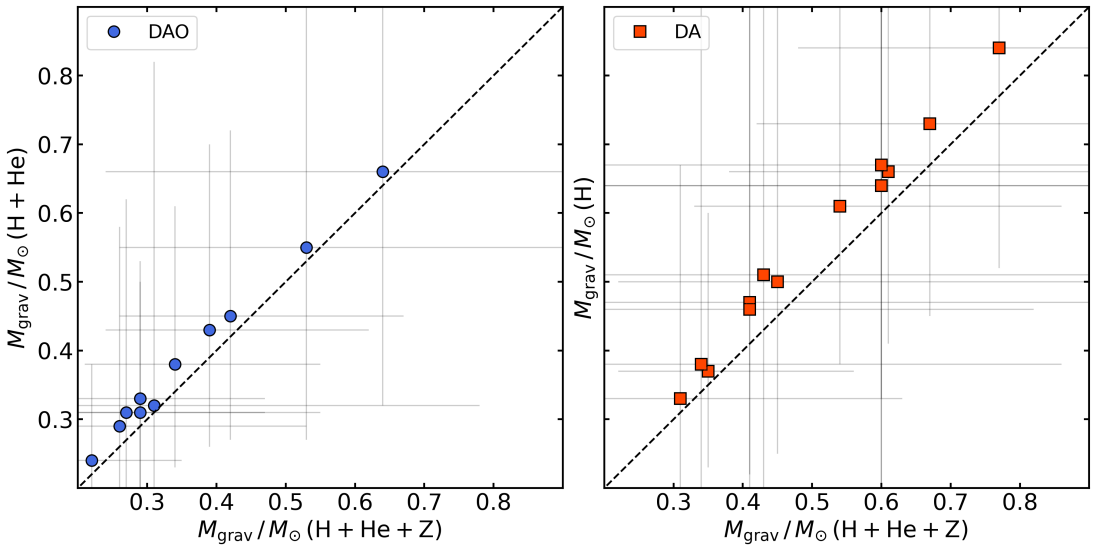


Figure 19: Comparison between gravity masses determined using metal-line blanketed and metal free models. DAO and DA WDs are depicted with blue dots and red squares, respectively. The dashed line refers to a 1:1 comparison.

4 Outlook

This study was initiated with the aim of providing a better understanding on the spectral evolution of hot H-rich WDs. The spectral analysis conducted in Paper I confirms, in the most straightforward manner yet, the evolutionary channel between DAO and DA WDs that has been introduced in previous studies. Availability of UV spectra is the key factor that allowed us to precisely determine the atmospheric parameters and, hence, to glimpse at the element transport mechanisms that shape the abundance patterns. The photometry performed in Paper II further supports the occurrence of radiation driven winds in the hot hybrid WD atmospheres. Moreover, it demonstrates that abundance patterns of the objects within the same spectral type do not deviate between single WDs and objects with (possible) companions, decreasing the possibility of accretion from external sources.

While the sample of 32 hot H-rich WDs builds a clear case, a larger sample with objects located below and above the DAO/DA transition region would allow us to map the changes in the abundance patterns more precisely. On the other hand, availability of more STIS spectra would allow us to determine the actual C, N, and O abundances of DA WDs rather than predicting an upper limit. This is especially important for comparisons to diffusion theory. Furthermore, inclusion of more opacities in the model atoms, such as Ne, Cl, and Ar would create more opportunities to test the effects of gravitation settling and mass-loss by comparing to nebular abundances. Since these elements are not expected to be processed in the AGB phase of low and intermediate stars, the abundance pattern of the nebula and, if not altered by diffusion, the central star should reflect the metallicity of the local interstellar matter (e.g., thin disk).

A major complication encountered in this work is mass discrepancy detected between different measurement methods. Contrary to expectations, inclusion of metal opacities did not resolve the issue. Due to heavy contamination of ISM lines in the UV spectra, $\log g$ derivation heavily relies on the optical spectra. Unluckily, spectral analysis of this work relied on low resolution optical spectra. It would be naive to expect that having high resolution data will present a solution to this long-standing problem. If a tighter constraint on $\log g$, however, could be placed, an improvement in the gravity mass derivations might be possible. Finally, the periodic brightness variations detected in WD 1056+516 and WD 1342+443, can be better characterized by high S/N follow-up time-series photometry in multiple band and time-resolved spectroscopy with additional IR observations, respectively.

Bibliography

Alam, S. et al. The Eleventh and Twelfth Data Releases of the Sloan Digital Sky Survey: Final Data from SDSS-III. ApJS, 219(1):12, July 2015. doi: 10.1088/0067-0049/219/1/12.

Allard, F. The PHOENIX Model Atmosphere Grid for Stars. In Reylé, C. et al, editors, *SF2A-2016: Proceedings of the Annual meeting of the French Society of Astronomy and Astrophysics*, pages 223–227, December 2016.

Aller, A. et al. Planetary nebulae seen with TESS: Discovery of new binary central star candidates from Cycle 1. A&A, 635:A128, March 2020. doi: 10.1051/0004-6361/201937118.

Aller, A., Lillo-Box, J. and Jones, D. Planetary nebulae seen with TESS: New and revisited short-period binary central star candidates from Cycles 1 to 4. A&A, 690: A190, October 2024. doi: 10.1051/0004-6361/202450942.

Asplund, M. et al. The Chemical Composition of the Sun. ARA&A, 47(1):481–522, September 2009. doi: 10.1146/annurev.astro.46.060407.145222.

Barker, T. The ionization structure of planetary nebulae. IV. NGC 6853. ApJ, 284: 589–596, September 1984. doi: 10.1086/162441.

Barstow, M.A. et al. A ROSAT survey of hot DA white dwarfs in non-interacting binary systems. MNRAS, 270:499–515, October 1994. doi: 10.1093/mnras/270.3.499.

Barstow, M.A. et al. Resolving Sirius-like binaries with the Hubble Space Telescope. MNRAS, 322(4):891–900, April 2001. doi: 10.1046/j.1365-8711.2001.04203.x.

Barstow, M.A. et al. A comparison of DA white dwarf temperatures and gravities from FUSE Lyman line and ground-based Balmer line observations. MNRAS, 344(2): 562–574, September 2003a. doi: 10.1046/j.1365-8711.2003.06838.x.

Barstow, M.A. et al. Heavy-element abundance patterns in hot DA white dwarfs. MNRAS, 341(3):870–890, May 2003b. doi: 10.1046/j.1365-8711.2003.06462.x.

Barstow, M.A. et al. Evidence for an external origin of heavy elements in hot DA white dwarfs. MNRAS, 440(2):1607–1625, May 2014. doi: 10.1093/mnras/stu216.

Bédard, A. et al. On the Spectral Evolution of Hot White Dwarf Stars. I. A Detailed Model Atmosphere Analysis of Hot White Dwarfs from SDSS DR12. ApJ, 901(2):93, October 2020. doi: 10.3847/1538-4357/abafbe.

Bédard, A., Bergeron, P. and Brassard, P. On the Spectral Evolution of Hot White Dwarf Stars. III. The PG 1159-DO-DB-DQ Evolutionary Channel Revisited. ApJ, 930 (1):8, May 2022. doi: 10.3847/1538-4357/ac609d.

Bédard, A. The spectral evolution of white dwarfs: where do we stand? Ap&SS, 369(4): 43, April 2024. doi: 10.1007/s10509-024-04307-5.

Bellm, E.C. et al. The Zwicky Transient Facility: Surveys and Scheduler. PASP, 131 (1000):068003, June 2019. doi: 10.1088/1538-3873/ab0c2a.

Benedict, G.F. et al. Interferometric Astrometry of the Detached White Dwarf-M Dwarf Binary Feige 24 Using HST Fine Guidance Sensor 3: White Dwarf Radius and Component Mass Estimates. AJ, 119(5):2382–2390, May 2000. doi: 10.1086/301355.

Bergeron, P. et al. A Spectroscopic Analysis of DAO and Hot DA White Dwarfs: The Implications of the Presence of Helium and the Nature of DAO Stars. ApJ, 432:305, September 1994. doi: 10.1086/174571.

Bergeron, P., Saumon, D. and Wesemael, F. New Model Atmospheres for Very Cool White Dwarfs with Mixed H/He and Pure He Compositions. ApJ, 443:764, April 1995. doi: 10.1086/175566.

Bianchi, L., Shiao, B. and Thilker, D. Revised Catalog of GALEX Ultraviolet Sources. I. The All-Sky Survey: GUVcat_AIS. ApJS, 230(2):24, June 2017. doi: 10.3847/1538-4365/aa7053.

Bilíková, J. et al. Spitzer Search for Dust Disks around Central Stars of Planetary Nebulae. ApJS, 200(1):3, May 2012. doi: 10.1088/0067-0049/200/1/3.

Blöcker, T. et al. The impact of evolutionary envelope masses on the evolution of white dwarfs. In Isern, J., Hernanz, M. and Garcia-Berro, E., editors, *White dwarfs*, volume 214 of *Astrophysics and Space Science Library*, page 57, January 1997. doi: 10.1007/978-94-011-5542-7_8.

Bohlin, R.C., Hubeny, I. and Rauch, T. New Grids of Pure-hydrogen White Dwarf NLTE Model Atmospheres and the HST/STIS Flux Calibration. AJ, 160(1):21, July 2020. doi: 10.3847/1538-3881/ab94b4.

Bonifacio, P. et al. LTE model atmopsheres MARCS, ATLAS and CO5BOLD. *arXiv e-prints*, art. arXiv:1109.0717, September 2011. doi: 10.48550/arXiv.1109.0717.

Brown, J.M. et al. The Binary Fraction of Low-mass White Dwarfs. ApJ, 730(2):67, April 2011. doi: 10.1088/0004-637X/730/2/67.

Calcaferro, L.M. et al. Pulsational instability of high-luminosity H-rich pre-white dwarf star. In *European Physical Journal Web of Conferences*, volume 152 of *European Physical Journal Web of Conferences*, page 06012, September 2017. doi: 10.1051/epjconf/201715206012.

Chayer, P. Radiative levitation of silicon in the atmospheres of two Hyades DA white dwarfs. MNRAS, 437(1):L95–L99, January 2014. doi: 10.1093/mnrasl/slt149.

Chayer, P., Fontaine, G. and Wesemael, F. Radiative Levitation in Hot White Dwarfs: Equilibrium Theory. ApJS, 99:189, July 1995a. doi: 10.1086/192184.

Chayer, P. et al. Improved Calculations of the Equilibrium Abundances of Heavy Elements Supported by Radiative Levitation in the Atmospheres of Hot DA White Dwarfs. ApJ, 454:429, November 1995b. doi: 10.1086/176494.

Chayer, P., Fontaine, G. and Pelletier, C. Diffusion of silicon in the envelopes of hot DA white dwarfs. In Isern, J., Hernanz, M. and Garcia-Berro, E., editors, *White dwarfs*, volume 214 of *Astrophysics and Space Science Library*, page 253, January 1997. doi: 10.1007/978-94-011-5542-7_35.

Chayer, P. et al. Probing the Atmospheres of Hot DA White Dwarfs with O VI. In Sonneborn, G., Moos, H.W. and Andersson, B.G., editors, *Astrophysics in the Far Ultraviolet: Five Years of Discovery with FUSE*, volume 348 of *Astronomical Society of the Pacific Conference Series*, page 209, June 2006.

Chu, Y.H. et al. Spitzer 24 μm Survey for Dust Disks around Hot White Dwarfs. AJ, 142(3):75, September 2011. doi: 10.1088/0004-6256/142/3/75.

Ciardullo, R. et al. A Hubble Space Telescope Survey for Resolved Companions of Planetary Nebula Nuclei. AJ, 118(1):488–508, July 1999. doi: 10.1086/300940.

Colman, I.L. et al. Methods for the Detection of Stellar Rotation Periods in Individual TESS Sectors and Results from the Prime Mission. AJ, 167(5):189, May 2024. doi: 10.3847/1538-3881/ad2c86.

De Marco, O. et al. The binary fraction of planetary nebula central stars - I. A high-precision, I-band excess search. MNRAS, 428(3):2118–2140, January 2013. doi: 10.1093/mnras/sts180.

Delgado Inglada, G. et al. The Iron Abundance in Galactic Planetary Nebulae. ApJ, 694(2):1335–1348, April 2009. doi: 10.1088/0004-637X/694/2/1335.

Delgado-Inglada, G. and Rodríguez, M. C/O Abundance Ratios, Iron Depletions, and Infrared Dust Features in Galactic Planetary Nebulae. ApJ, 784(2):173, April 2014. doi: 10.1088/0004-637X/784/2/173.

Dobbie, P.D. et al. Photospheric phosphorus in the FUSE spectra of GD71 and two similar DA white dwarfs. MNRAS, 363(3):763–768, November 2005. doi: 10.1111/j.1365-2966.2005.09589.x.

Drake, A.J. et al. First Results from the Catalina Real-Time Transient Survey. ApJ, 696(1):870–884, May 2009. doi: 10.1088/0004-637X/696/1/870.

Dufour, P. et al. On the Spectral Evolution of Cool, Helium-Atmosphere White Dwarfs: Detailed Spectroscopic and Photometric Analysis of DZ Stars. ApJ, 663(2): 1291–1308, July 2007. doi: 10.1086/518468.

Dupuis, J. et al. A Study of Metal Abundance Patterns in Cool White Dwarfs. I. Time-dependent Calculations of Gravitational Settling. ApJS, 82:505, October 1992. doi: 10.1086/191728.

Dye, S. et al. The UKIRT Hemisphere Survey: definition and J-band data release. MNRAS, 473(4):5113–5125, February 2018. doi: 10.1093/mnras/stx2622.

Eggen, O.J. and Greenstein, J.L. Spectra, colors, luminosities and motions of the white dwarfs . ApJ, 141:83–108, January 1965. doi: 10.1086/148091.

El-Badry, K., Rix, H.W. and Heintz, T.M. A million binaries from Gaia eDR3: sample selection and validation of Gaia parallax uncertainties. MNRAS, 506(2):2269–2295, September 2021. doi: 10.1093/mnras/stab323.

Fazio, G.G. et al. The Infrared Array Camera (IRAC) for the Spitzer Space Telescope. ApJS, 154(1):10–17, September 2004. doi: 10.1086/422843.

Fitzpatrick, E.L. et al. An Analysis of the Shapes of Interstellar Extinction Curves. VII. Milky Way Spectrophotometric Optical-through-ultraviolet Extinction and Its R-dependence. ApJ, 886(2):108, December 2019. doi: 10.3847/1538-4357/ab4c3a.

Flewelling, H.A. et al. The Pan-STARRS1 Database and Data Products. ApJS, 251(1): 7, November 2020. doi: 10.3847/1538-4365/abb82d.

Fontaine, G. and Wesemael, F. Recent advances in the theory of white dwarf spectral evolution. In Philip, A.G.D., Hayes, D.S. and Liebert, J.W., editors, *IAU Colloquium 95: Second Conference on Faint Blue Stars*, pages 319–326, January 1987.

Fontaine, G., Brassard, P. and Bergeron, P. The Potential of White Dwarf Cosmochronology. PASP, 113(782):409–435, April 2001. doi: 10.1086/319535.

Fragkou, V. et al. The physical association of planetary nebula NGC 2818 with open cluster NGC 2818A. A&A, 696:A146, April 2025. doi: 10.1051/0004-6361/202453031.

Frew, D.J. *Planetary Nebulae in the Solar Neighbourhood: Statistics, Distance Scale and Luminosity Function*. PhD thesis, Macquarie University, Department of Physics and Astronomy, July 2008.

Gaia Collaboration et al. Gaia Data Release 3. Summary of the content and survey properties. A&A, 674:A1, June 2023. doi: 10.1051/0004-6361/202243940.

Gänsicke, B.T. et al. Accretion of a giant planet onto a white dwarf star. Nature, 576 (7785):61–64, December 2019. doi: 10.1038/s41586-019-1789-8.

García-Hernández, D.A. et al. Galactic planetary nebulae with precise nebular abundances as a tool to understand the evolution of asymptotic giant branch stars. MNRAS, 461(1):542–551, September 2016. doi: 10.1093/mnras/stw1349.

García-Rojas, J. et al. Analysis of chemical abundances in planetary nebulae with [WC] central stars. II. Chemical abundances and the abundance discrepancy factor. A&A, 558:A122, October 2013. doi: 10.1051/0004-6361/201322354.

Gesicki, K., Acker, A. and Zijlstra, A.A. Kinematics, turbulence and evolution of planetary nebulae. A&A, 400:957–969, March 2003. doi: 10.1051/0004-6361:20030079.

Gianninas, A. et al. Spectroscopic Analysis of Hot, Hydrogen-rich White Dwarfs: The Presence of Metals and the Balmer-line Problem. ApJ, 720(1):581–602, September 2010. doi: 10.1088/0004-637X/720/1/581.

Gianninas, A., Bergeron, P. and Ruiz, M.T. A Spectroscopic Survey and Analysis of Bright, Hydrogen-rich White Dwarfs. ApJ, 743(2):138, December 2011. doi: 10.1088/0004-637X/743/2/138.

González-Santamaría, I. et al. Planetary nebulae in Gaia EDR3: Central star identification, properties, and binarity. A&A, 656:A51, December 2021. doi: 10.1051/0004-6361/202141916.

Good, S.A. et al. Comparison of the effective temperatures, gravities and helium abundances of DAO white dwarfs from Balmer and Lyman line studies. MNRAS, 355 (3):1031–1040, December 2004. doi: 10.1111/j.1365-2966.2004.08406.x.

Good, S.A. et al. Heavy element abundances in DAO white dwarfs measured from FUSE data. MNRAS, 363(1):183–196, October 2005. doi: 10.1111/j.1365-2966.2005.09428.x.

Gräfener, G., Koesterke, L. and Hamann, W.R. Line-blanketed model atmospheres for WR stars. A&A, 387:244–257, May 2002. doi: 10.1051/0004-6361:20020269.

Greenstein, J.L. and Eggen, O.J. The calibration of the Hertzsprung-Russell diagram for sub-luminous stars. *Vistas in Astronomy*, 8(1):63–73, January 1966. doi: 10.1016/0083-6656(66)90021-3.

Guerrero, M.A. and De Marco, O. Analysis of far-UV data of central stars of planetary nebulae: Occurrence and variability of stellar winds. A&A, 553:A126, May 2013. doi: 10.1051/0004-6361/201220623.

Guillén, P.F. et al. Multiple outflows in the planetary nebula NGC 6058. MNRAS, 432 (4):2676–2684, July 2013. doi: 10.1093/mnras/stt612.

Guo, J. et al. White dwarfs identified in LAMOST DR 2. MNRAS, 454(3):2787–2797, December 2015. doi: 10.1093/mnras/stv2104.

Hamann, W.R. and Gräfener, G. A temperature correction method for expanding atmospheres. A&A, 410:993–1000, November 2003. doi: 10.1051/0004-6361:20031308.

Hartman, J.D. and Bakos, G.Á. VARTOOLS: A program for analyzing astronomical time-series data. *Astronomy and Computing*, 17:1–72, October 2016. doi: 10.1016/j.ascom.2016.05.006.

Heber, U., Irrgang, A. and Schaffenroth, J. Spectral energy distributions and colours of hot subluminous stars. *Open Astronomy*, 27(1):35–43, February 2018. doi: 10.1515/astro-2018-0008.

Henry, R.B.C., Kwitter, K.B. and Dufour, R.J. Morphology and Composition of the Helix Nebula. ApJ, 517(2):782–798, June 1999. doi: 10.1086/307215.

Henry, R.B.C., Kwitter, K.B. and Balick, B. Sulfur, Chlorine, and Argon Abundances in Planetary Nebulae. IV. Synthesis and the Sulfur Anomaly. AJ, 127(4):2284–2302, April 2004. doi: 10.1086/382242.

Herald, J.E. and Bianchi, L. The winds of hydrogen-rich central stars of planetary nebulae. MNRAS, 417(4):2440–2464, November 2011. doi: 10.1111/j.1365-2966.2011.19319.x.

Hermes, J.J. et al. When flux standards go wild: white dwarfs in the age of Kepler. MNRAS, 468(2):1946–1952, June 2017a. doi: 10.1093/mnras/stx567.

Hermes, J.J. et al. A Deep Test of Radial Differential Rotation in a Helium-atmosphere White Dwarf. I. Discovery of Pulsations in PG 0112+104. ApJ, 835(2):277, February 2017b. doi: 10.3847/1538-4357/835/2/277.

Higgins, M.E. and Bell, K.J. Localizing Sources of Variability in Crowded TESS Photometry. AJ, 165(4):141, April 2023. doi: 10.3847/1538-3881/acb20c.

Holberg, J.B. et al. Where are all the Sirius-like binary systems? MNRAS, 435(3): 2077–2091, November 2013. doi: 10.1093/mnras/stt1433.

Hollands, M.A. et al. Cool DZ white dwarfs - I. Identification and spectral analysis. MNRAS, 467(4):4970–5000, June 2017. doi: 10.1093/mnras/stx250.

Holovatyy, V.V. and Havrilova, N.V. The Chemical Composition of Galactic Planetary Nebulae with Regard to Inhomogeneity in the Gas Density in Their Envelopes. *Astronomy Reports*, 49(5):390–404, May 2005. doi: 10.1134/1.1923548.

Huang, C.X. et al. TESS Discovery of a Transiting Super-Earth in the pi Mensae System. ApJ, 868(2):L39, December 2018. doi: 10.3847/2041-8213/aaef91.

Husser, T.O. et al. A new extensive library of PHOENIX stellar atmospheres and synthetic spectra. A&A, 553:A6, May 2013. doi: 10.1051/0004-6361/201219058.

Iben, Jr., I. On the frequency of planetary nebula nuclei powered by helium burningand on the frequency of white dwarfs with hydrogen-deficient atmospheres. ApJ, 277: 333–354, February 1984. doi: 10.1086/161700.

Iben, Jr., I. et al. On the evolution of those nuclei of planetary nebulae that experiencea final helium shell flash. ApJ, 264:605–612, January 1983. doi: 10.1086/160631.

Irrgang, A. et al. A proto-helium white dwarf stripped by a substellar companion via common-envelope ejection. Uncovering the true nature of a candidate hypervelocity B-type star. A&A, 650:A102, June 2021. doi: 10.1051/0004-6361/202038757.

Jenkins, J.M. et al. The TESS science processing operations center. In Chiozzi, G. and Guzman, J.C., editors, *Software and Cyberinfrastructure for Astronomy IV*, volume 9913 of *Society of Photo-Optical Instrumentation Engineers (SPIE) Conference Series*, page 99133E, August 2016. doi: 10.1117/12.2233418.

Jura, M. A Tidally Disrupted Asteroid around the White Dwarf G29-38. ApJ, 584(2): L91–L94, February 2003. doi: 10.1086/374036.

Kaler, J.B., Shaw, R.A. and Kwitter, K.B. Large Planetary Nebulae and Their Significance to the Late Stages of Stellar Evolution. ApJ, 359:392, August 1990. doi: 10.1086/169073.

Kalirai, J.S. The age of the Milky Way inner halo. Nature, 486(7401):90–92, June 2012. doi: 10.1038/nature11062.

Kawaler, S.D. The Hydrogen Shell Game: Pulsational Instabilities in Hydrogen Shell–Burning Planetary Nebula Nuclei. ApJ, 334:220, November 1988. doi: 10.1086/166832.

Kawka, A. et al. Orbital Parameters and Chemical Composition of Four White Dwarfs in Post-Common-Envelope Binaries. ApJ, 675(2):1518–1530, March 2008. doi: 10.1086/526411.

Kilic, M. et al. Debris Disks around White Dwarfs: The DAZ Connection. ApJ, 646(1): 474–479, July 2006. doi: 10.1086/504682.

Kilic, M. et al. The Ages of the Thin Disk, Thick Disk, and the Halo from Nearby White Dwarfs. ApJ, 837(2):162, March 2017. doi: 10.3847/1538-4357/aa62a5.

Koester, D. Accretion and diffusion in white dwarfs. New diffusion timescales and applications to GD 362 and G 29-38. A&A, 498(2):517–525, May 2009. doi: 10.1051/0004-6361/200811468.

Koester, D. White dwarf spectra and atmosphere models. Mem. Soc. Astron. Italiana, 81:921–931, January 2010.

Koester, D. and Kepler, S.O. DB white dwarfs in the Sloan Digital Sky Survey data release 10 and 12. A&A, 583:A86, November 2015. doi: 10.1051/0004-6361/201527169.

Krtička, J., Kubát, J. and Krtičková, I. Stellar wind models of central stars of planetary nebulae. A&A, 635:A173, March 2020. doi: 10.1051/0004-6361/201937150.

Kwitter, K.B. and Henry, R.B.C. Sulfur, Chlorine, and Argon in Planetary Nebulae. I. Observations and Abundances in a Northern Sample. ApJ, 562(2):804–823, December 2001. doi: 10.1086/322505.

Lindegren, L. et al. Gaia Early Data Release 3. Parallax bias versus magnitude, colour, and position. A&A, 649:A4, May 2021. doi: 10.1051/0004-6361/202039653.

Löbling, L. et al. First discovery of trans-iron elements in a DAO-type white dwarf (BD-223467). MNRAS, 492(1):528–548, February 2020. doi: 10.1093/mnras/stz3247.

Maeda, K. and Shibahashi, H. Pulsations of pre-white dwarfs with hydrogen-dominated atmospheres. PASJ, 66(4):76, July 2014. doi: 10.1093/pasj/psu051.

Manseau, P.M., Bergeron, P. and Green, E.M. A Spectroscopic Search for Chemically Stratified White Dwarfs in the Sloan Digital Sky Survey. ApJ, 833(2):127, December 2016. doi: 10.3847/1538-4357/833/2/127.

Manser, C.J. et al. A planetesimal orbiting within the debris disc around a white dwarf star. *Science*, 364(6435):66–69, April 2019. doi: 10.1126/science.aat5330.

Manser, C.J. et al. The frequency of gaseous debris discs around white dwarfs. MNRAS, 493(2):2127–2139, April 2020. doi: 10.1093/mnras/staa359.

Marocco, F. et al. The CatWISE2020 Catalog. ApJS, 253(1):8, March 2021. doi: 10.3847/1538-4365/abd805.

Martin, D.C. et al. The Galaxy Evolution Explorer: A Space Ultraviolet Survey Mission. ApJ, 619(1):L1–L6, January 2005. doi: 10.1086/426387.

Masci, F.J. et al. The Zwicky Transient Facility: Data Processing, Products, and Archive. PASP, 131(995):018003, January 2019. doi: 10.1088/1538-3873/aae8ac.

McMahon, R.G. et al. First Scientific Results from the VISTA Hemisphere Survey (VHS). *The Messenger*, 154:35–37, December 2013.

Melis, C. et al. Serendipitous Discovery of Nine White Dwarfs with Gaseous Debris Disks. ApJ, 905(1):56, December 2020. doi: 10.3847/1538-4357/abbdfa.

Miller Bertolami, M.M. Primer on Formation and Evolution of Hydrogen-Deficient Central Stars of Planetary Nebulæ and Related Objects. *Galaxies*, 12(6):83, November 2024. doi: 10.3390/galaxies12060083.

Miller Bertolami, M.M. New models for the evolution of post-asymptotic giant branch stars and central stars of planetary nebulae. A&A, 588:A25, April 2016. doi: 10.1051/0004-6361/201526577.

Müller-Ringat, E.M. *Spektralanalyse im Virtuellen ObservatoriumSpektralanalyse im Virtuellen ObservatoriumSpectral Analysis in the Virtual Observatory;*. PhD thesis, Eberhard Karls University of Tubingen, Germany, January 2013.

Napiwotzki, R. Spectroscopic investigation of old planetaries. IV. Model atmosphere analysis. A&A, 350:101–119, October 1999. doi: 10.48550/arXiv.astro-ph/9908181.

Napiwotzki, R. Spectroscopic investigation of old planetaries. V. Distance scales. A&A, 367:973–982, March 2001. doi: 10.1051/0004-6361:20000431.

Nebot Gómez-Morán, A. et al. Post common envelope binaries from SDSS. XII. The orbital period distribution. A&A, 536:A43, December 2011. doi: 10.1051/0004-6361/201117514.

Oliveira da Rosa, G. et al. Photometric White Dwarf Rotation. ApJ, 974(2):314, October 2024. doi: 10.3847/1538-4357/ad6987.

Onken, C.A. et al. SkyMapper Southern Survey: Second data release (DR2). PASA, 36: e033, August 2019. doi: 10.1017/pasa.2019.27.

Pedersen, M.G. and Bell, K.J. Contamination in TESS Light Curves: The Case of the Fast Yellow Pulsating Supergiants. AJ, 165(6):239, June 2023. doi: 10.3847/1538-3881/accc31.

Pottasch, S.R., Surendiranath, R. and Bernard-Salas, J. Abundances in planetary nebulae: NGC 1535, NGC 6629, He2-108, and Tc1. A&A, 531:A23, July 2011. doi: 10.1051/0004-6361/201116669.

Press, W.H. et al. *Numerical recipes in C. The art of scientific computing*. 1992.

Preval, S.P. et al. A far-UV survey of three hot, metal-polluted white dwarf stars: WD0455-282, WD0621-376, and WD2211-495. MNRAS, 487(3):3470–3487, August 2019. doi: 10.1093/mnras/stz1506.

Raddi, R. et al. Testing the mass-radius relation of white dwarfs in common proper-motion pairs: I. Hydrogen-dominated atmospheres. A&A, 695:A131, March 2025. doi: 10.1051/0004-6361/202452135.

Rauch, T. Panchromatic Calibration of Astronomical Observations with State-of-the-Art White Dwarf Model Atmospheres. *arXiv e-prints*, art. arXiv:1210.7636, October 2012. doi: 10.48550/arXiv.1210.7636.

Rauch, T. and Deetjen, J.L. Handling of Atomic Data. In Hubeny, I., Mihalas, D. and Werner, K., editors, *Stellar Atmosphere Modeling*, volume 288 of *Astronomical Society of the Pacific Conference Series*, page 103, January 2003. doi: 10.48550/arXiv.astro-ph/0403239.

Rauch, T. et al. High-resolution FUSE and HST ultraviolet spectroscopy of the white dwarf central star of <ASTROBJ>Sh 2-216</ASTROBJ>. A&A, 470(1):317–329, July 2007. doi: 10.1051/0004-6361:20077166.

Rauch, T. et al. Stellar laboratories: new Ge V and Ge VI oscillator strengths and their validation in the hot white dwarf RE 0503-289. A&A, 546:A55, October 2012. doi: 10.1051/0004-6361/201220014.

Rauch, T. et al. The virtual observatory service TheoSSA: Establishing a database of synthetic stellar flux standards. I. NLTE spectral analysis of the DA-type white dwarf <ASTROBJ>G191-B2B</ASTROBJ>. A&A, 560:A106, December 2013. doi: 10.1051/0004-6361/201322336.

Rauch, T. et al. Stellar laboratories. IV. New Ga iv, Ga v, and Ga vi oscillator strengths and the gallium abundance in the hot white dwarfs <ASTROBJ>G191-B2B</ASTROBJ> and RE 0503-289. A&A, 577:A6, May 2015. doi: 10.1051/0004-6361/201425326.

Rauch, T. et al. Stellar laboratories. VI. New Mo iv-vii oscillator strengths and the molybdenum abundance in the hot white dwarfs G191-B2B and RE 0503-289. A&A, 587:A39, March 2016. doi: 10.1051/0004-6361/201527324.

Rauch, T. et al. Stellar laboratories. X. New Cu IV-VII oscillator strengths and the first detection of copper and indium in hot white dwarfs. A&A, 637:A4, May 2020. doi: 10.1051/0004-6361/201936620.

Reindl, N. et al. Analysis of cool DO-type white dwarfs from the Sloan Digital Sky Survey data release 10. A&A, 572:A117, December 2014a. doi: 10.1051/0004-6361/201424861.

Reindl, N. et al. On helium-dominated stellar evolution: the mysterious role of the O(He)-type stars. A&A, 566:A116, June 2014b. doi: 10.1051/0004-6361/201423498.

Reindl, N. et al. Unravelling the baffling mystery of the ultrahot wind phenomenon in white dwarfs. MNRAS, 482(1):L93–L98, January 2019. doi: 10.1093/mnrasl/sly191.

Reindl, N. et al. Mysterious, variable, and extremely hot: White dwarfs showing ultra-high excitation lines. I. Photometric variability. A&A, 647:A184, March 2021. doi: 10.1051/0004-6361/202140289.

Reindl, N. et al. The bright blue side of the night sky: Spectroscopic survey of bright and hot (pre-) white dwarfs. A&A, 677:A29, September 2023. doi: 10.1051/0004-6361/202346865.

Reindl, N. et al. Spectroscopic survey of faint planetary-nebula nuclei: VI. Seventeen hydrogen-rich central stars. A&A, 690:A366, October 2024. doi: 10.1051/0004-6361/202451591.

Renedo, I. et al. New Cooling Sequences for Old White Dwarfs. ApJ, 717(1):183–195, July 2010. doi: 10.1088/0004-637X/717/1/183.

Rieke, G.H. et al. The Multiband Imaging Photometer for Spitzer (MIPS). ApJS, 154 (1):25–29, September 2004. doi: 10.1086/422717.

Riello, M. et al. Gaia Early Data Release 3. Photometric content and validation. A&A, 649:A3, May 2021. doi: 10.1051/0004-6361/202039587.

Schlafly, E.F., Meisner, A.M. and Green, G.M. The unWISE Catalog: Two Billion Infrared Sources from Five Years of WISE Imaging. ApJS, 240(2):30, February 2019. doi: 10.3847/1538-4365/aafbea.

Schoening, T. and Butler, K. Stark broadening of He II lines. A&AS, 78:51–87, April 1989.

Skrutskie, M.F. et al. The Two Micron All Sky Survey (2MASS). AJ, 131(2):1163–1183, February 2006. doi: 10.1086/498708.

Stanghellini, L. et al. Planetary Nebula Abundances and Morphology: Probing the Chemical Evolution of the Milky Way. ApJ, 651(2):898–905, November 2006. doi: 10.1086/507840.

Stanghellini, L. et al. Abundances of Planetary Nebulae and Evolved Stars: Iron and Sulfur Depletion, and Carbon and Nitrogen Enrichment, in Low- and Intermediate-mass Stellar Populations in the Milky Way. ApJ, 972(2):130, September 2024. doi: 10.3847/1538-4357/ad5963.

Steen, M. et al. Measuring White Dwarf Variability from Sparsely Sampled Gaia DR3 Multi-epoch Photometry. ApJ, 967(2):166, June 2024. doi: 10.3847/1538-4357/ad3e60.

Swan, A. et al. Planetesimals at DZ stars - I. Chondritic compositions and a massive accretion event. MNRAS, 526(3):3815–3831, December 2023. doi: 10.1093/mnras/stad2867.

Thorstensen, J.R. et al. Spectroscopy of the extreme-ultraviolet source Feige 24: the binary orbit and the mass of the white dwarf. ApJ, 223:260–265, July 1978. doi: 10.1086/156258.

Tonry, J.L. et al. ATLAS: A High-cadence All-sky Survey System. PASP, 130(988): 064505, June 2018. doi: 10.1088/1538-3873/aabadf.

Tremblay, P.E. and Bergeron, P. Spectroscopic Analysis of DA White Dwarfs: Stark Broadening of Hydrogen Lines Including Nonideal Effects. ApJ, 696(2):1755–1770, May 2009. doi: 10.1088/0004-637X/696/2/1755.

Unglaub, K. Mass Loss Predictions for Hot (Pre-)White Dwarfs. In Napiwotzki, R. and Burleigh, M.R., editors, *15th European Workshop on White Dwarfs*, volume 372 of *Astronomical Society of the Pacific Conference Series*, page 201, September 2007.

Unglaub, K. and Bues, I. The effect of diffusion and mass loss on the helium abundance in hot white dwarfs and subdwarfs. A&A, 338:75–84, October 1998.

Unglaub, K. and Bues, I. The chemical evolution of hot white dwarfs in the presence of diffusion and mass loss. A&A, 359:1042–1058, July 2000.

Vanderburg, A. et al. A giant planet candidate transiting a white dwarf. Nature, 585 (7825):363–367, September 2020. doi: 10.1038/s41586-020-2713-y.

Vennes, S. and Thorstensen, J.R. Spectroscopic, Orbital, and Physical Properties of the Binary Feige 24 and Detection of Transient He II Absorption in the System. AJ, 108: 1881, November 1994. doi: 10.1086/117201.

Vennes, S. et al. The Presence of Helium in Hot DA White Dwarfs: The Role of Radiative Levitation and the Case for Stratified Atmospheres. ApJ, 331:876, August 1988. doi: 10.1086/166606.

Vennes, S. et al. An Explanation for the Peculiar EUV Spectrum of the Hot DA White Dwarf Feige 24. ApJ, 336:L25, January 1989. doi: 10.1086/185353.

Vennes, S. The Constitution of the Atmospheric Layers and the Extreme Ultraviolet Spectrum of Hot Hydrogen-rich White Dwarfs. ApJ, 390:590, May 1992. doi: 10.1086/171310.

Vennes, S. and Fontaine, G. An Interpretation of the Spectral Properties of Hot Hydrogen-rich White Dwarfs with Stratified H/He Model Atmospheres. ApJ, 401:288, December 1992. doi: 10.1086/172060.

Vennes, S. and Lanz, T. A Comparative Study of the Atmospheric Composition of the DA White Dwarfs Feige 24 and G191-B2B. ApJ, 553(1):399–404, May 2001. doi: 10.1086/320653.

Vennes, S. et al. The Binary Feige 24: The Mass, Radius, and Gravitational Redshift of the DA White Dwarf. ApJ, 372:L37, May 1991. doi: 10.1086/186018.

Vennes, S. et al. Discovery of Photospheric Sulfur and Phosphorus in ORFEUS Spectra of the Hot White Dwarfs G191-B2B and MCT O455-2812. ApJ, 468:898, September 1996. doi: 10.1086/177745.

Vennes, S., Christian, D.J. and Thorstensen, J.R. Hot White Dwarfs in the Extreme-Ultraviolet Explorer Survey. IV. DA White Dwarfs with Bright Companions. ApJ, 502(2):763–787, August 1998. doi: 10.1086/305926.

Vennes, S. et al. Hubble Space Telescope Imaging Spectrograph Observations of the Hot White Dwarf in the Close Binary Feige 24. ApJ, 544(1):423–436, November 2000. doi: 10.1086/317205.

Weidmann, W.A. et al. Catalogue of the central stars of planetary nebulae. Expanded edition. A&A, 640:A10, August 2020. doi: 10.1051/0004-6361/202037998.

Werner, K. and Dreizler, S. The classical stellar atmosphere problem. *Journal of Computational and Applied Mathematics*, 109(1):65–93, September 1999. doi: 10.48550/arXiv.astro-ph/9906130.

Werner, K. et al. Model Photospheres with Accelerated Lambda Iteration. In Hubeny, I., Mihalas, D. and Werner, K., editors, *Stellar Atmosphere Modeling*, volume 288 of *Astronomical Society of the Pacific Conference Series*, page 31, January 2003. doi: 10.48550/arXiv.astro-ph/0209535.

Werner, K., Rauch, T. and Kruk, J.W. Discovery of photospheric argon in very hot central stars of planetary nebulae and white dwarfs. A&A, 466(1):317–322, April 2007. doi: 10.1051/0004-6361:20077101.

Werner, K., Rauch, T. and Kruk, J.W. Far-UV spectroscopy of two extremely hot, helium-rich white dwarfs. A&A, 601:A8, May 2017. doi: 10.1051/0004-6361/201630266.

Werner, K., Rauch, T. and Kruk, J.W. Metal abundances in hot white dwarfs with signatures of a superionized wind. A&A, 609:A107, January 2018a. doi: 10.1051/0004-6361/201731740.

Werner, K., Rauch, T. and Kruk, J.W. The hot white dwarf in the peculiar binary nucleus of the planetary nebula EGB 6. A&A, 616:A73, August 2018b. doi: 10.1051/0004-6361/201833200.

Werner, K., Rauch, T. and Reindl, N. Spectral analysis of the extremely hot DA white dwarf PG 0948+534. MNRAS, 483(4):5291–5300, March 2019. doi: 10.1093/mnras/sty3408.

Werner, K. and Herwig, F. The Elemental Abundances in Bare Planetary Nebula Central Stars and the Shell Burning in AGB Stars. PASP, 118(840):183–204, February 2006. doi: 10.1086/500443.

Werner, K., Dreizler, S. and Rauch, T. TMAP: Tübingen NLTE Model-Atmosphere Package. Astrophysics Source Code Library, record ascl:1212.015, December 2012.

Wesemael, F., Green, R.F. and Liebert, J. Spectrophotometric and model-atmosphere analyses of the hot DO and DAO white dwarfs from the Palomar-Green survey. ApJS, 58:379–411, July 1985. doi: 10.1086/191046.

Wright, E.L. et al. The Wide-field Infrared Survey Explorer (WISE): Mission Description and Initial On-orbit Performance. AJ, 140(6):1868–1881, December 2010. doi: 10.1088/0004-6256/140/6/1868.

Zechmeister, M. and Kürster, M. The generalised Lomb-Scargle periodogram. A new formalism for the floating-mean and Keplerian periodograms. A&A, 496(2):577–584, March 2009. doi: 10.1051/0004-6361:200811296.

Ziegler, M. *(F)UV spectral analysis of 15 hot, hydrogen-rich central stars of PNe.* PhD thesis, Eberhard Karls University of Tubingen, Germany, January 2012.

Zuckerman, B. et al. Metal Lines in DA White Dwarfs. ApJ, 596(1):477–495, October 2003. doi: 10.1086/377492.

Appendix A: Original publications

Paper I

Semih Filiz, Klaus Werner, Thomas Rauch, and Nicole Reindl

"Spectral evolution of hot hybrid white dwarfs I. Spectral analysis"

Astronomy & Astrophysics, 2024, 691, A290

© 2024 Reproduced with permission from Astronomy & Astrophysics.
All rights reserved. The original publication is available at:
https://doi.org/10.1051/0004-6361/202451886

A&A, 691, A290 (2024)
https://doi.org/10.1051/0004-6361/202451886
© The Authors 2024

Astronomy & Astrophysics

Spectral evolution of hot hybrid white dwarfs

I. Spectral analysis

Semih Filiz[1,⋆], Klaus Werner[1], Thomas Rauch[1], and Nicole Reindl[2]

[1] Institut für Astronomie und Astrophysik, Kepler Center for Astro and Particle Physics, Eberhard Karls Universität, Sand 1, 72076 Tübingen, Germany
[2] Landessternwarte Heidelberg, Zentrum für Astronomie, Ruprecht-Karls-Universität, Königstuhl 12, 69117 Heidelberg, Germany

Received 14 August 2024 / Accepted 3 October 2024

ABSTRACT

Context. Hydrogen-rich white dwarfs (WDs) comprise the majority of the WD population, but are only rarely found at the very hot end of the WD cooling sequence. A small subgroup that exhibits both hydrogen and helium lines in their spectra, the so-called hybrid (or DAO) WDs, represents the majority of hydrogen-rich WDs at effective temperatures $T_{\rm eff} \approx 100$ kK.
Aims. We aim to understand the spectral evolution of hot hybrid WDs. Although small in number, they represent an evolutionary phase for most (≈75%) WDs.
Methods. We conducted a nonlocal thermodynamic equilibrium (NLTE) analysis with fully metal line blanketed model atmospheres for the ultraviolet (UV) and optical spectra of a sample of 19 DA and 13 DAO WDs with $T_{\rm eff} > 60$ kK. The UV spectra allow us to precisely measure the temperature through model fits to metal lines in different ionization stages. This enables us to place the WDs accurately on the cooling sequence.
Results. In contrast to earlier studies that typically relied on temperature measurements made from hydrogen lines alone, all DAOs in our sample are clearly hotter than the DAs. DAOs transform into DAs when they cool to $T_{\rm eff} \approx 75$–85 kK, depending on their mass. Along the cooling sequence, we witness a gradual decrease in the abundance of helium and the CNO elements in the DAOs due to gravitational settling. Simultaneously, iron and nickel abundances increase up to the transition region because radiative forces act more efficiently on them. This is followed by a steady decline. We discuss the implications of our results on atomic diffusion theory and on the role of weak radiation-driven winds in hot hydrogen-rich WDs.

Key words. stars: abundances – stars: atmospheres – stars: evolution – white dwarfs

1. Introduction

White dwarfs (WDs) represent the final stage in the evolution of low- and intermediate-mass stars ($M < 8\ M_\odot$). They are the predominant end products of stellar evolution. From the *Gaia* mission, approximately 359 000 high-confidence WD candidates were identified in the Milky Way (Gentile Fusillo et al. 2021b), and more than 37 000 WDs are spectroscopically confirmed (Kepler et al. 2021, and references therein). With the upcoming space-based gravitational-wave detector Laser Interferometer Space Antenna (LISA), optically faint WD binaries will be studied. This in turn will help us to uncover Galaxy regions that are otherwise hard to observe (Lamberts et al. 2019).

In addition to their substantial numbers, WDs present an incontrovertible prospect of investigating physics under extreme conditions. In this sense, hot WDs offer a unique opportunity besides connecting the final stages of stellar evolution to earlier phases. They are reliable sources for deriving atomic data of elements beyond the iron group (Rauch et al. 2012, 2014a,b, 2015a,b, 2016a,b, 2017a,b, 2020) and for testing theories of the influence of gravity on the fundamental constants (Hu et al. 2021).

In the aftermath of the asymptotic giant branch (AGB) phase, the post-AGB star enters the WD cooling sequence with either an H-rich (spectral type DA) or He-rich (spectral type DO) envelope of the main constituent. About three-quarters of all WDs are born H-rich (Bédard et al. 2020), but along the cooling track, this fraction does not remain constant because atmospheric processes alter the main spectroscopic marker (Bédard et al. 2022). As in this case, the drastic change in the atmospheric composition is referred to as spectral evolution. In the course of cooling off, WD atmospheres are prone to transformation by multiple processes, such as mass loss, radiative levitation, gravitational settling, atomic diffusion, convection, and accretion. Our current understanding of the spectral evolution of WDs has been established through the collective efforts of nearly four decades, and addressing every milestone in this endeavor is beyond the scope of this introduction. Therefore, we only mention the required aspects and developments for hot H-rich and hybrid WDs (spectral type DAO) that show a weak He II λ4686 Å line. For an extensive review of the spectral evolution of WDs, we refer to Bédard (2024).

The presence of helium in the hot hydrogen-rich WD atmospheres has been the subject of several discussions. Extreme-ultraviolet (EUV) and X-ray observations of hot DA WDs revealed a flux deficiency in the shorter wavelengths (Vennes et al. 1988), which is opposed to what is expected for hot WDs with pure H envelopes. It was initially proposed that traces of He in the atmosphere provide the opacity for the observed EUV and X-ray flux deficiency. However, Vennes et al. (1988) demonstrated that the required amount of He could not be radiatively levitated. They showed that EUV observations can instead be

⋆ Corresponding author; filiz@astro.uni-tuebingen.de

Open Access article, published by EDP Sciences, under the terms of the Creative Commons Attribution License (https://creativecommons.org/licenses/by/4.0), which permits unrestricted use, distribution, and reproduction in any medium, provided the original work is properly cited.
This article is published in open access under the Subscribe to Open model. Subscribe to A&A to support open access publication.

reproduced with models that consider stratified atmospheres in which a thin layer of H ($M_H/M_* = 10^{-15}$–10^{-13}) floats above the He envelope. However, this contradicts standard stellar evolution theory, which predicts $M_H/M_* = 10^{-4}$ for the H envelope (Blöcker et al. 1997). Subsequent studies showed that the EUV and X-ray fluxes of several other hot DA WDs cannot be reproduced with stratified atmospheres (Vennes et al. 1989; Vennes 1992; Vennes & Fontaine 1992). Metal opacities were instead identified as the likely source of the observed flux deficiency in these objects.

The discovery of hybrid WDs (Koester et al. 1979) helped to clarify the situation. Bergeron et al. (1994) demonstrated that models with homogeneous atmospheres yielded better fits than stratified atmospheres in the optical spectra of DAO WDs (except for one object[1] at that time). Since the radiation pressure is proven insufficient to prevent the gravitational settling of He (Vennes et al. 1988), they suggested that weak mass-loss might induce the homogenized hybrid atmospheres. Bergeron et al. (1994) also reported that their analysis was heavily hindered by the Balmer-line problem (BLP), which commonly emerges in the optical spectra of hot DA and DAO WDs and prevents simultaneous fits to all Balmer lines with the same parameters. The authors concluded that the BLP is linked to the presence of metals in the atmosphere, which reinforced the idea that metal-driven winds shape the atmospheres of hot hybrid WDs. The BLP and the trace-metal connection was later supported by the quantitative and qualitative spectral analyses of Werner (1996) and Gianninas et al. (2010), respectively. On the other hand, the origin of the metals in hot WD atmospheres has been heavily debated because of the mismatch between observations and diffusion theory that assumes an equilibrium between gravitational settling and radiative levitation (Chayer et al. 1995a,b). Mass loss was mainly regarded as the missing ingredient in theoretical diffusion calculations. Only Barstow et al. (2014) and Preval et al. (2019) speculated that the accretion of planetary material might explain the observed metal abundances.

The occurrence of stellar winds in hot WDs cannot be shown directly because the expected mass-loss rates are too low (Unglaub & Bues 2000) for a spectroscopic detection in P Cygni profiles. Nonetheless, indications of mass loss can still be deduced from the spectra of hot WDs. The first indication for the occurrence of winds was the detection of ultra-highly excited (UHE) metals in the optical spectra of hot WDs (Werner et al. 1995). Because of the asymmetrical shapes of the line profiles, it was speculated that UHE features stem from shock fronts in the stellar wind. Reindl et al. (2019) showed that recurrent spectroscopic variations of UHE lines and the light curve can be explained with rotational modulation of a magnetosphere that traps the ejected material. In this case, magnetically confined wind shocks can heat the plasma to the required extreme temperatures (10^6 K) for the occurrence of the UHE phenomenon. Another indirect evidence for radiation-driven winds was shown by Napiwotzki (1999). They reported a decreasing He abundance with decreasing luminosity in their hybrid WD sample.

Theoretical calculations of the influence of radiation-driven winds on the atmospheric composition by Unglaub & Bues (1998, 2000) revealed that mass-loss rates of $\approx 10^{-11}\ M_\odot \mathrm{yr}^{-1}$ can retard the gravitational settling of He in the hybrid atmospheres. The inevitable cessation of the mass loss expedites the effects of gravity, and a spectral transition from DAO to DA is expected. This paints a clear picture in the Kiel diagram, which has a well-defined theoretical wind limit. However, observations of hot DA and DAO WDs showed a lower effective temperature ($T_{\rm eff}$) range for the transition (Gianninas et al. 2010). Additionally, the measured temperature and surface gravity ($\log g$) values of both H-rich and hybrid WDs revealed that DA and DAO WDs partially overlap along the cooling sequence (Bergeron et al. 1994; Napiwotzki 1999; Barstow et al. 2003b; Good et al. 2004; Gianninas et al. 2010, 2011). When we accept that the mass loss in hybrid WDs is strong enough to prevent He from sinking out of the atmosphere, then we have to ask why the winds of DAs with similar $T_{\rm eff}$ and $\log g$ are insufficient to sustain He in the atmosphere. This indicates that other factor(s) in addition to $T_{\rm eff}$ and $\log g$ are involved in inducing the spectral transformation along the cooling track. The scatter of hot DA and DAOs in the $T_{\rm eff}$-$\log g$ diagram was indeed speculated to be a consequence of the initial metallicity or of different masses (Unglaub & Bues 2000; Bédard et al. 2020). Therefore, our immediate aim is to measure the element abundances in UV spectra of hot DA and DAO WDs in order to determine the atmospheric and stellar parameters. We also wish to shed light on whether a well-defined limit exists in the Kiel diagram that separates DA and DAO WDs, and if the metal abundances change along the cooling track.

In this paper, we analyze the ultraviolet (UV) and optical spectra of DA and DAO WDs[2]. In Sect. 2, the sample selection and observations are described. We explain the spectral analysis procedure for measuring atmospheric and stellar parameters in Sects. 3 and 4. Finally, we discuss the implications of our results in Sect. 5 and give a brief summary in Sect. 6.

2. Sample selection and observations

We selected a sample of hot WDs with $T_{\rm eff} \geq 60$ kK, above which homogeneous hybrid WDs are found. Our sample comprised 13 DAO, and 19 DA WDs (Table B.1) for which the main selection criterion was the availability of archival Far Ultraviolet Spectroscopic Explorer (FUSE) or Space Telescope Imaging Spectrograph (STIS) spectra. All objects have archival FUSE spectra, except for WD 0939+262. Archival STIS spectra are present only for 4 DAOs and 8 DAs.

2.1. FUSE

We retrieved FUSE spectra for 31 objects observed with the low-resolution spectrograph (LWRS; resolving power $R \approx 20\,000$) aperture from Mikulski Archive for Space Telescopes (MAST)[3]. The entire FUSE wavelength range (905–1188 Å) consists of eight overlapping segments. Therefore, an inspection of flux levels from each segment as well as each exposure was necessary. When any exposure-to-exposure flux variation exceeded ≈10%, we discarded the corresponding exposure. The majority of exposures made with the LiF1b channel suffer from a flux decrease because the detector area is shadowed by grid wires, known as the "worm" (FUSE Data Handbook[4]). When the overall flux level of a particular LiF1b spectrum did not drastically

[1] This object is an example for DAO WDs with stratified atmospheres, which are found at $T_{\rm eff} \leq 55$ kK (Manseau et al. 2016; Bédard et al. 2020) and advance through the DO-to-DA evolutionary channel (Manseau et al. 2016).

[2] Conventionally, the WD spectral classification is based on evaluated optical spectra. In this paper, we exclude secondary letters denoting weaker spectral features detected in other parts of the electromagnetic spectrum for simplicity (e.g., Z in the case of a metal detection for DAZ and DAOZ WDs).

[3] https://archive.stsci.edu

[4] https://archive.stsci.edu/fuse/instrumenthandbook/contents.html

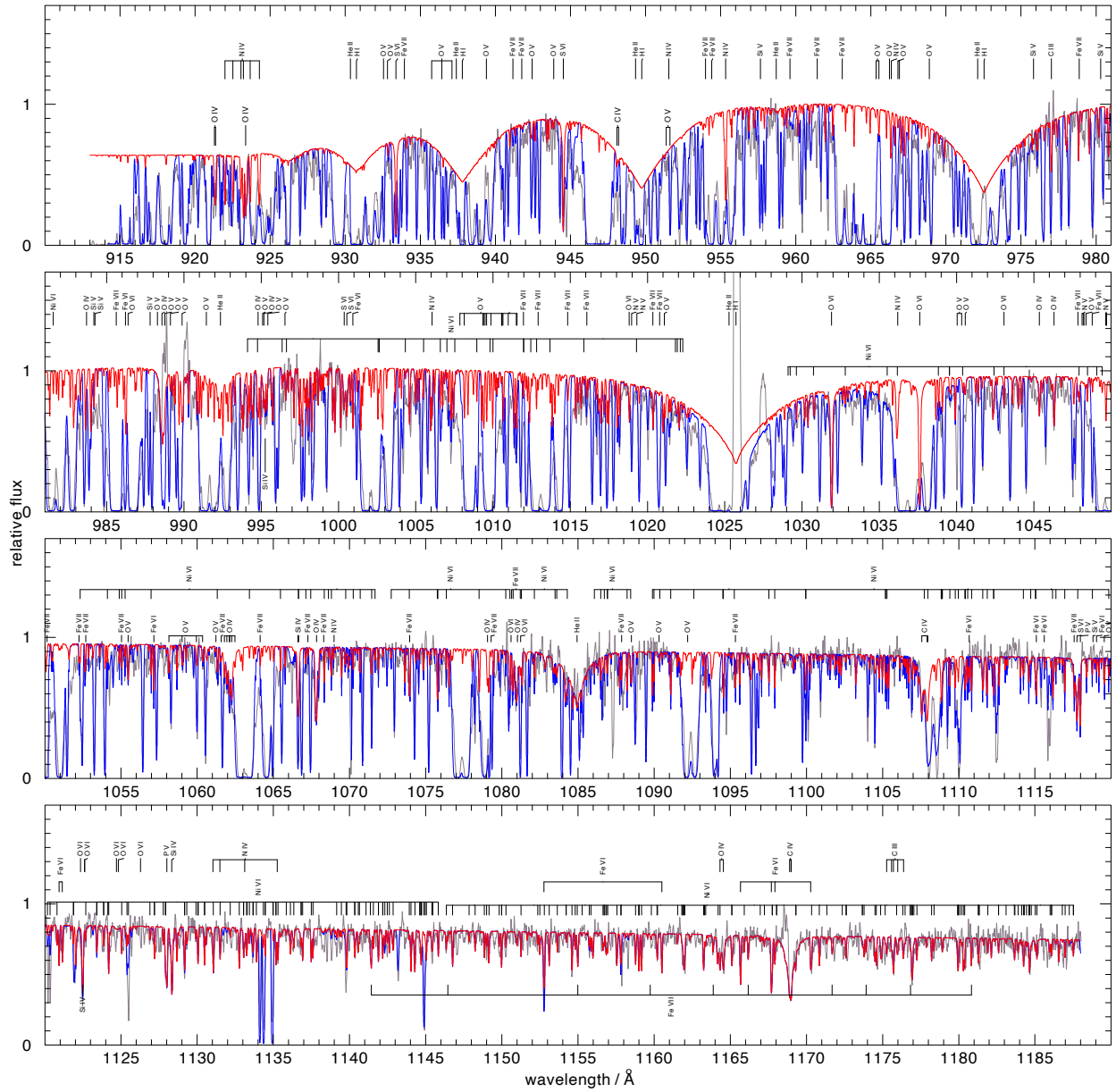


Fig. 1. FUSE spectrum (gray) of the DAO WD 2342+806 (red shows the model with $T_{\rm eff}$ = 83 kK, $\log g$ = 7.2 (cm/s^2), and blue shows the same model including the ISM lines). All model spectra displayed in this paper are convolved with Gaussians according to the instrument resolution. Additionally, all UV spectra are smoothed with a low-bandpass filter.

deviate from the spectra of other channels, the wavelength range in which the worms prevailed was eliminated. Otherwise, the entire LiF1b spectrum was discarded, which was our action in most cases. Then, each available exposure from a particular segment was coadded into a single spectrum. Moreover, the coadded spectrum of each overlapping segment was then coaligned to already identified ISM lines and combined into a single composite spectrum. Finalized composite FUSE spectra of DAO WD 2342+806 and DA WD 2211–495 with their best-fit models are shown as examples in Figs. 1 and 2, respectively.

2.2. HST

The archival spectra of 12 sample objects were observed with the STIS on board the *Hubble* Space Telescope (HST) using the FUV-MAMA detector. For 9 of the objects (4 DAO and 5 DA), observations were carried out with the E140M grating (≈1144–1729 Å, $R \approx 45\,800$), and the remainder were observed with the E140H grating ($R \approx 114\,000$), which consists of prime and secondary tilts. In the MAST archive, observations made with E140H only contain prime tilt with a central wavelength of 1416 Å, meaning that we only had access to the spectral range of 1317–1517 Å for these 3 DAs. When more than one observation was available, the observations were coadded to increase the signal-to-noise ratio (S/N). In Figs. A.1 and A.2, STIS spectra of WD 2342+806 (E140M) and WD 2211−495 (E140H), respectively, are shown as examples with their best-fit models.

2.3. Optical

Archival optical spectra for all sample objects were acquired from the Montreal White Dwarf Database (MWDD, Dufour et al. 2017), except for Longmore 1, WD 0851+090, WD 1111+552,

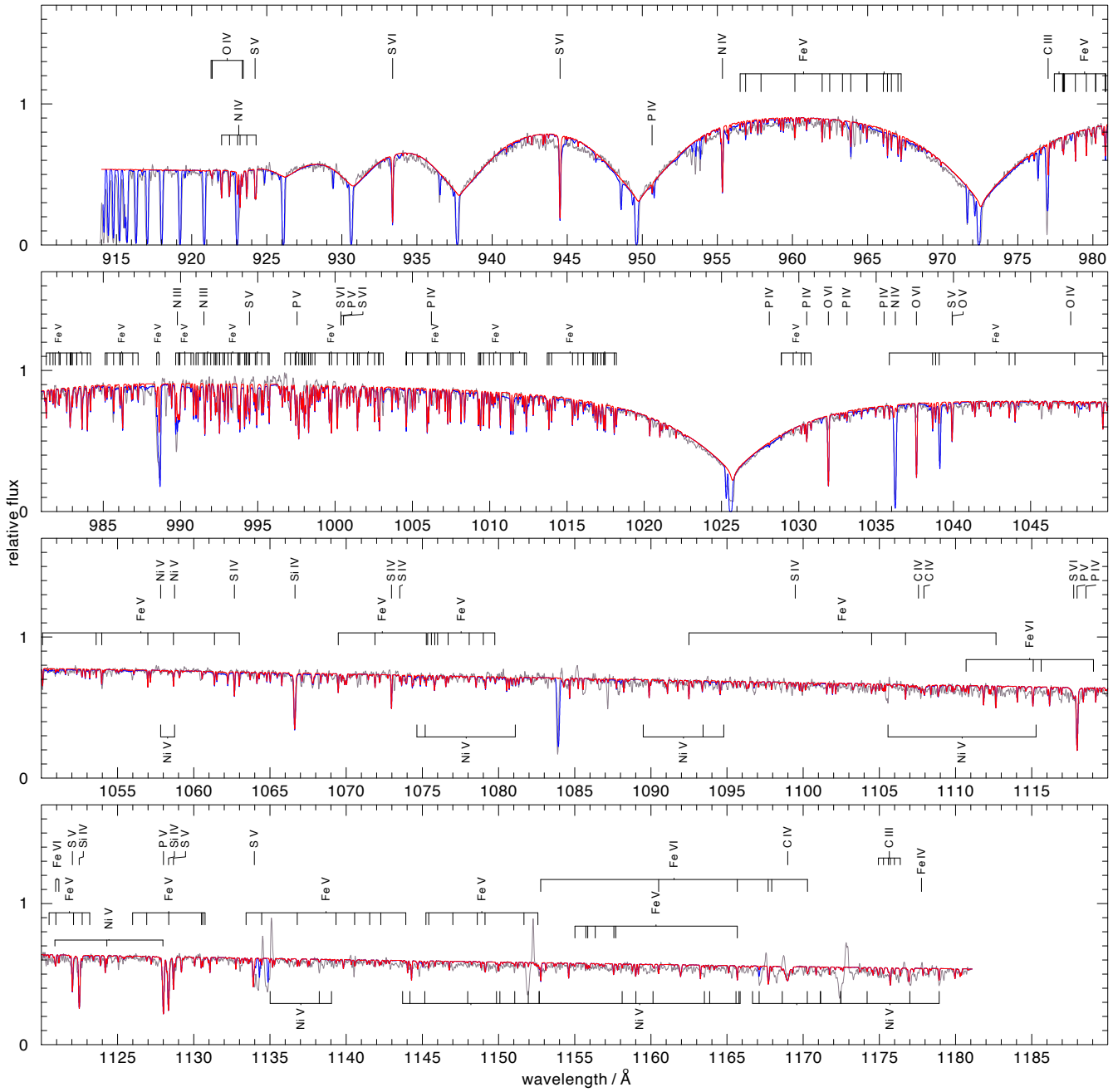


Fig. 2. FUSE spectrum of the DA WD 2211−495 (red shows the model with $T_{\rm eff}$ = 68 kK, log g = 7.4, and blue shows the model including the ISM lines).

and WD 2350−706. The typical resolution for the MWDD spectra is ≈3–6 Å. Observations of the MWDD spectra are described in detail by Gianninas et al. (2010, 2011), Lépine et al. (2011). We found no optical spectrum of WD 1111+552 and WD 2350−706, but archival Ultraviolet and Visual Echelle Spectrograph (UVES; $R \approx 40\,000$) spectra are available for Longmore 1 and WD 0851+090. UVES spectra of WD 0621−376 and WD 2211−495 were also used to make comparisons. For the same reason, we acquired Sloan Digital Sky Survey (SDSS, Abazajian et al. 2009) spectra of three other DAs (WD 1056+516, WD 1342+443, WD 1827+778), which were also available in MWDD. We should note that for nine other objects (two DAOs and seven DAs) UVES and (four DAOs and five DAs), LAMOST spectra are available. However, conducting an extensive optical analysis is beyond the scope of this study. Therefore, we simply analyzed optical spectra to constrain log g and investigated whether common ground between optical and UV results can be found.

2.4. Interstellar absorption and reddening

Absorption lines from the interstellar medium (ISM) may heavily contaminate FUSE spectra, and they need to be disentangled from photospheric lines to precisely determine the atmospheric parameters. Therefore, we identified ISM lines employing the line-fitting procedure OWENS (Lemoine et al. 2002; Hébrard et al. 2002; Hébrard & Moos 2003), which individually models radial and turbulent velocities, column densities, temperatures,

Table 1. Number of NLTE levels and lines of extended classical model ions.

	II	III	IV	V	VI
C	1, 0	56, 242	54, 295		
N	1, 0	34, 129	90, 547	54, 297	
O	1, 0	72, 322	83, 637	103, 729	54, 291
Si		17, 27	30, 102	25, 59	27, 74
P		3, 1	21, 25	18, 49	
S		1, 0	37, 150	39, 107	25, 48

Notes. Each cell in the table shows the number of NLTE levels and lines. The highest ionization stage of each element is only included as ground state and is not listed here.

and chemical compositions of different clouds. In general, the detected ISM lines included D I, H I, H_2, C I–III, N I–III, O I, P II, S II–III, Ar I, and Fe II.

We determined the interstellar reddening for each star by comparing the model fluxes to *Tycho2*, SDSS, and 2MASS magnitudes. The model spectra were normalized to fluxes observed with the filter in the longest wavelength when no 2MASS K flux was available. Then, the reddening law by Fitzpatrick (1999) with $R_V = 3.1$ was employed to determine the *E(B–V)* values of the sample objects.

3. Spectral analysis

We conducted a spectral analysis with the Tübingen Model-Atmosphere package (TMAP[5], Werner & Dreizler 1999; Werner et al. 2003, 2012), which computes nonlocal thermodynamic equilibrium (NLTE) model atmospheres in radiative and hydrostatic equilibrium assuming plane-parallel geometry. The opacities of H, He, C, N, O, Si, P, S, Fe, and Ni were included in our models. Classical model atoms (hydrogen to sulfur) were constructed with atomic data from the Tübingen Model Atom Database (TMAD, Rauch & Deetjen 2003). For Fe and Ni, we used the Tübingen Iron-group opacity interface (TIRO, Rauch & Deetjen 2003; Müller-Ringat 2013), which uses a statistical approach to manage the vast number of atomic levels and line transitions by combining energy levels and sampled lines of a particular ion to super levels and super lines, respectively. Additionally, we employed the Stark broadening tables of Tremblay & Bergeron (2009) and Schoening & Butler (1989) to calculate the synthetic line profiles of H I and He II.

Metal line blanketed models were initially built with relatively small model atoms for elements up to sulfur to avoid numerical instabilities and to optimize computation time. Subsequently, line formation iterations were executed with extended model atoms by keeping the atmospheric structure fixed. An overview of the extended classical model atoms is listed in Table 1. Additionally, ionization stages IV - IX were included for Fe and Ni (Table 2). We customized model atoms for each object by adjusting the ionization stages of a particular element according to individual parameter ranges.

The wide range in temperature and surface gravity and the numerous parameters of our sample did not facilitate either creating an extensive model atmosphere grid or taking a statistical approach in the spectral analysis. Instead, our method involved an iterative process of line-profile fitting by consecutively computing a series of models while improving the parameters and decreasing the uncertainty. Our analysis procedure is summarized below.

1. Calculate a small grid of pure H and H+He models close to the literature $T_{\rm eff}$ and $\log g$ values of DA and DAOs, respectively.
2. Roughly constrain $T_{\rm eff}$, $\log g$, and He abundance from the UV H and He lines.
3. Compute a series of fully metal-line blanketed models around the updated values.
4. Refine $T_{\rm eff}$ and determine the metal abundances by fitting the UV metal lines.
5. Improve $\log g$ and He abundance from the optical spectra.
6. Recalculate models with the fine-tuned parameters.

[5] http://astro.uni-tuebingen.de/~TMAP

Table 2. Number of super levels and super lines of the iron and nickel model atoms.

	Super levels	Super lines	Sample lines
Fe IV	7	25	3102371
Fe V	7	25	3266247
Fe VI	7	25	991935
Fe VII	7	24	200455
Fe VIII	7	27	19587
Fe IX	1	0	0
Ni IV	7	25	2512561
Ni V	7	27	2766664
Ni VI	7	27	7407763
Ni VII	7	25	4195381
Ni VIII	7	27	1473122
Ni IX	1	0	0

3.1. DAO analyses

3.1.1. Effective temperature and surface gravity

H+He models for each object were computed assuming a solar He content, with $T_{\rm eff}$ and $\log g$ close to the values determined by Gianninas et al. (2010) through their analysis of optical spectra via Balmer-line fitting. When the latter authors did not analyze a particular object, we selected values close to those derived by Ziegler (2012). Then, we constrained $T_{\rm eff}$ and $\log g$ from the Lyman lines in the FUSE spectra. In the next step, we included metal opacities in our model atoms. A set of strategic lines from several ions was identified since the absence or presence of a particular line would indicate a certain $T_{\rm eff}$. While keeping $\log g$ fixed, we exploited multiple ionization equilibria such as C III/C IV, N IV/N V, O IV/O V/O VI, Fe V/Fe VI/Fe VII/Fe VIII, and Ni V/Ni VI to constrain $T_{\rm eff}$ (Fig. 3). A detailed overview of each element is presented in Sect. 3.1.3.

Contamination due to interstellar H I and other interstellar absorption hinders the correct assessment of the local continuum in the far-UV range. This in turn affects the precise measurement of $\log g$ via fitting the Lyman lines. Thus, investigation of optical spectra was necessary to verify our $\log g$ values. In general, the parameters determined with UV analysis lay within the error range of the Balmer-line analysis.

3.1.2. He abundance

A preliminary He abundance was determined from isolated lines of He II $n = 2 \rightarrow n$' line series in the FUSE range. While we fine-tuned the temperature and gravity, the He abundance was further adjusted accordingly. Finally, we compared and, if necessary,

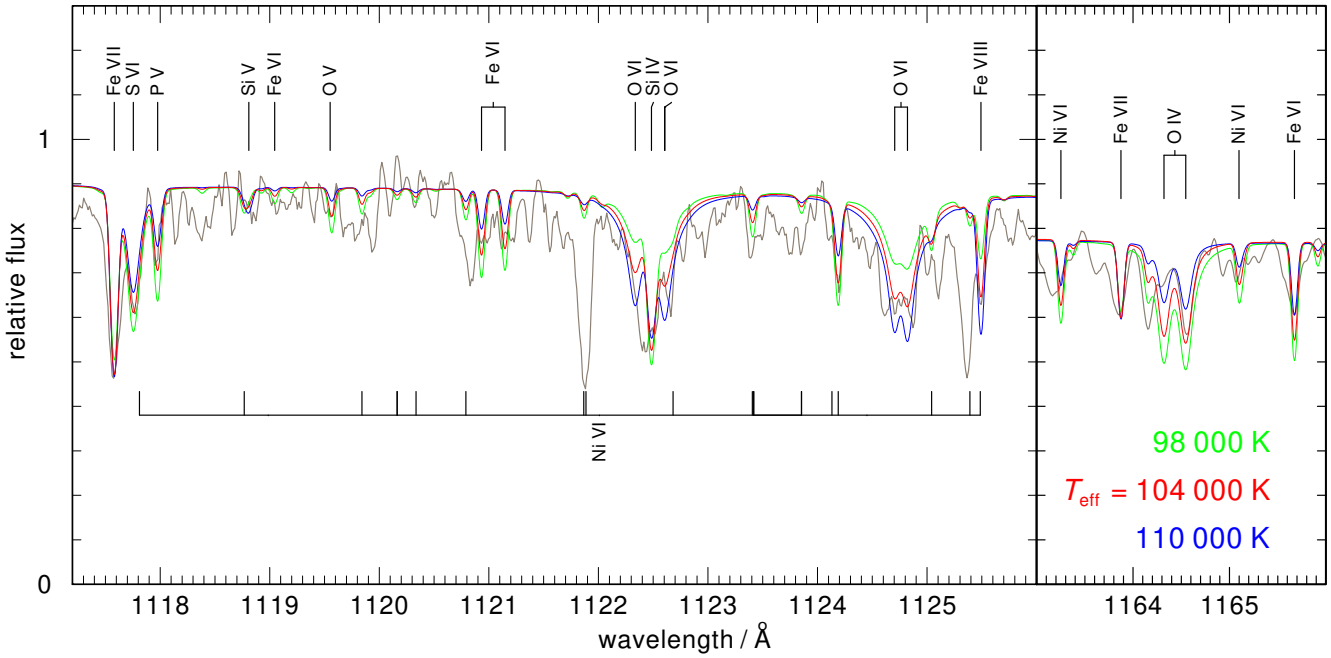


Fig. 3. Details of the FUSE spectrum of the DAO WD 0500−156 compared to three models with different temperatures $T_{\rm eff}$ = 104 ± 6 kK, log g = 7.2.

modified our previous measurement by using He II λ 1640 Å ($n - n'$ = 2–3) and He II λ 4686 Å, which are the optimal lines to adjust the He abundance in their respective wavelength regions.

3.1.3. Metal abundances

Carbon. The C IV $\lambda\lambda$ 1107, 1169 Å doublet was mainly used to determine the C abundance. In several cases, C IV λ 1169 Å is contaminated by an airglow line. When this was the case, we only relied on C IV λ 1107 Å. Although weak C III features can be observed below 100 kK, only WD 2342+806 displays the C III λ 1175 Å multiplet, which is a blend with N VI lines. The STIS wavelength range contains C IV multiplets at 1198 and 1239 Å as well as the C IV resonance doublet. Without exception, the line fits of the former two agree with the other C lines from the FUSE spectra, whereas the latter is weaker in our models. However, a quick inspection revealed that this must be due to ISM contribution. We achieved a good fit to the line cores of the photospheric components, which are clearly separated from the blueshifted ISM component.

Nitrogen. The relative strengths of identified N IV and N V lines in the FUSE range can be exploited to confine $T_{\rm eff}$ within a rather wide range. The N IV λ 923 Å multiplet and the N IV λ 955 Å singlet disappear around 120 kK, whereas N V λ 1048.2 Å and N V λ 1049.7 Å quickly become weaker below 90 kK. The latter two are blended with ISM lines and cannot be identified in our sample. Therefore, the N IV λ 923 Å multiplet and the N IV λ 955 Å singlet were mainly used to determine the N abundance. When STIS spectra were available, the N V $\lambda\lambda$ 1238.2, 1242.8 Å resonance doublet and the N IV λ 1718.5 Å were used as well. Compared to our photospheric models, we encountered a stronger N V resonance doublet in the observations of WD 1957+225 and WD 2226−210, which is expected to be dominated by interstellar absorption.

Oxygen. Multiple O IV, O V, and O VI lines are detectable in the FUSE spectra. A rather tight constraint can be made with the O ionization balance since O lines strongly react to $T_{\rm eff}$ changes. A weak O VI doublet at 1124 Å becomes visible around 95 kK and becomes stronger with increasing $T_{\rm eff}$, in contrast to the O IV lines (Fig. 3). At 110 kK, the O V lines in the FUSE wavelength range still display strong features (Fig. 4). However, above this temperature and below 90 kK, they diminish quickly. We encountered problems with the O VI $\lambda\lambda$ 1031.9, 1037.6 Å resonance doublet of the objects with $T_{\rm eff}$ below 115 kK. Without exception, the line cores are too deep in our final models. This issue was also reported by Rauch et al. (2007) and Werner et al. (2018b). In the STIS wavelength range, O V λ 1371.7 Å and O IV $\lambda\lambda$ 1338.6, 1342.9, 1343.5 Å were identified. STIS spectra of WD 1957+225 and WD 2226−210 display O VI λ 1291 Å. However, in both cases, the observations show very broad features, and we were unable to model this line well.

Silicon. The most prominent silicon lines are Si IV $\lambda\lambda$ 1066.61, 1066.65 Å and Si IV $\lambda\lambda$ 1122, 1128 Å in the FUSE range. However, Si IV λ 1066 Å is blended with interstellar absorption. Therefore, the Si IV $\lambda\lambda$ 1122, 1128 Å doublet was used to determine the Si abundance. Only three objects with $T_{\rm eff}$ above 110 kK display a weak Si V λ 1118.8 Å feature. Additionally, STIS spectra show the Si IV $\lambda\lambda$ 1394, 1402 Å resonance doublet, which is dominated by interstellar absorption, like the other two resonance lines (C IV, N V) identified in the STIS spectra. As opposed to the FUSE spectra, we detected Si V lines (Si V $\lambda\lambda$ 1245.7, 1251.4, 1276 Å) above 97 kK, which become stronger with increasing $T_{\rm eff}$.

Phosphorus. The P abundances were determined by fitting the P V $\lambda\lambda$ 1118, 1128 Å resonance doublet. The other detected P V lines are quite weak and blend with other lines. Our DAOs

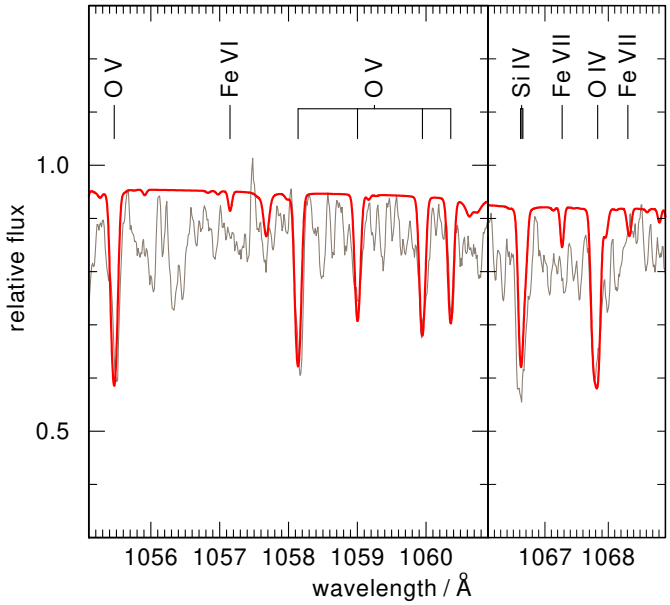


Fig. 4. Sections of the FUSE spectrum (gray) of the DAO WD 1111+552 showing the ionization balance of O IV and O V (red shows the model with $T_{\rm eff}$ = 111 kK, log g = 7.1).

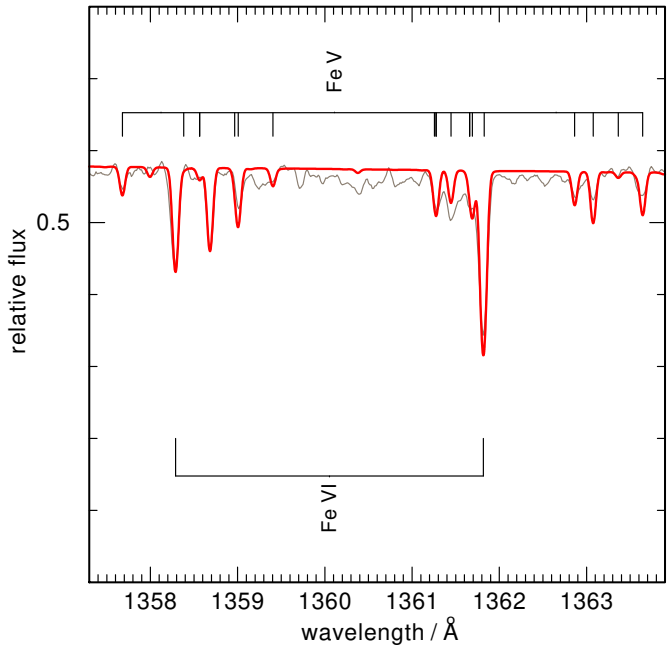


Fig. 5. Section of the STIS spectrum (gray) of the DAO WD 0439+466 (red shows the model with $T_{\rm eff}$ = 97 kK, log g = 7.0).

are too hot to show P IV lines. No phosphorus lines were detected in the STIS spectra.

Sulfur. We identified the S VI $\lambda\lambda$ 933, 945 Å resonance doublet, S VI λ 1000 Å, and S VI λ 1117.7 Å in the FUSE spectra. Only one object resides in the temperature range in which S V lines can be displayed. Only S VI λ 1419.4, 1419.7 Å and S VI λ 1423.8 Å were detected in the STIS spectra of WD 0439+466 and WD 2342+806.

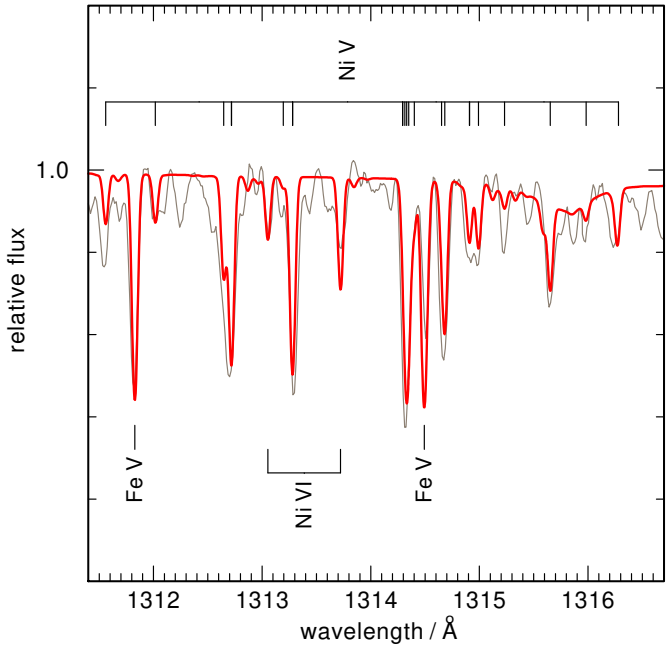


Fig. 6. Detail of the STIS spectrum (gray) of the DAO WD 2342+806 (red shows the model with $T_{\rm eff}$ = 83 kK, log g = 7.2).

Iron. Prominent Fe VI – VIII lines were detected in the FUSE spectra, and they serve as excellent $T_{\rm eff}$ indicators. In Fig. 3, the $T_{\rm eff}$ assessment of WD 0500–156 is depicted as an example. As opposed to Fe VI, the relative strength of the Fe VIII lines intensifies above 98 kK, whereas the increase is minor for the Fe VII lines. At 110 kK, the Fe VIII lines become too strong, while the Fe VI lines weaken substantially. In addition to the mentioned ions, Fe V lines were also identified in the STIS spectra of objects below 100 kK (Fig. 5).

Nickel. FUSE spectra contain many Ni VI lines. The line strength of Ni VI lines diminishes quickly above 100 kK (Fig. 3). In the STIS spectra of WD 0439+466 and WD 2342+806, a number Ni V and Ni VI lines were identified (Fig. 6).

3.2. DA analyses

3.2.1. Effective temperature and surface gravity

We followed the same procedure as for the DAOs, but started by computing pure H models with literature values of $T_{\rm eff}$ and log g (Gianninas et al. 2010, 2011; Barstow et al. 2014). In addition to adding the metal opacities, we also included a small amount of He in our model atmospheres. In their far-UV analysis of G191-B2B, Rauch et al. (2013) opted for log He < −4.7 (mass fraction) as an upper limit. Since G191-B2B resides at the lower limit of the temperature criterion in our sample selection, this value was chosen as our starting He abundance and was adjusted to upper limits from He II $n - n'$ = 2–11 line series for each object. Additionally, we were able to fine-tune the upper limit with He II λ 1640 Å for the objects with STIS spectra. Since the DAs in our sample have considerably lower temperatures than the DAOs, the ionization equilibria that we relied on also slightly altered (C III/C IV, N III/N IV/N V, O IV/O V/O VI, P IV/P V, S IV/S V/S VI, Fe V/Fe VI/Fe VII, and Ni V/Ni VI). Because of the low metal abundance and poor data quality, it was not possible to use the ionization balance of

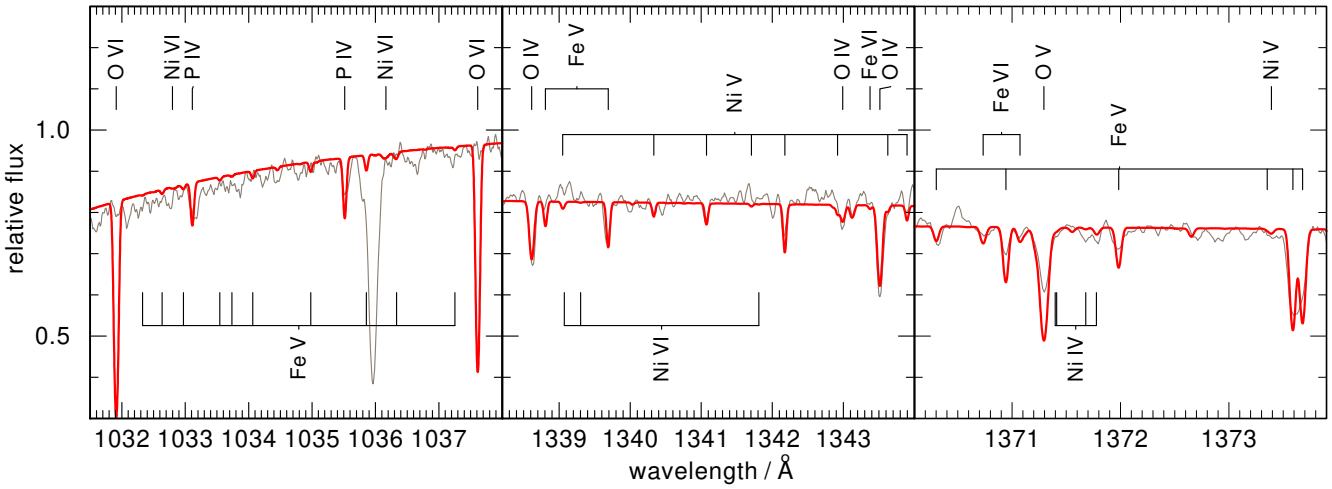


Fig. 7. Sections of FUSE (left panel) and STIS (middle and right panels) spectra (gray) of the DA WD 0232+035 (red shows the model with $T_{\rm eff}$ = 63 kK, log g = 7.5), illustrating stratification effects on oxygen ions.

multiple elements in some cases. For these objects, higher error limits were imposed. In contrast to the DAO WDs, log g values determined utilizing Lyman lines were not compatible with the Balmer lines. Therefore, we readjusted log g according to the Balmer lines. However, in some cases, the disparity between the Lyman and the lower-order Balmer lines (e.g., Hα and Hβ) was too large, but the surface gravity determined from Lyman lines completely agreed with the higher-order Balmer lines. Since fitting higher-order Balmer lines corresponds to a more accurate log g measurement (Werner 1996) and $T_{\rm eff}$ could be tightly constrained from UV, we opted in these cases for log g measured in the UV and adopted a larger error margin.

3.2.2. Metal abundances

Carbon. The C III λ 1175 Å multiplet was mainly used to determine C abundances. Multiple objects show a weak C IV λ 1169 Å doublet. Similar to DAOs, this feature is contaminated in several FUSE spectra. When HST spectra were available in addition to C IV multiplets at 1198 and 1239 Å, we used the C IV $\lambda\lambda$ 1548, 1550 Å resonance doublet to confirm the C abundance.

Nitrogen. Most of the sample objects display the N IV multiplet at 923 Å and the singlet at 955 Å. N III λ 991 Å was also identified in the spectra of objects with $T_{\rm eff} \leq 75$ kK. However, this line is blended with a Fe V line, and it would be unrealistic to determine the N abundance with it, although it is still useful for assessing the temperature with the N III/N IV ionization balance. Therefore, the former two lines were mainly used to determine the N abundance. When the STIS spectrum was present, we exploited the N V $\lambda\lambda$ 1238.2, 1242.8 Å resonance doublet as well.

Oxygen. In the FUSE spectra of multiple objects, a weak O VI $\lambda\lambda$ 1031.9, 1037.6 Å resonance doublet was identified. A handful of objects display the short-wavelength component of the O IV 921–923 Å multiple, but the other component is a blend with the N IV λ 923 Å multiplet. No additional oxygen lines were identified in the FUSE spectra. We detected O V λ 1371.7 Å and O IV $\lambda\lambda$ 1338.6, 1342.9, 1343.5 Å in the STIS spectra. However, it was not possible to achieve a simultaneous fit to the lines of all three ionization stages (see Fig. 7). We further discuss this in Sect. 5.

Silicon. The Si IV $\lambda\lambda$ 1066.61, 1066.65 Å, and Si IV $\lambda\lambda$ 1122, 1128 Å doublets were mainly used to determine the Si abundance, which agreed with fits to the Si IV resonance lines. The Si III lines were identified.

Phosphorus. The P V $\lambda\lambda$ 1118, 1128 Å resonance doublet was identified. Objects below ≈70 kK also display P IV $\lambda\lambda$ 950, 1028 Å. No other P lines were identified in the STIS spectra.

Sulfur. Multiple cooler objects show the S IV $\lambda\lambda$ 1072.97, 1073.52 Å doublet. This line quickly weakens above 70 kK. In addition to S V λ 1028 Å, S V λ 1222 Å, and S V λ 1501.7 Å, the S VI resonance doublet was also identified. However, in multiple cases, we encountered a similar problem with the O VI resonance doublet, in which the line cores were slightly stronger in our models.

Iron and nickel. Numerous Fe V and Fe VI as well as Ni V and Ni VI lines can be detected in FUSE and STIS spectra. The line strengths of both Fe VI and Ni VI start to diminish around 80 kK, whereas Ni V and Fe V become stronger.

4. Masses

We relied on the atmospheric parameters from our spectroscopic analysis to disclose the masses of the sample objects. To interpolate masses from the Kiel ($T_{\rm eff}$–g) diagram, we followed the same steps as Reindl et al. (2023) and used the griddata[6] function in Python, which can rescale data points to the unit grid before making the interpolation. To estimate the Kiel masses, we considered the evolutionary tracks by Renedo et al. (2010) and Hall et al. (2013) (Fig. 8), which were devised for CO-core WDs (metallicity Z = 0.01) and He-core WDs, respectively. However, none of the object spectroscopic parameters match the He-core tracks.

[6] https://docs.scipy.org/doc/scipy/reference/generated/scipy.interpolate.griddata.html

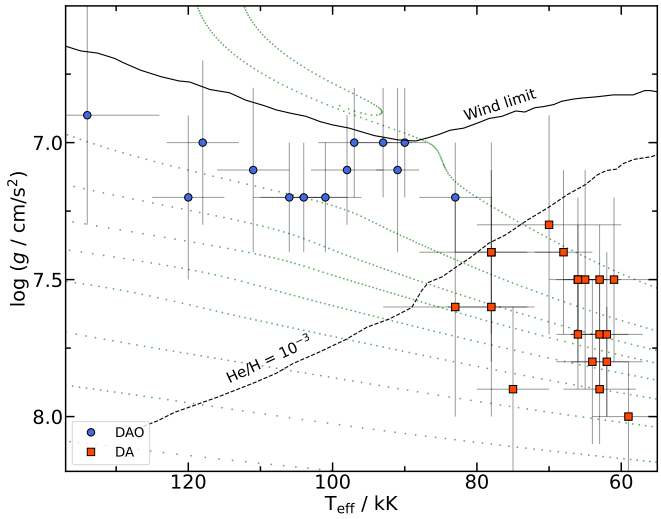


Fig. 8. Sample objects illustrated in the Kiel diagram. The dotted lines are evolutionary tracks of H-rich WDs (Z = 0.01) from Renedo et al. (2010), representing in order 0.525, 0.570, 0.593, 0.609, 0.632, 0.659, 0.705, 0.767, and 0.837 $M_{\odot}$. The solid and dashed black lines correspond to the theoretical wind limit and to the He abundance (N(He)/N(H) = 10^{-3}) calculated with the predicted mass-loss rates by Unglaub & Bues (2000, see their Fig. 6), respectively. The latter also coincides with the approximate optical detection limit of He.

The uncertainties were assessed using a Monte Carlo method. We found that DAOs in our sample ($\langle M_{\rm DAO}\rangle$ = 0.55 $M_{\odot}$, σ = 0.02 $M_{\odot}$) are on average less massive than DAs ($\langle M_{\rm DA}\rangle$ = 0.59 $M_{\odot}$, σ = 0.05 $M_{\odot}$), which was also found by Gianninas et al. (2010), Bédard et al. (2020), and Reindl et al. (2023).

5. Results and discussion

In this section, we present the general outcome of the spectral analysis and discuss the implications of the results. $T_{\rm eff}$, log g, and the mass fractions of the elements are listed in Table B.2. The abundance of a particular element for all objects is also depicted in the Kiel diagram in comparison to the solar values (Figs. 9 and 10). Moreover, in Fig. 11, a comparison between metal abundances of DA WDs and theoretical diffusion calculations by Chayer et al. (1995b) and Vennes et al. (1996) is shown.

5.1. Mass loss and accretion

The winds of hot stars mainly emerge due to radiative forces acting on the metals. The metals in turn transfer momentum with Coulomb collisions to H and He, on which the radiative forces are very low (Krtička et al. 2020). Unglaub & Bues (1998, 2000) showed that chemically homogeneous winds could prevent gravitational settling of He in DAO atmospheres. When the WD crosses the wind limit and mass-loss ceases, He can no longer be sustained in the atmosphere, and a quick transition from DAO to DA is then expected.

This is exactly what we observe. The DAO WDs in our sample exhibit a solar He content at high $T_{\rm eff}$. As the temperature decreases, the He abundance diminishes as well (Fig. 10). While CNO abundances follow the same trend (Fig. 9), other light metals are slightly subsolar. He is more rapidly depleted than CNO, as predicted by Unglaub & Bues (2000). In contrast, the Fe and Ni abundances of DAOs exceed the solar value (Fig. 10), excluding Longmore 1, WD 1111+552, and WD 1957+225, which are comparable to the Sun. Interestingly, the latter three also display solar He abundance. This implies that the effects of a weak stellar wind are prominent, while gravitational settling did not influence the photospheric abundances (Werner et al. 2018b). An increase in the abundances of heavy elements already indicates the influence of the radiative levitation (Rauch et al. 2016a), which can be noted in the case of WD 2226−210 because it, in contrast, has a lower He abundance than other objects with similar $T_{\rm eff}$. Therefore, we argue that the abundance pattern of the remaining objects signifies an interplay between diffusion and stellar winds (Werner et al. 2018a; Löbling et al. 2020).

In contrast to DAOs, CNO is extremely depleted in DA atmospheres, whereas the decrease in other light metals is less severe, especially for P. On the other hand, both Fe and Ni abundances are roughly solar. However, a trend is apparent here: With decreasing $T_{\rm eff}$ and increasing log g, the Fe and Ni abundances diminish (Fig. 10). This implies that atomic diffusion is the main driving mechanism in the DA atmospheres (Werner et al. 2019). However, as we showed in Fig. 11, the comparison of the observed abundance pattern of DA WDs to theoretical diffusion calculations of Chayer et al. (1995b) and Vennes et al. (1996) revealed inconsistencies, except for iron. Different results between observations and the diffusion theory were also previously reported in several studies (Chayer et al. 1995a,b; Barstow et al. 2003b; Dobbie et al. 2005; Good et al. 2005a; Werner et al. 2007; Rauch et al. 2013; Barstow et al. 2014; Preval et al. 2019). The common ground in these papers was that at least one more mechanism is required to explain the discrepancy and should be included in theoretical calculations in addition to equilibrium theory. Competing ideas were that either weak mass-loss or accretion shapes the observed abundance pattern.

The mismatch in the Si abundance is particularly curious because Si is the only element that was consistently found in all previous studies to be more abundant than predicted by diffusion theory. Barstow et al. (2014) stated that overabundant phosphorus and silicon resemble the bulk material of terrestrial planets. The authors argued that the observed metal abundances arise due to accretion from short-lived gaseous disks rather than innately containing them. Then, accreted elements are radiatively levitated in the atmosphere, hence possibly marking the source of accretion as tidally disrupted planetary debris. Preval et al. (2019) showed that hot DA WDs in their sample exhibited Fe and Si abundances that were higher by an order of magnitude than the theoretical estimates. The authors interpreted the overabundance of metals as an indication of ongoing accretion from external sources. The existence of gaseous and dusty debris disks around WDs is indeed very well established (Jura 2003; Manser et al. 2016, 2020), and there is strong evidence that the debris disks originate in tidally disrupted planetary material (Gänsicke et al. 2019; Manser et al. 2019; Cunningham et al. 2022). However, to the best of our knowledge, the $T_{\rm eff}$ of any observed WD hosting a debris disk does not exceed ∼30 kK (Koester et al. 2014; Manser et al. 2020; Melis et al. 2020; Gentile Fusillo et al. 2021a).

From the theoretical standpoint, Chayer et al. (1997) demonstrated that when either accretion or mass loss is included in the diffusion calculations, the observed overabundance of Si for a WD with $T_{\rm eff}$ = 60 kK and log g = 7.36 can be explained. Moreover, Wesemael et al. (1984) explored the possibility of accretion from the M dwarf companion to Feige 24 as the source of the observed element abundances. Assuming a mass-loss rate of 10^{-13} $M_{\odot}$yr^{-1} for the M dwarf, they calculated the ram pressure in the stellar wind midway and compared this to the radiative

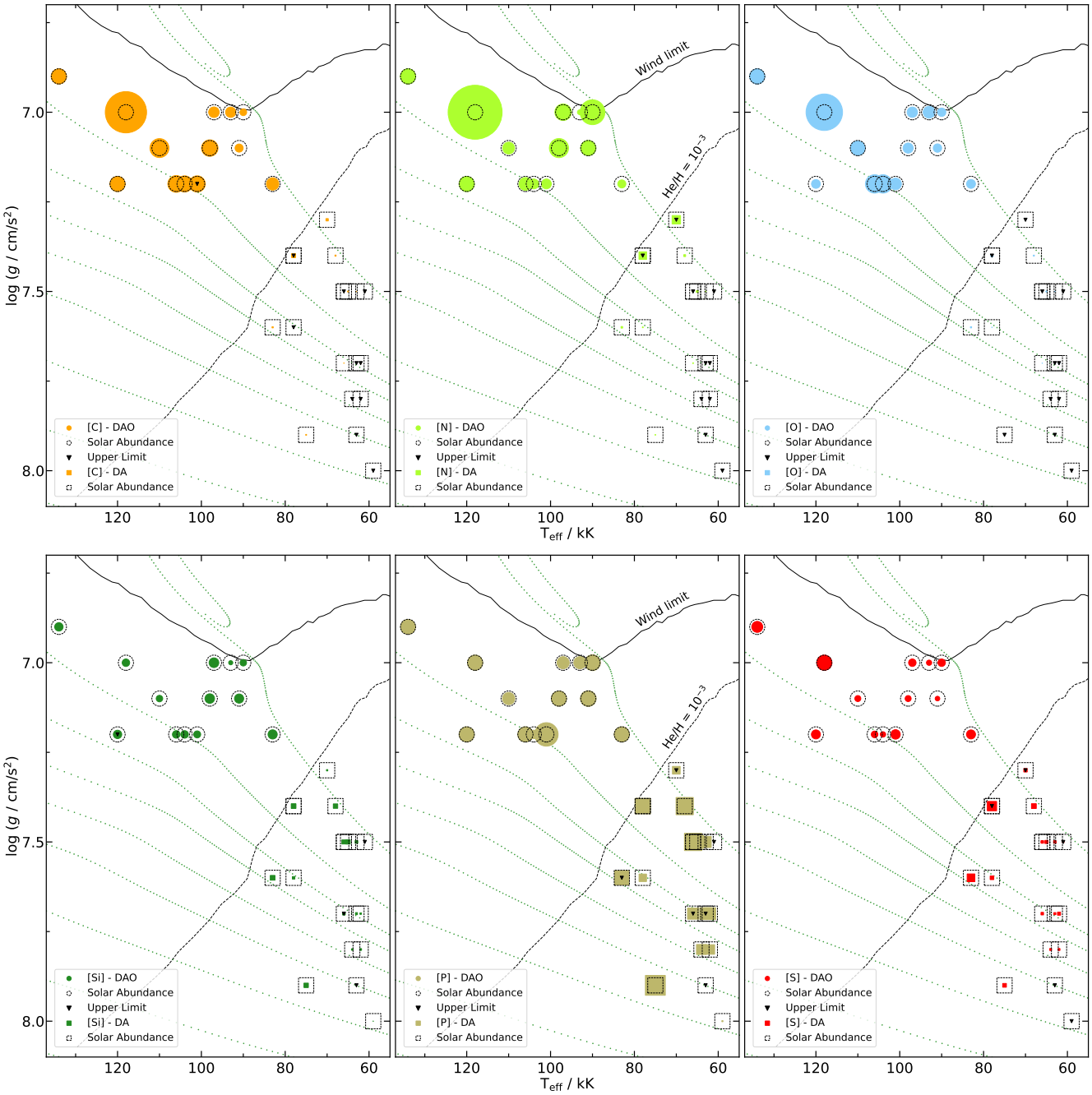


Fig. 9. Element abundances of our sample objects in the Kiel diagram (panels from upper left to lower right: C, N, O, Si, P, and S). The abundances are illustrated with filled circles and squares for DAOs and DAs, respectively. The symbol size is proportional to the mass fraction of the respective element. The dashed symbols represent solar values (Asplund et al. 2009). The upper limits are marked with an upside triangle, which does not scale with the abundances.

pressure gradient of the WD. Accordingly, they demonstrated that the intense radiation field of the WD ($T_{\rm eff} \approx 60$ kK) can substantially retard the accretion rate and counteract the accretion. Since our sample objects have similar or higher $T_{\rm eff}$, first, any grain material originating from supposed planetary debris would be sublimated due to the high luminosity of our objects compared to their cooler counterparts (von Hippel et al. 2007). Second, it is plausible that the intense radiation pressure from the hot WDs in our sample ($T_{\rm eff} \geq 59$ kK) could halt the infall of the sublimated material, preventing the formation of even short-lived gaseous disks. Finally, it should be considered that the hot DA WD sample of Barstow et al. (2014) consisted of objects with lower $T_{\rm eff}$ (16–77 kK) than ours, and only ≈20% of them exceed 50 kK. Although the observed Si abundance of a cool Hyades WD ($T_{\rm eff} \approx 20$ kK) can be explained with radiative levitation, for another object in the same cluster with a similar $T_{\rm eff}$, accretion from external sources is needed (Chayer 2014). Therefore, the accretion-impacted abundance pattern of the DAs might only be a viable scenario for cooler objects (at about $T_{\rm eff} \leq 30$ kK).

In Sect. 3.2.2 we mentioned that it was not possible to fit all oxygen ions simultaneously in the DA WD spectra. When only O VI resonance lines are fit, the O abundance is far lower, and O IV and O V lines cannot be fit properly, and vice versa. It was suggested that inhomogeneous oxygen stratification causes this

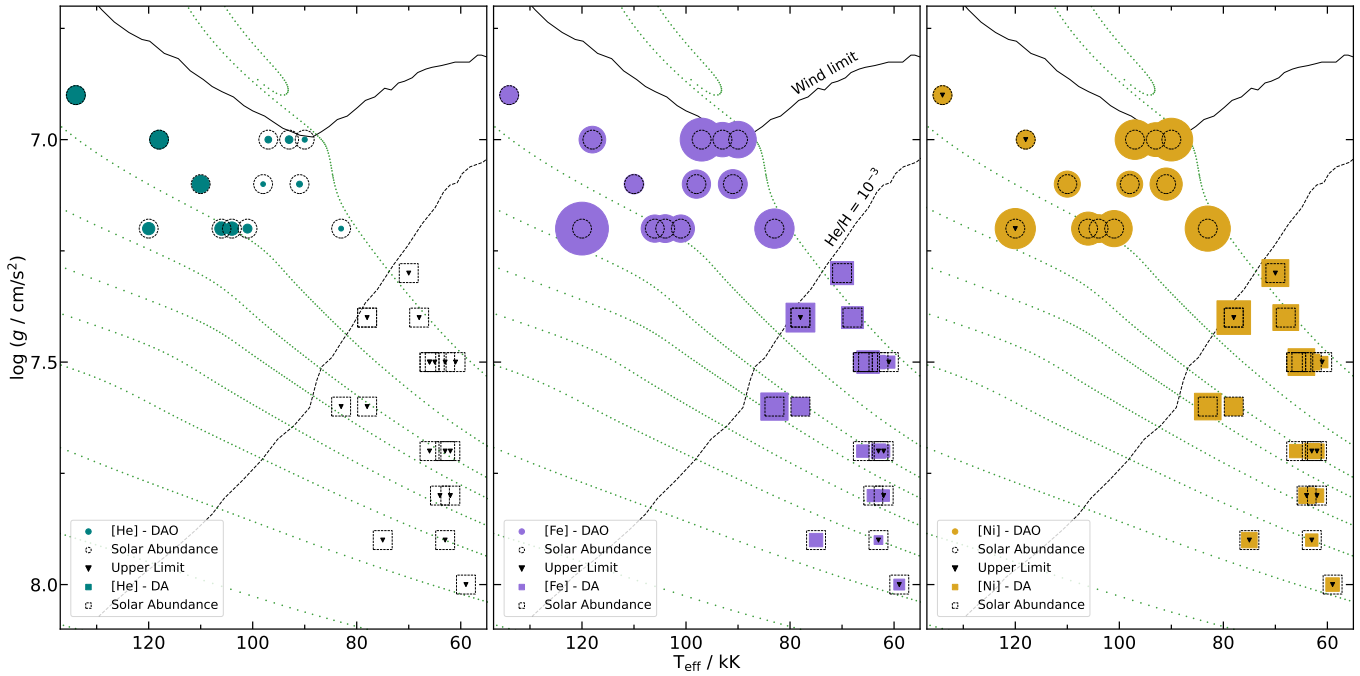


Fig. 10. Similar to Fig. 9, but for helium, iron, and nickel (from left to right).

problem (Vennes et al. 2000; Vennes & Lanz 2001; Chayer et al. 2006; Rauch et al. 2013). By calculating self-consistent diffusion models, Rauch et al. (2013) showed that an improvement can be achieved when the O abundance is only decreased in the outer atmosphere, where the observed weak O VI resonance lines form. They suggested that a weak mass loss might diminish the O abundance in the outer atmosphere and might cause the observed O VI resonance line profiles.

However, chemically homogeneous line-driven winds are not expected above $\log g = 7.0$ for a WD with $T_{\rm eff} = 60$ kK and (sub-) solar metallicity (Unglaub 2007). Fundamentally, abundance patterns of objects with similar parameters should be predicted by the equilibrium between gravitational settling and radiative levitation. Nonetheless, selective winds (or outflows) that only act on metal ions can still be expected (Babel 1995; Krtička et al. 2020) and influence the observed metal abundances. Unglaub (2007) showed that selective winds are predicted for the WDs ($\log g \approx 7$) with mass-loss rate $\dot{M} < 10^{-11}\ M_{\odot}{\rm yr}^{-1}$. Therefore, the discrepancy between observed abundances of DA WDs and theoretical predictions might arise from the exclusion of mass loss in the diffusion calculations (Unglaub 2007, 2008).

5.2. Wind limit

Unglaub & Bues (2000) commented that if all WD progenitors had the same composition, they should be clearly separated in the Kiel diagram, and the previously observed coexistence of DAO and DA WDs in the same region can be explained by the difference in initial metallicity. A quick glance at Fig. 8 reveals otherwise: DAO and DA WDs are clearly separated in the Kiel diagram, and no DA resides above the predicted He abundance limit. Figures 9 and 10 illustrate the metal abundances of individual objects in the Kiel diagram. In these plots, no substantial deviation in the abundances of DAOs and DAs among each other can be recognized. In comparison, the difference in the abundance pattern from one species to the next is conspicuous. In Fig. 10, the change in the He abundance in the Kiel diagram is depicted. When we accept that solar He abundance indicates a weak mass loss, our observational wind limit falls below the theoretical predictions. Around 105 kK, the decrease in He abundance can be observed. This was also reported by Werner et al. (2018b, 2019, 2020). All points above indicate that all hydrogen-rich WDs are born as DAOs and evolve into DAs. Therefore, the initial composition of our sample WDs probably does not substantially deviate in the objects, and the clear detachment of DAOs from DAs supports this claim. However, we should note that the termination point of mass loss probably differs for objects with different metallicities. Therefore, we speculate that finding DAOs far below the He limit, or vice versa for DAs, could be a direct indication of the difference in initial metallicity.

It is common practice to compile $T_{\rm eff}$ and $\log g$ values from several studies for a broad overview of the evolutionary state of the WDs (Napiwotzki 1999; Unglaub & Bues 1998, 2000). However, it should be noted that the compiled studies might employ different stellar atmosphere codes and atomic data. Even minor deviations between codes can have a severe impact on the results, as shown by Rauch (2008), who reported an (E)UV flux difference between models calculated with TMAP and TLUSTY[7] due to different cutoff frequencies of the H I Lyman bound-free opacity. Therefore, conducting a homogeneous spectral analysis with the same code and atomic data is a key factor in our results. Even though other homogeneously performed analyses identified a tendency for DAOs to be hotter than DAs, a partial overlap of DAs and DAOs in the Kiel diagram persisted (Gianninas et al. 2010, 2011; Bédard et al. 2020). A result similar to ours can be observed in the $T_{\rm eff}$– $\log g$ diagram by Reindl et al. (2023), although several DA WDs inhabit a region slightly beyond the predicted He limit (see their Fig. 6). In all of these cases, the missing ingredient probably is the UV spectroscopy, which enables the inclusion of metal opacities in the model atoms and consequently paves the way to accurately assess $T_{\rm eff}$ by exploiting the ionization balance of metal lines.

[7] http://nova.astro.umd.edu

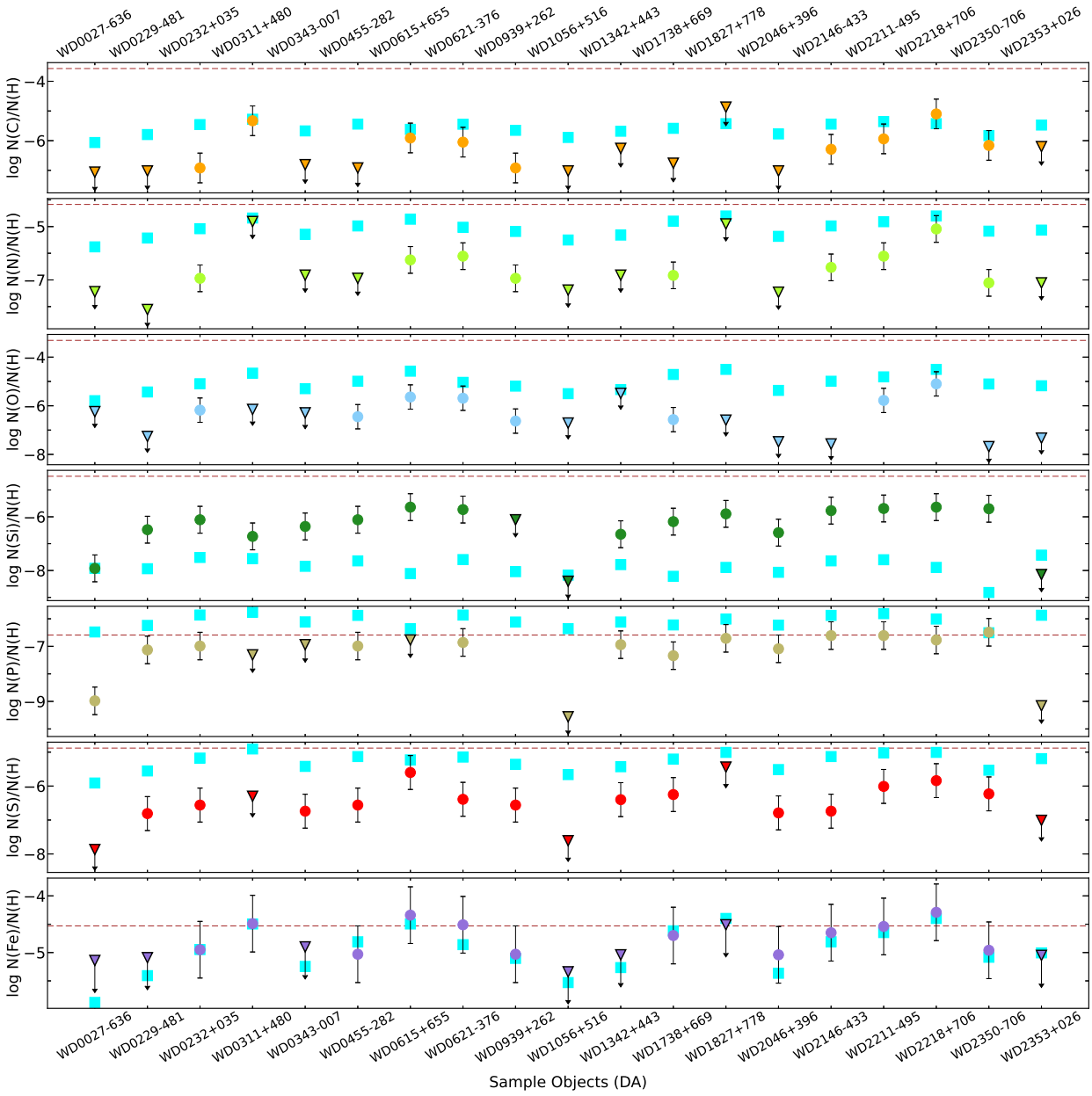


Fig. 11. Comparison of the C, N, O, Si, S, and Fe abundances (from top to bottom) in our DAs with predictions of diffusion theory by Chayer et al. (1995b) and for P by Vennes et al. (1996). The predictions are represented by turquoise squares. The solar abundances are indicated by horizontal dashed lines. The upper limits are marked with triangles.

5.3. Balmer-line problem

The occurrence of the BLP in a large fraction of DAO WDs has already been reported (Bergeron et al. 1994; Napiwotzki 1999; Gianninas et al. 2010; Bédard et al. 2020; Reindl et al. 2023), and the severity of this problem was tied to the high metal abundance by qualitatively comparing UV spectra of DAO and DA WDs (Gianninas et al. 2010). To evaluate the impact of the metallicity on the Balmer lines and the BLP, we calculated a set of models with finally adopted parameters that only included H and H+He in the model atoms for DA and DAOs, respectively. With this configuration, we achieved satisfactory fits within the error range for 13 DA WDs. For the remaining 6 DAs, the BLP is more or less apparent with pure H models (Fig. 12). Notably, the latter 6 have a higher metal abundance than the rest of the DA WDs in our sample. Implementing a similar approach for DAOs yielded insufficient fits to He II λ 4686 Å and Balmer lines without exception (Fig. 13). Although we did not try to achieve good fits with this configuration, a tendency for lower $T_{\rm eff}$ can be expected with H+He models. This might explain the large disparity in $T_{\rm eff}$ (up to 40 and 20 kK for DAOs and DAs, respectively) and log g between previous optical studies and ours. However, a large discrepancy in $T_{\rm eff}$ compared to optical results by Gianninas et al. (2010, 2011) is still observed (Fig. 14), even though their models include (solar) C, N, and O opacities. While for DAOs, our models systematically predict higher $T_{\rm eff}$, a general trend for DAs is not apparent.

Considering our models with finally accepted $T_{\rm eff}$, log g and meticulously derived metal abundances from UV, we did not encounter severe cases of the BLP in our sample, except for two

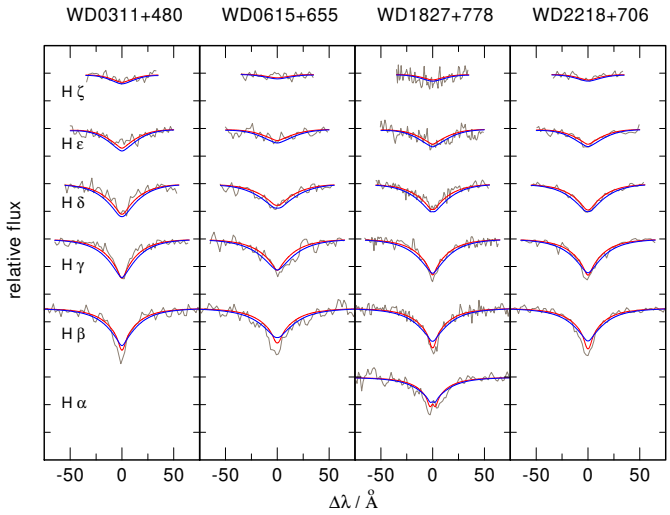


Fig. 12. Balmer lines (gray) of the DA WDs compared to the final model, including metal opacities (red) and pure H models (blue).

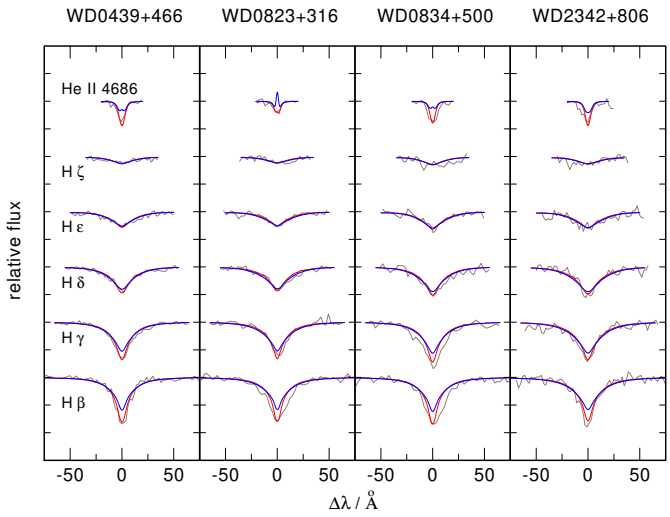


Fig. 13. He II and Balmer lines (gray) of the DAO WDs compared to the final model, including metal opacities (red) and H+He models (blue).

DAOs (Fig. 13; WD 0823+316 and WD 0834+500) and two DA WDs (Fig. 12; WD 0311+480 and WD 0615+655), which respectively showed broader and deeper Hβ than our models predict. However, the issues observed in the last four cases might depend on several factors, for instance, the data quality, data reduction, and normalization of the spectra. On the other hand, the data quality is of critical importance in detecting the BLP, as already remarked by Bédard et al. (2020) and Reindl et al. (2023). A high fraction of MWDD spectra in our sample have a reasonably high S/N (≈50), but most of the observations do not contain the Hα region. Additionally, the NLTE line-core emissions are not resolved because of the low resolution, which acts as a proxy for $T_{\rm eff}$. Reindl et al. (2023) noted that they encountered the BLP more often in the higher-quality X-shooter data than in those from the Intermediate Dispersion Spectrograph (IDS) at the Isaac Newton Telescope (INT). The same outcome was also reported by Werner et al. (2018b) in the case of EGB6, for which the BLP was undetected in the low-resolution MWDD spectra (Gianninas et al. 2010). In contrast, the BLP still manifests in low-resolution, low S/N spectra even when the model atmosphere contains metal opacities (Werner et al. 2019). Therefore, our low-rate detection of BLP does not build a clear case for the solution being the inclusion of metals, but metals rather present an improvement to the results.

Finally, we would like to comment on the observed differences in log g inferred from the Lyman and Balmer lines. We achieved satisfactory fits to the Lyman lines of WD 0621−373 and WD 2211−495 (see Fig. 2 as an example). However, Hα and Hβ cannot be reproduced properly with the same parameters, and a rather large decrease in log g (0.3–0.4 dex) is needed, while the higher-order Balmer-line series agree. Both problematic objects have UVES and MWDD spectra, and the same effect can be observed in both datasets. A similar effect but in a more severe form has already been reported, where large scatter between UV and optical parameters is noticeable (Barstow et al. 2003b; Good et al. 2004). For objects above 50 kK, Vennes et al. (2005) showed that $T_{\rm eff}$ measured from Lyman lines exceeds up to ≈15%. However, they demonstrated that when heavy elements are included in the model calculations, a decrease of up to 16 kK in the Lyman-line temperature could be expected. Their sample also included WD 0621−373 and WD 2211−495, and for both objects, they derived $T_{\rm eff} > 70$ kK and ≈65 kK with pure H models from UV and optical spectra, respectively. Both of their Lyman-line temperatures are above our error limit, and their log g values from UV are lower, but consistent with ours within the uncertainty. Our case demonstrates that with the inclusion of metals and employing ionization equilibria, a common ground for $T_{\rm eff}$ can be found for both wavelength regimes. Since the temperature is fixed, our results from different bands do not substantially deviate from one another in general, as opposed to previous studies. In the case of problematic objects, another factor should perhaps be considered (e.g., data reduction or normalization).

6. Summary and conclusion

We analyzed a sample of 19 DA and 13 DAO WDs, which have $T_{\rm eff} > 60$ kK and for which UV spectra are available, using state-of-the-art metal-line blanketed NLTE model atmospheres to extract crucial information about the spectral evolution of hot H-rich WDs. The effective temperatures and gravities were derived accurately by exploiting the ionization balances of the metal lines in the UV spectra. The abundances of helium and metals were measured with high accuracy. Our main results are listed below.

(i) In contrast to earlier studies, we find a clear separation of DAs and DAOs in the Kiel diagram (Fig. 8). Hydrogen-rich WDs are born as DAOs and turn into DAs when they cool to $T_{\rm eff} \approx 75$–85 kK. At around this temperature, helium becomes depleted by gravitational settling, as predicted by the combined theory of diffusion and mass loss.

(ii) In agreement with theory, we witness a gradual decrease in the helium abundance when DAOs cool (Fig. 10). The abundances of CNO elements also decrease, but less rapidly, again in accordance with theory (Fig. 9). Other light metals (Si, P, and S) follow a similar trend (Fig. 9).

(iii) According to the He abundance pattern of DAOs, the observational wind limit is slightly shifted downward in the Kiel diagram compared to the theoretical predictions (Fig. 10).

(iv) As DAOs approach the transformation into DAs, an increase in the iron and nickel abundances is observed (Fig. 10). Along with the decrease in the abundance of other elements, this indicates that mass loss can no longer efficiently homogenize the atmosphere.

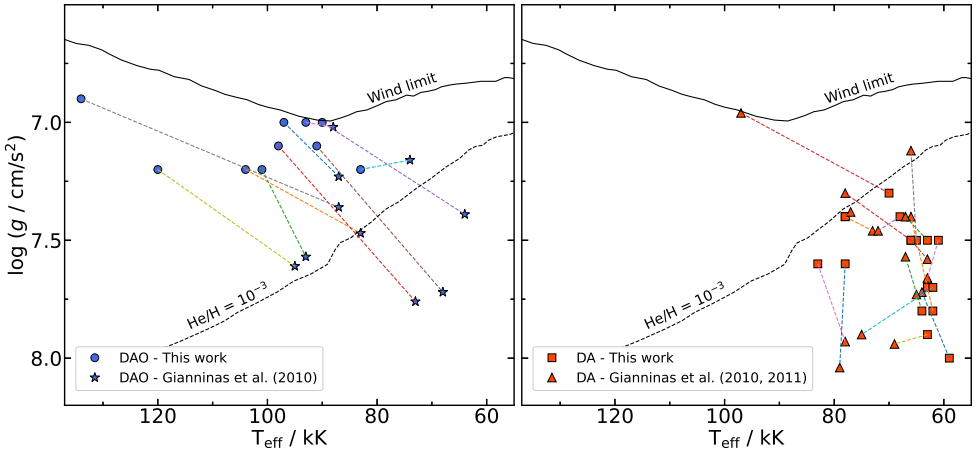


Fig. 14. $T_{\rm eff}$ and $\log g$ values of the sample objects (DAO shown as blue circles, and DA shown as red squares) compared to the optical results (DAO shown as blue stars, and DA shown as red triangles) by Gianninas et al. (2010, 2011).

(v) Diffusion theory assuming equilibrium of radiative acceleration and gravity generally fails to explain the observed metal abundances in hot DAs. This has been stated in many earlier works. However, we report clear systematic trends in our homogeneous sample. For virtually all DAs in our sample, theory overpredicts the abundances of C, N, O, P, and S, but underpredicts the abundance of Si (Fig. 11). Theory and observation agree for iron. The causes of the discrepancies remain unclear, but, as reasoned before by others, residual weak mass loss might be the cause.

(vi) There is no indication that the accretion of circumstellar material is relevant in our sample. All DAs have a similar metal abundance pattern.

(vii) The Balmer-line problem in DAOs is mitigated by the inclusion of metals with abundances determined from the UV analyses, but it does not disappear.

(viii) In contrast to earlier work, we generally encountered no large discrepancies between Balmer- and Lyman-line fits; hence, we find no indication of problems with the line-broadening theory. Larger deviations in gravity determinations are detected for a few objects, but this may be introduced by uncertainties in data reduction and normalization of the optical spectra or by strong ISM line blending in the case of UV spectra.

In conclusion, we emphasize that UV spectroscopy is the key to a reliable parameter determination of hot hydrogen-rich WDs and, hence, their spectral evolution.

Data availability

The model fits to the UV and optical spectra of the sample objects as well as the comparison of $T_{\rm eff}$, $\log g$, and abundances to previous studies are available at https://doi.org/10.5281/zenodo.13940390 as online supplementary material.

Acknowledgements. We thank the referee for a constructive report that helped to improve the paper. We also thank Simon Preval and Martin Barstow for sending us the STIS spectrum of WD0455-282. S.F. is supported by the Deutsche Forschungsgemeinschaft (grant WE1312/58-1). N.R. is supported by the Deutsche Forschungsgemeinschaft (DFG) through grant RE3915/2-1. The TMAD (http://astro.uni-tuebingen.de/~TMAD) and TIRO tool (http://astro.uni-tuebingen.de/~TIRO) used for this paper was constructed as part of the activities of the German Astrophysical Virtual Observatory. Some of the data presented in this paper were obtained from the Mikulski Archive for Space Telescopes (MAST). This work is based on observations made with the NASA/ESA *Hubble* Space Telescope obtained from the Space Telescope Science Institute (STScI), which is operated by the Association of Universities for Research in Astronomy, Inc., under NASA contract NAS 5–26555. Funding for the SDSS and SDSS-II has been provided by the Alfred P. Sloan Foundation, the Participating Institutions, the National Science Foundation, the U.S. Department of Energy, the National Aeronautics and Space Administration, the Japanese Monbukagakusho, the Max Planck Society, and the Higher Education Funding Council for England. The SDSS Web Site is http://www.sdss.org/. This work is based on data obtained from the ESO Science Archive Facility. This research has made use of NASA's Astrophysics Data System and the SIMBAD database, operated at CDS, Strasbourg, France. This research has made use of the VizieR catalogue access tool, CDS, Strasbourg, France. This research made use of TOPCAT, an interactive graphical viewer and editor for tabular data (Taylor 2005).

References

Abazajian, K. N., Adelman-McCarthy, J. K., Agüeros, M. A., et al. 2009, ApJS, 182, 543
Adamczak, J., Werner, K., Rauch, T., et al. 2012, A&A, 546, A1
Asplund, M., Grevesse, N., Sauval, A. J., & Scott, P. 2009, ARA&A, 47, 481
Babel, J. 1995, A&A, 301, 823
Barstow, M. A., Holberg, J. B., Fleming, T. A., et al. 1994, MNRAS, 270, 499
Barstow, M. A., Hubeny, I., & Holberg, J. B. 1998, MNRAS, 299, 520
Barstow, M. A., Bannister, N. P., Holberg, J. B., et al. 2001a, MNRAS, 325, 1149
Barstow, M. A., Bond, H. E., Burleigh, M. R., & Holberg, J. B. 2001b, MNRAS, 322, 891
Barstow, M. A., Good, S. A., Holberg, J. B., et al. 2002, MNRAS, 330, 425
Barstow, M. A., Good, S. A., Burleigh, M. R., et al. 2003a, MNRAS, 344, 562
Barstow, M. A., Good, S. A., Holberg, J. B., et al. 2003b, MNRAS, 341, 870
Barstow, M. A., Barstow, J. K., Casewell, S. L., Holberg, J. B., & Hubeny, I. 2014, MNRAS, 440, 1607
Bédard, A. 2024, Ap&SS, 369, 43
Bédard, A., Bergeron, P., & Fontaine, G. 2017, ApJ, 848, 11
Bédard, A., Bergeron, P., Brassard, P., & Fontaine, G. 2020, ApJ, 901, 93
Bédard, A., Brassard, P., Bergeron, P., & Blouin, S. 2022, ApJ, 927, 128
Bergeron, P., Wesemael, F., Beauchamp, A., et al. 1994, ApJ, 432, 305
Bergeron, P., Wesemael, F., Fontaine, G., et al. 2021, AJ, 162, 188
Blöcker, T., Herwig, F., Driebe, T., Bramkamp, H., & Schönberner, D. 1997, Astrophys. Space Sci. Lib., 214, 57
Bragaglia, A., Renzini, A., & Bergeron, P. 1995, ApJ, 443, 735
Chayer, P. 2014, MNRAS, 437, L95
Chayer, P., Fontaine, G., & Wesemael, F. 1995a, ApJS, 99, 189
Chayer, P., Vennes, S., Pradhan, A. K., et al. 1995b, ApJ, 454, 429
Chayer, P., Fontaine, G., & Pelletier, C. 1997, Astrophys. Space Sci. Lib., 214, 253
Chayer, P., Oliveira, C., Dupuis, J., Moos, H. W., & Welsh, B. Y. 2006, ASP Conf. Ser., 348, 209
Cunningham, T., Wheatley, P. J., Tremblay, P.-E., et al. 2022, Nature, 602, 219
Delgado Inglada, G., Rodríguez, M., Mampaso, A., & Viironen, K. 2009, ApJ, 694, 1335
Dobbie, P. D., Barstow, M. A., Hubeny, I., et al. 2005, MNRAS, 363, 763
Dufour, P., Blouin, S., Coutu, S., et al. 2017, ASP Conf. Ser., 509, 3
Finley, D. S., Koester, D., & Basri, G. 1997, ApJ, 488, 375
Fitzpatrick, E. L. 1999, PASP, 111, 63
Frew, D. J. 2008, PhD thesis, Macquarie University, Department of Physics and Astronomy, Australia
Frew, D. J., & Parker, Q. A. 2010, PASA, 27, 129
Frew, D. J., Parker, Q. A., & Bojičić, I. S. 2016, MNRAS, 455, 1459
Gänsicke, B. T., Schreiber, M. R., Toloza, O., et al. 2019, Nature, 576, 61

Gentile Fusillo, N. P., Manser, C. J., Gänsicke, B. T., et al. 2021a, MNRAS, 504, 2707
Gentile Fusillo, N. P., Tremblay, P. E., Cukanovaite, E., et al. 2021b, MNRAS, 508, 3877
Gianninas, A., Bergeron, P., Dupuis, J., & Ruiz, M. T. 2010, ApJ, 720, 581
Gianninas, A., Bergeron, P., & Ruiz, M. T. 2011, ApJ, 743, 138
Good, S. A., Barstow, M. A., Holberg, J. B., et al. 2004, MNRAS, 355, 1031
Good, S. A., Barstow, M. A., Burleigh, M. R., Dobbie, P. D., & Holberg, J. B. 2005a, MNRAS, 364, 1082
Good, S. A., Barstow, M. A., Burleigh, M. R., et al. 2005b, MNRAS, 363, 183
Greenstein, J. L., & Eggen, O. J. 1966, Vistas Astron., 8, 63
Guo, J., Zhao, J., Tziamtzis, A., et al. 2015, MNRAS, 454, 2787
Hall, P. D., Tout, C. A., Izzard, R. G., & Keller, D. 2013, MNRAS, 435, 2048
Hébrard, G., & Moos, H. W. 2003, ApJ, 599, 297
Hébrard, G., Friedman, S. D., Kruk, J. W., et al. 2002, Planet. Space Sci., 50, 1169
Henry, R. B. C., Kwitter, K. B., & Balick, B. 2004, AJ, 127, 2284
Herald, J. E., & Bianchi, L. 2004, PASP, 116, 391
Holberg, J. B., Wesemael, F., & Basile, J. 1986, ApJ, 306, 629
Holberg, J. B., Barstow, M. A., Buckley, D. A. H., et al. 1993, ApJ, 416, 806
Homeier, D., Koester, D., Hagen, H. J., et al. 1998, A&A, 338, 563
Hu, J., Webb, J. K., Ayres, T. R., et al. 2021, MNRAS, 500, 1466
Joyce, S. R. G., Barstow, M. A., Casewell, S. L., et al. 2018, MNRAS, 479, 1612
Jura, M. 2003, ApJ, 584, L91
Kawka, A., Vennes, S., Schmidt, G. D., Wickramasinghe, D. T., & Koch, R. 2007, ApJ, 654, 499
Kepler, S. O., Pelisoli, I., Koester, D., et al. 2019, MNRAS, 486, 2169
Kepler, S. O., Koester, D., Pelisoli, I., Romero, A. D., & Ourique, G. 2021, MNRAS, 507, 4646
Koester, D., Liebert, J., & Hege, E. K. 1979, A&A, 71, 163
Koester, D., Napiwotzki, R., Christlieb, N., et al. 2001, A&A, 378, 556
Koester, D., Rollenhagen, K., Napiwotzki, R., et al. 2005, A&A, 432, 1025
Koester, D., Voss, B., Napiwotzki, R., et al. 2009, A&A, 505, 441
Koester, D., Gänsicke, B. T., & Farihi, J. 2014, A&A, 566, A34
Krtička, J., Kubát, J., & Krtičková, I. 2020, A&A, 635, A173
Lajoie, C. P., & Bergeron, P. 2007, ApJ, 667, 1126
Lamberts, A., Blunt, S., Littenberg, T. B., et al. 2019, MNRAS, 490, 5888
Lei, Z., He, R., Németh, P., et al. 2023, ApJ, 942, 109
Lemoine, M., Vidal-Madjar, A., Hébrard, G., et al. 2002, ApJS, 140, 67
Lépine, S., Bergeron, P., & Lanning, H. H. 2011, AJ, 141, 96
Liebert, J., Bergeron, P., & Holberg, J. B. 2005, ApJS, 156, 47
Limoges, M. M., & Bergeron, P. 2010, ApJ, 714, 1037
Löbling, L., Maney, M. A., Rauch, T., et al. 2020, MNRAS, 492, 528
Madsen, G. J., Frew, D. J., Parker, Q. A., Reynolds, R. J., & Haffner, L. M. 2006, IAU Symp., 234, 455
Manseau, P. M., Bergeron, P., & Green, E. M. 2016, ApJ, 833, 127
Manser, C. J., Gänsicke, B. T., Marsh, T. R., et al. 2016, MNRAS, 455, 4467
Manser, C. J., Gänsicke, B. T., Eggl, S., et al. 2019, Science, 364, 66
Manser, C. J., Gänsicke, B. T., Gentile Fusillo, N. P., et al. 2020, MNRAS, 493, 2127
Marsh, M. C., Barstow, M. A., Buckley, D. A., et al. 1997, MNRAS, 286, 369
McCarthy, J. K., Mendez, R. H., & Kudritzki, R. P. 1997, IAU Symp., 180, 120
McCook, G. P., & Sion, E. M. 1999, ApJS, 121, 1
Melis, C., Klein, B., Doyle, A. E., et al. 2020, ApJ, 905, 56
Mendez, R. H., Kudritzki, R. P., Gruschinske, J., & Simon, K. P. 1981, A&A, 101, 323
Mendez, R. H., Kudritzki, R. P., & Simon, K. P. 1985, A&A, 142, 289
Mendez, R. H., Kudritzki, R. P., Herrero, A., Husfeld, D., & Groth, H. G. 1988, A&A, 190, 113
Miller Bertolami, M. M. 2016, A&A, 588, A25
Müller-Ringat, E. M. 2013, PhD thesis, Eberhard Karls University of Tubingen, Germany
Napiwotzki, R. 1999, A&A, 350, 101
Napiwotzki, R., & Schonberner, D. 1993, IAU Symp., 155, 495
Preval, S. P., Barstow, M. A., Bainbridge, M., et al. 2019, MNRAS, 487, 3470
Ransom, R. R., Kothes, R., Geisbuesch, J., Reich, W., & Landecker, T. L. 2015, ApJ, 799, 198
Rauch, T. 2008, A&A, 481, 807
Rauch, T., & Deetjen, J. L. 2003, ASP Conf. Ser., 288, 103
Rauch, T., Ziegler, M., Werner, K., et al. 2007, A&A, 470, 317
Rauch, T., Werner, K., Biémont, É., Quinet, P., & Kruk, J. W. 2012, A&A, 546, A55
Rauch, T., Werner, K., Bohlin, R., & Kruk, J. W. 2013, A&A, 560, A106
Rauch, T., Werner, K., Quinet, P., & Kruk, J. W. 2014a, A&A, 564, A41
Rauch, T., Werner, K., Quinet, P., & Kruk, J. W. 2014b, A&A, 566, A10
Rauch, T., Hoyer, D., Quinet, P., Gallardo, M., & Raineri, M. 2015a, A&A, 577, A88
Rauch, T., Werner, K., Quinet, P., & Kruk, J. W. 2015b, A&A, 577, A6
Rauch, T., Quinet, P., Hoyer, D., et al. 2016a, A&A, 587, A39
Rauch, T., Quinet, P., Hoyer, D., et al. 2016b, A&A, 590, A128
Rauch, T., Gamrath, S., Quinet, P., et al. 2017a, A&A, 599, A142
Rauch, T., Quinet, P., Knörzer, M., et al. 2017b, A&A, 606, A105
Rauch, T., Gamrath, S., Quinet, P., et al. 2020, A&A, 637, A4
Reindl, N., Bainbridge, M., Przybilla, N., et al. 2019, MNRAS, 482, L93
Reindl, N., Islami, R., Werner, K., et al. 2023, A&A, 677, A29
Renedo, I., Althaus, L. G., Miller Bertolami, M. M., et al. 2010, ApJ, 717, 183
Schoening, T., & Butler, K. 1989, A&AS, 78, 51
Schuh, S. L., Dreizler, S., & Wolff, B. 2002, A&A, 382, 164
Stanghellini, L., Guerrero, M. A., Cunha, K., Manchado, A., & Villaver, E. 2006, ApJ, 651, 898
Taylor, M. B. 2005, ASP Conf. Ser., 347, 29
Traulsen, I., Hoffmann, A. I. D., Rauch, T., et al. 2005, ASP Conf. Ser., 334, 325
Tremblay, P. E., & Bergeron, P. 2009, ApJ, 696, 1755
Tremblay, P. E., Bergeron, P., & Gianninas, A. 2011, ApJ, 730, 128
Tremblay, P. E., Cukanovaite, E., Gentile Fusillo, N. P., Cunningham, T., & Hollands, M. A. 2019, MNRAS, 482, 5222
Tweedy, R. W., & Napiwotzki, R. 1994, AJ, 108, 978
Unglaub, K. 2007, ASP Conf. Ser., 372, 201
Unglaub, K. 2008, A&A, 486, 923
Unglaub, K., & Bues, I. 1998, A&A, 338, 75
Unglaub, K., & Bues, I. 2000, A&A, 359, 1042
Vennes, S. 1992, ApJ, 390, 590
Vennes, S., & Fontaine, G. 1992, ApJ, 401, 288
Vennes, S., & Lanz, T. 2001, ApJ, 553, 399
Vennes, S., Pelletier, C., Fontaine, G., & Wesemael, F. 1988, ApJ, 331, 876
Vennes, S., Chayer, P., Fontaine, G., & Wesemael, F. 1989, ApJ, 336, L25
Vennes, S., Chayer, P., Thorstensen, J. R., Bowyer, S., & Shipman, H. L. 1992, ApJ, 392, L27
Vennes, S., Chayer, P., Hurwitz, M., & Bowyer, S. 1996, ApJ, 468, 898
Vennes, S., Thejll, P. A., Génova Galvan, R., & Dupuis, J. 1997, ApJ, 480, 714
Vennes, S., Polomski, E. F., Lanz, T., et al. 2000, ApJ, 544, 423
Vennes, S., Chayer, P., Dupuis, J., & Lanz, T. 2005, ASP Conf. Ser., 334, 185
von Hippel, T., Kuchner, M. J., Kilic, M., Mullally, F., & Reach, W. T. 2007, ApJ, 662, 544
Werner, K. 1996, ApJ, 457, L39
Werner, K., & Dreizler, S. 1999, J. Comput. Appl. Math., 109, 65
Werner, K., Dreizler, S., Heber, U., et al. 1995, A&A, 293, L75
Werner, K., Deetjen, J. L., Dreizler, S., et al. 2003, ASP Conf. Ser., 288, 31
Werner, K., Rauch, T., & Kruk, J. W. 2007, A&A, 466, 317
Werner, K., Dreizler, S., & Rauch, T. 2012, Astrophysics Source Code Library [record ascl:1212.015]
Werner, K., Rauch, T., & Kruk, J. W. 2018a, A&A, 609, A107
Werner, K., Rauch, T., & Kruk, J. W. 2018b, A&A, 616, A73
Werner, K., Rauch, T., & Reindl, N. 2019, MNRAS, 483, 5291
Werner, K., Reindl, N., Löbling, L., et al. 2020, A&A, 642, A228
Wesemael, F., Henry, R. B. C., & Shipman, H. L. 1984, ApJ, 287, 868
Wesemael, F., Green, R. F., & Liebert, J. 1985, ApJS, 58, 379
Ziegler, M. 2012, PhD thesis, Eberhard Karls University of Tubingen, Germany

Appendix A: Remarks on individual objects

In this section we give a brief remark on each object and compare our spectroscopic results to previous analyses (Tables B.3 and B.4). If the same authors analyzed a particular object more than once, only the latest reported $T_{\rm eff}$ and $\log g$ values were compared, excluding results acquired from a different waveband.

A.1. DAO white dwarfs

Longmore 1 For the central star of Longmore 1, we found $T_{\rm eff}$ = 118 ± 5 kK and $\log g$ = 7.0 ± 0.3 which are in agreement with the values determined in other FUV analyses (Herald & Bianchi 2004; Ziegler 2012). This is the only object in our sample that shows C, N, and O enhancement (up to 1.1 dex). We determined solar He, P, S, Ni, and almost two times solar Fe abundances. All abundance measurements of Ziegler (2012) lie within our error limits except for N and Fe for which the discrepancy approaches ≈ 1 dex. Likewise, the abundance of several ions (C, N, Si) differs more than 0.5 dex from the results of Herald & Bianchi (2004). Additionally, multiple C IV, N IV, N V, O V, and O VI lines were identified in the UVES spectrum. Especially, O V and O VI lines in the optical range and NLTE-core emission of He II λ4686 Å and H α are extremely sensitive to temperature change, and our fit to the UVES spectrum affirms our measured parameters. Nonetheless, we achieved poor fits to H β, H γ, and He II λ5412 Å. This issue does not appear as a case of conventional Balmer-line problem since we achieve very good fits to He II λ4686 Å and H α as well as the higher order of Balmer-line series. Utilizing evolutionary tracks of Miller Bertolami (2016) revealed a post-AGB age of 36 ± 14 kyr for the central star, which is consistent with the expected lifespan of PNe.

WD 0439+466 is the DAO-type central star of the planetary nebula (PN) Sh 2-216. We estimate $T_{\rm eff}$ = 97 ± 5 kK and $\log g$ = 7.0 ± 0.2. Napiwotzki (1999) reports $T_{\rm eff}$ = 83.2 ± 3.3 kK and $\log g$ = 6.74 ± 0.19 from their NLTE analysis of optical spectra consisting of H+He models. Another optical study by Gianninas et al. (2010) reached a similar conclusion for $T_{\rm eff}$ and $\log g$ (87 kK, 7.23). The slight difference to our results can be attributed to the exclusion of metal opacities in the previous optical analyses. On the other hand, our results are in agreement with the values determined by Traulsen et al. (2005, $T_{\rm eff}$ = 93 kK, $\log g$ = 6.9) and Rauch et al. (2007, $T_{\rm eff}$ = 95 ± 2 kK, $\log g$ = 6.9 ± 0.2), who employed HST and FUSE spectra. Our study indicates 0.9 dex sub-solar He abundance, whereas C and O are slightly sub-solar, and N is solar. In contrast to light metals, we found Fe and Ni enhancement for this object (0.6–0.7 dex). Traulsen et al. (2005) derived abundances only for He, C, N, O, and Si. Among these ions, only N abundance substantially differs from our results. Also, our abundances agree very well with those from Rauch et al. (2007), the largest difference being less than 0.4 dex for Si.

WD 0500−156 Optical and UV spectra of the DAO-type central star of PN Abell 7 were investigated multiple times since it has been analyzed by Mendez et al. (1981, $T_{\rm eff}$ = 75 ± 10 kK, $\log g$ = 7.0 ± 0.5). Earlier optical studies with LTE and NLTE models reported a wide $T_{\rm eff}$ (60–100 kK) and $\log g$ (6.60–7.47) range (Wesemael et al. 1985; McCarthy et al. 1997; Napiwotzki 1999; Good et al. 2004; Gianninas et al. 2010). Although FUV analyses reach a smaller discrepancy in $T_{\rm eff}$ (99–109 kK), the $\log g$ difference (7.00–7.68) remains large (Good et al. 2004; Ziegler 2012). From our FUV plus optical study, we determined $T_{\rm eff}$ = 104 ± 6 kK and $\log g$ = 7.20 ± 0.2. We found the He abundance as half of the solar value. C and O abundances are around the solar value, whereas N is slightly depleted. Other light metals (Si, P, S) were also found as sub-solar, while Fe and Ni are lightly enhanced. In general, our abundances agree very well with other studies (Good et al. 2005b; Ziegler 2012); however, C and N abundances by Good et al. (2005b) reside slightly outside of our error limit.

WD 0615+556 is the DAO-type central star of PN PuWe 1. We derived $T_{\rm eff}$ = 101 ± 5 kK and $\log g$ = 7.2 ± 0.2. In general, $T_{\rm eff}$ difference is less than 10 kK compared to previous optical or UV analyses (McCarthy et al. 1997; Napiwotzki 1999; Gianninas et al. 2010; Ziegler 2012) and only $\log g$ value of Gianninas et al. (2010) and Good et al. (2004, from Lymann lines) lies 0.2 dex out of our error limit. We did not find an agreement with the optical study of (Good et al. 2004), estimating $T_{\rm eff}$ = 74.2 ± 4.8 kK, $\log g$ = 7.02 ± 0.20. He abundance was determined to be one-fifth of the solar value. We found that N, O, Si, and S are slightly depleted, whereas P, Fe, and Ni are 0.3 to 0.5 dex enhanced. An upper limit to C abundance can be assigned as the solar value. Abundance measurements of Ziegler (2012) are similar to ours, the only statistically significant difference being the P and S abundance. We find a larger disagreement with values from Good et al. (2005b), except for Ni abundance.

WD 0823+316 is the DAO-type central star of PN TK 1. We estimate $T_{\rm eff}$ = 98 ± 5 kK and $\log g$ = 7.1 ± 0.2. The He abundance was derived as log (He/H) = -2.41, one of the lowest in the sample. We found solar C and P abundances, N is slightly over-solar, and O is slightly sub-solar. Si and S are highly depleted. We encounter over-solar Fe and Ni abundances. Previous optical analyses of this object yielded lower $T_{\rm eff}$ values ranging from 64 kK to 79 kK (Bergeron et al. 1994; Good et al. 2004; Gianninas et al. 2010; Tremblay et al. 2011; Bédard et al. 2020). However, we found a perfect agreement with the only other UV analysis by Good et al. (2004, $T_{\rm eff}$ = 99 ± 4 kK, $\log g$ = 7.26 ± 0.07). Our abundances also assent with Good et al. (2005b), except for C and O, which are ∼6 and 50 times less than ours.

WD 0834+500 is the second coolest DAO-type WD in our sample with $T_{\rm eff}$ = 90 ± 3 kK, $\log g$ = 7.0 ± 0.2 and log (He/H) = -2.33. We achieved an excellent fit to the FUSE spectrum, resulting in slightly sub-solar to solar light metal and over-solar Fe and Ni abundances. In contrast to the FUV, our optical fits are not in perfect coherence for given parameters. The line core of H γ is deeper, and the overall line strength is stronger than our model. On the other hand, our model gives a satisfactory fit to the line core of β, yet the equivalent width of the line is larger than the model predicts. However, higher orders of the Balmer-line series fit very well, indicating an accurate $\log g$ measurement. Former optical studies indicate much lower $T_{\rm eff}$, around 60 kK; in contrast, $\log g$ values always reside within our error limits (Bergeron et al. 1994; Good et al. 2004; Gianninas et al. 2010). This is anticipated since not including metal opacities is compensated with a lower $T_{\rm eff}$.

WD 0851+090 We derived $T_{\rm eff}$ = 106 ± 5 kK, $\log g$ = 7.2 ± 0.2 for the DAO-type central star of Abell 31. We encounter the same issue as with Longmore 1 in the UVES spectrum of Abell 31. All of the Balmer and He II line fits are satisfactory except for H γ and He II λ5412 Å. We estimate the He abundance as half of the solar value. C, N, and O are determined as roughly solar, but Si and S are up to 0.7 dex sub-solar. In comparison, Fe and Ni are slightly enhanced. Our abundances match very well with Ziegler (2012), S and Fe being the only ions with a large discrepancy. While Good et al. (2005b) reported significantly (76

and 20 times) lower N and O content than ours, for other elements, deviations are less than one dex. Additionally, previous studies largely deviate from one another regarding $T_{\rm eff}$ and log g. On one hand, Balmer fits of Good et al. (2004) resulted in $T_{\rm eff} = 74.7 \pm 6.0$ kK, log $g = 9.95 \pm 0.15$, on the other hand, Ziegler (2012) inferred $T_{\rm eff} = 114 \pm 10$ kK, log $g = 7.4 \pm 0.3$ from FUSE spectra.

WD 1111+552 is the only object for which we did not have optical spectra. We only utilized FUSE observations of the DAO-type central star of PN M 97 (NGC 3587) and determined $T_{\rm eff} = 110 \pm 5$ kK and log $g = 7.1 \pm 0.3$. Other than Si and S, which are 0.7 and 0.8 dex sub-solar, element abundances are derived as roughly solar. He, N, and O abundances agree well with the PN abundances derived by Stanghellini et al. (2006), but Fe, which is roughly two dex higher than inferred from PN by Delgado Inglada et al. (2009). While in general, these measurements, including $T_{\rm eff}$ and log g, are in good agreement with Ziegler (2012), we estimate ≈ 12 times more N content. Furthermore, $T_{\rm eff}$ and log g parameters are comparable to early optical analyses (McCarthy et al. 1997), with only Napiwotzki (1999) reporting a temperature 10 kK below our error range.

WD 1214+267 is the third coolest DAO WD in our sample ($T_{\rm eff} = 91 \pm 3$ kK, log $g = 7.1 \pm 0.3$). While early optical studies reported 20 to 30 kK lower temperature and 0.5 to 0.6 dex higher surface gravity (Bergeron et al. 1994; Good et al. 2004; Gianninas et al. 2010), by fitting Lyman lines in the FUSE spectra, Good et al. (2004) conclude $T_{\rm eff} = 87.6 \pm 3.7$ kK, log $g = 6.96 \pm 0.04$. Guo et al. (2015) derived $T_{\rm eff} = 80.3 \pm 4.9$ kK, log $g = 7.05 \pm 0.20$ by utilizing LAMOST spectra; however, they misclassified the object as DA WD. We estimate a roughly one dex sub-solar He abundance. All light metals are sub-solar, with S being the least abundant (one dex sub-solar) among them, whereas heavier elements are slightly enhanced. Good et al. (2005b) reported only C, O, Si, and Fe abundances. Among them, only O drastically differs from our measurements.

WD 1253+378 Since it has been discovered (Koester et al. 1979), the prototype DAO WD HZ 34 was observed and analyzed multiple times, generating a wide parameter range for temperature (60–91 kK) and surface gravity (6.51–7.02) of the object (Wesemael et al. 1985; Bergeron et al. 1994; Napiwotzki 1999; Good et al. 2004; Gianninas et al. 2010). With $T_{\rm eff} = 93 \pm 4$ kK and log $g = 7.0 \pm 0.2$, our results reside at the high end of this parameter range. Additionally, we found 0.7 dex sub-solar He abundance. While we measured slightly sub-solar C, O, and P abundances, N, Si, and S are 10 times sub-solar. On the other hand, ≈ 0.5 dex Fe and Ni enhancement was detected compared to the Sun. Besides He and Si, our abundances significantly differ than Good et al. (2005b).

WD 1957+225 is the hottest DAO-type CSPN (NGC 6853) in our sample ($T_{\rm eff} = 134 \pm 10$ kK and log $g = 6.9 \pm 0.4$). We found roughly solar abundances for all elements except for Si, which is ≈ 0.5 dex sub-solar. PN abundances (He, N, and O) derived by Stanghellini et al. (2006) reside within our error range. In general, our $T_{\rm eff}$, log g and abundance values are consistent with previous FUV analyses (Traulsen et al. 2005; Ziegler 2012), except for Fe abundance reported by Ziegler (2012) which is 1.5 dex sub-solar. However, $T_{\rm eff}$ and log g parameters derived in optical analyses reveal notable differences. For instance, the disparity in $T_{\rm eff}$, considering our lower limit, extends to ∼15 kK compared to Napiwotzki (1999, $T_{\rm eff} = 108.6 \pm 6.8$ kK log $g = 6.72 \pm 0.23$). The deviation is even larger in comparison to Gianninas et al. (2010, $T_{\rm eff} = 86.7 \pm 5.4$ kK, log $g = 7.36 \pm 0.18$). We encountered issues fitting the Balmer lines, especially Hβ, which is significantly stronger than our models. However, we appoint this to over-correction of the spectrum during background subtraction because forbidden nebular lines (O[III]) are also in absorption instead of emission. This issue was also reported by Gianninas et al. (2010) and might be the reason for their significantly lower $T_{\rm eff}$.

WD 2226−210 is the central star of Helix nebula (NGC 7293). We derived $T_{\rm eff} = 120 \pm 5$ kK and log $g = 7.2 \pm 0.3$ and 0.4 dex sub-solar He abundance. O, Si, and S are slightly depleted, and other light metals are comparable to solar abundance. On the other hand, Fe and Ni are enriched by 0.9 and 0.7 dex super-solar, respectively. S abundance determined from PN by Henry et al. (2004) is in agreement with the photospheric abundances, whereas He, N, and O abundances lie 0.1 dex above our error limit. Aside from the substantial log g difference (0.9 dex) with Traulsen et al. (2005), all parameters from other FUV analyses (Traulsen et al. 2005; Ziegler 2012) remain within our error range. While previous optical studies report lower $T_{\rm eff}$ in a consistent manner, ranging from 90 kk to 104 kK (Mendez et al. 1985, 1988; McCarthy et al. 1997; Napiwotzki 1999; Gianninas et al. 2010), log g values differ significantly (6.6–7.6 dex).

WD 2342+806 is the coolest ($T_{\rm eff} = 83 \pm 5$ kK, log $g = 7.2 \pm 0.2$) DAO-type WD (GD 561) with one of the lowest He content (1.2 dex sub-solar) in our sample. C, N, O, Si, and S abundances range between ∼ 0.2 to 0.5 dex sub-solar, whereas Fe and Ni are enriched up to 6 times the solar content. He, Si, P, and S abundances determined by Ziegler (2012) remain out of our error limits; other species agree. Except for Fe, our results are consistent with Good et al. (2005b). All previous studies report lower $T_{\rm eff}$ and log g values than ours.

GD 561 was associated with PN Sh 2-174 (Napiwotzki & Schonberner 1993; Tweedy & Napiwotzki 1994). Bergeron et al. (1994) suggests that the spectroscopic parameters are consistent with a post-EHB star that did not go through the AGB phase. Napiwotzki (1999) argues that any ejected material on the red giant branch (RGB) would not persist due to long evolutionary time scales on the horizontal branch, and the mass of the remaining EHB star would be too low to create the associated nebula. Tweedy & Napiwotzki (1994) reports the possibility of GD 561 being a low-mass post-RGB object that was produced through binary interaction, which, in that case, makes Sh 2-174 the envelope lost in the common envelope evolution. However, the vast disparity between the kinematical age of the PN and the supposed post-RGB lifetime of the WD (Napiwotzki 1999) decreases the likelihood. Additionally, the common envelope evolution scenario requires presence of a companion. However, Good et al. (2005a) did not detect a statistically significant RV shift. Also, there is no infrared excess, indicating a close companion (Filiz et al. in prep.). Ransom et al. (2015) identifies the system as a PN-ISM interaction through their radio analysis. On the other hand, Madsen et al. (2006) reports the kinematics of the gas inferred from optical emission lines. Frew (2008) concluded that the determined nebular velocity is statistically different from the stellar velocity, and the presence of a strong bowshock is required if the associated star is co-moving with the PN. Instead, they suggested that Sh 2-174 is an HII region in the ambient ISM, mimicking a true PN (Frew & Parker 2010; Frew et al. 2016).

Our estimated mass from the Kiel diagram (0.53 ± 0.04 $M_{\odot}$) is higher than previous analyses and indicates that GD

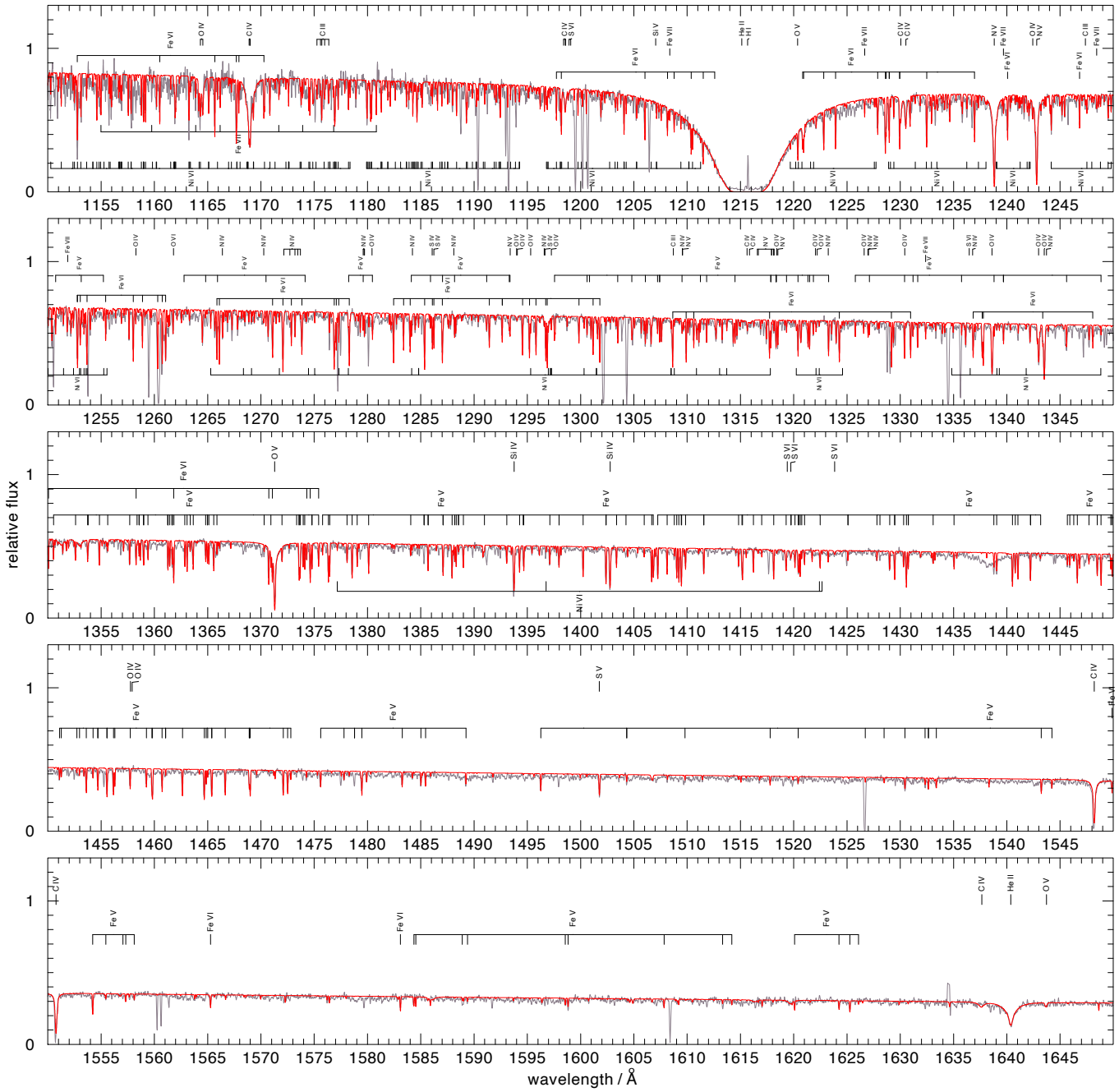


Fig. A.1: HST spectrum of the DAO WD 2342+806 (red: model with $T_{\rm eff}$ = 83 kK, log g = 7.2).

561 is likely a post-AGB star. From the evolutionary tracks of Miller Bertolami (2016), we determined a post-AGB age of 230 ± 73 kyr. Our estimated age of the WD is higher than the expected lifetime (10–100 kyr) of a bona fide PN. This agrees with Sh 2-174 being an HII region.

A.2. DA white dwarfs

WD 0027−636 is the coolest DA WD in our sample ($T_{\rm eff}$ = 59 ± 5 kK, log g = 8.0 ± 0.2). The given parameters are in unison with former studies, and only log g values determined by Vennes et al. (1997), Gianninas et al. (2011) and Bergeron et al. (2021) remain 0.2 dex out of our error range. All light metals are extremely sub-solar, whereas Fe and Ni are lightly depleted. Except for Si and P, we report upper-limit abundances. Only C, O, and Fe values are in agreement with the diffusion calculations of Chayer et al. (1995b). To the best of our knowledge, no other abundance measurements have been reported for this object. In their FUV analysis, Barstow et al. (2014) only report $T_{\rm eff}$ and log g values.

WD 0229−481 We estimate $T_{\rm eff}$ = 62 ± 5 kK and log g = 7.8 ± 0.2 for this DA WD. With CNO being highly depleted and given as upper limits, the abundance pattern shows a sub-solar content, though the P, Fe, and Ni deficit is about 0.4 dex. Only Fe and P abundances are comparable to theoretical calculations of Chayer et al. (1995b) and Vennes et al. (1996), respectively. Barstow et al. (2014) determined the C, Si, P, and S abundances of this object, and except for C, abundances lie within our er-

ror limits. Other than $T_{\rm eff}$ reported by Bragaglia et al. (1995) and Lajoie & Bergeron (2007), the highest temperature difference is 5 kK in comparison to previous studies. However, we find larger discrepancies in surface gravity.

WD 0232+035 Feige 24 is one of the most often analyzed hot-DA WDs with observations from EUV to infrared, of which binary nature has been long known (Greenstein & Eggen 1966). Contamination by the irradiated M dwarf can be recognized in the optical spectra (Gianninas et al. 2011; Guo et al. 2015). However, the optical spectrum we obtained from MWDD (Gianninas et al. 2011) does not cover the H α region and is not contaminated. As a result of stringent error margins imposed in this work ($T_{\rm eff}$ = 63 ± 3 kK and log g = 7.5 ± 0.2), only 5 of 15 previously reported $T_{\rm eff}$ and log g combinations statistically agree with ours, though deviations in $T_{\rm eff}$ do not exceed 8 kK. In contrast, a comparison of abundances with former studies (Vennes et al. 1992, 2000; Barstow et al. 2003b, 2014) reveals a consistent outcome, except for the mismatch in Ni and C abundances derived by Barstow et al. (2003b, 2014), respectively. CNO being on the lower end, we measured below solar abundances for all elements. Among these, only the Fe abundance is in agreement with the diffusion theory (Chayer et al. 1995b). Since this object has comparable metal abundances to DA WDs with similar parameters, accretion of wind material from the M dwarf is unlikely.

WD 0311+480 FUSE spectra of this DA WD are heavily contaminated by interstellar absorption, which substantially hinders the measurement of stellar parameters. Only the C III and C IV ionization balance provided a constraint for the temperature. Therefore, setting a large error range was needed ($T_{\rm eff}$ = 70 ± 10 kK). Also, successfully fitting all the Balmer lines was not possible. We managed to replicate line cores other than H β, which is too deep in the observation. However, line wings of H δ and H ϵ are slightly broader in our model. The higher order members of the Balmer-line series, as well as the Lyman lines in the FUSE spectrum, indicate a higher gravity; thus, we opted for log g = 7.3 ± 0.4. To the best of our knowledge, spectroscopic parameters of this object were previously derived only by Gianninas et al. (2010, $T_{\rm eff}$ = 97.8 kK and log g = 6.96). Although they utilized three different grids containing H/He, solar-CNO, and 10 × solar-CNO models, the inclusion of light metals, even in large quantities, did not prevent the Balmer-line problem. Their best-fit parameters were derived from the models that include solar-CNO. However, analyzing FUSE spectra uncovered a sub-solar light metal content, including CNO. In contrast, a slight Fe and Ni enhancement was detected. Except for C, Si, and Fe, we present upper-limit abundances. Only C, N, and Fe abundances yield results similar to predictions of the diffusion theory (Chayer et al. 1995b).

WD 0343−007 We derived $T_{\rm eff}$ = 63 ± 4 kK and log g = 7.7 ± 0.2, which are statistically in perfect agreement with previous results from optical spectroscopy (Babel 1995; Finley et al. 1997; Lajoie & Bergeron 2007; Koester et al. 2009; Limoges & Bergeron 2010; Gianninas et al. 2011). All of the element abundances were derived as sub-solar, while the depletion is less than 0.3 dex sub-solar for P, Fe and Ni. Excluding Si and S, element abundances are given as upper limits. Only the Fe abundance agrees with the theoretical calculations of Chayer et al. (1995b).

WD 0455−282 Previously, EUV, FUV, and optical analyses of this DA WD have been made multiple times. However, we found that only values derived by Limoges & Bergeron (2010) reside within our $T_{\rm eff}$ = 66 ± 3 kK and log g = 7.5 ± 0.2 boundaries in the Kiel diagram. Nonetheless, the temperature differences to our lower and upper limits are smaller than 10 kK and 3 kK, respectively, while early studies except for a few reported a tendency of log $g \geq$ 7.80. As previously stated, the Balmer-line problem was not detected in our optical fits. We measured sub-solar element abundances, with C, N, O, and Fe, Ni being extremely and slightly depleted, respectively. Only the Fe abundance is consistent with diffusion theory. Our element abundances generally agree with Vennes et al. (1996) and Preval et al. (2019) except for the differences in P and C, respectively. Also, among C, N, O, Si, Fe, Ni, O and Si are the only elements that show a large discrepancy compared to Barstow et al. (2003b). In contrast, C and S measurements of Barstow et al. (2014) significantly differ from ours, whereas Si and P[8] remain in our error range.

WD 0615+655 is the hottest DA WD in our sample ($T_{\rm eff}$ = 83 ± 10 kK and log g = 7.6 ± 0.4). While $T_{\rm eff}$ and log g derived by Homeier et al. (1998) and Lajoie & Bergeron (2007) lie out of our range, our results are in agreement with Gianninas et al. (2010). However, we were unable to fit the line core of H β, whereas other Balmer lines are reproduced better. Element abundances were measured by utilizing HST spectra, except for P, which shows no lines in the HST wavelength range. A slightly sub-solar upper limit was estimated for P from FUSE spectra. Fe and Ni are the only species derived above the solar value. The remaining elements were found to be sub-solar. C, P, S, and Fe abundances match with theoretical predictions (Chayer et al. 1995b).

WD 0621−376 Exploiting multiple ionization balances e.g. C III/C IV, O IV/O V, P IV/P V, Fe V/Fe VI, and Ni V/Ni VI enabled us to constrain the temperature tightly ($T_{\rm eff}$ = 65 ± 3 kK). Thanks to high S/N FUSE spectra and dearth of ISM contribution, a perfect fit to Lyman lines could be achieved with log g =7.5. On the other hand, except for the higher orders, the same parameters resulted in poor Balmer-line fits, emerging as deeper line cores and narrower wings of H δ - H α. Decreasing log g to 7.10 solved the issue for deep lines but diminished the quality of higher-order line fits; therefore, imposing a large error limit was inevitable log g = 7.5 ± 0.4. In comparison, other studies in various bands report a lower log g, excluding Barstow et al. (2003b) and Preval et al. (2019) which report similar results. On the other hand, previous abundance measurements reside either within or slightly out of our error limits (Holberg et al. 1993; Barstow et al. 2003b, 2014; Preval et al. 2019). However, C and N abundances derived by Barstow et al. (2014) and Holberg et al. (1993) significantly differ from our parameters, respectively. Our study indicates sub-solar light metal and roughly solar Fe and Ni content. C, O, and Fe abundances are comparable to the diffusion theory.

WD 0939+262 is the only DA WD in our sample without a FUSE spectrum. Consequently, we could not derive the P abundance for this object since relevant P lines are only found in the FUSE wavelength range. We derived $T_{\rm eff}$ = 66 ± 3 kK and log g = 7.7 ± 0.2. With Si indicating an upper limit, light metals are heavily depleted compared to the Sun, while Fe and Ni were measured as slightly sub-solar. Only the Fe abundance coincides with the theoretical predictions. All abundances derived by Barstow et al. (2003b) are within our error range, but Fe and Ni. Only $T_{\rm eff}$ and log g determined by Liebert et al. (2005) and

[8] Barstow et al. (2014) provide P abundances determined by fitting P IV and P V lines. Their measurements from P V lines are very similar to ours, though abundances determined from P IV lie ∼0.3 dex below our error range.

Lajoie & Bergeron (2007) are statistically in agreement within set limits in the Kiel diagram.

WD 1056+516 FUSE spectra of this DA WD indicate extremely low metal content. Due to poor data quality, detecting any photospheric line was not possible. Therefore, we increased the element abundances to upper limits where the model lines disappear in the noise of the observation. Adamczak et al. (2012) reports similar upper limits from the analysis of the FUSE spectra. However, they opt for a lower temperature ($T_{\rm eff}$ = 56 ± 2 kK,log g = 7.90 ± 0.3) due to the EUV flux of the *Chandra* spectrum, which is slightly below our error limit. We estimate $T_{\rm eff}$ = 63 ± 5 kK and log g = 7.9 ± 0.2. Parameters derived by Vennes et al. (1997), Lajoie & Bergeron (2007), and Bédard et al. (2020) through Balmer-line fitting statistically agree with ours.

WD 1342+443 We derived $T_{\rm eff}$ = 62 ± 5 kK and log g = 7.7 ± 0.3, which statistically only agree with parameters measured by Barstow et al. (2014). Both the MWDD and SDSS spectra of this object show unusually weak Hβ, while we could reproduce the remaining Balmer lines accurately. This might explain the large disparity between FUV and optical analyses, which tend to find higher $T_{\rm eff}$ and log g. We measured sub-solar abundances for all elements, among which C, N, O, Fe, and Ni were given as upper limits. Our results partially agree with abundances derived by Barstow et al. (2003b, 2014), who derived C, O, Si, Fe, and Ni; and C, Si, P, and S, respectively. From their first study, O and Si, and their second study, Si, P, and S abundances are comparable to ours.

WD 1738+669 is one of the hottest DA WDs in our sample ($T_{\rm eff}$ = 78 ± 6 kK and log g = 7.6 ± 0.4). Temperature and surface gravity derived by Lajoie & Bergeron (2007) and Gianninas et al. (2010) through Balmer-line fitting and by Barstow et al. (2003a) through Lyman-line fitting statistically agree with our results. Light-metal abundances were measured as sub-solar, whereas Fe and Ni show solar abundance. Only the Fe abundance is comparable to theoretical predictions. We find an agreement with light metal abundances determined by Barstow et al. (2003b), whereas their Fe and Ni abundances are significantly lower than ours.

WD 1827+778 This object shows a high metal content compared to the rest of the DAs in our sample. All light metals were measured close to solar value except O and Si, whereas Fe and Ni are slightly over solar. However, these results might be deemed questionable due to the poor quality of the FUSE spectra, which also complicated the ionization balance assessment. Therefore, a wider error margin had to be imposed on temperature ($T_{\rm eff}$ = 78 ± 10 kK). Uncertainty on the surface gravity is also large due to the line core of Hβ being weaker in our model (log g = 7.4 ± 0.4).

WD 2046+396 We estimate $T_{\rm eff}$ = 64 ± 5 kK and log g = 7.8 ± 0.3 for this DA WD. The uncertainty in log g arises from poor fits to Hα and Hβ that indicate a lower log g. However, this contradicts what was inferred from Lyman and higher-order Balmer lines. In general, these results are in agreement with previous works (Finley et al. 1997; Lajoie & Bergeron 2007; Gianninas et al. 2011; Lépine et al. 2011). Additionally, all element abundances were measured as sub-solar, and only the Fe abundance was comparable to diffusion theory.

WD 2146−433 Due to good quality FUSE spectra, we were able to use multiple ionization balances. Hence, we could impose a tight constraint on the temperature ($T_{\rm eff}$ = 66 ± 4 kK). Moreover, metal abundances for this object were measured as sub-solar, excluding P, Fe, and Ni, which are roughly solar. These abundances are in agreement with those derived by Barstow et al. (2014) except for Si. In addition, Fe and P abundances match with theoretical predictions by Chayer et al. (1995b) and Vennes et al. (1996), respectively. Generally, both Lyman and Balmer lines indicate a similar gravity (log g = 7.5 ± 0.3), though a slight mismatch between the observed and model spectrum of Hβ enforces a rather high error range for log g.

WD 2211−495 We utilized FUSE, HST, UVES, and MWDD spectra to determine the parameters of this object ($T_{\rm eff}$ = 68 ± 4 kK and log g = 7.4 ± 0.3). Thanks to the high S/N of the UV spectra, $T_{\rm eff}$ and metal abundances could be measured precisely. However, like WD 0621−376, the surface gravity inferred from Lyman and Balmer lines indicates different values. While log g = 7.10 reproduces Hα and Hβ in both MWDD and UVES spectra, log g = 7.40 perfectly fits Lyman lines and up to Hγ. Most of the previous analyses report $T_{\rm eff}$ and log g within our error limits. Except for P, Fe, and Ni, sub-solar metal abundances were measured. Our abundances are in agreement with those derived by Holberg et al. (1993), Barstow et al. (2003b), and Preval et al. (2019), where only mismatch occurs in N abundance for the former two analyses. On the other hand, excluding S, Barstow et al. (2014) reports much lower light metal content than ours. Our C and Fe abundances are comparable to theoretical predictions.

WD 2218+706 is the only DA WD in our sample that displays a weak He II λ 1640 Å feature. We derived N(He)/N(H) = 1.3 × 10^{-4}, which is the highest among DAs in our sample and clearly lower than the estimated He abundance limit (Fig. A.3). We estimate $T_{\rm eff}$ = 78 ± 5 kK and log g = 7.4 ± 0.3, which statistically agrees only with values derived by Gianninas et al. (2010). Moreover, we derived light metal abundances as sub-solar, while Fe and Ni are slightly over solar. Interestingly, WD 2218+706 is the only DA WD in our sample that shows element abundances close to the theoretical predictions, where C, N, O, and Fe abundances agree very well, and S and P slightly lie outside of our error limits.

WD 2350−706 HD 223816 is a wide binary system consisting of an F5IV star and a DA WD (Barstow et al. 1994), which has been resolved in HST imaging (Barstow et al. 2001b). We determined $T_{\rm eff}$ = 75 ± 5 kK and log g = 7.9 ± 0.3 for the WD of the system. Since we did not have optical spectra, the log g error could only be assessed by Lyman lines. Our $T_{\rm eff}$ and log g values agree with those determined by Barstow et al. (2014) and Joyce et al. (2018). On the other hand, only Si and S abundances derived by Barstow et al. (2014) reside in our error range. We find C, P, and Fe abundances similar to theoretical predictions.

WD 2353+026 This DA WD has poor quality FUSE spectra. Considering the low metal content, distinguishing spectral lines from noise was not possible. Therefore, all abundances are given as upper limits. We derived $T_{\rm eff}$ = 61 ± 5 kK and log g = 7.5 ± 0.3 which agrees with the previous studies.

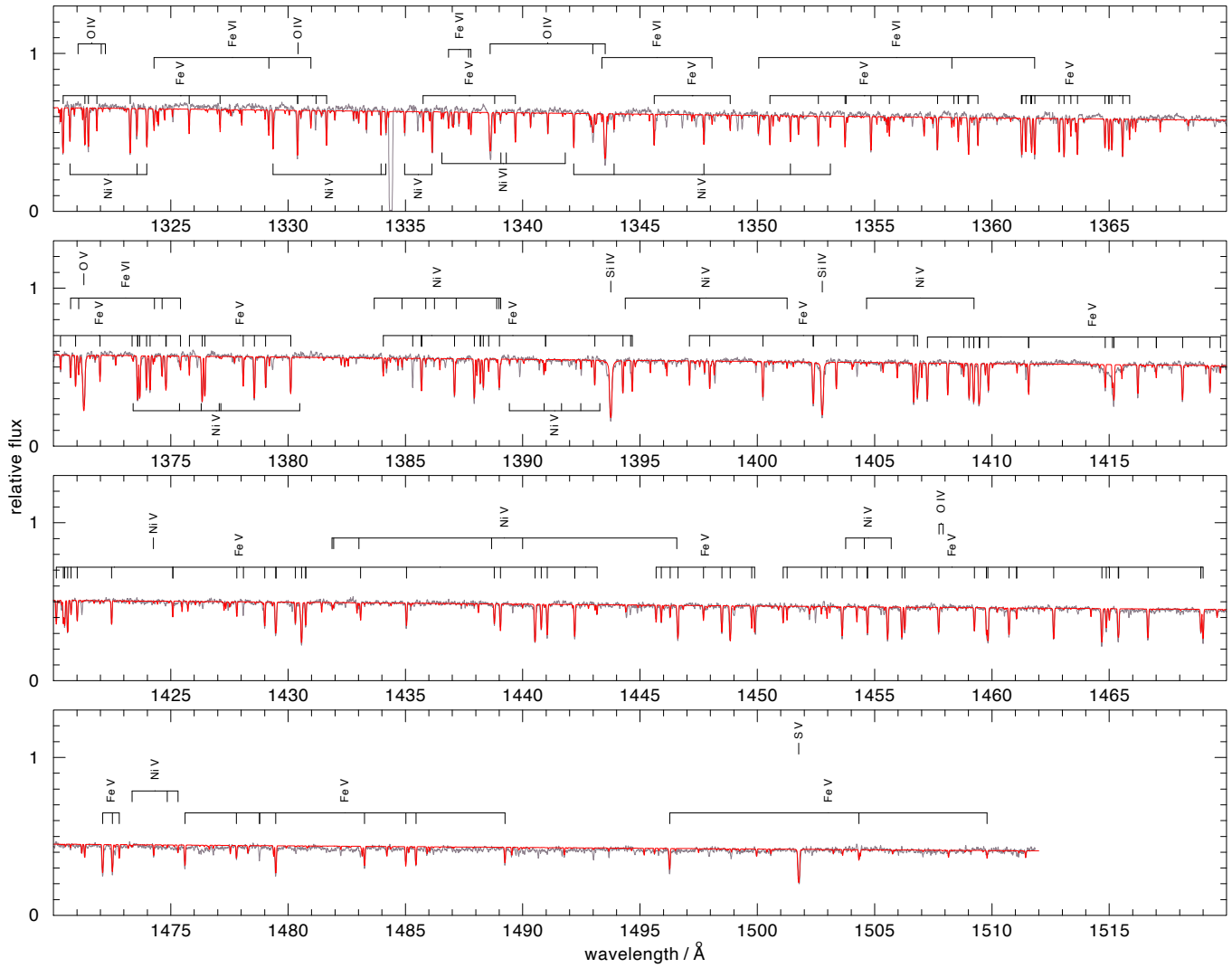


Fig. A.2: HST spectrum of the DA WD 2211−495 (red: model with $T_{\rm eff}$ = 68 kK, log g = 7.4).

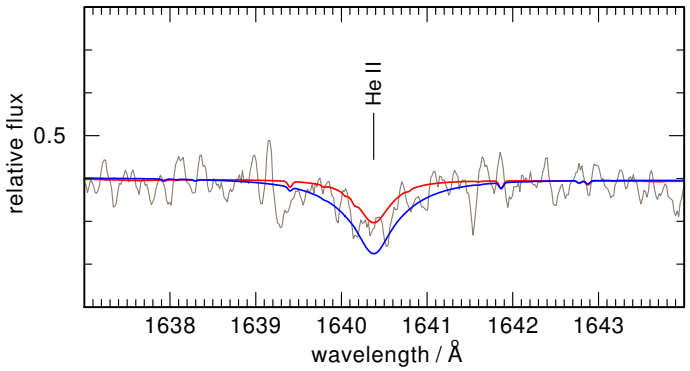


Fig. A.3: Section of the STIS spectrum (gray) of the DA WD 2218+706 compared to models ($T_{\rm eff}$ = 78 kK, log g = 7.4) with measured He abundance (red; N(He)/N(H) = 1.3 × 10^{-4}) and theoretical He limit (blue; N(He)/N(H) = 10^{-3}).

Appendix B: Tables

Table B.1: Our WD sample and observations used in the spectral analysis.

WD Name[a]	Other Name	Program ID (FUSE)	Proposal ID (HST)	Optical[b]
		DAO		
	Longmore 1	P133	–	UVES
0439+466	LS V +46 21	M107	8638	G10
0500−156	Abell 7	B052	–	G10
0615+556	PuWe 1	B052	–	G10
0823+316	Ton 320	B053	–	G10
0834+500	PG 0834+501	B053	–	G10
0851+090	Abell 31	B052	–	UVES
1111+552	NGC 3587	B052	–	-
1214+267	LB 2	B053	–	G10
1253+378	HZ 34	B053	–	G10
1957+225	NGC 6853	M107	8638	G10
2226−210	NGC 7293	C177	8638	G10
2342+806	GD 561	B052	8329	G10
		DA		
0027−636	RE J0029−632	Z903	–	G11
0229−481	LB 1628	M105	–	G11
0232+035	Feige 24	P104	7755	G11
0311+480	KPD 0311+4801	Z904	–	G10
0343−007	KUV03439−0048	E568	–	G11
0455−282	RE J0457−280	P104	14791	G10
0615+655	HS 0615+6535	E568	8636	G10
0621−376	RE J0623−374	P104	14791	G10, UVES
0939+262	Ton 21	–	8179	G11
1056+516	LB 1919	D003	–	G11, SDSS
1342+443	PG 1342+444	A034	–	G11, SDSS
1738+669	RE J1738+665	M105	8179	G10
1827+778	HS 1827+7753	E568	–	G11, SDSS
2046+396	KPD 2046+3940	E568	–	G11
2146−433	MCT2146−4320	Z903	–	G10
2211−495	RE J2214−491	M103	14791	G10, UVES
2218+706	DeHt 5	A034	8179	G10
2350−706	HD 223816	B120, A054	–	–
2353+026	PG 2353+027	E568	–	G11

Notes. [a] WD names from McCook & Sion (1999). [b] G10 and G11 refer to MWDD spectra used in Gianninas et al. (2010, 2011), respectively.

Table B.2: $T_{\rm eff}$, log g, and abundances (mass fractions) of DAO and DA WDs.

(WD) Name	$T_{\rm eff}$ [kK]	log g [cm/s^2]	H	He	C	N	O	Si	P	S	Fe	Ni
						DAO						
Longmore 1	118 ± 5	7.0 ± 0.3	6.93×10^{-1}	2.45×10^{-1}	1.74×10^{-2}	8.69×10^{-3}	3.29×10^{-2}	1.63×10^{-4}	5.81×10^{-6}	3.08×10^{-4}	2.40×10^{-3}	$\triangledown 6.78 \times 10^{-5}$
0439+466	97 ± 5	7.0 ± 0.2	9.57×10^{-1}	3.16×10^{-2}	1.15×10^{-3}	8.18×10^{-4}	2.69×10^{-3}	2.71×10^{-4}	3.79×10^{-6}	7.54×10^{-5}	6.20×10^{-3}	2.98×10^{-4}
0500−156	104 ± 6	7.2 ± 0.2	8.61×10^{-1}	1.25×10^{-1}	2.67×10^{-3}	2.95×10^{-4}	8.37×10^{-3}	1.65×10^{-4}	1.82×10^{-6}	3.90×10^{-5}	2.61×10^{-3}	1.48×10^{-4}
0615+556	101 ± 5	7.2 ± 0.2	9.35×10^{-1}	5.56×10^{-2}	$\triangledown 2.68 \times 10^{-3}$	2.95×10^{-4}	3.39×10^{-3}	1.42×10^{-4}	1.39×10^{-5}	1.19×10^{-4}	2.52×10^{-3}	2.49×10^{-4}
0823+316	98 ± 5	7.1 ± 0.2	9.75×10^{-1}	1.52×10^{-2}	2.77×10^{-3}	1.09×10^{-3}	2.55×10^{-3}	2.63×10^{-4}	5.81×10^{-6}	4.88×10^{-5}	2.70×10^{-3}	1.28×10^{-4}
0834+500	90 ± 3	7.0 ± 0.2	9.73×10^{-1}	1.82×10^{-2}	4.72×10^{-4}	1.84×10^{-3}	1.75×10^{-3}	1.22×10^{-4}	6.30×10^{-6}	7.44×10^{-5}	4.30×10^{-3}	3.47×10^{-4}
0851+090	106 ± 5	7.2 ± 0.2	8.60×10^{-1}	1.25×10^{-1}	2.87×10^{-3}	4.95×10^{-4}	8.37×10^{-3}	1.65×10^{-4}	5.82×10^{-6}	5.90×10^{-5}	2.51×10^{-3}	2.08×10^{-4}
1111+552	110 ± 5	7.1 ± 0.3	7.82×10^{-1}	2.07×10^{-1}	3.66×10^{-3}	4.25×10^{-4}	5.24×10^{-3}	1.22×10^{-4}	3.81×10^{-6}	4.87×10^{-5}	1.30×10^{-3}	1.30×10^{-4}
1214+267	91 ± 3	7.1 ± 0.3	9.69×10^{-1}	2.42×10^{-2}	6.73×10^{-4}	6.94×10^{-4}	1.75×10^{-3}	2.42×10^{-4}	6.20×10^{-6}	2.87×10^{-5}	1.93×10^{-3}	1.18×10^{-4}
1253+378	93 ± 4	7.0 ± 0.2	9.50×10^{-1}	4.07×10^{-2}	1.10×10^{-3}	7.22×10^{-5}	3.50×10^{-3}	5.00×10^{-5}	3.78×10^{-6}	3.72×10^{-5}	3.39×10^{-3}	1.18×10^{-4}
1957+225	134 ± 10	6.9 ± 0.4	7.39×10^{-1}	2.50×10^{-1}	2.36×10^{-3}	6.98×10^{-4}	5.77×10^{-3}	2.05×10^{-4}	5.55×10^{-6}	1.61×10^{-4}	1.21×10^{-3}	$\triangledown 6.80 \times 10^{-5}$
2226−210	120 ± 5	7.2 ± 0.3	8.80×10^{-1}	1.05×10^{-1}	2.36×10^{-3}	6.94×10^{-4}	1.93×10^{-3}	$\triangledown 2.03 \times 10^{-4}$	5.81×10^{-6}	1.08×10^{-4}	9.40×10^{-3}	$\triangledown 3.08 \times 10^{-4}$
2342+806	83 ± 5	7.2 ± 0.2	9.74×10^{-1}	1.63×10^{-2}	1.57×10^{-3}	1.94×10^{-4}	1.96×10^{-3}	2.43×10^{-4}	5.81×10^{-6}	1.09×10^{-4}	5.22×10^{-3}	3.88×10^{-4}
						DA						
0027−636	59 ± 5	8.0 ± 0.2	9.99×10^{-1}	$\triangledown 3.98 \times 10^{-5}$	$\triangledown 1.05 \times 10^{-6}$	$\triangledown 5.04 \times 10^{-7}$	$\triangledown 9.04 \times 10^{-6}$	3.32×10^{-7}	3.20×10^{-8}	$\triangledown 4.30 \times 10^{-7}$	$\triangledown 3.98 \times 10^{-4}$	$\triangledown 3.49 \times 10^{-5}$
0229−481	62 ± 5	7.8 ± 0.2	9.99×10^{-1}	$\triangledown 1.98 \times 10^{-5}$	$\triangledown 1.14 \times 10^{-6}$	$\triangledown 1.08 \times 10^{-7}$	$\triangledown 8.80 \times 10^{-7}$	9.22×10^{-6}	2.30×10^{-6}	4.98×10^{-6}	$\triangledown 4.51 \times 10^{-4}$	$\triangledown 3.49 \times 10^{-5}$
0232+035	63 ± 3	7.5 ± 0.2	9.99×10^{-1}	$\triangledown 5.98 \times 10^{-5}$	1.45×10^{-6}	1.61×10^{-6}	1.04×10^{-5}	2.16×10^{-5}	3.14×10^{-6}	8.80×10^{-6}	6.20×10^{-4}	4.81×10^{-5}
0311+480	70 ± 10	7.3 ± 0.4	9.98×10^{-1}	$\triangledown 1.98 \times 10^{-5}$	5.55×10^{-5}	$\triangledown 2.14 \times 10^{-4}$	$\triangledown 1.11 \times 10^{-5}$	5.22×10^{-6}	$\triangledown 1.50 \times 10^{-6}$	$\triangledown 1.58 \times 10^{-5}$	1.80×10^{-3}	$\triangledown 1.38 \times 10^{-4}$
0343−007	63 ± 4	7.7 ± 0.2	9.99×10^{-1}	$\triangledown 1.98 \times 10^{-5}$	$\triangledown 1.85 \times 10^{-6}$	$\triangledown 2.08 \times 10^{-6}$	$\triangledown 8.10 \times 10^{-6}$	1.22×10^{-5}	$\triangledown 3.50 \times 10^{-6}$	5.78×10^{-6}	$\triangledown 6.91 \times 10^{-4}$	$\triangledown 4.48 \times 10^{-5}$
0455−282	66 ± 3	7.5 ± 0.2	9.99×10^{-1}	$\triangledown 3.98 \times 10^{-5}$	$\triangledown 1.45 \times 10^{-6}$	$\triangledown 1.61 \times 10^{-6}$	5.69×10^{-6}	2.16×10^{-5}	3.14×10^{-6}	8.80×10^{-6}	5.20×10^{-4}	3.20×10^{-5}
0615+655	83 ± 10	7.6 ± 0.4	9.97×10^{-1}	$\triangledown 3.98 \times 10^{-5}$	1.45×10^{-5}	7.84×10^{-6}	3.61×10^{-5}	6.42×10^{-5}	$\triangledown 5.20 \times 10^{-6}$	7.98×10^{-5}	2.51×10^{-3}	1.35×10^{-4}
0621−376	65 ± 3	7.5 ± 0.4	9.98×10^{-1}	$\triangledown 1.98 \times 10^{-5}$	1.06×10^{-5}	1.08×10^{-5}	3.22×10^{-5}	5.22×10^{-5}	4.20×10^{-6}	1.30×10^{-5}	1.72×10^{-3}	1.36×10^{-4}
0939+262	66 ± 3	7.7 ± 0.2	9.99×10^{-1}	$\triangledown 3.98 \times 10^{-5}$	1.45×10^{-6}	1.61×10^{-6}	3.69×10^{-6}	$\triangledown 2.16 \times 10^{-5}$		8.80×10^{-6}	5.20×10^{-4}	3.40×10^{-5}
1056+516	63 ± 5	7.9 ± 0.2	9.99×10^{-1}	$\triangledown 1.98 \times 10^{-5}$	$\triangledown 1.15 \times 10^{-6}$	$\triangledown 5.84 \times 10^{-7}$	$\triangledown 3.10 \times 10^{-6}$	$\triangledown 1.11 \times 10^{-7}$	$\triangledown 8.49 \times 10^{-9}$	$\triangledown 7.77 \times 10^{-7}$	$\triangledown 2.54 \times 10^{-4}$	$\triangledown 2.89 \times 10^{-5}$
1342+443	62 ± 5	7.7 ± 0.3	9.99×10^{-1}	$\triangledown 1.98 \times 10^{-5}$	$\triangledown 6.48 \times 10^{-6}$	$\triangledown 2.08 \times 10^{-6}$	$\triangledown 5.10 \times 10^{-5}$	6.22×10^{-6}	3.50×10^{-6}	1.28×10^{-5}	$\triangledown 5.04 \times 10^{-4}$	$\triangledown 3.88 \times 10^{-5}$
1738+669	78 ± 6	7.6 ± 0.4	9.99×10^{-1}	$\triangledown 9.18 \times 10^{-5}$	$\triangledown 2.08 \times 10^{-6}$	$\triangledown 2.04 \times 10^{-6}$	4.25×10^{-6}	1.84×10^{-5}	1.40×10^{-6}	1.78×10^{-5}	1.10×10^{-3}	6.09×10^{-5}
1827+778	78 ± 10	7.4 ± 0.4	9.98×10^{-1}	$\triangledown 1.98 \times 10^{-5}$	$\triangledown 1.59 \times 10^{-4}$	$\triangledown 1.74 \times 10^{-4}$	$\triangledown 4.04 \times 10^{-6}$	3.62×10^{-5}	6.00×10^{-6}	$\triangledown 1.16 \times 10^{-4}$	$\triangledown 1.69 \times 10^{-3}$	$\triangledown 1.03 \times 10^{-4}$
2046+396	64 ± 5	7.8 ± 0.3	9.99×10^{-1}	$\triangledown 1.98 \times 10^{-5}$	$\triangledown 1.15 \times 10^{-6}$	$\triangledown 4.84 \times 10^{-7}$	$\triangledown 5.23 \times 10^{-7}$	7.21×10^{-6}	2.50×10^{-6}	5.17×10^{-6}	5.04×10^{-4}	$\triangledown 4.64 \times 10^{-5}$
2146−433	66 ± 4	7.5 ± 0.3	9.99×10^{-1}	$\triangledown 1.98 \times 10^{-5}$	6.15×10^{-6}	4.08×10^{-6}	$\triangledown 4.23 \times 10^{-7}$	4.72×10^{-5}	7.50×10^{-6}	5.77×10^{-6}	1.23×10^{-3}	6.49×10^{-5}
2211−495	68 ± 4	7.4 ± 0.3	9.98×10^{-1}	$\triangledown 1.98 \times 10^{-5}$	1.35×10^{-5}	1.08×10^{-5}	2.63×10^{-5}	5.62×10^{-5}	7.49×10^{-6}	3.08×10^{-5}	1.61×10^{-3}	1.27×10^{-4}
2218+706	78 ± 5	7.4 ± 0.3	9.96×10^{-1}	5.10×10^{-4}	9.45×10^{-5}	1.12×10^{-4}	1.26×10^{-4}	6.42×10^{-5}	5.20×10^{-6}	4.58×10^{-5}	2.81×10^{-3}	2.15×10^{-4}
2350−706	75 ± 5	7.9 ± 0.3	9.99×10^{-1}	$\triangledown 1.98 \times 10^{-5}$	8.15×10^{-6}	1.08×10^{-6}	$\triangledown 3.32 \times 10^{-7}$	5.62×10^{-5}	9.95×10^{-6}	1.88×10^{-5}	6.04×10^{-4}	$\triangledown 4.58 \times 10^{-5}$
2353+026	61 ± 5	7.5 ± 0.3	9.99×10^{-1}	$\triangledown 1.98 \times 10^{-5}$	$\triangledown 7.59 \times 10^{-6}$	$\triangledown 1.08 \times 10^{-6}$	$\triangledown 7.38 \times 10^{-7}$	$\triangledown 1.97 \times 10^{-7}$	$\triangledown 2.11 \times 10^{-8}$	$\triangledown 3.08 \times 10^{-6}$	$\triangledown 4.99 \times 10^{-4}$	$\triangledown 2.48 \times 10^{-5}$

Notes. Upper limits are marked with triangles. Error limits for abundances do not exceed ± 0.5 dex.

Table B.3: Previous analyses whose results are compared to the DAO WDs in our sample.

Name	Optical	UV	Optical + UV	Abundances
		DAO		
Longmore 1	(1)	(2), (3)	–	(2), (3)
WD 0439+466	(4), (5), (6)	(7)	(8)	(7), (8)
WD 0500−156	(5), (6), (9), (10), (11), (12)	(3), (12)	–	(3), (13)
WD 0615+556	(5), (6), (11), (12)	(3), (12)	–	(3), (13)
WD 0823+316	(4), (6), (12), (14), (15), (16)	(12)	–	(13)
WD 0834+500	(4), (6), (12)	(12)	–	(13)
WD 0851+090	(5), (12)	(3), (12)	–	(3), (13)
WD 1111+552	(5), (11)	(3)	–	(3)
WD 1214+267	(4), (6), (12), (17)	(12)	–	(13)
WD 1253+378	(4), (5), (6), (10), (12), (18)	(12)	–	(13)
WD 1957+225	(5), (6)	(7)	(3)	(3), (7)
WD 2226−210	(1), (5), (6), (11), (19)	(7)	(3)	(3), (7)
WD 2342+806	(4), (5), (6), (12)	(3), (12)	–	(3), (13)

References. (1)Mendez et al. (1985), (2)Herald & Bianchi (2004), (3)Ziegler (2012), (4)Bergeron et al. (1994), (5)Napiwotzki (1999), (6)Gianninas et al. (2010), (7)Traulsen et al. (2005), (8)Rauch et al. (2007), (9)Mendez et al. (1981), (10)Wesemael et al. (1985), (11)McCarthy et al. (1997), (12)Good et al. (2004), (13)Good et al. (2005b), (14)Tremblay et al. (2011), (15)Kepler et al. (2019), (16)Bédard et al. (2020), (17)Guo et al. (2015), (18)Lei et al. (2023), (19)Mendez et al. (1988).

Notes. The second and third columns list studies that only utilized optical and UV data, respectively, or the analyses derived separate parameters for both wavebands, whereas the fourth column displays the ones that reached a common $T_{\rm eff}$ and log g from both wavelength ranges. The fifth column lists works that performed abundance analyses.

Table B.4: Like Table B.3, but for DAs and including EUV analyses as well.

Name	Optical	UV	EUV	Optical + UV	Abundances
WD 0027−636	(1), (2), (3), (4), (5), (6), (7), (8)	(5), (9)	(10)	–	–
WD 0229−481	(1), (2), (6), (7), (11), (12), (13)	(9), (13)	–	–	(9)
WD 0232+035	(1), (2), (3), (7), (13), (14), (15)	(5), (9), (13), (16), (17), (18), (19)	(10), (20)	–	(9), (14), (17), (18)
WD 0311+480	(22)	–	–	–	–
WD 0343−007	(1), (6), (7), (11), (13), (23)	(13)	–	–	–
WD 0455−282	(1), (2), (3), (5), (6), (8), (12), (13), (14), (22), (24), (25)	(5), (9), (21), (24), (26), (27)	(10)	(24)	(9), (14), (26), (27)
WD 0615+655	(13), (22), (28),	(13)	–	–	–
WD 0621−376	(1), (2), (3), (5), (6), (13), (14), (22), (25)	(5), (9), (13), (21), (27)	(10)	(29)	(9), (14), (27), (29)
WD 0939+262	(1), (7), (13), (14), (30), (31)	(13)	–	–	(14)
WD 1056+516	(3), (7), (13), (32), (33), (34), (35)	(13), (36)	(10) (36)	–	(36)
WD 1342+443	(7), (14), (30), (31), (33), (34), (35)	(9), (14)	–	(37)	(9), (14), (37)
WD 1738+669	(1), (2), (13), (14), (22)	(13), (21)	–	–	(14)
WD 1827+778	(7), (28), (33), (34), (35)	–	–	–	–
WD 2046+396	(1), (7), (13), (38)	(13)	–	–	–
WD 2146−433	(1), (4), (6), (8), (13), (22)	(9), (13)	–	–	(9)
WD 2211−495	(1), (2), (3), (5), (6), (12), (14), (22), (25)	(5), (9), (21), (27)	(10)	(29)	(9), (14), (27), (29)
WD 2218+706	(14), (22), (39), (40)	(40)	–	(41)	(14), (42)
WD 2350−706	–	(9), (14)	–	–	(9)
WD 2353+026	(1), (4), (6), (7), (13), (28), (31)	(13)	–	–	–

References. (1)Finley et al. (1997), (2)Marsh et al. (1997), (3)Vennes et al. (1997), (4)Koester et al. (2005), (5)Vennes et al. (2005), (6)Koester et al. (2009), (7)Gianninas et al. (2011), (8)Bergeron et al. (2021), (9)Barstow et al. (2014), (10)Schuh et al. (2002), (11)Bragaglia et al. (1995), (12)Koester et al. (2001), (13)Lajoie & Bergeron (2007), (14)Barstow et al. (2003b), (15)Bédard et al. (2017), (16)Holberg et al. (1986), (17)Vennes et al. (1992), (18)Vennes et al. (2000), (19)Joyce et al. (2018), (20)Vennes et al. (1989), (21)Barstow et al. (2003a), (22)Gianninas et al. (2010), (23)Limoges & Bergeron (2010), (24)Barstow et al. (1998), (25)Kawka et al. (2007), (26)Vennes et al. (1996), (27)Preval et al. (2019), (28)Homeier et al. (1998), (29)Holberg et al. (1993), (30)Bergeron et al. (1994), (31)Liebert et al. (2005), (32)Tremblay et al. (2011), (33)Kepler et al. (2019), (34)Tremblay et al. (2019), (35)Bédard et al. (2020), (36)Adamczak et al. (2012), (37)Barstow et al. (2002), (38)Lépine et al. (2011), (39)Napiwotzki (1999), (40)Good et al. (2004), (41)Barstow et al. (2001a), (42)Good et al. (2005b)

Paper II

Semih Filiz, Nicole Reindl, David Jones, Paulina Sowicka, Matti Dorsch, Thomas Rauch, and Klaus Werner

"Spectral evolution of hot hybrid white dwarfs II. Photometry"

Astronomy & Astrophysics, 2026, 706, A152

© 2026 Reproduced with permission from Astronomy & Astrophysics. All rights reserved. The original publication is available at: https://doi.org/10.1051/0004-6361/202557071

A&A, 706, A152 (2026)
https://doi.org/10.1051/0004-6361/202557071
© The Authors 2026

Astronomy & Astrophysics

Spectral evolution of hot hybrid white dwarfs

II. Photometry

Semih Filiz[1,2,⋆], Nicole Reindl[1], David Jones[3,4], Paulina Sowicka[3,4], Matti Dorsch[5], Thomas Rauch[2], and Klaus Werner[2]

[1] Landesternwarte Heidelberg, Zentrum für Astronomie, Ruprecht-Karls-Universität, Königstuhl 12, 69117 Heidelberg, Germany
[2] Institut für Astronomie und Astrophysik, Kepler Center for Astro and Particle Physics, Eberhard Karls Universität, Sand 1, 72076 Tübingen, Germany
[3] Instituto de Astrofisica de Canarias, 38205 La Laguna, Tenerife, Spain
[4] Departamento de Astrofisica, Universidad de La Laguna, 38206 La Laguna, Tenerife, Spain
[5] Institut für Physik und Astronomie, Universität Potsdam, Haus 28, Karl-Liebknecht-Str. 24/25, 14476 Potsdam, Germany

Received 2 September 2025 / Accepted 29 October 2025

ABSTRACT

We present a photometric analysis of 19 DA and 13 DAO white dwarfs (WDs) with effective temperatures exceeding 60 000 K, building on the spectral analysis reported in the first paper of this two-part study. By examining archival light curves for periodic signals, we identify that four of the 32 objects (13^{+8}_{-4}%) exhibit photometric variability. Spectral energy distribution (SED) fitting allowed us to derive radii, luminosities, and gravity masses, as well as to characterise the infrared excesses observed in six sources. A notable discovery is the identification of a 1.87 d period in the ZTF light curves of WD 1342+443 and weak emission lines in the optical spectra of this star, which strongly indicate an irradiation effect system. Our SED fit indicates the presence of cool dust, which must be located farther from the star, and that any companion with a spectral type earlier than L2.0 would appear in the SED. This leads us to speculate that WD 1342+443 might have an irradiated, sub-stellar companion. We also highlight that we uncovered, for the first time, a 4.23 d photometric period in the well-known, close DA+dM binary WD 0232+035, based on TESS data. We find that the phase and amplitude of the light curve variations are consistent with expectations from an irradiation effect. Intriguingly, we detected an additional, mysterious period at 1.39 days, which is approximately one-third of the orbital period. Moreover, we revisited the longstanding discrepancy between Kiel and gravity masses for the hottest WDs. To address this, we explored fully metal line blanketed model atmospheres as a potential solution, contrasting them with the results from pure-hydrogen and hydrogen-helium models. Our results show that including metal opacities does not resolve the discrepancy – in fact, it slightly deteriorates the agreement. Finally, we reaffirm the previously observed correlation between helium abundance and luminosity.

Key words. binaries: general – stars: variables: general – white dwarfs

1. Introduction

Large photometric surveys and missions are generally devised for specific research interests in astronomy, such as exploring transient phenomena (Law et al. 2009), monitoring asteroids and comets (Tonry et al. 2018), discovering exoplanets (Ricker et al. 2015), or investigating stellar populations in our Galaxy (Alonso-García et al. 2018). However, the obtained data are useful for purposes other than their intended science objectives, from which white dwarf (WD) studies also benefit substantially. For instance, photometry of a large sample of WDs can be used as a benchmark to validate theories of their internal physical processes (Bédard et al. 2024).

On the one hand, time-series observations uncover important aspects of stars, e.g., stellar activity and multiplicity, pulsations, magnetic fields, and rotation. Excluding GW Vir pulsators with inherently hydrogen-deficient atmospheres (Werner & Herwig 2006), close binarity is perhaps the first suspected mechanism that leads to photometric variability in hot WDs (Steen et al. 2024; Oliveira da Rosa et al. 2024). In particular, so-called irradiation effect systems, in which the phase-varying projection of the cooler companion leads to periodic variations in brightness, are well documented (Brinkworth et al. 2006; Aungwerojwit et al. 2007; Parsons et al. 2010). In these systems, the rotational period of the cool companion is expected to be synchronised to the orbital period (Nebot Gómez-Morán et al. 2011). In recent years, the first indications of bright spots on hot WDs have been reported (Reindl et al. 2019, 2021, 2023). The partly unusual light curve shapes of these objects are thought to be caused by bright spots on the surfaces of these stars, which in turn are believed to form through interactions of metals with weak magnetic fields (Hermes et al. 2017b). Furthermore, it is speculated that the onset of diffusion could be an additional decisive factor in the development of spots on hot WDs (Reindl et al. 2023).

On the other hand, photometry acquired in multiple bands enables us to construct spectral energy distributions (SEDs). By fitting synthetic spectra to the observed photometry, we can derive the angular diameter of the source. This, in combination with high-precision parallaxes provided by the *Gaia* space mission (Gaia Collaboration 2016, 2018, 2023), yields stellar radii and, in combination with previously derived surface

⋆ Corresponding author: sfiliz@lsw.uni-heidelberg.de

Open Access article, published by EDP Sciences, under the terms of the Creative Commons Attribution License (https://creativecommons.org/licenses/by/4.0), which permits unrestricted use, distribution, and reproduction in any medium, provided the original work is properly cited.
This article is published in open access under the Subscribe to Open model. Subscribe to A&A to support open access publication.

gravities (log g), also masses independently of theoretical evolutionary calculations. This method is widely used to derive fundamental parameters for large samples of both H-rich and H-deficient WDs (Bergeron et al. 2019; Genest-Beaulieu & Bergeron 2019; Tremblay et al. 2019). It has been used to construct a (semi)empirical initial–final mass relation (Barnett et al. 2021; Cunningham et al. 2024) and to test theoretical predictions of the mass–radius relationship (Bédard et al. 2017; Tremblay et al. 2017; Raddi et al. 2025). By fitting the SED, it is also possible to determine the effective temperature ($T_{\rm eff}$), which remains a free parameter in the fitting procedure along with the angular diameter (Gentile Fusillo et al. 2019, 2021). However, a larger discrepancy in the atmospheric parameters of hot WDs can be identified between photometry and spectroscopy (Bergeron et al. 2019; Tremblay et al. 2019). Hot WD masses derived from a combination of photometry and spectroscopy also show disagreement with those inferred from evolutionary tracks (Löbling et al. 2020; Reindl et al. 2023).

Besides offering a method to derive stellar radii and masses independently of evolutionary models, SED fitting also allows us to search for an infrared (IR) excess. Such an excess can indicate the presence of a cooler (sub-)stellar companion, or hot and cold dust discs (Chu et al. 2011; De Marco et al. 2013; Reindl et al. 2024).

In this paper, we finalise the study reported in Filiz et al. (2024, hereafter Paper I), which focuses on the spectral evolution of hot DA and DAO (hybrid) WDs via ultraviolet (UV) and optical spectroscopy. Here, we present a photometric analysis of our sample of WDs that was introduced in Paper I. In Sect. 2, we introduce the time-series observations and the analysis method. In Sect. 3, we explain our SED fitting process. We discuss the implications of our results in Sect. 4 and conclude with a brief summary in Sect. 5.

2. Light curves

2.1. Datasets

We collected archival light curves from several surveys, as listed below. All 32 targets from Paper I have at least one archival light curve.

TESS. The Transiting Exoplanet Survey Satellite (TESS) missions comprised individual sectors that were scanned for two orbits (≈27.4 d). The satellite is equipped with a red-optical bandpass covering the range 6000–10 000 Å. The Science Processing Operations Center (SPOC) pipeline (Jenkins et al. 2016) provides pre-processed light curves, which we acquired from the Mikulski Archive for Space Telescopes (MAST)[1] along with their corresponding target pixel files (TPFs). We used 2 min and 20 s cadence light curves and the pre-search data conditioning simple aperture photometry (PDCSAP) fluxes from which long-term trends have been removed. Two-minute cadence observations are available for all objects, whereas only 21 of them have 20 s cadence data.

ZTF. The Zwicky Transient Facility (ZTF; Bellm et al. 2019; Masci et al. 2019) survey is conducted with the Palomar 48-inch telescope at the Palomar Observatory, which scans the northern sky with a wide field of view (FOV; 47 deg^2) at 2 d cadence. We retrieved time-series data with an exposure time of 30 s in the g and r-band for 21 objects, while i-band observations are available for only ten objects. The data were obtained from the 22nd data release (DR22), spanning March 2018 to June 2024.

CSS. The Catalina Sky Survey (CSS; Drake et al. 2009) is designed to detect and track near-Earth objects, which employs three 1-m class telescopes located at the Steward Observatory of the University of Arizona. Spanning from 11.5 to 21.5 magnitudes, the second data release of the CSS contains V-band photometry of objects in the range of $-75° < \delta < 70°$ and $|b| > 15°$. Observations are separated into fields, with each field observed four times every 30 minutes. We found CSS light curves for 25 objects, but most observations do not have enough data points to detect variability.

ATLAS. The Asteroid Terrestrial-impact Last Alert System (ATLAS, Tonry et al. 2018) is operated with four automated 0.5 m telescopes (located in Hawaii, South Africa, and Chile) that contain 'cyan' (4200–6500 Å) and 'orange' (5600–8200 Å) bandpass filters. We found ATLAS light curves only for two of our objects.

Gaia multi-epoch photometry. The third data release of the *Gaia* mission (Gaia Collaboration 2023) contains multi-epoch broadband photometry in G, $G_{\rm BP}$, and $G_{\rm RP}$ bands, in which variable objects were detected using statistical and machine-learning methods (Eyer et al. 2023). Only one object[2] in our sample has *Gaia* multi-epoch photometry.

2.2. Analysis

Our light curve analysis method builds upon the procedure described in Reindl et al. (2021, 2023, 2024). We used VARTOOLS software (Hartman & Bakos 2016) and calculated a generalised Lomb-Scargle (LS) periodogram (Zechmeister & Kürster 2009; Press et al. 1992) to detect periodic sinusoidal signals. We relied on the false alarm probability (FAP) of the periodic signal to classify variability. If the periodic signal from a particular object showed log(FAP) ≤ −4, we classified that object as variable. In cases where the periodogram generated more than one significant period for an object, we removed the strongest periodic signal (including its harmonics and sub-harmonics) from the light curve and recalculated the periodogram. This procedure was repeated until no periodic signal could be found above the set variability threshold (log(FAP) ≤ −4). We measured peak-to-peak amplitudes by fitting a harmonic series to each light curve, defined as the difference between the maximum and minimum of the fit.

The first run of the LS periodogram on the 2 min cadence TESS data revealed periodic variability for 16 objects. Eight of these objects still showed variability even after the third whitening cycle. In addition, only seven of the variable candidates have a value of `crowdsap` ≥ 0.9, with the median value being 0.74; this parameter in the TPF header estimates the fraction of the collected light in the aperture that comes from the target. In fact, TESS has a large plate scale (21″/pixel), which makes crowding problems unavoidable. Therefore, validating the source of the periodic signal obtained from the light curve is essential.

We inspected the TPFs of the 16 candidate variables mentioned above in all sectors using `tpfplotter`[3] (Aller et al. 2020) to detect possible blending sources or nearby contaminants in the aperture. The TPF plots show the aperture mask used by the pipeline and all sources in the TPF file with a magnitude difference down to Δm = 6. For only nine objects were no blending sources detected in the aperture of all sectors, whereas in two cases at least one sector did not reveal any contamination in the aperture. However, the absence or scarcity

[1] https://archive.stsci.edu

[2] Periodicity search for WD 2353+026 resulted in non-detection.

[3] https://github.com/jlillo/tpfplotter

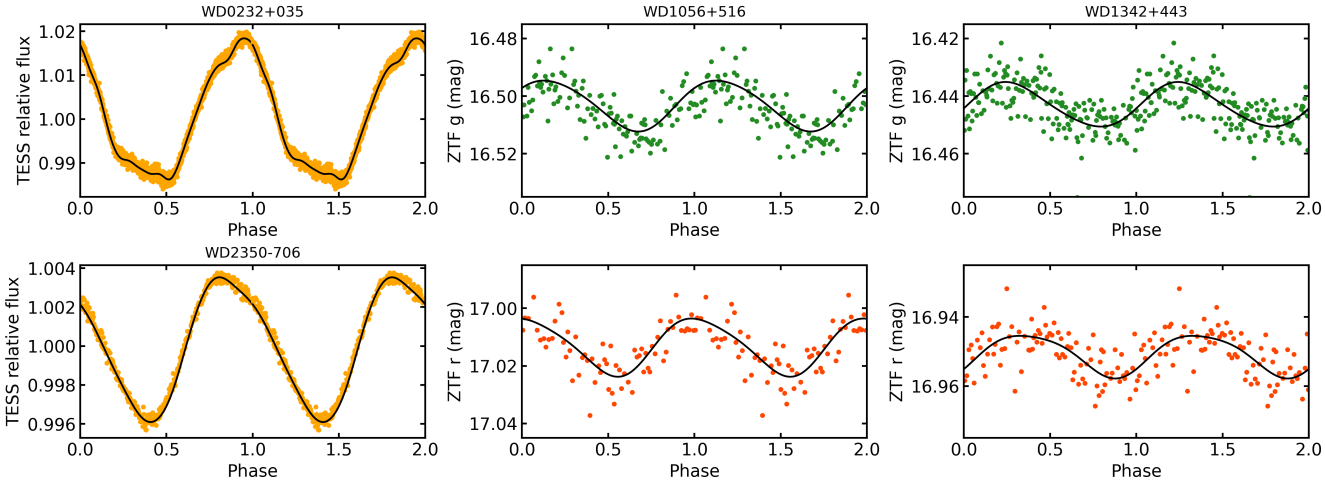


Fig. 1. Phase-averaged TESS (orange) and phase-averaged ZTF (green and red) light curves of the variable objects. Peak-to-peak amplitudes were measured by fitting a harmonic series, shown by the black lines.

of contamination does not directly imply that the target object is the source of the periodic signal (Aller et al. 2024). Therefore, we used `TESS_localize`[4] (Higgins & Bell 2023), which locates the source of variability on the sky for a given set of frequencies and TESS pixels, as well as the most likely *Gaia* sources within the selected TPF. For detection to be statistically significant, the `height` parameter should be less than 20% (equivalent of $5\,\sigma$, Higgins & Bell 2023). Consequently, only two objects (WD 0232+035 and WD 2350–706) were attributed to the detected signal. The same procedure was applied to the 20 s cadence data, but the periodogram reproduced the same periods as the 2 min light curves for only WD 0232+035 and WD 0311+480. However, in all sectors for both datasets, TESS_localize was unable to identify WD 0311+480 as the source of variability or statistically associate the detected signal with any other *Gaia* source.

We identified periodic signals for only two objects (WD 1056+516 and WD 1342+443) in the ZTF light curves. Both stars show the same periods in the *g*- and *r*-bands, but no variability is found in the *i*-band (229 and 463 data points, respectively). WD 1056+516 does not show variability in the TESS data. In contrast, we find variability in the TESS data for WD 1342+443 . However, the period detected in the TESS data does not match that found in the ZTF data and TESS_localize confirms that WD 1342+443 is not the source of the signal detected in the TESS data. Given that both objects are fainter than G = 16.6 mag and that TESS is designed for objects brighter than 15 mag, this result is not surprising. Fig. 1 shows phase folded light curves of the photometrically variable objects. An overview of the periods and amplitudes derived from the available datasets is shown in Table 1.

3. SED fits

We used the χ^2 fitting routine explained in Heber et al. (2018) and Irrgang et al. (2021) to determine the radius, R, luminosity, L, and gravity mass, $M_{\rm grav}$, of each sample object. In essence, the procedure converts the model spectra to filter-averaged magnitudes and compares them with the photometric data collected from several surveys and catalogues, including *Gaia* (Riello et al. 2021), the Galaxy Evolution Explorer (GALEX; Martin et al. 2005; Bianchi et al. 2017), the Panoramic Survey Telescope and Rapid Response System (Pan-STARRS; Flewelling et al. 2020), Two Micron All Sky Survey (2MASS; Skrutskie et al. 2006), Sloan Digital Sky Survey (SDSS; Alam et al. 2015), the Spitzer Space Telescope (Fazio et al. 2004; Rieke et al. 2004), the Wide-field Infrared Survey Explorer (WISE; Wright et al. 2010; Schlafly et al. 2019; Marocco et al. 2021), Skymapper (Onken et al. 2019), the UK Infra-Red Telescope (UKIRT) Hemisphere Survey (UHS; Dye et al. 2018) and the Visible and Infrared Survey Telescope Survey (VISTA; McMahon et al. 2013). While we fixed the atmospheric parameters (effective temperature, $T_{\rm eff}$, surface gravity, $\log g$, and He abundance) to the values determined in Paper I, the angular diameter, Θ, and the colour excess, $E(44–55)$, remained free parameters. We adopted the interstellar reddening law of Fitzpatrick et al. (2019) with an extinction coefficient of R_{55} = 3.02, which uses $E(44–55)$ measured with monochromatic filters at 4400 and 5500 Å, rather than the Johnson B and V filters used in $E(B–V)$. For high $T_{\rm eff}$, such as our sample objects, $E(44–55)$ is indistinguishable from $E(B–V)$.

We relied on *Gaia* parallaxes to calculate the stellar parameters, which were corrected for their zero-point offset according to Lindegren et al. (2021). Parallax uncertainties were corrected with the function suggested by El-Badry et al. (2021). The radii were then calculated as $R = \Theta/\ 2\varpi$, using Θ derived from the SED fitting and *Gaia* parallaxes (ϖ). Using the spectroscopic values ($T_{\rm eff}$ and $\log g$) from Paper I, we derived the luminosities as $L/L_{\odot} = (R/R_{\odot})^2 (T_{\rm eff}/T_{\rm eff,\odot})^4$ and gravity masses as $M_{\rm grav} = gR^2/G$, where G is the gravitational constant.

We followed two different procedures to calculate R and $M_{\rm grav}$ using SED fitting. First, we used the model flux of each object from Paper I, computed with the Tübingen Model-Atmosphere package (TMAP[5]; Werner & Dreizler 1999; Werner et al. 2003, 2012), since creating an extensive grid of fully metal line blanketed models is computationally expensive (see Paper I). Then, to test the effects of metals on the SED fits, we used the pure H and H+He model grids of Reindl et al. (2023) for the DA and DAO WDs, respectively. Table A.1 lists the radii, luminosities, gravity masses, and colour excesses derived using the former method. The differences between these results and those

[4] https://github.com/Higgins00/TESS-Localize

[5] http://astro.uni-tuebingen.de/~TMAP

Table 1. Names, spectral types, observed bands, false alarm probabilities, periods, and peak–to–peak amplitudes of the variable objects, as well as the temperatures, radii, and surface ratios of the IR-excess sources.

Name	Spectral Type	Band	log(FAP)	Period [d]	Amplitude [mag]	$T_{\rm eff\,1}$ [K]	R_1 [$R_\odot$]	Surface Ratio$_1$	$T_{\rm eff\,2}$ [K]	Surface Ratio$_2$
WD 0232+035	DA	TESS	–25834.57	4.231915	0.032	3710^{+70}_{-60}	$0.395^{+0.011}_{-0.011}$	–	–	–
			–3304.41	1.391210	0.007					
		ATLAS-*c*	–	–	0.029					
		ATLAS-*o*	–12.60	4.229050	0.046					
		CSS-V	–9.28	4.368181	0.160					
WD 0851+090	DAO	–	–	–	–	2920^{+210}_{-380}	$0.260^{+0.040}_{-0.040}$	–	–	–
WD 1056+516	DA	ZTF-*g*	–20.15	0.113279	0.018	–	–	–	–	–
		ZTF-*r*	–20.81	0.113279	0.020					
		ZTF-*i* [(a)]	–	–	0.020					
WD 1253+378	DAO	–	–	–	–	3220^{+120}_{-100}	$0.337^{+0.022}_{-0.020}$	–	–	–
WD 1342+443	DA	ZTF-*g*	–27.60	1.873020	0.015	346^{+17}_{-17}	-	$1.4^{+0.5}_{-0.5} \times 10^5$	–	–
		ZTF-*r*	–10.15	1.873207	0.012					
		ZTF-*i* [(a)]	–	–	0.010					
WD 2218+706	DA	–	–	–	–	560^{+190}_{-210}	–	$1.7^{+11.0}_{-1.1} \times 10^3$	80^{+16}_{-20}	$5^{+49}_{-4} \times 10^8$
WD 2350−706	DA	TESS	−5306.25	1.373420	0.008	6280^{+50}_{-40}	$1.210^{+0.070}_{-0.070}$	–	–	–

Notes. a. To measure ZTF *i*-band amplitudes of WD 1056+516 and WD 1342+443, we phased the light curves to a significant period found in the respective ZTF *g*-band. b. Radii of the IR-excess sources were calculated assuming the same distance as the WD. c. Surface ratios are given relative to the WD.

obtained using the metal-free models are discussed in further detail in Sect. 4.

We find that two DAO and four DA WDs in our sample exhibit an IR excess. For WD 1342+443 and WD 2218+706, we performed a multi-component fit using the model fluxes obtained in Paper I, together with one or two blackbody components. The other four objects that exhibit an IR excess are already known binaries. For these objects, instead of the blackbody components, we included PHOENIX models (Husser et al. 2013) spanning from 500 to 55 000 Å and temperatures 2300 K ≤ $T_{\rm eff}$ ≤ 15 000 K. Figure 2 depicts the SED fits for sample objects with IR excess. For comparison, the top row shows one DAO and one DA WD without IR excess. The $T_{\rm eff}$ and R of the IR sources are listed in Table 1.

4. Discussion

4.1. Variability and IR excess

For all 32 WDs in our sample, at least one archival light curve was available, and four objects were found to be photometrically variable. This implies a variability rate of 13^{+8}_{-4}%, which agrees with the variability rate of normal hot, H-rich WDs that do not exhibit the ultra-high excitation (UHE) phenomenon, of 14^{+6}_{-3}% as reported by Reindl et al. (2021). In the following paragraphs, we discuss stars that are either (possibly) photometrically variable or show IR excess, considering the origin of the variability and/or the excess.

WD 0232+035. Also known as Feige 24, WD 0232+035 is one of the most studied hot DA WDs, with its close binary nature long established (Greenstein & Eggen 1966). Contamination by the irradiated M dwarf is evident in the optical spectra as photospheric absorption (mainly TiO absorption bands) and chromospheric Balmer emission. In previous studies, phase-resolved spectroscopy in the optical and UV enabled the determination of the radial velocity (RV) curves of the M-dwarf and the WD, respectively, yielding an orbital period of 4.23 d (Vennes et al. 1991; Vennes & Thorstensen 1994; Gianninas et al. 2011; Guo et al. 2015).

We used PHOENIX models to reproduce the IR excess in the SED (Fig. 2), resulting in $T_{\rm eff}$ = 3710^{+70}_{-60} K and R = 0.395 ± 0.011 $R_\odot$ for the companion. This radius is slightly lower than the average radius of an M dwarf with the corresponding $T_{\rm eff}$ (Cifuentes et al. 2020). Kawka et al. (2008) reported R = 0.43 ± 0.02 $R_\odot$ for the secondary and classified it as an M2 dwarf.

We find that the TESS light curve of this object exhibits a 4.23 d variability, which can be detected in both 2 min and 20 s cadence data. The same period is also present in the *o*-band ATLAS light curve, but not in the *c*-band, possibly due to a low number of data points. Therefore, we phased the *c*-band light curve to the period detected in the *o*-band. Heinze et al. (2018) reported a period of 8.45 d from the ATLAS data and listed the variability as dubious. The LS periodogram on CSS data yielded 0.81 d as the strongest signal (log(FAP) = −10.75). However, 4.37 d is also one of the five most significant detected signals (log(FAP) = −9.28), to which we phased the CSS light curve. Moreover, the amplitude measured in the CSS light curves is not consistent with those determined from the TESS and ATLAS data.

Although light variation was previously detected with the Hubble Space Telescope (HST) Fine Guidance Sensor 3 (Benedict et al. 2000), to the best of our knowledge, the 4.23 d photometric period is reported here for the first time and is consistent with the system's orbital period inferred from phase-resolved spectroscopy (Thorstensen et al. 1978; Vennes et al. 1991; Vennes & Thorstensen 1994).

The H α emission varies with orbital phase, as expected for an irradiation(reflection) effect system; however, the shape of the light curve of WD 0232+035 (Fig. 1, lower left panel) does not resemble this at first glance (Schaffenroth et al. 2018, see their Fig. 1). In contrast, the observed saw-tooth light curve morphology is often indicative of rotational modulation due to

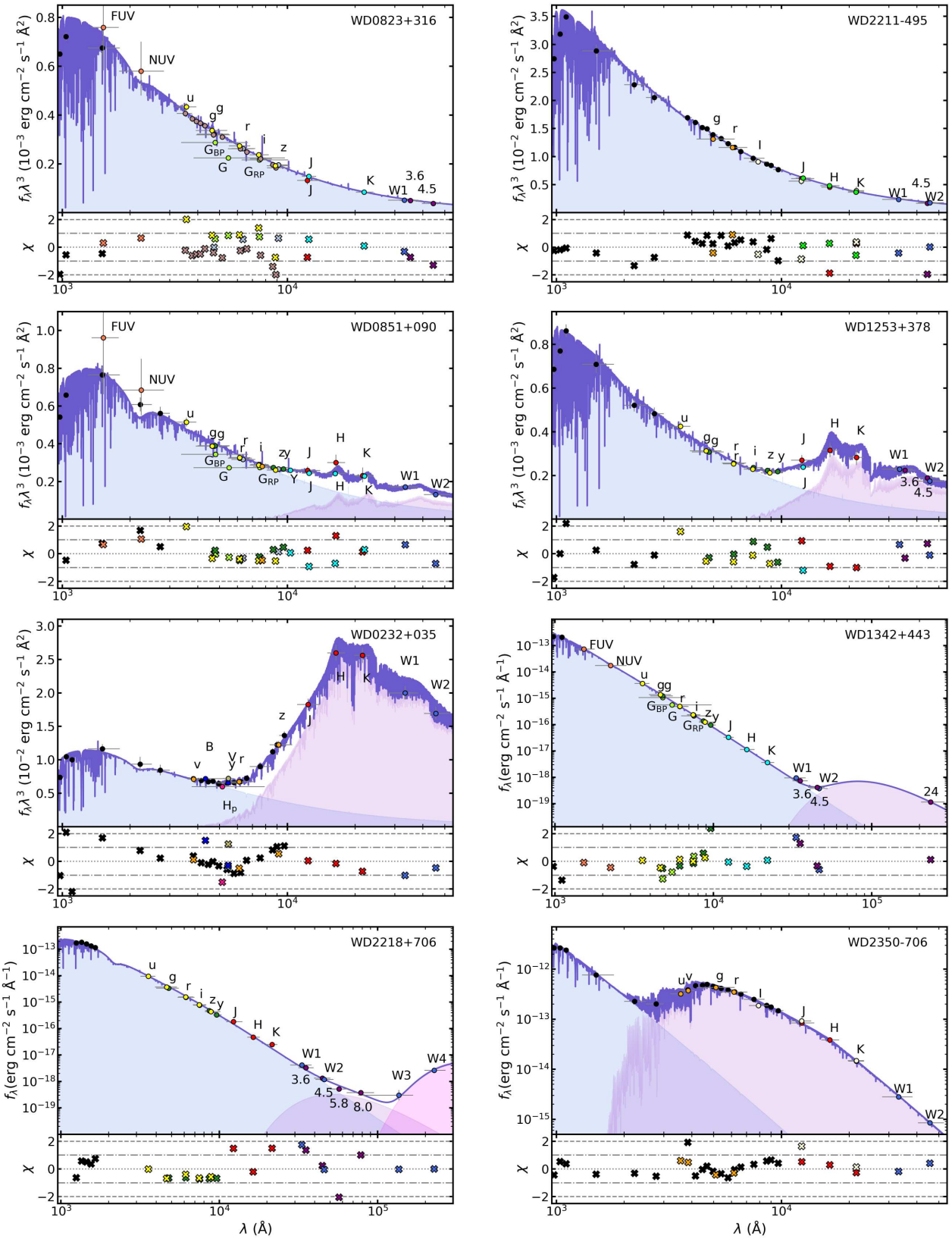


Fig. 2. Spectral energy distribution fits to the sample objects (top of each panel) and residuals to the fits (bottom of each panel). The top panels show the SED fits to a DAO (left column) and a DA (right column) WD that do not show an IR excess. The remaining panels (second row: DAO; third and fourth row: DA) depict objects with a near- and/or mid-IR excess modelled with our best fit TMAP models from Paper I and either a best-fit late-type star model from the PHOENIX grid or one or two blackbody component(s). Dots represent observations from different bands, whereas residuals are shown by crosses. Each colour represents a single survey or mission. The dark purple line shows the best-fit (combined) model. Blue and purple areas show the fluxes from the WD and the cool component, respectively. For clarity, the y axis of all panels are shown in the form $f_\lambda\,\lambda^3$, except for WD 1342+443, WD 2218+706, and WD 2350−706 where f_λ is shown on a logarithmic scale.

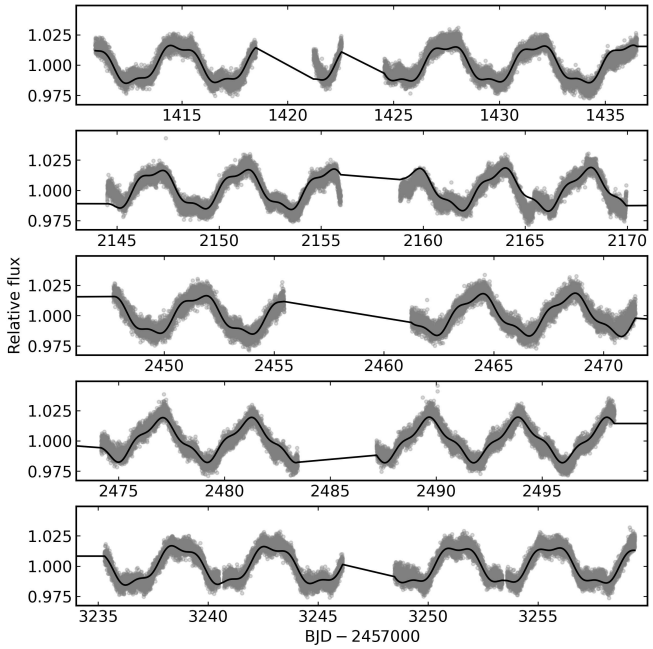


Fig. 3. Time-series TESS photometry (grey) of WD 0232+035. Each panel represents a TESS sector. A fit of a harmonic series, as a combination of two significant periods (4.23 and 1.39 d), to the entire TESS dataset is overplotted in black.

spots (Reindl et al. 2021). Interestingly, the light curve morphology does not remain constant throughout the TESS observations (Fig. 3), albeit with seemingly periodic repetitions (e.g. data from the start of sector 4, Fig. 3 upper panel, present a similar light curve morphology as the data from sector 71, Fig. 3 lower panel). Fitting and subtracting the dominant 4.23 d periodicity to the light curve using Period04 (Lenz & Breger 2005) reveals a second statistically significant periodicity at 1.39 d (approximately one third of the orbital period). The beating of these two signals likely causes the variation in light curve morphology.

A simulated light curve created with Phoebe2 (Prša et al. 2016; Conroy et al. 2020) suggests that the amplitude and phasing of the photometric variability at the orbital period may be consistent with irradiation. However, the origin of the shorter, lower amplitude 1.39 d periodicity is less clear. It may be due to spots, but this would imply that the spotted component of the binary is not tidally locked but rather rotating super-synchronously, which is not generally encountered in post-common envelope binaries (Nebot Gómez-Morán et al. 2011). We note that by respectively convolving the flux contributions of the WD and M-dwarf with the TESS spectral response function, we find that both components contribute equally to the observed flux in the TESS band. Intriguingly, the WD-main sequence (MS) binary LAMOST J172900.17+652952.8 was found to display somewhat similar variability, attributed by Zheng et al. (2022, see their Fig. 5) to strong stellar activity of the MS companion.

WD 0851+090. We did not detect any photometric variability for the DAO-type central star of planetary nebula (CSPN) Abell 31, consistent with the findings of Aller et al. (2024) based on their analysis of TESS light curves. However, we find an IR excess for this object (Fig. 2), whose origin had previously been attributed to an M4V companion (Ciardullo et al. 1999; Frew 2008; De Marco et al. 2013). We therefore performed a multi-component fit using the PHOENIX grid. We derive $T_{\rm eff} = 2920^{+210}_{-380}$ K and $R = 0.26^{+0.04}_{-0.04}\,R_\odot$ for the cool companion, values that are comparable to the average parameters of an M5 dwarf (Cifuentes et al. 2020). The system is not resolved by *Gaia*, but Ciardullo et al. (1999) derived a separation of 0.26 arcsec using HST imaging. Using the updated *Gaia* eDR3 parallax ($\varpi_{Gaia} = 1.86$ mas), we calculate a separation of 140 AU, which implies that the system is wide but physically bound and most likely did not undergo an interaction phase.

WD 1056+516. This DA WD is one of the two objects that show photometric variability in the ZTF dataset. Both *g*- and *r*-band light curves show a 0.11 d variability. No period is detected in the *i*-band (229 data points), likely because of the small amplitude of the light curve variability and/or because the object is fainter in the *i*-band than in the *g*- and *r*-bands. Notably, we find no statistically significant signal in the TESS light curves. However, this object may be too faint for TESS (G = 16.7 mag). Moreover, the low `crowdsap` value (0.24) indicates that most of the flux detected by TESS originates from nearby sources.

Since there is no significant difference between the amplitudes between the ZTF *g*- and *r*-bands and we did not detect any IR excess in the SED fit, an irradiation effect system seems unlikely. The presence of any hypothetical MS companion can also be excluded, as it would have been revealed by the SED fit. Therefore, the detected variability could be intrinsic. The occurrence of *g*-mode pulsations excited by the ϵ mechanism is theoretically predicted for hot H-rich post-asymptotic giant branch stars with initial solar metallicity (Kawaler 1988; Maeda & Shibahashi 2014) and for (pre-)WDs for subsolar progenitor metallicity (Calcaferro et al. 2017). However, the predicted periods (~40–200 s) are much shorter than the hour- to day-long periods that we detect for this object. Thus, pulsations can be ruled out as the source of the photometric variability in the present dataset.

Because our sample WDs are too hot to have convective atmospheres, a possible explanation for the observed variability is rotational modulation caused by surface inhomogeneities generated by magnetic fields. Aggregated metals near the magnetic poles are predicted to form bright spots in WD atmospheres (Hermes et al. 2017b), and such features have been detected in several hot WDs with $T_{\rm eff} > 30$ kK (Hermes et al. 2017a). Weak magnetic fields have also been linked to the UHE phenomenon observed in the optical spectra of hot WDs, which display photometric and spectroscopic variability due to geometrical effects of a wind-fed circumstellar magnetosphere and/or star spots (Reindl et al. 2019, 2021). Although no UHE lines appear present in the optical spectra of WD 1056+516, the detected periods and measured amplitudes of these two objects are quite similar to those of H-rich UHE variables (Reindl et al. 2023). The SDSS spectra show no evidence of Zeeman splitting; however, weaker (below 1 MG) magnetic field strengths could still lead to the formation of spots (Reindl et al. 2019). Finally, we note that with a period of 0.11 d, a mass of 0.66 $M_\odot$, and a radius of 0.011 $R_\odot$, the expected rotational velocity is only 5 km/s, and rotational broadening would therefore not be detectable in the available spectra.

WD 1253+378. Brown et al. (2011) reported this DAO WD as a spectroscopic binary with an M5 type companion. Using time-resolved spectroscopy, the same authors could not detect any significant RV variations larger than 20−30 km/s. The absence of RV variability is also supported by an earlier study by Good et al. (2005), who likewise failed to detect RV variations in the UV spectra of this WD. Brown et al. (2011) suggested that the system may either be a longer orbital period binary or a system that is viewed relatively pole-on. Chu et al. (2011) did not report any

excess in Spitzer 24 μm observations. The system is not resolved by *Gaia*, but the renormalised unit weight error (RUWE) from the *Gaia* DR3 is 1.20. This is slightly higher than the expected value of ∼1.0 for the single-star astrometric solution (Lindegren et al. 2018; Gaia Collaboration 2021).

We did not find photometric variability for WD 1253+378 in any dataset. This was also confirmed by Faedi et al. (2011) through their analysis of the WASP light curves. Heinze et al. (2018) reports a period of 2.64 d from ATLAS light curves, but this value is marked as dubious in their catalogue.

In our multicomponent SED fit we used PHOENIX models for the M-dwarf companion, finding $T_{\rm eff} = 3220^{+120}_{-100}$ K and $R = 0.337^{+0.022}_{-0.020}\,R_{\odot}$. Both the temperature and radius are consistent with those of an M4 dwarf located at the same distance as the WD. Therefore, the system is physically bound but, given the absence of RV and photometric variability, is most likely a wide binary.

WD 1342+443. We find that this DA WD shows a variability of 1.87 d in the ZTF *g*- and *r*-band light curves, which is, to the best of our knowledge, detected for the first time in this study. This period is not confirmed in the TESS data. Instead, we find a variability of 5.42 d, although TESS_localize did not confirm our WD as the source of this latter period. We stress that the `crowdsap` value is only 0.26, and given that WD 1342+443 is relatively faint ($G = 16.6$ mag), the non-detection of the low-amplitude ZTF variability in the TESS data is not surprising.

Chu et al. (2011) reported an excess in the Spitzer 24 μm band due to cold dust (≈150 K). We note that an IR excess is already apparent in the Spitzer IRAC 3.6 and 4.5 μm band observations (Barber et al. 2016), indicating an excess comparable to the *W1* and *W2* bands. We find that the mid-IR excess in all bands (including the Spitzer 24 μm band) can be reproduced with a blackbody temperature of 346 ± 17 K and a surface ratio of $(1.4^{+0.5}_{-0.4}) \times 10^5$ relative to the WD (Fig. 2).

The observed mid-IR excess may be caused by cool dust, which is likely the remnant of expelled mass during the asymptotic giant branch phase of the star (Clayton et al. 2014). Our temperature is slightly higher than that reported by Chu et al. (2011), which can be attributed to their lack of mid-IR observations except for 24 μm band. This cool dust must be located several AU from the star Chu et al. 2011), since, given the high $T_{\rm eff}$ of WD 1342+443, any dust material close to the star would be sublimated (von Hippel et al. 2007). A gaseous (debris) disc as the source of the mid-IR excess seems unlikely given the absence of the Ca II triplet, which is considered the most important marker of gaseous debris discs (Gänsicke et al. 2006).

Although the cool dust scenario explains the mid-IR excess well, it offers no explanation for the observed photometric variability. To search for hints of a close binary nature, we re-investigated the optical spectra of WD 1342+443. We find that the emission line complex around 4650 Å is clearly visible in the SDSS and BOSS spectra (Fig. B.1. These lines cannot originate from either the photosphere of the WD (Paper I), or from cold dust, whose associated emission lines would not be visible in the optical or NIR range. However, such lines are often seen in irradiation effect systems, where they are produced in the irradiated hemisphere of a cooler companion (e.g. Hillwig et al. 2017). Moreover, we identify another emission line at 7726 Å which may be due to Fe I (Fig. B.1). We stress that the signal-to-noise ratio (S/N) of the SDSS sub-spectra is insufficient to check for RV variations in either the weak emission lines or the WD absorption lines.

Furthermore, we investigated what type of hypothetical companion could be concealed in the observed SED using the BT-Settl model grid for low-mass stars and brown dwarfs (BDs; Allard et al. 2011). Our test indicates that any substellar companion later than L2.0 (∼1800 K, Cifuentes et al. 2020) could be hidden in the SED.

Only 0.5% of WDs are predicted to have a BD companion (Steele et al. 2011), and these are generally found around cooler WDs[6] ($T_{\rm eff} \leq 37$ kK, Lothringer & Casewell 2020). Several close WD+BD binaries are known in which the substellar companion is irradiated by the WD, and their periods range from ≈1 h − 1 d (Casewell et al. 2018, 2020; Rebassa-Mansergas et al. 2022; Casewell et al. 2024). We speculate that the 1.87 d period detected in WD 1342+443 may be related to its higher $T_{\rm eff}$, which could produce an irradiation effect even at longer orbital periods.

WD 2218+706. This DA WD was previously considered to be the central star of DeHt 5, later reported to be an HII region ionised by the same WD (Frew 2008; De Marco et al. 2013; Frew et al. 2016). Tweedy & Kwitter (1996) describe the surrounding environment as a dusty region. Near-IR and mid- IR excesses have been reported for this object (Frew 2008; Bilíková et al. 2012; De Marco et al. 2013). Our SED fit also reveals mid-IR excess, which we modelled with two blackbody components. The shorter wavelength component of the mid-IR excess can be reproduced with a blackbody temperature of 560^{+190}_{-210} K and a surface ratio of 1700^{+11000}_{-1100} relative to the WD, whereas a temperature of 80^{+16}_{-20} K and a surface ratio of $5^{+49}_{-4} \times 10^8$ are required to model the *W3* and *W4* bands. However, a large scatter in the residuals between ∼3–6 μm is noticeable (Fig. 2). These parameters are consistent with the presence of warm and cool dust (Chu et al. 2011). We do not detect any photometric variability for this object.

WD 2350−706. This DA WD is a component of a known non-interacting binary. Vennes et al. (1998) reported a constant RV on a short timescale. The system is not resolved by *Gaia* but was resolved with the HST (Barstow et al. 2001). Using the PHOENIX grid to reproduce the companion in the SED fit, we derive $T_{\rm eff} = 6280^{+50}_{-40}$ K and $R = 1.21^{+0.07}_{-0.07}\,R_{\odot}$. These values are consistent with previously reported parameters of an MS F-type star (Barstow et al. 1994; Vennes et al. 1998; Holberg et al. 2013). Our derived $T_{\rm eff}$ for the companion agrees with the reported values from the sixth data release of the Radial Velocity Experiment (RAVE) survey ($T_{\rm eff} = 6267$ K, Steinmetz et al. 2020) and the third data release of the *Gaia* mission ($T_{\rm eff} = 6261$ K, Gaia Collaboration 2022; De Angeli et al. 2023). The 1.38 d variability we find in the TESS light curve was also reported by Colman et al. (2024) and likely corresponds to the rotational period of an F-type star (Santos et al. 2021). Given the 0.574 arcsec separation reported by Barstow et al. (2001) and the zero-point corrected *Gaia* parallax $\varpi_{Gaia} = 6.69$ mas, we calculate a separation of 86 AU.

4.2. Kiel masses versus gravity masses

In Paper I, we used the atmospheric parameters measured from our spectroscopic analysis to interpolate masses from the evolutionary tracks of H-rich WDs by Renedo et al. (2010) in the

[6] Perhaps the only WD that challenges this convention is PG 1234+482 with $T_{\rm eff} \approx 55$ kK. However, the substellar nature of the companion is not confirmed, because the determined spectral type lies on the BD–dM boundary owing to uncertainties in the IR excess (Steele et al. 2007).

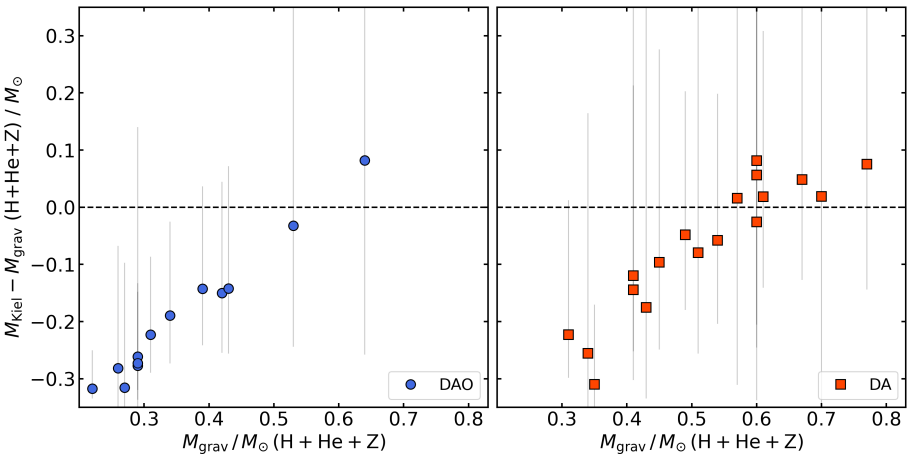


Fig. 4. Comparison between gravity and Kiel masses of DAO (blue) and DA (red) WDs. The dashed line represents a 1:1 comparison. Gravity masses were calculated using the radii and surface gravities derived by employing metal line blanketed models in the SED fits and spectral analysis, respectively.

Kiel diagram ($M_{\rm Kiel}$). In Sect. 3 in this paper, we additionally calculated gravity masses ($M_{\rm grav} = gR^2/G$) using the log g and R obtained from spectral analysis and SED fitting, respectively. Comparing[7] the results of these two methods revealed that gravity and Kiel masses agree within 1 σ for 83% (15/18) of DA and 38% (5/13) of DAO WDs in our sample.

The conspicuous disparity between Kiel and gravity masses, particularly for the DAO WDs, is evident in Fig. 4. This issue manifests systematically as a lower $M_{\rm grav}$ compared to $M_{\rm Kiel}$ in all cases where a statistical disagreement is identified. It is evident that DAO WDs are more severely affected by this problem than DAs, consistent with the findings of Reindl et al. (2023). We emphasise that unlike Reindl et al. (2023) who report only statistical errors from a metal-free χ^2 analysis, our errors also include systematic errors. Despite including systematic errors, the discrepancy between Kiel and gravity masses persists.

We consider Kiel masses to be more reliable than gravity masses. That is because the mean Kiel mass derived in Paper I ($\langle M_{\rm Kiel\text{-}DAO}\rangle = 0.55\ M_\odot$, $\sigma = 0.02\ M_\odot$) is close to the mean Kiel mass of DAs from Paper I ($\langle M_{\rm Kiel\text{-}DA}\rangle = 0.59\ M_\odot$, $\sigma = 0.05\ M_\odot$) and the mean Kiel masses for DAs reported by Gianninas et al. (2010), Bédard et al. (2020), and Reindl et al. (2023). Conversely, the mean gravity mass for DAOs in our sample ($\langle M_{\rm grav\text{-}DAO}\rangle = 0.36\ M_\odot$, $\sigma = 0.12\ M_\odot$) is significantly lower than the mean Kiel masses mentioned above, as well as the mean gravity mass for cool hydrogen-rich WDs ($\langle M_{\rm grav}\rangle = 0.61^{+0.14}_{-0.08}\ M_\odot$reported by Raddi et al. (2025).

The discrepancy between the mass determination methods based on theoretical tracks and those based on observed parallaxes is a known problem for hot WDs (Löbling et al. 2020; Reindl et al. 2023). The same issue also appears in other forms. Several studies have reported a mismatch between spectroscopic and parallax distances, with the former generally reported to be larger than the latter (Napiwotzki 2001; Rauch et al. 2007; Ziegler et al. 2012; Reindl et al. 2024). Although in good agreement overall, tests of the theoretical mass–radius relation[8] show that the radii and masses of hot WDs derived from parallax measurements and stellar spectroscopy tend to deviate more from theoretical predictions than those of cooler objects (Bédard et al. 2017; Tremblay et al. 2017; Joyce et al. 2018). In all of these studies, the larger uncertainties in the atmospheric parameters are considered to be the source of the observed spread, affecting both hot and cool WDs. Revisiting the results of Bédard et al. (2017), Bergeron et al. (2019) report that, in tests of the theoretical mass−radius relationship, the number of objects lying above the 1σ uncertainty level does not change substantially even after the release of the improved *Gaia* DR2 parallaxes.

Measuring atmospheric parameters of hot WDs is notoriously difficult because the analysis of their optical spectra is heavily hindered by the Balmer line problem (BLP; see Paper I and references therein). Reindl et al. (2023) argue that quantitative UV spectral analysis using metal line blanketed nonlocal thermodynamic equilibrium model atmospheres could improve the atmospheric parameters and thereby mitigate the mismatch between the masses determined via different methods. Contrary to these expectations, our study does not support this idea, in which we determined Kiel and gravity masses for the largest sample of the hottest WDs to date using the former method. In fact, including metal opacities seems to slightly worsen the discrepancy between Kiel and gravity masses. This is illustrated in Fig. 5, where we compare the gravity masses obtained from the SED fits using our fully metal line blanketed models from Paper I, with those obtained from the SED fits using the metal-free H+He grid from Reindl et al. (2023). The SED fits using the metal-free grid predict radii and gravity masses that are on average 54 and 10% higher, respectively, than those derived from fully metal line blanketed models. This occurs because models that include metals predict slightly higher fluxes from the far-UV to the near-IR compared to pure H+He models. Given the fixed $T_{\rm eff}$ and log g, this leads to a lower angular diameter compared to H+He models and, consequently, lower R and $M_{\rm grav}$ for a given observed flux and parallax. However, the differences in radii and gravity masses between the two methods are minor.

Neither photometric variability nor the presence of the IR excess appear to be correlated with the mass inconsistency. We also find no correlation between the mismatch with the values we derived for interstellar reddening (Table A.1). Conversely, a possible correlation may exist between $T_{\rm eff}$ and the occurrence of mass disagreement. While only 15% of the objects with $T_{\rm eff} \leq 70$ kK show mass disagreement, this value is 50% for objects above 70 kK. Since log g correlates directly with gravity mass, one might argue that log g values derived in Paper I are systematically underestimated. To test this argument, we increased log g of the sample WDs by 0.3 dex and recalculated the Kiel and gravity masses. However, this approach resulted in unrealistically

[7] WD 0455−282 was excluded from this comparison due to its unusual RUWE value of 8.65, which is not suitable for the single star astrometric solution implemented by *Gaia* (Lindegren et al. 2018; Gaia Collaboration 2021).

[8] WD 0232+025 was analysed in all mentioned mass−radius studies, whereas WD 2350−706 was only included in the sample of Joyce et al. (2018).

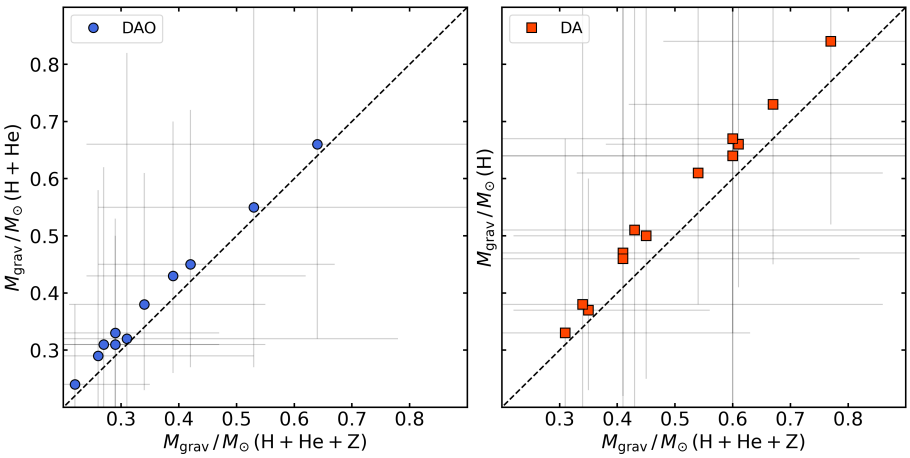


Fig. 5. Comparison of gravity masses obtained using metal line blanketed models and pure H and/or H+He models. The dashed line represents a 1:1 comparison.

large gravity masses for 65% of the objects, with differences of up to ~0.8 $M_\odot$ compared to Kiel masses. Although a tighter constraint on log g might mitigate the problem, a systematic error in the log g derivation is unlikely.

In addition to the impact of the results from the quantitative spectral analysis, parallax measurements from the *Gaia* mission might also influence the observed discrepancy. We find that 27% of objects with a parallax measurement larger than 5 mas show a mismatch between M_{grav} and M_{Kiel}, while this value is 40% for objects with parallaxes smaller than 5 mas. However, this may simply reflect the fact that the closest objects also tend to be cooler. As parallax increases, it is also unlikely that the mismatch is solely due to the zero-point correction (Reindl et al. 2023). We cannot identify a specific cause for the observed mass disagreement. Most likely, a combination of systematic uncertainties in the observations and in the atmospheric parameters is responsible for the detected inconsistency.

4.3. Evolution of He abundance in the Hertzsprung–Russell diagram

We conclude this section by discussing the measured luminosities of our sample WDs. Napiwotzki (1999) reported a decreasing He abundance with decreasing luminosity in their DAO-type CSPNe sample, which they interpreted as indirect evidence for radiation-driven winds. A similar correlation is evident in our sample, as shown in Fig. 6. The decline in He abundance with luminosity is apparent; at $L \approx 300\ L_\odot$, we observe approximately solar He abundance. A sharper decline begins at $L \approx 100\ L_\odot$. The characteristic change in He abundance is consistent with previous studies (Napiwotzki 1999; Unglaub & Bues 2000). Some scatter emerges at $L \approx 65\ L_\odot$, which is expected and occurs because the theoretically predicted termination of mass loss varies with different masses and initial metallicity (Unglaub & Bues 2000), as was also observationally confirmed in Paper I.

Finally, a clear separation of DAO and DA WDs is evident in the Hertzsprung-Russell diagram (HRD; Fig. B.2) consistent with that observed in the Kiel Diagram in Paper I. Our photometric results further reinforce the conclusion of our spectral analysis that all hydrogen-rich WDs are born as DAOs and transform into DA WDs as they cool.

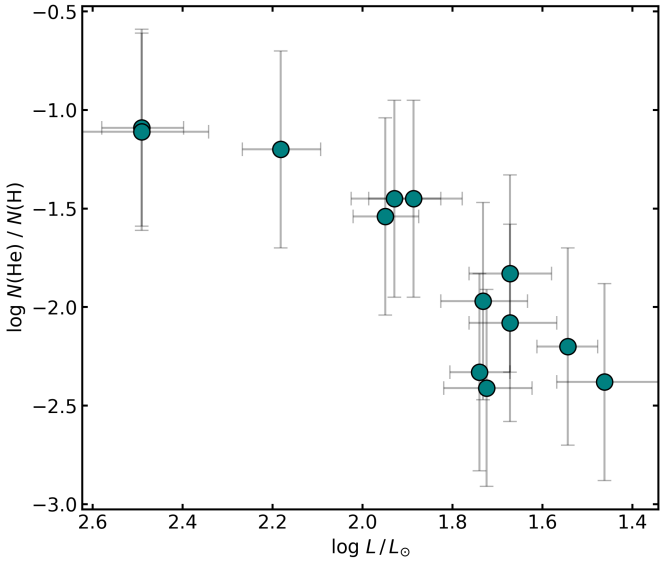


Fig. 6. Helium abundance - luminosity relation of the sample DAO WDs.

5. Summary and conclusions

We performed a photometric analysis of a sample of 19 DA and 13 DAO WDs with $T_{eff} > 60$ kK. All sample objects had at least one archival light curve available from TESS, ZTF, CSS, ATLAS, or *Gaia*. By searching for periodic signals in these datasets, we find that four of the 32 objects in our sample exhibit photometric variability. This corresponds to a variability rate of 13^{+8}_{-4}%, which agrees with the variability rate reported for H-rich, non-UHE WDs by Reindl et al. (2021). Furthermore, we analysed the SEDs of all WDs in our sample and identified an IR excess in six of 32 sample objects.

For the known close DA+dM binary system WD 0232+035, we report, for the first time, a photometric period of 4.23 d based on the TESS light curve. We find that the phase and amplitude of the 4.23 d photometric variability are consistent with expectations for irradiation of the companion. Moreover, we detect an additional lower-amplitude photometric variability with a period of 1.39 d which is roughly one third of the orbital period. The beating of these two signals produces an unusual light curve shape. The origin of the 1.39 d period remains unclear. We find that WD 1056+516 exhibits a 0.11 d variability in the ZTF g- and r-bands, with similar amplitudes in both bands. We speculate that this variability could be caused by a spot on the surface of the WD, due to the lack of an IR excess. One of the most notable discoveries is the photometric variability of

WD 1342+443, which exhibits similar, low-amplitude variations in the ZTF g- and r-bands with a period of 1.87 d. We have detected, for the first time, weak emission lines in the optical spectra of this object, which strongly suggests that it is an irradiation effect system. Our SED fit suggests that the mid-IR excess arises from cool dust (≈350 K) that must be located farther from the star. We also demonstrate that any companion with a spectral type earlier than L2.0 would be detectable in the SED, prompting speculation that WD 1342+443 may host an irradiated sub-stellar companion. Future IR and time-resolved spectroscopic observations are required to better characterise the system. For WD 2218+760 we show that the IR excess can be explained by warm (≈560 K) and cold (≈80 K) dust. Finally, we suggest that the 1.37 d period detected in WD 2350−706 likely corresponds to the rotational period of its wide F-type companion.

The SED fitting also yielded radii, luminosities and, in combination with $\log g$ from spectroscopy, gravity masses for the WDs. Consequently, the separation of DA and DAO WDs in the $T_{\rm eff}$ −$\log g$ plane seen in Paper I is also reproduced in the HRD. In addition, we reinvestigated a longstanding issue in the hottest WDs: the disagreement of Kiel and gravity masses. Specifically, for the first time in a large sample, we assessed if the inclusion of metal opacities in both spectroscopic analysis and SED fitting mitigates this problem. We find that, despite sophisticated metal line blanketed model atmosphere analysis, Kiel and gravity masses agree only in 65% of cases. In particular, for DAO WDs, the gravity masses appear unrealistically low, and, unexpectedly, including metal opacities mildly exacerbates the problem. Although we cannot resolve this problem, we note that this discrepancy worsens with increasing effective temperatures and possibly decreasing parallaxes. We strongly encourage further investigations into this issue.

Acknowledgements. We thank the referee for a constructive report that helped to improve the paper. We also thank Veronika Schaffenroth, and JJ Hermes for the helpful discussions. S.F. is supported by the Deutsches Zentrum für Luft- und Raumfahrt (DLR) through grant 50 OR 2315. N.R. is supported by the Deutsche Forschungsgemeinschaft (DFG) through grant RE3915/2-1. D.J. acknowledges support from the Agencia Estatal de Investigación del Ministerio de Ciencia, Innovación y Universidades (MCIU/AEI) under grant "Nebulosas planetarias como clave para comprender la evolución de estrellas binarias" and the European Regional Development Fund (ERDF) with reference PID-2022-136653NA-I00 (DOI:10.13039/501100011033). D.J. also acknowledges support from the Agencia Estatal de Investigación del Ministerio de Ciencia, Innovación y Universidades (MCIU/AEI) under grant "Revolucionando el conocimiento de la evolución de estrellas poco masivas" and the European Union NextGenerationEU/PRTR with reference CNS2023-143910 (DOI:10.13039/501100011033). P.S. acknowledges support from the Agencia Estatal de Investigación del Ministerio de Ciencia, Innovación y Universidades (MCIU/AEI) under grant "Revolucionando el conocimiento de la evolución de estrellas poco masivas" and the European Union NextGenerationEU/PRTR with reference CNS2023-143910 (DOI:10.13039/501100011033). M.D. was supported by the Deutsches Zentrum für Luft- und Raumfahrt (DLR) through grant 50-OR-2304. The TMAD (http://astro.uni-tuebingen.de/~TMAD) and TIRO tool (http://astro.uni-tuebingen.de/~TIRO) used for this paper was constructed as part of the activities of the German Astrophysical Virtual Observatory. This work has made use of data from the European Space Agency (ESA) mission *Gaia* (https://www.cosmos.esa.int/gaia), processed by the *Gaia* Data Processing and Analysis Consortium (DPAC, https://www.cosmos.esa.int/web/gaia/dpac/consortium). Based on observations obtained with the Samuel Oschin 48-inch Telescope at the Palomar Observatory as part of the Zwicky Transient Facility project. Supported by the National Science Foundation under Grants No. AST-1440341 and AST-2034437 and a collaboration including current partners Caltech, IPAC, the Oskar Klein Center at Stockholm University, the University of Maryland, University of California, Berkeley , the University of Wisconsin at Milwaukee, University of Warwick, Ruhr University, Cornell University, Northwestern University and Drexel University. Operations are conducted by COO, IPAC, and UW. This work includes data from the Asteroid Terrestrial-impact Last Alert System (ATLAS) project. ATLAS is primarily funded to search for near earth asteroids through NASA grants NN12AR55G, 80NSSC18K0284, and 80NSSC18K1575; byproducts of the NEO search include images and catalogs from the survey area. The ATLAS science products have been made possible through the contributions of the University of Hawaii Institute for Astronomy, the Queen's University Belfast, the Space Telescope Science Institute, and the South African Astronomical Observatory. The CSS survey is funded by the National Aeronautics and Space Administration under Grant No. NNG05GF22G issued through the Science Mission Directorate Near-Earth Objects Observations Program. The CRTS survey is supported by the U.S. National Science Foundation under grants AST0909182 and AST-1313422. The UHS is a partnership between the UK STFC, The University of Hawaii, The University of Arizona, Lockheed Martin and NASA. This paper includes data collected with the TESS mission, obtained from the MAST data archive at the Space Telescope Science Institute (STScI). Funding for the TESS mission is provided by the NASA Explorer Program. STScI is operated by the Association of Universities for Research in Astronomy, Inc., under NASA contract NAS 5–26555. This work made use of tpfplotter by J. Lillo-Box (publicly available in www.github.com/jlillo/tpfplotter), which also made use of the python packages astropy, lightkurve, matplotlib and numpy. This research has made use of NASA's Astrophysics Data System and the SIMBAD database, operated at CDS, Strasbourg, France. This research has made use of the VizieR catalogue access tool, CDS, Strasbourg, France. This research made use of TOPCAT, an interactive graphical viewer and editor for tabular data (Taylor 2005).

References

Alam, S., Albareti, F. D., Allende Prieto, C., et al. 2015, ApJS, 219, 12
Allard, F., Homeier, D., & Freytag, B. 2011, ASP Conf. Ser., 448, 91
Aller, A., Lillo-Box, J., Jones, D., Miranda, L. F., & Barceló Forteza, S. 2020, A&A, 635, A128
Aller, A., Lillo-Box, J., & Jones, D. 2024, A&A, 690, A190
Alonso-García, J., Saito, R. K., Hempel, M., et al. 2018, A&A, 619, A4
Aungwerojwit, A., Gänsicke, B. T., Rodríguez-Gil, P., et al. 2007, A&A, 469, 297
Barber, S. D., Belardi, C., Kilic, M., & Gianninas, A. 2016, MNRAS, 459, 1415
Barnett, J. W., Williams, K. A., Bédard, A., & Bolte, M. 2021, AJ, 162, 162
Barstow, M. A., Holberg, J. B., Fleming, T. A., et al. 1994, MNRAS, 270, 499
Barstow, M. A., Bond, H. E., Burleigh, M. R., & Holberg, J. B. 2001, MNRAS, 322, 891
Bédard, A., Bergeron, P., & Fontaine, G. 2017, ApJ, 848, 11
Bédard, A., Bergeron, P., Brassard, P., & Fontaine, G. 2020, ApJ, 901, 93
Bédard, A., Blouin, S., & Cheng, S. 2024, Nature, 627, 286
Bellm, E. C., Kulkarni, S. R., Barlow, T., et al. 2019, PASP, 131, 068003
Benedict, G. F., McArthur, B. E., Franz, O. G., et al. 2000, AJ, 119, 2382
Bergeron, P., Dufour, P., Fontaine, G., et al. 2019, ApJ, 876, 67
Bianchi, L., Shiao, B., & Thilker, D. 2017, ApJS, 230, 24
Bilíková, J., Chu, Y.-H., Gruendl, R. A., Su, K. Y. L., & De Marco, O. 2012, ApJS, 200, 3
Brinkworth, C. S., Marsh, T. R., Dhillon, V. S., & Knigge, C. 2006, MNRAS, 365, 287
Brown, J. M., Kilic, M., Brown, W. R., & Kenyon, S. J. 2011, ApJ, 730, 67
Calcaferro, L. M., Córsico, A. H., Camisassa, M. E., Althaus, L. G., & Shibahashi, H. 2017, EPJ Web Conf., 152, 06012
Casewell, S. L., Braker, I. P., Parsons, S. G., et al. 2018, MNRAS, 476, 1405
Casewell, S. L., Debes, J., Braker, I. P., et al. 2020, MNRAS, 499, 5318
Casewell, S. L., Burleigh, M. R., Napiwotzki, R., et al. 2024, MNRAS, 535, 753
Chu, Y.-H., Su, K. Y. L., Bilikova, J., et al. 2011, AJ, 142, 75
Ciardullo, R., Bond, H. E., Sipior, M. S., et al. 1999, AJ, 118, 488
Cifuentes, C., Caballero, J. A., Cortés-Contreras, M., et al. 2020, A&A, 642, A115
Clayton, G. C., De Marco, O., Nordhaus, J., et al. 2014, AJ, 147, 142
Colman, I. L., Angus, R., David, T., et al. 2024, AJ, 167, 189
Conroy, K. E., Kochoska, A., Hey, D., et al. 2020, ApJS, 250, 34
Cunningham, T., Tremblay, P.-E., & W. O'Brien, M. 2024, MNRAS, 527, 3602
De Angeli, F., Weiler, M., Montegriffo, P., et al. 2023, A&A, 674, A2
De Marco, O., Passy, J.-C., Frew, D. J., Moe, M., & Jacoby, G. H. 2013, MNRAS, 428, 2118
Drake, A. J., Djorgovski, S. G., Mahabal, A., et al. 2009, ApJ, 696, 870
Dye, S., Lawrence, A., Read, M. A., et al. 2018, MNRAS, 473, 5113
El-Badry, K., Rix, H.-W., & Heintz, T. M. 2021, MNRAS, 506, 2269
Eyer, L., Audard, M., Holl, B., et al. 2023, A&A, 674, A13
Faedi, F., West, R. G., Burleigh, M. R., Goad, M. R., & Hebb, L. 2011, MNRAS, 410, 899
Fazio, G. G., Hora, J. L., Allen, L. E., et al. 2004, ApJS, 154, 10
Filiz, S., Werner, K., Rauch, T., & Reindl, N. 2024, A&A, 691, A290
Fitzpatrick, E. L., Massa, D., Gordon, K. D., Bohlin, R., & Clayton, G. C. 2019, ApJ, 886, 108

Flewelling, H. A., Magnier, E. A., Chambers, K. C., et al. 2020, ApJS, 251, 7
Frew, D. J. 2008, PhD thesis, Macquarie University, Department of Physics and Astronomy, Australia
Frew, D. J., Parker, Q. A., & Bojičić, I. S. 2016, MNRAS, 455, 1459
Gaia Collaboration 2022, VizieR Online Data Catalog: Gaia DR3 Part 1. Main source (Gaia Collaboration, 2022), VizieR On-line Data Catalog: I/355
Gaia Collaboration (Brown, A. G. A., et al.) 2016, A&A, 595, A2
Gaia Collaboration (Brown, A. G. A., et al.) 2018, A&A, 616, A1
Gaia Collaboration (Brown, A. G. A., et al.) 2021, A&A, 649, A1
Gaia Collaboration (Vallenari, A., et al.) 2023, A&A, 674, A1
Gänsicke, B. T., Marsh, T. R., Southworth, J., & Rebassa-Mansergas, A. 2006, Science, 314, 1908
Genest-Beaulieu, C., & Bergeron, P. 2019, ApJ, 871, 169
Gentile Fusillo, N. P., Tremblay, P.-E., Gänsicke, B. T., et al. 2019, MNRAS, 482, 4570
Gentile Fusillo, N. P., Tremblay, P. E., Cukanovaite, E., et al. 2021, MNRAS, 508, 3877
Gianninas, A., Bergeron, P., Dupuis, J., & Ruiz, M. T. 2010, ApJ, 720, 581
Gianninas, A., Bergeron, P., & Ruiz, M. T. 2011, ApJ, 743, 138
Good, S. A., Barstow, M. A., Burleigh, M. R., Dobbie, P. D., & Holberg, J. B. 2005, MNRAS, 364, 1082
Greenstein, J. L., & Eggen, O. J. 1966, Vistas Astron., 8, 63
Guo, J., Zhao, J., Tziamtzis, A., et al. 2015, MNRAS, 454, 2787
Hartman, J. D., & Bakos, G. Á. 2016, Astron. Comp., 17, 1
Heber, U., Irrgang, A., & Schaffenroth, J. 2018, Open Astron., 27, 35
Heinze, A. N., Tonry, J. L., Denneau, L., et al. 2018, AJ, 156, 241
Hermes, J. J., Gänsicke, B. T., Gentile Fusillo, N. P., et al. 2017a, MNRAS, 468, 1946
Hermes, J. J., Kawaler, S. D., Bischoff-Kim, A., et al. 2017b, ApJ, 835, 277
Higgins, M. E., & Bell, K. J. 2023, AJ, 165, 141
Hillwig, T. C., Frew, D. J., Reindl, N., et al. 2017, AJ, 153, 24
Holberg, J. B., Oswalt, T. D., Sion, E. M., Barstow, M. A., & Burleigh, M. R. 2013, MNRAS, 435, 2077
Husser, T. O., Wende-von Berg, S., Dreizler, S., et al. 2013, A&A, 553, A6
Irrgang, A., Geier, S., Heber, U., et al. 2021, A&A, 650, A102
Jenkins, J. M., Twicken, J. D., McCauliff, S., et al. 2016, SPIE Conf. Ser., 9913, 99133E
Joyce, S. R. G., Barstow, M. A., Casewell, S. L., et al. 2018, MNRAS, 479, 1612
Kawaler, S. D. 1988, ApJ, 334, 220
Kawka, A., Vennes, S., Dupuis, J., Chayer, P., & Lanz, T. 2008, ApJ, 675, 1518
Law, N. M., Kulkarni, S. R., Dekany, R. G., et al. 2009, PASP, 121, 1395
Lenz, P., & Breger, M. 2005, Commun. Asteroseismol., 146, 53
Lindegren, L., Hernández, J., Bombrun, A., et al. 2018, A&A, 616, A2
Lindegren, L., Bastian, U., Biermann, M., et al. 2021, A&A, 649, A4
Löbling, L., Maney, M. A., Rauch, T., et al. 2020, MNRAS, 492, 528
Lothringer, J. D., & Casewell, S. L. 2020, ApJ, 905, 163
Maeda, K., & Shibahashi, H. 2014, PASJ, 66, 76
Marocco, F., Eisenhardt, P. R. M., Fowler, J. W., et al. 2021, ApJS, 253, 8
Martin, D. C., Fanson, J., Schiminovich, D., et al. 2005, ApJ, 619, L1
Masci, F. J., Laher, R. R., Rusholme, B., et al. 2019, PASP, 131, 018003
McMahon, R. G., Banerji, M., Gonzalez, E., et al. 2013, The Messenger, 154, 35
Napiwotzki, R. 1999, A&A, 350, 101
Napiwotzki, R. 2001, A&A, 367, 973
Nebot Gómez-Morán, A., Gänsicke, B. T., Schreiber, M. R., et al. 2011, A&A, 536, A43
Oliveira da Rosa, G., Kepler, S. O., Soethe, L. T. T., Romero, A. D., & Bell, K. J. 2024, ApJ, 974, 314
Onken, C. A., Wolf, C., Bessell, M. S., et al. 2019, PASA, 36, e033
Parsons, S. G., Marsh, T. R., Copperwheat, C. M., et al. 2010, MNRAS, 402, 2591
Press, W. H., Teukolsky, S. A., Vetterling, W. T., & Flannery, B. P. 1992, Numerical Recipes in C. The art of Scientific Computing (Cambridge: Cambridge University Press)
Prša, A., Conroy, K. E., Horvat, M., et al. 2016, ApJS, 227, 29
Raddi, R., Rebassa-Mansergas, A., Torres, S., et al. 2025, A&A, 695, A131
Rauch, T., Ziegler, M., Werner, K., et al. 2007, A&A, 470, 317
Rebassa-Mansergas, A., Xu, S., Raddi, R., et al. 2022, ApJ, 927, L31
Reindl, N., Bainbridge, M., Przybilla, N., et al. 2019, MNRAS, 482, L93
Reindl, N., Schaffenroth, V., Filiz, S., et al. 2021, A&A, 647, A184
Reindl, N., Islami, R., Werner, K., et al. 2023, A&A, 677, A29
Reindl, N., Bond, H. E., Werner, K., & Zeimann, G. R. 2024, A&A, 690, A366
Renedo, I., Althaus, L. G., Miller Bertolami, M. M., et al. 2010, ApJ, 717, 183
Ricker, G. R., Winn, J. N., Vanderspek, R., et al. 2015, J. Astron. Teles. Instrum. Syst., 1, 014003
Rieke, G. H., Young, E. T., Engelbracht, C. W., et al. 2004, ApJS, 154, 25
Riello, M., De Angeli, F., Evans, D. W., et al. 2021, A&A, 649, A3
Santos, A. R. G., Breton, S. N., Mathur, S., & García, R. A. 2021, ApJS, 255, 17
Schaffenroth, V., Geier, S., Heber, U., et al. 2018, A&A, 614, A77
Schlafly, E. F., Meisner, A. M., & Green, G. M. 2019, ApJS, 240, 30
Skrutskie, M. F., Cutri, R. M., Stiening, R., et al. 2006, AJ, 131, 1163
Steele, P. R., Burleigh, M. R., Dobbie, P. D., & Barstow, M. A. 2007, MNRAS, 382, 1804
Steele, P. R., Burleigh, M. R., Dobbie, P. D., et al. 2011, MNRAS, 416, 2768
Steen, M., Hermes, J. J., Guidry, J. A., et al. 2024, ApJ, 967, 166
Steinmetz, M., Guiglion, G., McMillan, P. J., et al. 2020, AJ, 160, 83
Taylor, M. B. 2005, ASP Conf. Ser., 347, 29
Thorstensen, J. R., Charles, P. A., Margon, B., & Bowyer, S. 1978, ApJ, 223, 260
Tonry, J. L., Denneau, L., Heinze, A. N., et al. 2018, PASP, 130, 064505
Tremblay, P. E., Gentile-Fusillo, N., Raddi, R., et al. 2017, MNRAS, 465, 2849
Tremblay, P. E., Cukanovaite, E., Gentile Fusillo, N. P., Cunningham, T., & Hollands, M. A. 2019, MNRAS, 482, 5222
Tweedy, R. W., & Kwitter, K. B. 1996, ApJS, 107, 255
Unglaub, K., & Bues, I. 2000, A&A, 359, 1042
Vennes, S., & Thorstensen, J. R. 1994, AJ, 108, 1881
Vennes, S., Thorstensen, J. R., Thejll, P., & Shipman, H. L. 1991, ApJ, 372, L37
Vennes, S., Christian, D. J., & Thorstensen, J. R. 1998, ApJ, 502, 763
von Hippel, T., Kuchner, M. J., Kilic, M., Mullally, F., & Reach, W. T. 2007, ApJ, 662, 544
Werner, K., & Dreizler, S. 1999, J. Comput. Appl. Math., 109, 65
Werner, K., & Herwig, F. 2006, PASP, 118, 183
Werner, K., Deetjen, J. L., Dreizler, S., et al. 2003, ASP Conf. Ser., 288, 31
Werner, K., Dreizler, S., & Rauch, T. 2012, Astrophysics Source Code Library [record ascl:1212.015]
Wright, E. L., Eisenhardt, P. R. M., Mainzer, A. K., et al. 2010, AJ, 140, 1868
Zechmeister, M., & Kürster, M. 2009, A&A, 496, 577
Zheng, L.-L., Gu, W.-M., Sun, M., et al. 2022, ApJ, 936, 33
Ziegler, M., Rauch, T., Werner, K., Köppen, J., & Kruk, J. W. 2012, A&A, 548, A109

Appendix A: Tables

Table A.1: Effective temperatures, surface gravities, radii, luminosities, gravity and Kiel masses, color excesses, *Gaia* parallaxes and RUWE factors of DAO and DA WDs.

Name	$T_{\rm eff}$ [kK]	log g [cm/s^2]	R [$R_\odot$]	L [$L_\odot$]	$M_{\rm grav}$ [$M_\odot$]	$M_{\rm Kiel}$ [$M_\odot$]	$E(44–55)$ [mag]	ϖ_{Gaia} [mas]	RUWE
				DAO					
Longmore1	118000 ± 5000	7.0 ± 0.3	$0.0419^{+0.0015}_{-0.0014}$	$310.0^{+70.0}_{-60.0}$	$0.64^{+0.70}_{-0.40}$	0.56 ± 0.06	$0.0236^{+0.0024}_{-0.0024}$	1.24 ± 0.05	1.08
WD 0439+466	97000 ± 5000	7.0 ± 0.2	$0.0243^{+0.0002}_{-0.0002}$	$47.0^{+11.0}_{-10.0}$	$0.22^{+0.13}_{-0.08}$	0.54 ± 0.06	$0.0439^{+0.0028}_{-0.0027}$	7.88 ± 0.07	0.65
WD 0500−156	104000 ± 6000	7.2 ± 0.2	$0.0270^{+0.0007}_{-0.0007}$	$77.0^{+20.0}_{-17.0}$	$0.42^{+0.25}_{-0.16}$	0.57 ± 0.06	$0.0608^{+0.0024}_{-0.0024}$	1.95 ± 0.05	1.06
WD 0615+556	101000 ± 5000	7.2 ± 0.2	$0.0223^{+0.0007}_{-0.0007}$	$47.0^{+11.0}_{-9.0}$	$0.29^{+0.18}_{-0.11}$	0.57 ± 0.05	$0.1270^{+0.0060}_{-0.0060}$	2.55 ± 0.07	0.98
WD 0823+316	98000 ± 4000	7.1 ± 0.2	$0.0251^{+0.0009}_{-0.0009}$	$53.0^{+13.0}_{-11.0}$	$0.29^{+0.18}_{-0.11}$	0.55 ± 0.05	$0.0270^{+0.0026}_{-0.0026}$	1.81 ± 0.07	1.02
WD 0834+500	90000 ± 3000	7.0 ± 0.3	$0.0306^{+0.0010}_{-0.0009}$	$55.0^{+9.0}_{-8.0}$	$0.34^{+0.21}_{-0.13}$	0.53 ± 0.05	$0.0496^{+0.0026}_{-0.0026}$	1.95 ± 0.06	1.03
WD 0851+090	106000 ± 5000	7.2 ± 0.2	$0.0273^{+0.0010}_{-0.0009}$	$85.0^{+21.0}_{-18.0}$	$0.43^{+0.28}_{-0.18}$	0.57 ± 0.07	$0.0616^{+0.0025}_{-0.0026}$	1.86 ± 0.06	1.03
WD 1111+552	110000 ± 5000	7.1 ± 0.3	$0.0339^{+0.0015}_{-0.0014}$	$152.0^{+33.0}_{-28.0}$	$0.53^{+0.54}_{-0.27}$	0.56 ± 0.06	$0.0100^{+0.0040}_{-0.0040}$	1.23 ± 0.05	1.04
WD 1214+267	91000 ± 3000	7.1 ± 0.3	$0.0240^{+0.0009}_{-0.0008}$	$35.0^{+6.0}_{-5.0}$	$0.26^{+0.27}_{-0.14}$	0.54 ± 0.06	$0.0151^{+0.0020}_{-0.0020}$	2.10 ± 0.08	1.27
WD 1253+378	93000 ± 4000	7.0 ± 0.2	$0.0282^{+0.0012}_{-0.0011}$	$54.0^{+13.0}_{-11.0}$	$0.29^{+0.19}_{-0.12}$	0.53 ± 0.05	$0.0143^{+0.0025}_{-0.0026}$	1.61 ± 0.06	1.20
WD 1957+225	134000 ± 10000	6.9 ± 0.4	$0.0325^{+0.0006}_{-0.0006}$	$310.0^{+110.0}_{-90.0}$	$0.31^{+0.47}_{-0.19}$	0.56 ± 0.06	$0.0410^{+0.0040}_{-0.0040}$	2.57 ± 0.05	1.16
WD 2226−210	120000 ± 5000	7.2 ± 0.3	$0.0218^{+0.0002}_{-0.0002}$	$89.0^{+16.0}_{-14.0}$	$0.27^{+0.28}_{-0.14}$	0.59 ± 0.06	$0.0102^{+0.0250}_{-0.0250}$	5.01 ± 0.06	0.95
WD 2342+806	83000 ± 5000	7.2 ± 0.2	$0.0259^{+0.0003}_{-0.0003}$	$29.0^{+8.0}_{-7.0}$	$0.39^{+0.23}_{-0.15}$	0.53 ± 0.05	$0.0638^{+0.0022}_{-0.0022}$	3.45 ± 0.04	1.01
				DA					
WD 0027−636	59000 ± 5000	8.0 ± 0.2	$0.0146^{+0.0001}_{-0.0001}$	$2.3^{+0.9}_{-0.7}$	$0.77^{+0.46}_{-0.29}$	0.69 ± 0.07	$0.0137^{+0.0025}_{-0.0025}$	5.09 ± 0.04	1.01
WD 0229−481	62000 ± 5000	7.8 ± 0.2	$0.0171^{+0.0002}_{-0.0001}$	$3.9^{+1.5}_{-1.2}$	$0.67^{+0.40}_{-0.25}$	0.62 ± 0.07	$0.0100^{+0.0040}_{-0.0040}$	5.93 ± 0.04	1.04
WD 0232+035	63000 ± 3000	7.5 ± 0.2	$0.0207^{+0.0003}_{-0.0003}$	$6.1^{+1.4}_{-1.2}$	$0.49^{+0.32}_{-0.20}$	0.54 ± 0.07	$0.0390^{+0.0040}_{-0.0040}$	12.91 ± 0.05	1.58
WD 0311+480	70000 ± 5000	7.3 ± 0.4	$0.0285^{+0.0004}_{-0.0004}$	$18.0^{+13.0}_{-9.0}$	$0.60^{+0.90}_{-0.40}$	0.52 ± 0.11	$0.1360^{+0.0050}_{-0.0050}$	4.34 ± 0.05	1.14
WD 0343−007	63000 ± 4000	7.7 ± 0.2	$0.0183^{+0.0002}_{-0.0002}$	$4.7^{+1.4}_{-1.1}$	$0.61^{+0.36}_{-0.23}$	0.59 ± 0.07	$0.0547^{+0.0017}_{-0.0017}$	4.96 ± 0.06	1.08
WD 0455−282	66000 ± 3000	7.5 ± 0.2	$0.0166^{+0.0007}_{-0.0007}$	$4.7^{+1.1}_{-0.9}$	$0.32^{+0.20}_{-0.12}$	0.55 ± 0.05	$0.0180^{+0.0040}_{-0.0040}$	8.00 ± 0.40	8.65
WD 0615+655	83000 ± 10000	7.6 ± 0.4	$0.0171^{+0.0003}_{-0.0003}$	$13.0^{+8.0}_{-6.0}$	$0.43^{+0.65}_{-0.26}$	0.61 ± 0.10	$0.0930^{+0.0040}_{-0.0040}$	2.92 ± 0.05	0.97
WD 0621−376	65000 ± 3000	7.5 ± 0.4	$0.0232^{+0.0001}_{-0.0001}$	$8.7^{+1.8}_{-1.5}$	$0.60^{+1.00}_{-0.40}$	0.54 ± 0.10	$0.0051^{+0.0018}_{-0.0018}$	13.09 ± 0.05	0.97
WD 0939+262	66000 ± 3000	7.7 ± 0.2	$0.0173^{+0.0002}_{-0.0002}$	$5.1^{+1.0}_{-0.9}$	$0.54^{+0.32}_{-0.21}$	0.60 ± 0.06	$0.0298^{+0.0023}_{-0.0023}$	5.46 ± 0.06	1.14
WD 1056+516	63000 ± 5000	7.9 ± 0.2	$0.0110^{+0.0003}_{-0.0002}$	$1.7^{+0.7}_{-0.5}$	$0.35^{+0.21}_{-0.13}$	0.66 ± 0.07	$0.0127^{+0.0023}_{-0.0023}$	3.41 ± 0.08	0.97
WD 1342+443	62000 ± 5000	7.7 ± 0.3	$0.0167^{+0.0005}_{-0.0005}$	$3.7^{+1.4}_{-1.1}$	$0.51^{+0.52}_{-0.26}$	0.59 ± 0.08	$0.0183^{+0.0015}_{-0.0015}$	2.33 ± 0.07	1.08
WD 1738+669	78000 ± 6000	7.6 ± 0.4	$0.0154^{+0.0001}_{-0.0001}$	$7.9^{+2.8}_{-2.2}$	$0.34^{+0.52}_{-0.21}$	0.60 ± 0.10	$0.0156^{+0.0018}_{-0.0018}$	5.82 ± 0.04	1.07
WD 1827+778	78000 ± 10000	7.4 ± 0.4	$0.0212^{+0.0004}_{-0.0004}$	$15.0^{+10.0}_{-7.0}$	$0.41^{+0.63}_{-0.25}$	0.55 ± 0.09	$0.0989^{+0.0030}_{-0.0030}$	2.31 ± 0.04	1.01
WD 2046+396	64000 ± 5000	7.8 ± 0.3	$0.0164^{+0.0001}_{-0.0001}$	$4.0^{+1.5}_{-1.2}$	$0.60^{+0.70}_{-0.40}$	0.63 ± 0.09	$0.0244^{+0.0027}_{-0.0027}$	6.76 ± 0.04	1.10
WD 2146−433	66000 ± 4000	7.5 ± 0.3	$0.0197^{+0.0004}_{-0.0004}$	$6.7^{+1.8}_{-1.5}$	$0.45^{+0.45}_{-0.23}$	0.55 ± 0.08	$0.0208^{+0.0029}_{-0.0029}$	2.93 ± 0.05	1.00
WD 2211−495	68000 ± 4000	7.4 ± 0.3	$0.0211^{+0.0001}_{-0.0000}$	$8.6^{+2.3}_{-1.9}$	$0.41^{+0.41}_{-0.21}$	0.53 ± 0.08	$0.0005^{+0.0018}_{-0.0005}$	17.02 ± 0.06	1.28
WD 2218+706	78000 ± 5000	7.4 ± 0.3	$0.0249^{+0.0010}_{-0.0008}$	$20.1^{+7.0}_{-6.0}$	$0.57^{+0.70}_{-0.40}$	0.55 ± 0.07	$0.1640^{+0.0140}_{-0.0120}$	2.99 ± 0.04	1.22
WD 2350−706	75000 ± 5000	7.9 ± 0.3	$0.0155^{+0.0008}_{-0.0004}$	$6.9^{+2.6}_{-2.1}$	$0.70^{+0.90}_{-0.50}$	0.68 ± 0.09	$0.0020^{+0.0088}_{-0.0020}$	6.69 ± 0.03	1.57
WD 2353+026	61000 ± 5000	7.5 ± 0.3	$0.0164^{+0.0004}_{-0.0004}$	$3.4^{+1.3}_{-1.0}$	$0.31^{+0.32}_{-0.16}$	0.53 ± 0.08	$0.0325^{+0.0028}_{-0.0028}$	3.64 ± 0.08	1.11

Notes. $T_{\rm eff}$, log g, and $M_{\rm Kiel}$ were derived in Paper I, whereas R, L, and $M_{\rm grav}$ were derived in this paper.

Appendix B: Figures

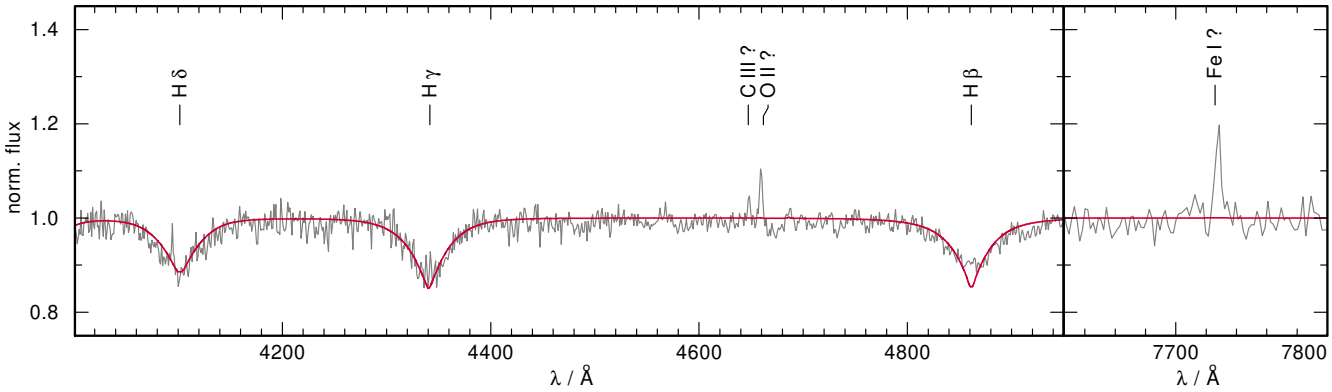


Fig. B.1: BOSS spectrum of WD 1342+443 (grey) and the best fit TMAP model (red, $T_{\rm eff}$ = 62 kK and log g = 7.7) from Paper I.

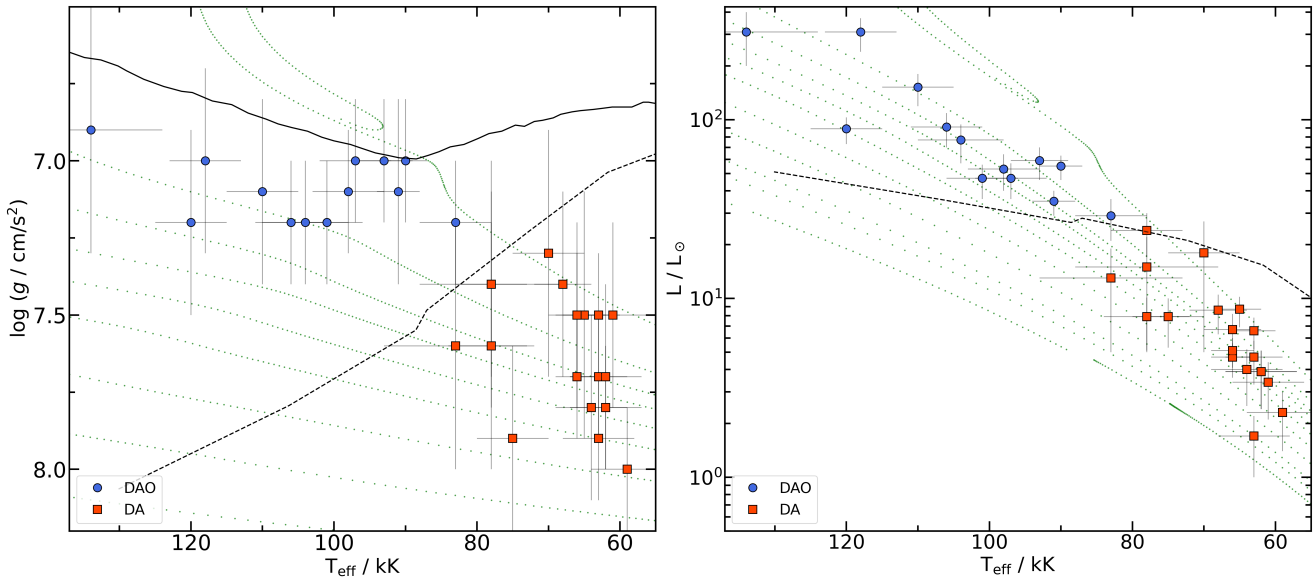


Fig. B.2: Sample WDs shown in the Kiel diagram (left) and HRD (right). Solid black line in the left panel corresponds to the theoretical wind limit by (Unglaub & Bues 2000). Dashed black lines in both panels represent predicted He abundance (N(He)/N(H) = 10^{-3}) in the cooling sequence by the same authors, which also matches with the approximate optical detection limit of He. Green dotted lines (left: 0.525, 0.570, 0.593, 0.609, 0.632, 0.659, 0.705, 0.767, and 0.837 $M_{\odot}$, right: 0.525 - 0.935 $M_{\odot}$) represent evolutionary tracks of H-rich WDs (Z = 0.01) from Renedo et al. (2010).